ABSTRACT

Title of dissertation: INSTABILITIES OF JOINED-WING AIRCRAFT USING ACCELERATED AEROELASTIC SIMULATIONS

Abu Bockarie Kebbie-Anthony
Doctor of Philosophy, 2021

Dissertation directed by: Professor Balakumar Balachandran
Department of Mechanical Engineering
Professor Shapour Azarm
Department of Mechanical Engineering

Several unmanned aircraft systems (UASs) have been and are being designed with long, thin flexible wings, such as the joined-wing SensorCraft, to enhance the operational capabilities. However, due to the long slender wings, these systems are susceptible to aeroelastic instabilities, such as flutter. Thus, there is a need for addressing nonlinear aeroelasticity and handling instabilities and post-instability behavior. Nonlinear aeroelastic models can be quite computationally expensive. In this dissertation, a nonlinear aeroelastic computational model is developed for the joined-wing SensorCraft and simulations are carried out in a co-simulation framework.

The aeroelastic model is composed of an unsteady vortex lattice method (UVLM) based aerodynamic model and a finite element based structural model for the joined-wing SensorCraft. Through computational cost profiling of the aeroelastic model, it is determined that the aerodynamic processes are the most computation-

ally expensive. This means that the focus of the attempts to accelerate aeroelastic computations should be on the aerodynamic computations. Specifically, computations of the field point velocities are found to increase the computational workload as the wake grows over time.

In this dissertation, the fast multipole method (FMM) algorithm has been integrated with the UVLM based aerodynamic model to reduce the computational workload of evaluating the wake velocities. Furthermore, an aeroelastic computational model for the joined-wing SensorCraft has been developed by using the accelerated aerodynamic model and a structural model. Flutter boundaries for various structural health conditions have been determined with respect to parameters such as freestream speed, freestream direction, and freestream density.

In terms of contributions, this is the first effort in which the speedup capabilities of FMM accelerated vortex methods have been carried out and used in nonlinear, unsteady UVLM based schemes. Also, computational studies on nonlinear aeroelastic behavior of joined-wing aircraft have been carried out to examine dynamic instabilities and the effects of structural degradation on these instabilities. Although the joined-wing SensorCraft has been used as an illustrative application, it is believed that the present work can be relevant to many other UASs. In addition, the aeroelastic computations can be useful for integration for data-driven dynamic application systems meant for UAS decision making applications.

INSTABILITIES OF JOINED-WING AIRCRAFT USING ACCELERATED AEROELASTIC SIMULATIONS

by

Abu Bockarie Kebbie-Anthony

Dissertation submitted to the Faculty of the Graduate School of the
University of Maryland, College Park in partial fulfillment
of the requirements for the degree of
Doctor of Philosophy
2021

Advisory Committee:
Professor Balakumar Balachandran, Chair/Advisor, Mechanical Engineering
Professor Shapour Azarm, Co-advisor, Mechanical Engineering
Professor James Baeder, Dean's Representative, Aerospace Engineering
Professor Peter Chung, Mechanical Engineering
Research Professor Nail Gumerov, UMIACS
Associate Professor Amir Riaz, Mechanical Engineering

Acknowledgments

First and foremost, I would like to thank my advisors Professor Balakumar Balachandran and Professor Shapour Azarm, who have supported me throughout my time at the University of Maryland. Thanks to their incredible amount of patience and understanding, especially, during the initial years of my dissertation research, I was able to accomplish as much as I did. I would express my deepest gratitude to thank Dr. Sergio Preidikman for the guidance and support he provided me during this dissertation work. I would also like to thank the members of my committee, Dr. Nail Gumerov, Dr. Peter Chung, Dr. Amir Riaz, and Dr. Baeder, for reviewing this PhD dissertation and providing valuable comments and suggestions.

In addition, I would like to express my gratitude to all my peers from the Design Decision Support lab, Computational Dynamics lab, Dynamics and Controls lab, and Vibrations lab for many helpful discussions and resource sharing.

I am thankful for all the funding agencies that supported this work. This includes the U.S. Air Force Office of Scientific Research DDDAS Program (Grant No. FA9550150134), the U.S. National Science Foundation (Grant No. CMMI-1250187). I am also grateful and proud of receiving support from the Minta Martin Foundation.

Lastly, I thank my family and friends who have been with through this journey for their unconditional support and love.

Table of Contents

List of Tables

List of Figures

Nomenclature

A	area of wing cross section
$A^h(\mathbf{r}, t)$	vector potential of fluid particle (field point) $\mathbf{r}$ due to far-field interactions at time t for each Cartesian component $(h = 1, 2, 3)$
${}^t\mathbf{A}$	aerodynamic influence coefficient matrix at time t
${}^t\mathbf{b}$	right hand side vector at time t
$\mathbf{A}(\mathbf{L}, \mathbf{r})$	velocity field kernel corresponding to vortex segment $\mathbf{L}$ and field point $\mathbf{r}$
c_D	drag coefficient for lifting surface
c_{D_i}	induced drag coefficient for lifting surface
c_L	lift coefficient for lifting surface
c_N	normal force coefficient for lifting surface
$C^m_{(i)n}$	expansion coefficients for vector potential
∂_t	partial time derivative
d_n	size of box in nth level of octree subdivision
$D^{(h)m}_n$	local expansion coefficients for each Cartesian component $(h = 1, 2, 3)$
$\hat{\mathbf{e}}_{1i}, \hat{\mathbf{e}}_{2i}$	unit vectors of $\mathbf{r}_{1i}$ and $\mathbf{r}_{2i}$, respectively
E	Young's modulus
$F_S(t), F_A(t)$	structural nodal forces and aerodynamic control point forces at time t, respectively
G	shear modulus
$G(\mathbf{r}, \mathbf{r}')$	multipole expansion of a monopole source located at $\mathbf{r}'$ for field point $\mathbf{r}$
$G(t)$	circulation of vortex ring at time t
${}^t\mathbf{G}$	vector vortex ring circulations at time t
h_e	structural element length

I_P	polar moment of inertia of wing cross section
I_y	planar moment of inertia about y-axis of wing cross section
I_z	planar moment of inertia about z-axis of wing cross section
J_T	torsion constant of wing cross section
k	time step index
k_i	modal stiffnesses
K	total number of time steps
$\mathbf{K}$	global stiffness matrix of structural model
l	level in the octree
$\mathbf{l}_i$	unit vector of $\mathbf{L}_i$
$\mathbf{L}$	vector along vortex segment
L	characteristic length
M	total number of field points (receivers)
$\mathbf{M}$	global mass matrix of structural model
$\hat{\mathbf{n}}$	unit vector normal to surface
n_S	number of nodal points in structural mesh
n_A^{cp}, n_A^{np}	number of panels and nodal points in aerodynamic mesh, respectively
N	total number of vortex segments (sources)
N_b	size of relatively small body meshes
N_q	order of Gauss-Legendre quadrature of FMM algorithm
$N_n^{(R)m}, N_n^{(S)m}$	normalization coefficient for regular and singular spherical basis function, respectively
$p(\mathbf{r}, t)$	pressure associated with fluid particle (field point) $\mathbf{r}$ at time t
p_F	truncation number of FMM algorithm
$\mathbf{q}(t)$, $\ddot{\mathbf{q}}(t)$	modal displacement and acceleration vectors
$\mathbf{r}$	position vector to fluid particle

$\mathbf{r}_{1i}, \mathbf{r}_{2i}$	position vectors from endpoints of vortex segment to field point $\mathbf{r}$
$\mathbf{r}_c$	center of receiver box
$\text{res}(\cdot)$	residual function
(r, θ, ϕ)	spherical coordinates of field point $\mathbf{r}$
$R_n^m(\mathbf{r}), S_n^m(\mathbf{r})$	regular and singular spherical basis function of field point $\mathbf{r}$, respectively
s	clustering parameter of FMM algorithm
S_2	global reference frame of aerodynamic and structural dynamic models
S_3	local reference frame of right forward wing
S_4	local reference frame of right aft wing
S_5	local reference frame of left forward wing
S_6	local reference frame of left aft wing
t	nondimensional computational time
t^*	physical time
T_c	characteristic time
$u_{1,2,3}$	structural nodal translations
$\mathbf{u}_S(t)$	generalized structural nodal displacements at time t
$\mathbf{u}_A^{np}(t), \dot{\mathbf{u}}_A^{cp}(t)$	generalized aerodynamic nodal displacements and control point velocities at time t, respectively
$\mathbf{V}(\mathbf{r}, t)$	velocity field of field point $\mathbf{r}$ at time t
$\mathbf{V}_\infty$	freestream velocity
$\mathbf{V}_{Body}$	velocity of body's surface
$\mathbf{V}_B(\mathbf{r}, t)$	velocity field associated with vorticity in boundary layers on body surface of field point $\mathbf{r}$ at time t
V_C	characteristic velocity

$\mathbf{V}_W(\mathbf{r}, t)$	velocity field associated with vorticity in free-vortex shed from wing's trailing edge of field point $\mathbf{r}$ at time t
w_a	weights for Gauss-Legendre quadrature
$W(t)$	total energy per unit mass at time t
$Y_n^m(\theta, \phi)$	spherical harmonics
α	yaw freestream angle
β	pitch freestream angle
Δt	change in time
δ	cutoff radius (radius of influence)
$\Gamma(t)$	circulation of vortex segment at time t
ν	Poisson's ratio
ϕ	roll freestream angle
$\varphi(\mathbf{r}, t)$	scalar velocity potential fluid particle $\mathbf{r}$ at time t
ρ	fluid density
ρ_m	structural material density
ρ_C	characteristic density
$\theta_{1,2,3}$	structural nodal rotations
ξ_a	abscissas for Gauss-Legendre quadrature

Acronyms

DDDAS	Dynamic Data-Driven Application Systems
DOF	Degrees of Freedom
DSS	Decision Support System
FE	Finite Element
FFT	Fast Fourier Transform
FMM	Fast Multipole Method

GPU	Graphics Processing Unit
HPC	High-Performance Computing
LCO	Limit Cycle Oscillation
MFC	Multi-Freedom Constraint
RHS	Right Hand Side
UAS	Unmanned Aircraft System
UVLM	Unsteady Vortex Lattice Method

Chapter 1: Introduction

In this chapter, the background and motivation of this dissertation is discussed. The overall research goal and the research questions to be addressed in this work are defined. Through a review of the literature, the research gaps and needs, which are addressed in this dissertation, are identified. To close the chapter, the organization of the dissertation is stated.

1.1 Background and Motivation

Mission success of unmanned aircraft systems (UASs) can be adversely influenced by unforeseen system responses and environmental conditions. For certain operational and environmental conditions, an UAS may be quite susceptible to aeroelastic instabilities, such as flutter. If an UAS is subjected to an aeroelastic instability for a long enough period of time, it can fail depending on the material properties and design of the aircraft and nature of the instability. With the increase in usefulness and demand for surveillance and observation platforms and data collection drones that have high aspect ratio wings for efficiency, the important need to model and predict aeroelastic instabilities is increased. This is because the increased aspect ratio results in high flexibility and brings forth the necessity for consideration

Figure 1.1: Boeing joined-wing SensorCraft design. [1]

of aeroelastic loads to provide realistic estimates of the aerodynamic performance and response of the aircraft. Predicting the onset of aeroelastic instabilities, such as flutter, can become more challenging due to variations in aircraft store configurations or external instrumentation. For thin wing airframes, such as the Boeing joined-wing SensorCraft [2, 3] shown in Figure 1.1, designed for efficient flight and long loiter times, flutter can be extremely limiting for operations. Thus, accurate offline estimation of flight envelopes and real-time dynamic flight envelop prediction based on in-situ conditions and mission requirements can help significantly increase mission capabilities.

Even though many tools are available to predict coupled aerodynamic-structural loads, these tools are typically limited to the linear regime for aerodynamic and structural force predictions. Systems with flexible wings can exhibit complex motions [4] and these behaviors, which tend to be nonlinear, cannot be sufficiently captured by a weak coupling of structural dynamics and aerodynamics. Nonlinear aeroelastic models tend to be very computationally expensive but they are needed to capture post-critical aeroelastic behavior and these models can be used to estimate reliable margins for aeroelastic instabilities; that is, to generate a safe maneuvering envelope. In this regard, there is an urgent need to develop a fast, accurate, and reliable nonlinear aeroelastic computational model model based on fully couple aerodynamics, structural dynamics, and nonlinear analysis. This is addressed in this dissertation work.

1.2 Problem Definition and Research Questions

The overall goal of this dissertation is to construct estimates of the aeroelastic stability envelope of the joined-wing SensorCraft by developing accelerated nonlinear aeroelastic computational abilities. The proposed stability envelope is expected to capture static and dynamic events, and the stability information will include post-instability motions, such as limit cycle oscillations (LCOs). With the aeroelastic computational model, the effects of wing damage on flutter boundary can also be investigated. To address the research goal, the following research questions will be addressed:

RQ1. ***How can the unsteady aerodynamics model be accelerated via an algorithmic approach and hardware support and how much speedup can be achieved?*** This question will be addressed in Chapter 2. It will be shown that the most computational expensive components of the aeroelastic model are in the aerodynamic model.

RQ2. ***How can the influence of structural wing damage be accounted for in the joined-wing aircraft structural model?*** Along with the development of the structural model, this question is addressed in Chapter 3.

RQ3. ***How can the accelerated aerodynamics model and structural dynamics model be integrated to construct the aeroelastic computational model for the joined-wing aircraft?*** The procedure used to combine the two models is presented in Chapter 4.

RQ4. ***How to determine the critical flutter speed and post-flutter motion of the joined-wing aircraft using computational aeroelasticity simulations?*** This question is addressed in Chapter 5, wherein the results of the numerical simulations will be presented.

In the next section, a review of the literature related to the research is provided in order to discuss the existing gaps in the literature and motivate the above-mentioned questions.

1.3 Literature Review

To address nonlinear aeroelasticity and handle instability and post-instability behavior for highly flexible structures, one requires nonlinear aeroelastic models. Related to this, a review of computational aeroelastic models for highly flexible structures is presented in Section 1.3.1. Then in Section 1.3.2, an overview is provided on how aerodynamic computations have been accelerated via Graphics Processing Unit (GPU) computing. The use of the Fast Multipole Method (FMM) for accelerating the aerodynamic model computations is discussed in Section 1.3.3. The integration of aeroelastic computations with the Dynamic Data-Driven Application System (DDDAS) paradigm for decision support applications is reviewed in Section 1.3.4. A review of how structural damage is considered in computational models is presented in Section 1.3.5. Finally, in Section 1.3.6, the literature gaps to be addressed in the dissertation are briefly discussed.

1.3.1 Modeling Aeroelasticity of Highly Flexible Structures

Highly flexible structures require nonlinear aeroelastic models to account for lifting surfaces undergoing complex motions and large deformations. The primary components of numerical aeroelastic simulations are the aerodynamic model, the structural dynamic model, and the communication between them. Preidikman [5] developed a method for simulating the interactions amongst aerodynamic, structural dynamics, and control systems. The aeroelastic model for this dissertation is developed through the integration of a FE based structural dynamics model, an UVLM based aerodynamic model, and a procedure for the inter-model connection; that is, for transferring information between the aerodynamic simulator and the structural dynamics simulator. The bi-directional exchange of information between the simulators for aerodynamics and structural dynamics is part of a co-simulation strategy [6–8]. With the advances in computational power, the co-simulation strategy was utilized in references [9–11] to further facilitate studies of highly flexible structures such as flapping and morphing wings. Vortex methods were also used in references [12–14] to create aeroelastic models to study motions of highly flexible wings.

In 1986, Wolkovitch [15] provided an overview of the joined-wing configuration concept and Livne [16] has brought up challenges of the design of a joined-wing configuration design. Rasmussen *et al.* [17] conducted a study to determine the optimal design of a joined-wing configuration. In recent years, studies on the nonlinear aeroelasticity of joined-wing aircraft [18–20] have been carried out using computational models. Cesnik and Su [18] modeled nonlinear aeroelastic behavior of a flexible joined-wing aircraft based on a nonlinear strained-based FE framework and Peter's [21] finite state aerodynamic theory. Snyder *et al.* [19] only focused on static aeroelastic analysis. While the authors in references [13,20] employ the UVLM based aerodynamic model for their nonlinear aeroelastic models, they did not attempt to speed up the computations in the aerodynamic model.

In the next subsection, a review of some methods wherein aerodynamic computations have been accelerated through hardware support is presented.

1.3.2 Accelerating Aerodynamic Computations via GPU Computing

As discussed in Section 1.1, the majority of the computational workload comes from the evaluation of the wake velocities. To calculate the velocity field by using the UVLM, based on the Biot-Savart law [22], the influence of N discrete finite vortex segments with spatially constant, time-varying circulations must be computed; the associated computational cost is of $O(N^2)$. As noted earlier, due to the convection of the wake, the value of N increases as time increases. To mitigate this computational cost, Chabalko *et al.* [23] and Chabalko and Balachandran [24, 25] sought to distribute two-dimensional vortex interaction calculations over the cores of a GPU. In the development of the aeroelastic computational framework called Flexit, Fleischmann *et al.* [26] utilized GPU computing to attain fast simulations for the UVLM aerodynamic model. While effective in dispersing the workload over more units, the speedup gained from GPU computing and parallel computing is hardware dependent, which limits the scaling of this framework to large sized problems. In this dissertation, an algorithmic approach is also explored to address this limit.

In the next subsection, the FMM and its applications to various problems are introduced.

1.3.3 Applications of Fast Multipole Method (FMM)

The FMM has been identified as one of the ten algorithms with the greatest influence on the development and practice of science and engineering in the 20th century [27]. With the FMM, the computational cost of the N-body problem is reduced from $O(N^2)$ to $O(N)$ or $O(N \log N)$, which is essential for any practical application when N becomes large. The FMM algorithm was first developed in 1987 by Greengard and Roklin [28] to calculate gravitational and electrostatic potentials.

This algorithm was further improved by Carrier *et al.* [29] for the evaluation of potential and force fields in systems involving large numbers of particles. In the work reported in references [30, 31], the FMM algorithm is used for the evaluation of Laplaces equation governing fluid flow. The FMM has been shown to be helpful with approximating fluid flows governed by the Navier-Stokes equations through vortex methods. In 2003, Gumerov *et al.* [32] reported on the generalized multilevel FMM and Gumerov and Duraiswami [33] went on to later publish a book on the use of the FMM for the Helmholtz equation in three dimensions. Gumerov and Duraiswami [34] implemented the FMM algorithm for simulations based on vortex methods via the Lamb-Helmholtz decomposition. The vortex filament method was integrated with the FMM in reference [35]. Recently, an application of the FMM algorithm with a discrete vortex method for free domain and periodic problems has been presented by Ricciardi *et al.* [36]. Cheung *et al.* [37] applied an octree data structure similar to that used in the FMM to speed up the calculations of wake velocities. The acceleration gained through the application of the FMM can be further enhanced through hardware usage, such as GPUs [38–40]. Recently, Deng *et al.* [41] have used the dipole panel FMM to accelerate velocity field computations in the UVLM. Jones *et al.* [42] developed methods for reducing the computational cost of UVLM by using tree structures to approximate the influences of groups of vortex rings. With faster aeroelastic computations, a larger variety of scenarios can be simulated to account for unforeseen events in the system and environment.

The above-mentioned fast simulations together with the DDDAS paradigm, which is discussed in the next subsection, can allow for better prediction and mitigation of nonlinear aeroelastic effects via a decision support system (DSS).

1.3.4 Dynamic Data-Driven Applications Systems (DDDAS)

Nonlinear aeroelastic simulations can be combined with measurement data through the DDDAS paradigm. This paradigm can be used to realize a framework in which measurement data, such as those obtained from sensors, are collected for a physical system and used to dynamically update the simulation. Darema [43] introduced the DDDAS concept in 2004. In the studies of Farhat and Amsallem [44] and Allaire *et al.* [45], the DDDAS paradigm has been utilized to predict the failure and degradation in UAS and tailor mission plans to best suit the remaining capabilities of the aircraft. Furthermore, meta-models can be developed to approximate the nonlinear models, thereby helping reduce the number of execution calls of the aeroelastic simulator [46–50].

With the DDDAS concept, the inclusion of damage in structures can be incorporated in the simulations. Related to this, questions on how to model damage and how it affects the behavior of structure come up. These concepts are discussed in the next subsection.

1.3.5 Structural Damage

From the literature, two of the main methods used to model structural wing damage are the following: 1) the incorporation of a breathing crack in a portion of the structure [51–56] and 2) through changes in the property matrices of the structure [57]. Stojanovic *et al.* [51] incorporated damage into their model by representing an open crack as a notch. New shape functions that included the damaged location were introduced into their FE model based on Timoshenko's beam theory. Wei and Shang [52] also used Timoshenko's beam theory to model the breathing effect of an open crack by using a signal function. Hoseini and Hodges [53–56] modeled the damaged section of the wing as a three-dimensional FE crack while the rest of the wing is modeled with an one-dimensional beam. This reduced the overall computational expense of modeling the entire wing as a three-dimensional FE model. By using the model, Hoseini and Hodges investigated the critical flutter regime of a damaged wing. Similar to what will be done in this dissertation, Tenenbaum *et al.* [57] modeled damage in a beam as a change in stiffness matrix of structure. Tomaszewska [58] and Mainini and Wilcox [59] focused more on the aspects of damage detection and monitoring.

Based on the literature review, research gaps that will be addressed in this dissertation are discussed in the next subsection.

1.3.6 Research Gaps and Needs

While there have been studies on the implementation and speedup capabilities of the FMM (and other tree structure algorithms) accelerated vortex methods, such as the discrete vortex method, the vortex filament method, and the quasi-steady vortex lattice method, not many have focused on the nonlinear, unsteady UVLM based scheme. There are a few studies on dynamic nonlinear aeroelastic analysis for the joined-wing SensorCraft. In these studies, there has been no focus on the effects of structural damage on the aeroelastic behavior of the joined-wing aircraft via numerical aeroelastic simulations. With the acknowledgement of what is missing in the literature, the following research gaps and needs are addressed through this dissertation:

(1) Exploration of the acceleration gained via the integration of the UVLM based aerodynamic model and the FMM

- Implementation of the FMM accelerated UVLM based aerodynamic model for a flat plate with high aspect ratio
- Examination of the tuning parameters in the FMM algorithm to study the tradeoff of accuracy and computational speed of the FMM accelerated UVLM based aerodynamic model
- Comparison of the computational speed of the standard UVLM based aerodynamic model versus the FMM accelerated UVLM based aerodynamic model

(2) Construction of an aeroelastic computational model, in which one utilizes the FMM accelerated UVLM based aerodynamic model and the FE based structural dynamic model for capturing flutter boundary of a joined-wing SensorCraft

- Development of FMM accelerated UVLM based aerodynamic model for joined-wing SensorCraft that takes into account the symmetry of the aerodynamic mesh

- Development of FE based structural dynamics model for joined-wing SensorCraft that takes into account structural damage of the system and rigid-body motion via multi-freedom constraints
- Integration of the aerodynamic and structural dynamic models of the joined-wing SensorCraft via mesh coupling and co-simulation strategy
- Study of the effects of structural damage of various magnitudes and types for the joined-wing SensorCraft on the flutter boundary via numerical aeroelastic simulations

1.4 Dissertation Organization

In Chapter 2, the accelerated aerodynamic model developed for the joined-wing SensorCraft is presented. This includes background on the UVLM and FMM and how the FMM and UVLM are integrated to attain the FMM accelerated UVLM aerodynamic model. The FE based structural dynamics model developed for the joined-wing SensorCraft is discussed in Chapter 3. Chapters 2 and 3 are independent of each other and can be read in whichever order the reader wants. In Chapter 4, the integration of the aerodynamic and structural dynamic models that make up the joined-wing aeroelastic model is discussed. Details presented in Chapter 4 require an understanding of information discussed in Chapters 2 and 3 and should be read after the preceding two chapters. The results of the structural damage on the joined-wings are presented and discussed in Chapter 5. It can be noted that

Chapter 5 should be read after reading Chapter 4. Finally, the conclusions, contributions, and possible future directions are stated in Chapter 6. The portions of code of the computational aeroelastic simulation program that benefit the most from parallelization are presented in Appendix A. In Appendix B, the modes used for the computational aeroelastic simulations of the joined-wing aircraft are shown. More details and reasoning for the settings used for the joined-wing aircraft aeroelasticity simulations can be found in Appendix C. Additional results of the aeroelastic responses from the computational aeroelastic simulations can be seen in Appendix D. Appendix A should be read after first reading Chapter 2, Appendix B should be read after first reading Chapter 3, Appendix C should be read before reading the results of the joined-wing aircraft aeroelasticity simulations presented in Chapter 5, and Appendix D should be read after a reading of Chapter 5.

Chapter 2: Aerodynamics: FMM Accelerated Scheme

In this chapter, the work carried out to integrate the UVLM based aerodynamic model and the FMM is detailed and the results obtained with this computational model are presented. Some of the work presented in this chapter is based on the author's papers [60, 61]. This chapter is used to answer research question **RQ1**. The implementation of the FMM accelerated aerodynamics, the examination of the accuracy versus speed tradeoff with the FMM, and the computational speed gained are explored. A flowchart for the computational aerodynamic model of the joined-wing SensorCraft is also presented along with details of the computational model used in this work.

The FMM accelerated aerodynamic model is presented in Section 2.1, which also includes details on the UVLM based scheme and the FMM. The results obtained from the numerical tradeoff study of the FMM accelerated aerodynamic model and the computational cost reductions are reported in Section 2.2. In Section 2.3, the aerodynamic computational model for the joined-wing aircraft is introduced and a flowchart for the aerodynamic simulation procedure is presented. Finally, in Section 2.4, a summary of the chapter is provided.

2.1 FMM Accelerated Aerodynamic Model

The aeroelastic computations are carried out by using a co-simulation strategy, which is described in reference [10]. Co-simulation here refers to subdivision of a system with coupled physics into subsystems that are simultaneously simulated and numerically combined with a suitable exchange of states at predefined time instances to account for the strong coupling. Co-simulations can consist of any number of subsystems but in this effort, two subsystems are included in the co-simulation strategy. For this work, in the aeroelastic simulator, the UVLM based scheme is used to predict the aerodynamic loads on the lifting surfaces. Additionally, the aerodynamic solver is coupled with a structural dynamics simulator to capture dynamic aeroelasticity. The first subsystem is the UAS structural model, which is obtained through the use of the FE method. The second subsystem is the UAS aerodynamic model, which is obtained on the basis of the UVLM based scheme.

An overview of the UVLM based scheme is provided in the following subsection.

2.1.1 Unsteady Vortex Lattice Method

Here, the UVLM based scheme is used to compute aerodynamic loads. The UVLM based scheme is a surface vorticity model that is used to accurately approximate the physics for a large Reynolds number, fully attached, flow. The infinitesimally thin layers of vorticity may be viewed as an infinite Reynolds number approximation to the actual boundary layers. The UVLM based scheme can be applied to lifting surfaces of any planform, camber, and twist, and the lifting surfaces may undergo any time dependent deformation and execute any maneuver in moving air. The flow surrounding the lifting surface is assumed to be inviscid, incompressible, and irrotational over the entire flowfield, except at the solid boundaries and in the wakes. Due to the relative motion between the wing and the fluid and the viscous effects, vorticity is generated in the fluid in a thin region next to the wing's surface (the boundary layer). The boundary layers on the upper and lower surfaces are merged into a single vortex sheet.

The bound vortex sheets are replaced by lattices of short, straight vortex segments with spatially constant/time-varying circulation $\Gamma(t)$. These segments are used to divide the wing surface into a finite number of typically nonplanar, quadrilateral elements of area with straight edges called panels. These closed loop of straight vortex line segments are also referred to as vortex rings. The model is completed by joining the free vortex lattices (wakes) to the bound vortex lattice (lifting surface) along the separation edges, such as the trailing edges and leading edges of the lifting surface. The separation locations are user supplied. Each vortex ring has a single unknown circulation $G(t)$ instead of the four unknown circulations around each of the short, vortex line segments along its edges. Consequently, the requirement of spatial conservation of circulation is automatically satisfied throughout the lattices. Once the values of $G(t)$ for each panel are known, the $\Gamma(t)$'s around all of the straight vortex segments can be conveniently determined. The governing equation is complemented with the following boundary conditions:

(i) *Regularity at infinity*: This condition requires that the velocity field associated with the disturbance decays away from the body and its wake. Hence,

$$\lim_{\|\mathbf{r}\|_2 \to \infty} \|\mathbf{V}_B(\mathbf{r}, t) + \mathbf{V}_W(\mathbf{r}, t)\|_2 = \|\mathbf{V}_\infty\|_2 \tag{2.1}$$

where $\mathbf{V}_B(\mathbf{r}, t)$ and $\mathbf{V}_W(\mathbf{r}, t)$ are the velocity fields associated with the vorticity in the boundary layers on the body surface and the vorticity in the free vortex shed from the wing's trailing edge (including the tip), respectively, and $\mathbf{V}_\infty$ is the freestream velocity. The velocity field obtained from the Biot-Savart law identically satisfies this condition. Although, not shown here, the velocity field associated with the leading edge can also be included on the left hand side of equation (2.1).

(ii) *No-penetration condition*: This condition requires that at every point of the solid surface, the normal component of the fluid velocity relative to the body's surface must be zero:

$$(\mathbf{V}_B(\mathbf{r}, t) + \mathbf{V}_W(\mathbf{r}, t) + \mathbf{V}_\infty - \mathbf{V}_{Body}) \cdot \hat{\mathbf{n}} = 0, \tag{2.2}$$

where $\mathbf{V}_{Body}$ is the velocity of the body's surface, and $\hat{\mathbf{n}}$ is a unit vector normal to the surface. Equation (2.2) is only imposed at the control point located in the geometric center of each panel.

Discretizing the no-penetration condition at each control point, equation (2.2) is written in the following form:

$$(\mathbf{V}_B \cdot \hat{\mathbf{n}})_i = \sum_{j=1}^{n_A^{cp}} A_{ij} G_j = [\mathbf{V}_W + \mathbf{V}_\infty - \mathbf{V}_{Body}]_i \cdot \hat{\mathbf{n}}_i \tag{2.3}$$

where $i, j = 1, 2, \cdots, n_A$ are the indices of the receiving panel and the sending panel, respectively, A_{ij} is the normal component of the velocity induced on panel i by panel j with unit circulation, G_j, and n_A^{cp} is the number of panels on the aerodynamic mesh. The $(n_A^{cp} \times n_A^{cp})$ matrix $\mathbf{A} = [A_{ij}]$ is the aerodynamic influence coefficient matrix. The $(n_A \times 1)$ right hand side (RHS) vector is defined as

$$\mathbf{b} = \{b_i\} = [\mathbf{V}_W + \mathbf{V}_\infty - \mathbf{V}_{Body}]_i \cdot \hat{\mathbf{n}}_i. \tag{2.4}$$

At every timestep, the no-penetration condition is satisfied by solving a time dependent set of linear algebraic equations:

$${}^t\mathbf{A}\,{}^t\mathbf{G} = {}^t\mathbf{b} \tag{2.5}$$

where $\mathbf{G} = \{G_j\}$ is the $(n_A^{cp} \times 1)$ vector of vortex ring circulations.

To satisfy the unsteady Kutta condition at each timestep, the vortex rings along the edges are shed into the flow where they have the same order as they had on the wing's surface. The vortex rings are moved downstream with the flow by moving the end points of their vortex segments, called nodes, with the local fluid-particle velocity $\mathbf{V}$ to new positions, denoted $\mathbf{r}(t + \Delta t)$ according to the first-order approximation:

$$\mathbf{r}(t + \Delta t) \approx \mathbf{r}(t) + \mathbf{V}(\mathbf{r}, t)\Delta t. \tag{2.6}$$

2.1.1.1 Nondimensionalization of Model

In order to have uniform elements in the lattice, the models are nondimensionalized by using the following characteristic variables of length, velocity, and density:

L_C is the chordwise length of one element on the bound lattice,

V_C is the magnitude of the freestream velocity of the fluid,

ρ_C is the freestream density of the fluid, and

T_C is the characteristic time

The characteristic time is defined as

$$T_C = \frac{L_C}{V_C}. \tag{2.7}$$

By the definition of the characteristic time, 1) an increase in the number of elements is the chordwise direction of the bound lattice automatically leads to a corresponding decrease in the physical timestep and 2) a nondimensional timestep of value one (i.e., $\Delta t = T_C$) creates wakes elements of approximately the same dimensions as the elements on the lifting surfaces.

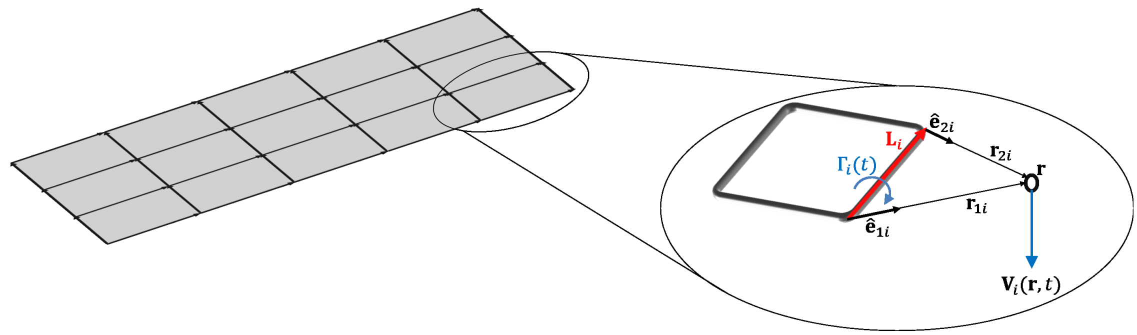

Figure 2.1: Application of Biot-Savart law to compute the velocity $\mathbf{V}_i(\mathbf{r}, t)$ at point $\mathbf{r}$ with respect to vortex segment.

2.1.1.2 Aerodynamic Loads

The aerodynamic loads acting on the lifting surface are computed as follows: for each element of the bound lattice, the force is determined based on the pressure jump across the lifting surface at the control point. This calculation is carried out by using the unsteady Bernoulli equation [22, 62]:

$$\frac{\partial}{\partial t}\varphi(\mathbf{r}, t) + \frac{1}{2}\mathbf{V}(\mathbf{r}, t) \cdot \mathbf{V}(\mathbf{r}, t) + \frac{p(\mathbf{r}, t)}{\rho_f} = W(t). \tag{2.8}$$

Here, ∂_t denotes the partial time derivative at a fixed location in an inertial reference frame, $\mathbf{V}(\mathbf{r}, t)$ is the spatial gradient of the scalar velocity potential $\varphi(\mathbf{r}, t)$, ρ_f is the fluid density, $p(\mathbf{r}, t)$ is the pressure, and $W(t)$ is the total energy per unit mass, which only depends on time and has the same value at every point in the domain of the flow.

2.1.1.3 Formulation

In Figure 2.1, the author shows a typical vortex ring, wherein the circulation of the individual vortex segments is the same as the circulation of the vortex ring, and how these vortex segments contribute to the velocity at the field point $\mathbf{r}$. The Bio-Savart integral [22] can be transformed as follows:

$$\mathbf{V}_i(\mathbf{r},t) = \frac{\Gamma_i(t)}{4\pi}\int_{\mathbf{L}_i}\frac{\mathrm{d}\mathbf{r}'\times(\mathbf{r}-\mathbf{r}')}{\|\mathbf{r}-\mathbf{r}'\|_2^3} = \Gamma_i(t)\,\nabla\times\int_{\mathbf{L}_i}G(\mathbf{r},\mathbf{r}')\,\mathrm{d}\mathbf{r} \tag{2.9}$$

where $G(\mathbf{r},\mathbf{r}')$ is the multipole expansion of a monopole source located at point $\mathbf{r}'$. The velocity field satisfying equation (2.9) at the field point $\mathbf{r}$ for time t, $\mathbf{V}_i(\mathbf{r},t)$, associated with a discrete segment of a straight line vortex, $\mathbf{L}_i$, $i = 1, 2, \cdots, N$, of circulation strength, $\Gamma_i(t)$, can be evaluated as follows:

$$\mathbf{V}_i(\mathbf{r},t) = \frac{\Gamma_i(t)}{4\pi}\frac{\mathbf{L}_i\times\mathbf{r}_{1i}}{\|\mathbf{L}_i\times\mathbf{r}_{1i}\|_2^2}\left[\mathbf{L}_i\cdot(\hat{\mathbf{e}}_{1i}-\hat{\mathbf{e}}_{2i})\right] \equiv \mathbf{A}(\mathbf{L}_i,\mathbf{r})\Gamma_i(t) \tag{2.10}$$

Here, $\mathbf{r}_{1i}$ and $\mathbf{r}_{2i}$ are the position vectors from the endpoints of the vortex segment, $\mathbf{L}_i = \mathbf{r}_{1i} - \mathbf{r}_{2i}$, to the field point $\mathbf{r}$, and $\hat{\mathbf{e}}_{1i}$ and $\hat{\mathbf{e}}_{2i}$ are unit vectors in the directions of $\mathbf{r}_{1i}$ and $\mathbf{r}_{2i}$, respectively. To avoid the singularity that appears when the point approaches the vortex line or its extension, the term $\delta\|\mathbf{L}_i\|_2$ can be introduced to equation (2.10) to obtain

$$\mathbf{V}_i(\mathbf{r},t) = \frac{\Gamma_i(t)}{4\pi}\frac{\mathbf{r}_{1i}\times\mathbf{r}_{2i}\left(\|\mathbf{r}_{1i}\|_2+\|\mathbf{r}_{2i}\|_2\right)}{\|\mathbf{r}_{1i}\|_2\,\|\mathbf{r}_{2i}\|_2\left(\|\mathbf{r}_{1i}\|_2\,\|\mathbf{r}_{2i}\|_2+\mathbf{r}_{1i}\cdot\mathbf{r}_{2i}\right)+\left(\delta\|\mathbf{L}_i\|_2\right)^2} \equiv \mathbf{A}(\mathbf{L}_i,\mathbf{r})\Gamma_i(t). \tag{2.11}$$

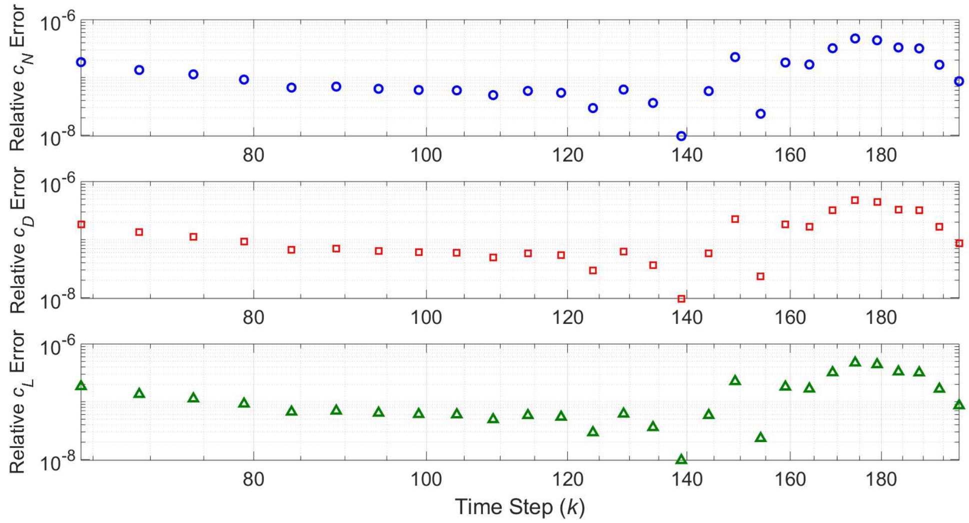

Figure 2.2: Relative errors in computed aerodynamic load coefficients (normal force coefficient c_N, drag coefficient c_D, and lift coefficient c_L) between the Biot-Savart law with equation (2.11) containing the smoothing parameter and equation (2.10) without the smoothing parameter.

The influence of the cutoff radius, or smoothing parameter δ on the velocity is strongly felt in the immediate vicinity of the considered vortex line but it is hardly noticeable elsewhere. The cutoff radius used for the aerodynamic model in this dissertation varies depending on the computational model. In Figure 2.2, the relative errors in the computed aerodynamic load coefficients obtained by using equations (2.10) and (2.11) are plotted. The corresponding simulations have been carried out for a planar, rectangular wing with an aspect ratio of 4 and subjected to a freestream speed of magnitude 125.00 m/sec, angle of attack 5°, and air density 1.255 kg/m^3. The wing has a chord length of 1.00 m with 9 panels in the chord-wise direction and a wing span of 4.00 m with 36 panels in the span-wise direction. Given the small magnitude of the error, there is good agreement between the aerodynamic loads computed obtained by using equations (2.10) and (2.11).

The velocity field at point $\mathbf{r}$ can be computed as the summation of velocity fields associated with each of the discrete vortex segments $\mathbf{L}_1, \mathbf{L}_2, \cdots, \mathbf{L}_N$, at the field point, $\mathbf{r}$:

$$\mathbf{V}(\mathbf{r}, t) = \sum_{i=1}^{N} \mathbf{V}_i(\mathbf{r}, t) = \sum_{i=1}^{N} \mathbf{A}(\mathbf{L}_i, \mathbf{r})\Gamma_i(t). \tag{2.12}$$

At each timestep, the velocity field needs to be evaluated at M field points, $\mathbf{r}_j$, $j = 1, 2, \cdots, M$, which leads to a computational cost of $O(NM)$. The computational cost of the simulation increases significantly with the number of field points and vortex segments. As time evolves, for a system on the scale of a full aircraft, these computations become intractable. Such computational expense motivates the need for the FMM to accelerate the velocity field calculations. The FMM can be used to reduce the computational cost from $O(NM)$ to $O(N + M)$, making the run time more practical.

Another way to reduce the computational cost of the aerodynamic model is to reduce the size of the problem. This can be done by truncating the wake at a specified number of timesteps but doing so introduces some error into the solution of the aerodynamic loads. This means that after a predefined number of timesteps, every new row added to the wake after convection, replaces oldest row in the wake. In doing so, the number of elements in the wake remain constant and so the number of elements in aerodynamic model remain constant. Ceballos [63] showed that truncating the wake at six chord lengths introduced a negligible level of error into the solution of the aerodynamic loads.

2.1.1.4 Validation of Aerodynamic Model

In order to validate the UVLM based aerodynamic model, the lift coefficient c_L and induced drag coefficient c_{D_i} obtained with the UVLM based scheme were compared against those obtained from Prandtls lifting line theory [**?**]. The results obtained for the lift and induced drag coefficients from the UVLM based scheme are found to be in good agreement with the values from Prandtls lifting line theory.

Prandtls lifting line theory was used to validate the accuracy of the UVLM calculated lift coefficients c_L and induced drag coefficients c_{D_i} for angles of attack between $0°$ and $20°$ for a rectangular wing of aspect ratio 4. In Figures 2.3 and 2.4, lift coefficient and induced drag coefficient are plotted against the angle of attack, respectively. By using the L^2 norm, the absolute error and relative error in the computed lift coefficients are 0.156 and 0.0389, respectively; and the absolute error and relative error in the computed induced drag coefficients are 0.0243 and 0.0849, respectively.

2.1.1.5 Computational Profiling

Through computational profiling of the UVLM aerodynamic simulator utilizing the UVLM based aerodynamic model and the FE structural dynamics model, it is discovered that the majority of the computational workload is associated with computations of the aerodynamics. The wall clock times of the aerodynamic computations reported are measured on an Intel® Xeon® CPU E3-1245 v5 (3.50 GHz) 8 core PC with 16 GB RAM. The dominant source of computational expense

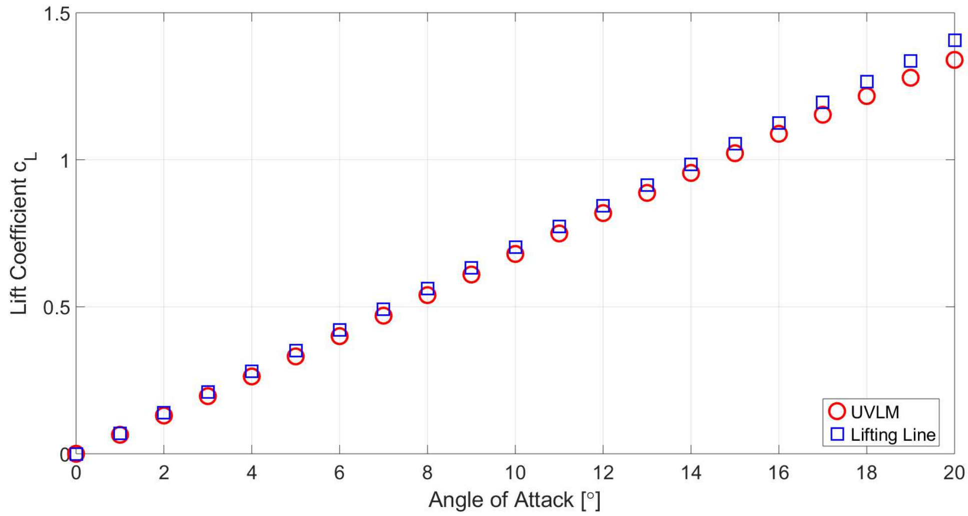

Figure 2.3: Lift coefficient versus angle of attack: Comparison between UVLM results and Prandtl's lifting line theory prediction.

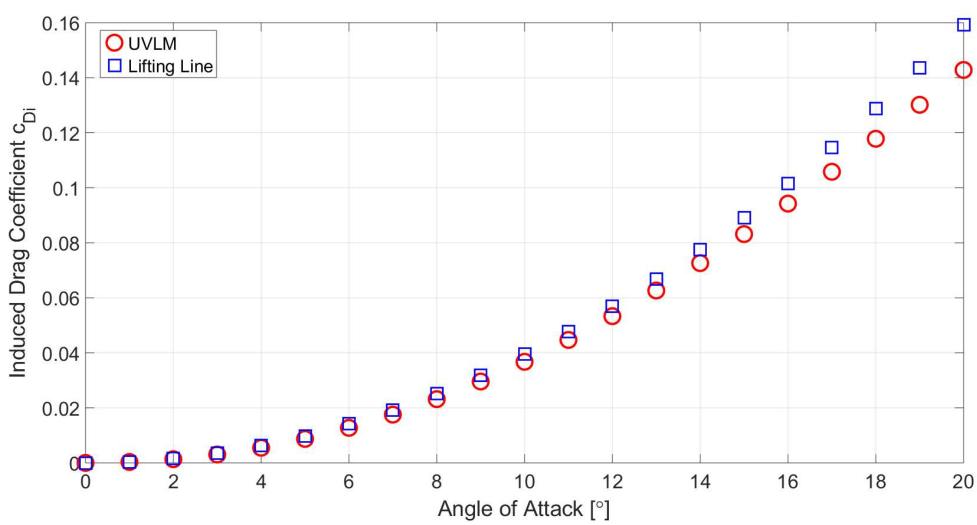

Figure 2.4: Induced drag coefficient versus angle of attack: Comparison between UVLM results and Prandtl's lifting line theory prediction.

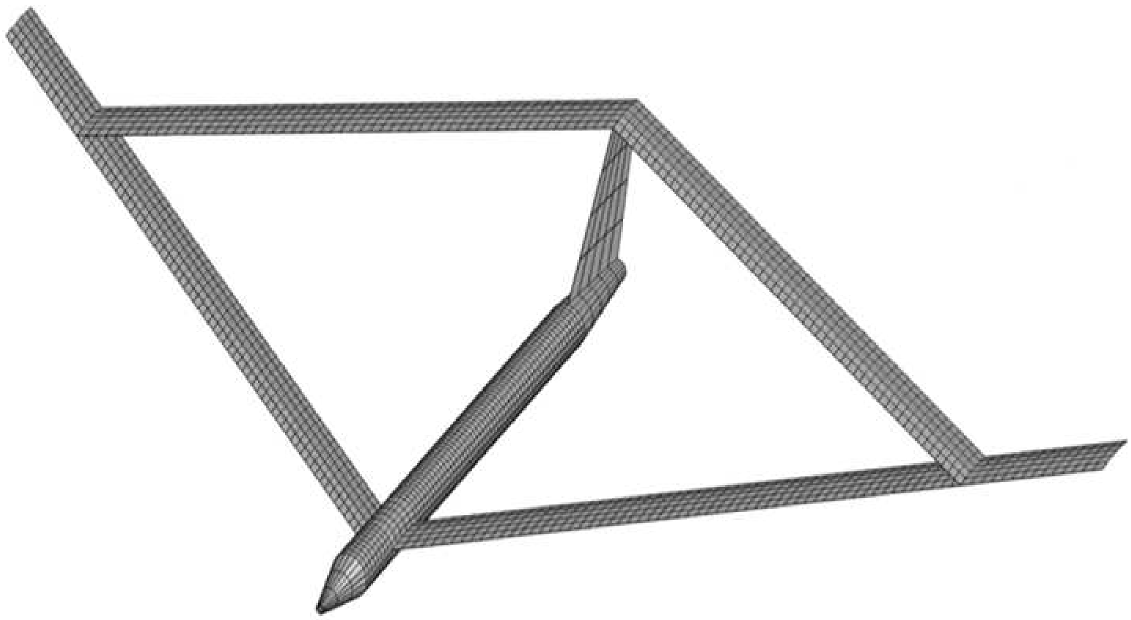

Figure 2.5: Aerodynamic mesh of a representative joined-wing aircraft configuration.

in the aerodynamic model lies in the computation of the wake (region of recirculating flow immediately behind lifting surface) velocities. The high computational cost can be observed in the aeroelastic simulation results obtained for a representative joined-wing SensorCraft and shown in Figure 2.5. In Figure 2.6, it can be seen that over 90% of the computation time involved in the aeroelastic simulation of the joined-wing SensorCraft is spent on evaluating the wake velocity. This is mainly due to the growth of the wake as time progresses as shown in Figure 2.7. As the wake continues to expand, the number of calculations required to evaluate the wake velocities also increases.

In Figure 2.8, it can be seen that when the number of sources (fields points on the trailing edges and wing-tips of lifting surface) and receivers (vortex segments on lifting surface and wake) exceed 100,000, the wall clock time for the evaluation of the wake velocities can take more than 15 minutes for each run. The compu-

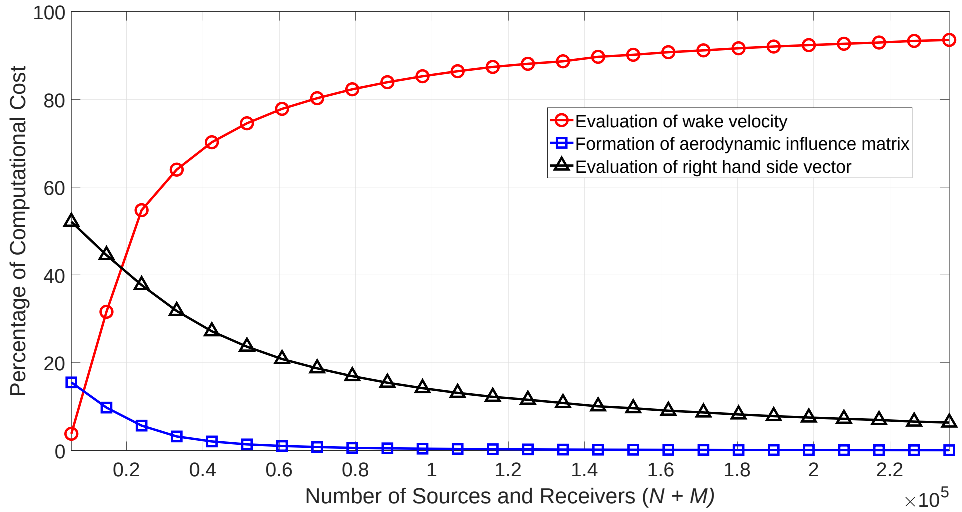

Figure 2.6: Percentage of total computational workload of aeroelastic simulator from aerodynamic model processes: evaluation of free deforming wake velocity (circle), formation of the aerodynamic influence matrix (square), and evaluation of the right hand side vector (triangle).

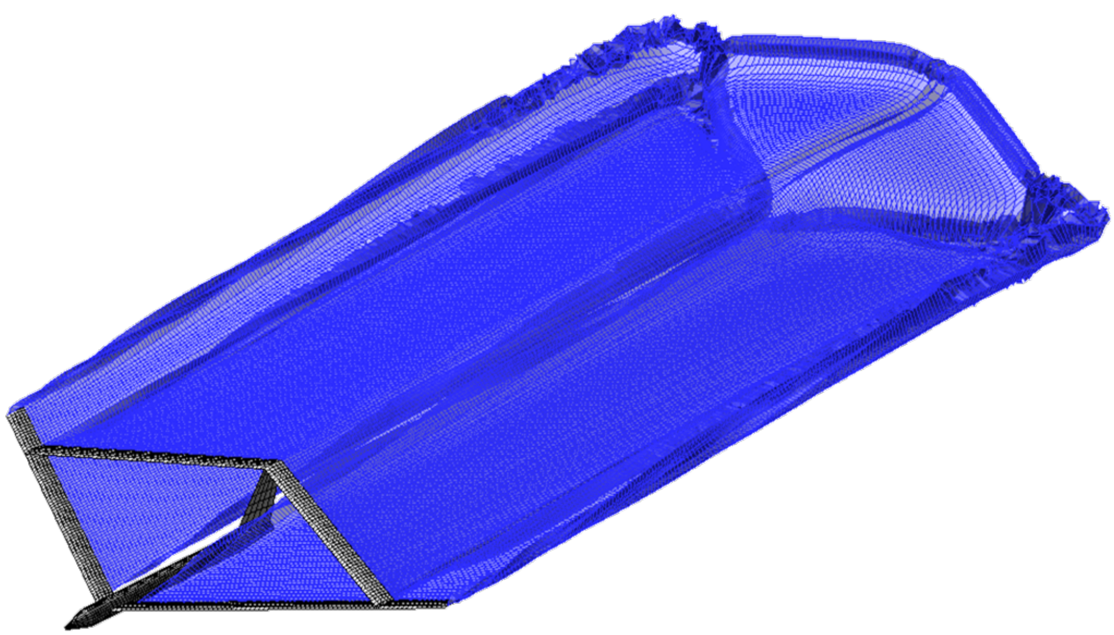

Figure 2.7: The longer the wake (blue area) becomes, the more computations that will be needed for evaluating wake velocities.

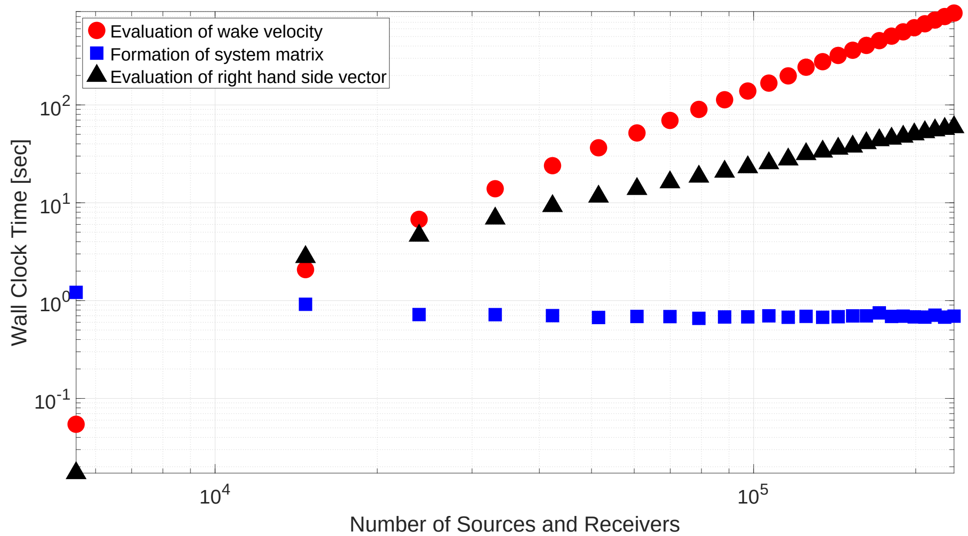

Figure 2.8: Wall clock time of total computational workload of aeroelastic simulator from aerodynamic model processes: evaluation of free deforming wake velocity (circle), formation of the aerodynamic influence matrix (square), and evaluation of the right hand side vector (triangle).

tational time required to compute the structural response; that is, to numerically integrate the structure's equations of motion, is neglected in the figure since this time is dwarfed by the time needed to carry out the unsteady aerodynamic calculations. For similar reasons, the processes of the aerodynamic model involving the evaluation of the distribution of circulation and the calculations of the aerodynamic loads are negligible. These observations emphasize the need for acceleration of the free deforming wake velocity computations in the aerodynamic model to accelerate the entire aeroelastic model. Given that over 90% of the computation workload is involved with wake velocity computations, accelerating these computations would produce a faster nonlinear aeroelastic computational model for generating safe maneuvering envelopes. To achieve this goal, the FMM is used in implementing the UVLM based aerodynamic model.

It is important to note that procedures such as the formation of the aerodynamic influence matrix and the evaluation of the RHS vector have been parallelized in the computations. Some portions of the code that have been parallelized are presented in Appendix A. Since these processes depend on the bound lattice panels, the number of required computations do not increase as the time increases. Even though this would a small reduction in required computational workload, this addition to the computational model becomes more noticeable with a more refined aerodynamic grid.

2.1.2 Fast Multipole Method

The FMM is a hierarchical algorithm, which can be used to speed up matrix-vector products. The main idea of the FMM is to split the computation associated with equation (2.12) into near-field interactions and far-field interactions. This is done through the decomposition of the dense matrix into sparse and dense parts as shown below:

$$\mathbf{V}(\mathbf{r}_j, t) = \sum_{i=1}^{N} \mathbf{A}(\mathbf{L}_i, \mathbf{r}_j)\,\Gamma_i(t) = \sum_{i=1}^{N} \mathbf{A}^{(\text{sparse})}(\mathbf{L}_i, \mathbf{r}_j)\,\Gamma_i(t) + \sum_{i=1}^{N} \mathbf{A}^{(\text{dense})}(\mathbf{L}_i, \mathbf{r}_j)\,\Gamma_i(t). \tag{2.13}$$

Here, $\mathbf{L}_1, \mathbf{L}_2, \cdots, \mathbf{L}_i, \cdots,$ and $\mathbf{L}_N$ are the sources (vortex segments) and $\mathbf{r}_1, \mathbf{r}_2, \cdots, \mathbf{r}_j,$ $\cdots,$ and $\mathbf{r}_M$ are the receivers (field points). The sparse matrix-vector product is performed directly, while the dense matrix-vector product is approximated via the use of data structures, the generation of multipole expansions, and the evaluation of local expansions. This means that the interactions between near-field pairs of field points and vortex segments are directly computed, while the interactions between the far-field pairs of field points and vortex segment pairs are approximated. More details on the basics of the FMM can be found elsewhere [28–34, 38]. In the following subsections, the main components of the FMM algorithm and the specifics for vortex filament computations and use in the UVLM based scheme are briefly described.

2.1.2.1 Data Structure

The hierarchical data structure (usually octree for three dimensional simulations) of the FMM serves two purposes. First, it is needed for a fast neighbor search to compute the near-field interactions directly by using $O(N)$ or $O(N \log N)$ operations. Second, it is needed to organize far-field interactions in a hierarchical way, which can be done with the same computational complexity as the near-field interactions. The entire computational domain is enclosed in a cube, or box, of size $d_0 \times d_0 \times d_0$, which is said to be subdivision level 0. This cube is partitioned into 8 equal cubes of size $d_1 = d_0/2$, which form subdivision level 1. This process of partitioning the volume is continued until the maximum number of source points (the centers of the vortex segments) in a box does not exceed some number s called the “clustering parameter”. The value of s depends on several parameters and is a subject for tuning, as discussed below. This level of subdivision is the maximum level in the octree, which is denoted by $l_{\max}$. So at this level, $8^{l_{\max}}$ cubes of size $d_{l_{\max}} = d_0/2^{l_{\max}}$ are used to partition the entire computational domain. In the

UVLM based scheme, the sources are located on a subset of surfaces and most of the cubes in such a tree are empty. Since the FMM is an adaptive algorithm, one skips all empty boxes and the actual number of cubes at some level l is much smaller than 8^l. There are variations of the FMM formulation, in which one uses data trees (in this case the "leaves" of the "tree" can be located at any level not exceeding $l_{\max}$, for example, [31]; this is called "fully adaptive" FMM) and data pyramids (all "leaves" of the tree are located at level $l_{\max}$, for example, [38]). Details and practical issues on efficient implementation of data structures and comparisons of "adaptive" and "fully adaptive" FMM variations can be found in reference [33]. It is noticeable that computations usually related to data structures do not exceed 10% of the complexity of the entire FMM. This is why the standard procedures (bit interleaving and sorting to form child, parent, and neighbor lists) are used in this dissertation.

2.1.2.2 Multipole Expansions

The velocity field generated by a vortex segment is not a potential, but can be expressed in terms of three dependent scalar harmonic functions or two independent scalar harmonic functions by using the Lamb-Helmholtz decomposition [34]. The FMM for harmonic functions is well developed and studied. The far-field, or multipole expansion of a monopole source located at point $\mathbf{r}'$ with respect to the center $\mathbf{r}_c$ of the cube containing the source, can be represented in the form of a series:

$$G(\mathbf{r},\mathbf{r}') = \frac{1}{4\pi\|\mathbf{r}-\mathbf{r}'\|_2} = \sum_{n=0}^{p_F-1}\sum_{m=-n}^{n} R_n^{-m}(\mathbf{r}_c-\mathbf{r}')S_n^m(\mathbf{r}-\mathbf{r}_c) + O\left(\left(\frac{\mathbf{r}'-\mathbf{r}_c}{\mathbf{r}-\mathbf{r}_c}\right)^{p_F}\right). \tag{2.14}$$

Here, $\mathbf{r}$ is a field point, such that $\|\mathbf{r}-\mathbf{r}_c\|_2 > \|\mathbf{r}'-\mathbf{r}_c\|_2$, p_F is the FMM truncation number, while R_n^m and S_n^m are regular and singular spherical basis functions, which, generally, can be written as follows:

$$R_n^m(\mathbf{r}) = r^n N_n^{(R)m} Y_n^m(\theta,\varphi),$$
$$S_n^m(\mathbf{r}) = r^{n-1} N_n^{(S)m} Y_n^m(\theta,\varphi)$$

Here (r,θ,φ) are the spherical coordinates of point $\mathbf{r}$, $Y_n^m(\theta,\varphi)$ are the spherical harmonics, and $N_n^{(R)m}$ and $N_n^{(S)m}$ are normalization coefficients. There are different normalizations of spherical harmonics in the literature. Also, real or complex harmonics can be used (see [30, 38]).

Consider the field of vortex segments specified by a unit vector $\mathbf{l}_i = \mathbf{L}_i/\|\mathbf{L}_i\|_2$, center $\mathbf{r}_i = (\mathbf{r}_{1i}+\mathbf{r}_{2i})/2$, and circulation $\Gamma_i(t)$. The Bio-Savart integral equation (2.9) can be transformed as follows:

$$\mathbf{V}_i(\mathbf{r},t) = \nabla \times \left(\frac{\Gamma_i(t)}{2}\mathbf{l}_i \int_{-1}^{1} G\left(\mathbf{r}, \mathbf{r}_i - \frac{1}{2}\mathbf{l}_i\xi\right) \mathrm{d}\xi \right) = \nabla \times \mathbf{A}(\mathbf{L}_i,\mathbf{r})\Gamma_i(t). \tag{2.15}$$

These expressions reveal several facts important for the FMM implementation. First, the sums of the fields of vortex segments can be represented as a curl of sums of the respective vector potentials $\mathbf{A}(\mathbf{L}_i,\mathbf{r})$. This means that the FMM can be applied to the summation of vector potentials, and then, the curl of the obtained field can be computed. Second, each Cartesian component of $\mathbf{A}(\mathbf{L}_i,\mathbf{r})$ is a scalar harmonic function. This means that the FMM for the scalar Laplace equation can be applied to each component independently. Third, equation (2.14) can be used to obtain the multipole expansion for the vector potential of each vortex segment:

$$\mathbf{A}(\mathbf{L}_i, \mathbf{r}) = \frac{\Gamma_i(t)}{2}\mathbf{l}_i \sum_{n=0}^{p_F-1} \sum_{m=-n}^{n} C_{(i)n}^{m} S_n^m(\mathbf{r}-\mathbf{r}_c) + O\left(\left(\frac{\max\left(\|\mathbf{r}_{1i}-\mathbf{r}_c\|_2, \|\mathbf{r}_{2i}-\mathbf{r}_c\|_2\right)}{\|\mathbf{r}-\mathbf{r}_c\|_2}\right)^{p_F}\right) \tag{2.16}$$

with

$$C_{(i)n}^{m} = \int_{-1}^{1} R_n^{-m}\left(\mathbf{r}_c - \mathbf{r}_i + \frac{1}{2}\mathbf{l}_i\xi\right) \mathrm{d}\xi.$$

The expansion coefficients $C_{(i)n}^{m}$ can be calculated by using Gauss-Legendre quadrature of order N_q with weights w_a, abscissae ξ_a, and residual $\mathrm{res}(N_q)$:

$$C_{(i)n}^{m} = \sum_{a=1}^{N_q} w_a R_n^{-m}\left(\mathbf{r}_c - \mathbf{r}_i + \frac{1}{2}\mathbf{l}_i\xi_a\right) + \mathrm{res}(N_q). \tag{2.17}$$

It is noted that functions $R_n^{-m}\left(\mathbf{r}_c - \mathbf{r}_i + \frac{1}{2}\mathbf{l}_i\xi_a\right)$ are polynomials of degree n of ξ_a. Hence the Gauss-Legendre quadrature equation (2.17) provides an exact result for $N_q > n/2$. According to equation (2.16), $n \leq p_F 1$. Hence, selection

$$N_q = \left[\frac{p_F - 1}{2}\right] + 1, \tag{2.18}$$

guarantees $\mathrm{res}(N_q) = 0$; that is, zero quadrature error in the FMM. However, this requirement is not necessary and may be relaxed, as for the overall accuracy of the method it is sufficient to balance residuals in equations (2.16) and (2.17). In many cases, selection $N_q = 1$ or $N_q = 2$ yields good results.

2.1.2.3 Use of Standard FMMs for the Laplace Equation

After the multipole expansions are computed for each source box at level $l_{\max}$, the rest of the FMM procedure is standard and follows along the lines of what is available in the literature (e.g. [31,38]). It consists of multipole-to-multipole translation in the upward pass, which recursively produces the multipole expansions for all source boxes at levels $l_{\max}, l_{\max}-1, \cdots, 2$, and multipole-to-local and local-to-local translations in the downward pass, which recursively produces local expansions for all receiver boxes at levels $2, 3, \cdots, l_{\max}$. Finally, for a receiver box centered at $\mathbf{r}_c$, the author obtained the values of local expansion coefficients $D_n^{(h)m}$ for each Cartesian component $h = 1, 2, 3$ of the vector potential due to far-field interactions

$$A^h(\mathbf{r}, t) = \sum_{n=0}^{p_F-1} \sum_{m=-n}^{n} D_n^{(h)m} R_n^m(\mathbf{r} - \mathbf{r}_c). \tag{2.19}$$

To complete the calculation of the dense matrix-vector product, one needs to compute the curl of the vector potential. This can be done by computing the gradient of each component of the vector potential and combining the results into a single vector. The gradient can be computed by using analytical expressions for the derivatives of functions $R_n^m(\mathbf{r})$.

According to equations (2.14), (2.16), and (2.17), the far-field approximation of the hth Cartesian component of the vector potential is given by

$$A^h(\mathbf{r}, t) = \frac{\Gamma_i(t)}{2} l_i^h \sum_{j=1}^{N_q} w_j G\left(\mathbf{r}, \mathbf{r}_i - \frac{1}{2}\mathbf{l}_i \xi_h\right) \tag{2.20}$$

This means that each vortex segment is represented by N_q monopole sources and that the case should be set for NN_q monopole sources of intensity $\frac{1}{2}\Gamma_i(t)l_i^h w_j$ located at $\mathbf{r}_i - \frac{1}{2}\mathbf{l}_i\xi_h$ and M receivers. The scalar FMM routine should be called three times, for each Cartesian component, $h = 1, 2, 3$. The result should be obtained in the form of gradients, which is standard for the FMMs computing forces, from which the curl of the vector potential can be formed. An additional user procedure should be created out of the core of the standard FMM that can be used to compute the near-field interactions and subtract from them the near-field of the standard FMM. In the dissertation, the author uses a specialized FMM code, that allows the amortization and vectorization of a number of operations.

2.1.2.4 Tuning Configuration of the FMM

It can be useful to estimate the complexity of the steps of the UVLM based scheme and its overall computational complexity with and without the FMM. Consider the case of relatively small body mesh of size N_b, which is fixed and the mesh representing the vortex sheets of size N, which is growing in time. Since at each timestep, the vorticity is emitted from some edges of the body, the author can estimate that for the kth timestep $N = O(N_b^{1/2}k)$. So the total complexity to compute K steps is a sum of the complexities for $k = 1, 2, \cdots, K$. In Tables 2.1 and 2.2, the author shows the estimates. From this table, it can be seen that the use of the FMM changes the complexity of the entire UVLM based scheme, whose complexity at large K grows proportionally to $O(K^2)$ as opposed to the $O(K^3)$ for the

Table 2.1: Estimation of computational complexity of the UVLM based scheme processes with and without FMM per timestep.

Step	Without FMM	With FMM
Form aerodynamic influence matrix	$O(N_b^2)$	$O(N_b^2)$
Evaluate right hand side vector	$O(N_b N)$	$O(N_b + N)$
Solve linear system	$O(N_b^3)$	$O(N_b^3)$
Evaluate wake velocity	$O(N_b N + N^2)$	$O(N_b + N)$
Evolve mesh	$O(N_b + N)$	$O(N_b + N)$
Total	$O(N_b^3 + N^2)$	$O(N_b^3 + N)$

Table 2.2: Estimation of computational complexity of the UVLM based scheme processes with and without FMM for K total timesteps.

Step	Without FMM	With FMM
Form aerodynamic influence matrix	$O(N_b^2)$	$O(N_b^2)$
Evaluate right hand side vector	$O(N_b^{3/2} K^2)$	$O(N_b K + N_b^{1/2} K^2)$
Solve linear system	$O(N_b^3 K)$	$O(N_b^3 K)$
Evaluate wake velocity	$O(N_b^3 K^2 + N_b^{3/2} K^3)$	$O(N_b K + N_b^{1/2} K^2)$
Evolve mesh	$O(N_b K + N_b^{1/2} K^2)$	$O(N_b K + N_b^{1/2} K^2)$
Total	$O(N_b^3 K + N_b^3 K^3)$	$O(N_b^3 K + N_b^{1/2} K^2)$

conventional UVLM based scheme.

Generally, the tuning process can be organized as follows. First, for some s (or $l_{\max}$), p_F should be varied to obtain a required accuracy of the FMM and stability of computations, while N_q should be related to p_F via equation (2.18) to eliminate quadrature errors. As soon as an acceptable range of p_F is determined, one should try to reduce N_q as much as possible to stay within the required FMM accuracy. Finally, the clustering parameter s (or $l_{\max}$), should be adjusted to obtain the maximum speed. Note that variation of this parameter has a small effect on the accuracy, but there exists a strong minimum of the computational time at some intermediate values of s. Theoretically, this happens when the times for computations of the sparse and dense products are equal.

2.2 Numerical Tradeoff Study

In this section, the results attained from the tuning procedure of FMM configurations described in Section 2.1.2.4 are shown. The tuning procedure of the FMM parameters was implemented on a planar, rectangular lifting surface by varying the large aspect ratio (wing span to chord length) in the range from 4 to 16 and the angle of attack in the range extending from 5° to 20°. The results reported in this section correspond to a planar, rectangular lifting surface that has an aspect ratio of 4, is subjected to a freestream speed of magnitude 125.00 m/sec, has angle of attack 5°, and the air density 1.255 kg/m^3. The wing has a chord length of 1.00 m with 9 panels in the chord-wise direction and a wing span of 4.00 m with 36 panels in the span-wise direction. It was found that variations in the flow speed, angle of attack, and air density have no noticeable effect on the computational time and accuracy of the simulations. Increasing (decreasing) the aspect ratio of the rectangular plate is accompanied by corresponding increase (decrease) in the number of vortex segments and field points required for calculations in the various UVLM processes. Thus, the change in computational time for different geometries will correspond with the estimated computational complexity presented in Tables 2.1 and 2.2. Therefore, the FMM parameters found in this study are general and can be applied to cases with various flow conditions and geometries. The wall clock times reported below were measured on an Intel® Xeon® CPU E3-1245 v5 (3.50 GHz) 8 core PC with 16 GB RAM.

2.2.1 Truncation Number

The first step in fine-tuning the FMM involves changing the truncation number p_F to obtain a required level of accuracy of the FMM and stability of computations. While varying p_F, the order of quadrature N_q should be consistent with p_F via equation (2.18) to eliminate quadrature errors. Also, the clustering parameter s (or maximum number of levels in octree $l_{\max}$) should be kept constant. For this study, the clustering parameter was set to $s = 200$ and the order of quadrature was set by equation (2.18) where the truncation number $p_F = 2, 4, 12,$ and 24.

From Figure 2.9, it can be seen that as p_F increases, the magnitude of the L^2 norm error of the evaluated wake velocities decreases. Since the far-field interactions are approximated by polynomials of the p_Fth degree in the neighborhood of the evaluation point, the higher p_F is, the more accurate approximations of the far-field interactions will be. At $p_F = 12$ and $p_F = 24$, the L^2 norm error becomes relatively low at orders 10^{-5} and 10^{-8}, respectively. In deciding which p_F to use, the author takes into account the wall clock time for the different p_F values shown in Figure 2.10. The wall clock time corresponding to $p_F = 24$ is significantly higher than that corresponding to $p_F = 12$. Given that the L^2 norm error of the evaluated wake velocities for $p_F = 12$ is at an acceptably low level, $p_F = 12$ is chosen as the best truncation number for this study.

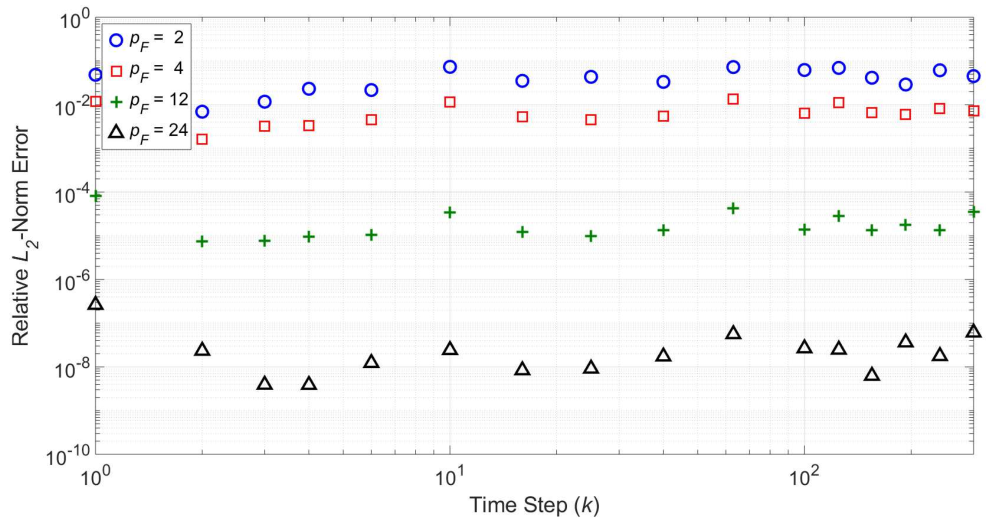

Figure 2.9: Relative L^2 norm errors for evaluated wake velocities for $p_F = 2$ (circle), $p_F = 4$ (square), $p_F = 12$ (plus sign), and $p_F = 24$ (triangle) with N_q relative to Eq. (2.18) and $s = 200$.

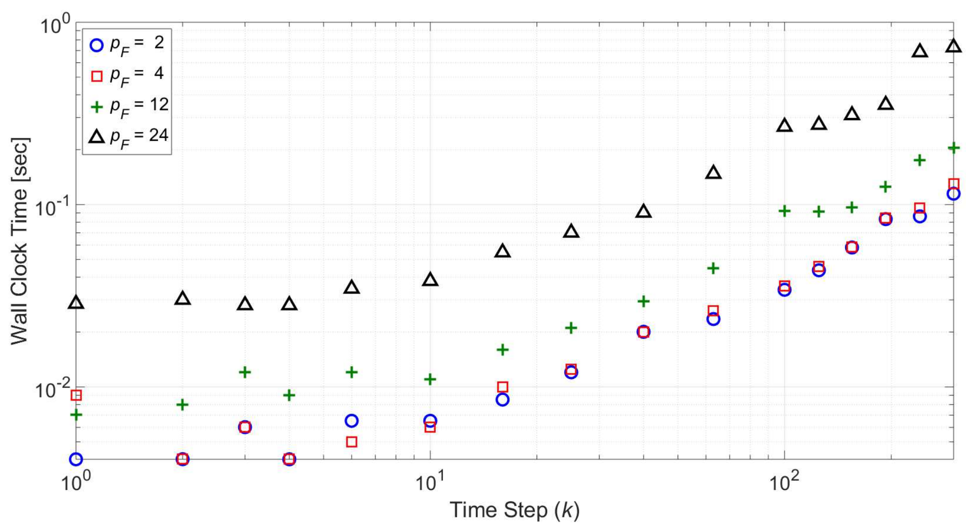

Figure 2.10: Wall clock time for evaluated wake velocities for $p_F = 2$ (circle), $p_F = 4$ (square), $p_F = 12$ (plus sign), and $p_F = 24$ (triangle) with N_q relative to Eq. (2.18) and $s = 200$.

Table 2.3: Relative L^2 norm errors of evaluated wake velocities for $N_q \geq 4$.

Timestep	Relative L^2 Norm Error (of magnitude 10^{-5})					
	$N_q = 4$	$N_q = 5$	$N_q = 6$	$N_q = 7$	$N_q = 8$	$N_q = 9$
1	0.000	0.000	0.000	0.000	0.000	0.000
10	1.930	1.930	1.930	1.930	1.930	1.930
50	5.290	5.290	5.290	5.290	5.290	5.290
100	9.780	9.780	9.780	9.780	9.780	9.780
150	1.030	1.030	1.030	1.030	1.030	1.030
200	0.355	0.355	0.355	0.355	0.355	0.355
250	0.818	0.818	0.818	0.818	0.818	0.818
300	0.842	0.827	0.827	0.825	0.825	0.824

2.2.2 Order of Quadrature

With $p_F = 12$ giving an L^2 norm error of order 10^{-5}, the order of quadrature N_q can be reduced as much as possible to stay within the required FMM accuracy. In Figure 2.11, the relative L^2 norm error of the evaluation of wake velocities is displayed when the truncation number is set to $p_F = 12$, the clustering parameter is set to $s = 200$, and the order of quadrature varies for $N_q = 1, 2, 3,$ and 4. The results for $N_q > 4$ show no noticeable difference in accuracy with respect to those for $N_q = 4$ and this revelation can be seen in Table 2.3. Note that other than $N_q = 1$, the accuracies attained for $N_q = 2, 3, 4$ match up well with each other. Given that the wall clock time, which is shown in Figure 2.11, corresponding to the different values of N_q follows the same trend with approximately the same values, it is best to use $N_q = 2$ as the accuracy of the evaluated wake velocities does not significantly increase as N_q is increased.

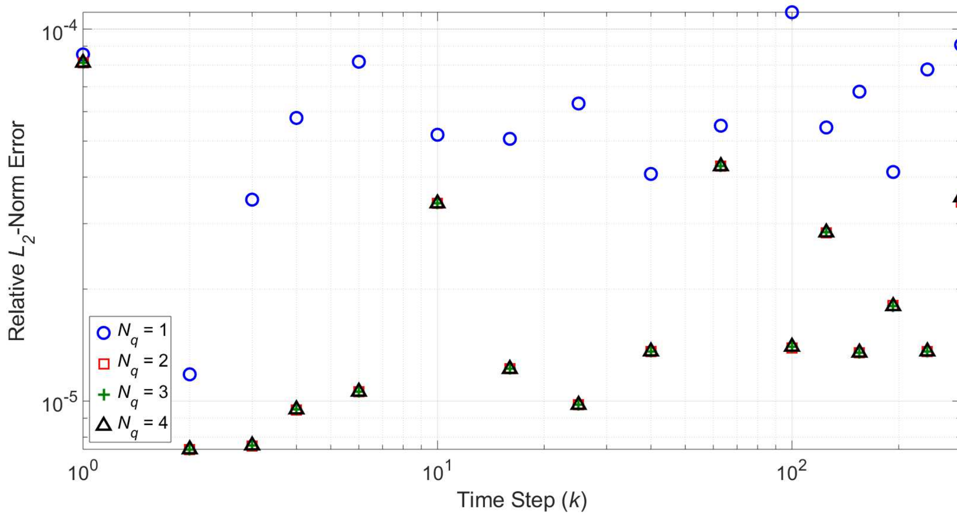

Figure 2.11: Relative L^2 norm errors of evaluated wake velocities for $N_q = 1$ (circle), $N_q = 2$ (square), $N_q = 3$ (plus sign), and $N_q = 4$ (triangle) with $p_F = 12$ and $s = 200$.

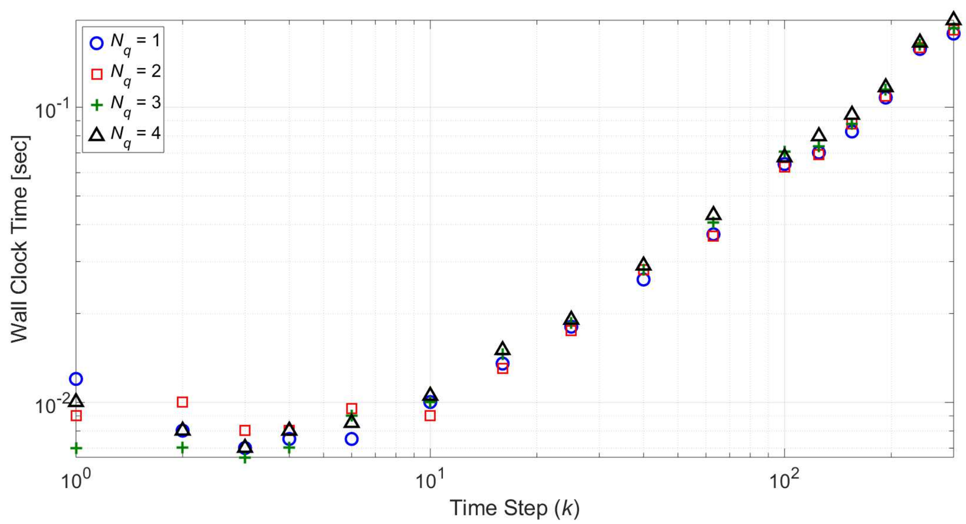

Figure 2.12: Wall clock time for evaluated wake velocities for $N_q = 1$ (circle), $N_q = 2$ (square), $N_q = 3$ (plus sign), and $N_q = 4$ (triangle) with $p_F = 12$ and $s = 200$.

Table 2.4: Wall clock time and accuracy of FMM for different clustering parameters.

s	Wall Clock Time [sec]	Maximum Levels in Octree	Average L^2 Norm Error
100	45.34	7	2.63×10^{-5}
200	28.06	6	1.86×10^{-5}
300	27.92	6	1.55×10^{-5}
400	29.58	5	1.10×10^{-5}
500	32.20	5	1.06×10^{-5}

2.2.3 Clustering Parameter

Finally, the clustering parameter s (or $l_{\max}$), is selected to obtain the maximum speed. In Table 2.4, the wall clock time, accuracy, and maximum number of levels in the octree $l_{\max}$ for fixed $p_F = 12$ and $N_q = 2$ and clustering parameters $s = 100, 200, 300, 400,$ and 500 are shown. The simulator was executed for $K = 200$ timesteps in each case. From this table, it is noted that the variation of s has a minor effect on the accuracy of the computed wake velocities. Also note that as the clustering parameter is increased, the maximum number of levels in the octree attained is decreased. Most notably, there exists a strong minimum of the computational time at $s = 300$. Hence, the configurations that produce that most accurate results while also providing the largest acceleration in computational time correspond to the truncation number $p_F = 12$, the order of quadrature $N_q = 2$, and the clustering parameter $s = 300$. These configuration settings for the FMM will be used when examining the computational cost reduction in the following subsection.

2.2.4 Computational Cost Reduction

In Figure 2.13, for $p_F = 12$, $N_q = 2$, and $s = 300$, the results of the speed performance of the UVLM based scheme with and without the FMM for the individual timesteps are depicted. In this figure, the computational time for the evaluation of the wake velocity fields of the UVLM is plotted against the number of timesteps. On a logarithmic scale, the slope of the dashed line is 2, which indicates the computational complexity of the standard UVLM evaluation of wake velocities for large K is of $O(K^2)$ where K is the total number of timesteps. The slope of the computational complexity of the FMM accelerated UVLM is indicated by the dotted line, which has a slope of 1 (i.e., grows proportionally to $O(K)$). Thus, with the FMM, the computational complexity of the evaluation of wake velocities reduced from $O(K^2)$ to $O(K)$. Notice that the FMM accelerated UVLM has better performance than the standard UVLM after about $k = 8$ timesteps (approximately $N = 1,500$ sources). This improvement in speed is achieved with no noticeable loss in accuracy. The relative L^2 norm error of the computed wake velocities of the FMM accelerated UVLM is of order 10^{-5}.

In Figure 2.14, for $p_F = 12$, $N_q = 2$, and $s = 300$, the results of the speed performance of the UVLM based scheme with and without the FMM for the cumulative timesteps is depicted. For significantly large K, the computational complexity of the standard UVLM evaluation of wake velocities is of $O(K^3)$, while the computational complexity of the FMM accelerated UVLM evaluation of wake velocities is of $O(K^2)$. These results show that the FMM does help significantly reduce to

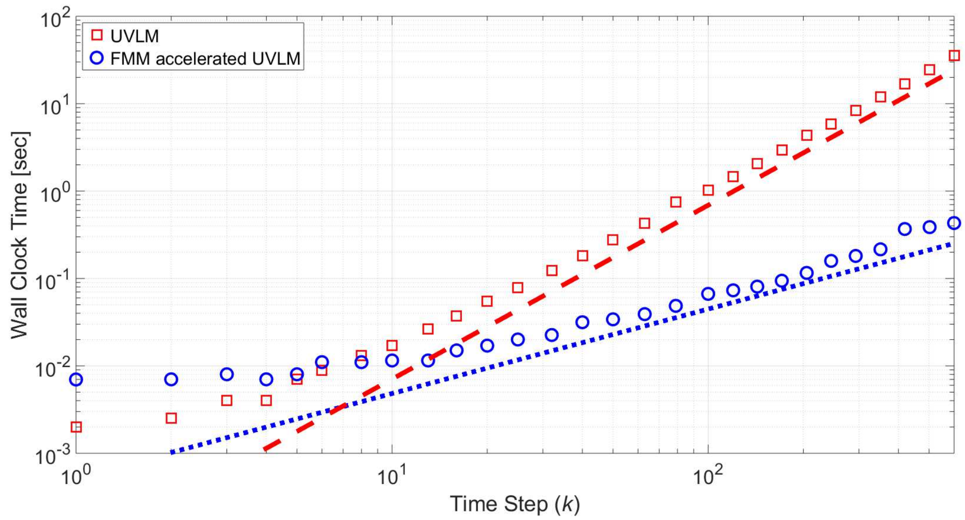

Figure 2.13: Wall clock time for evaluation of wake velocity in UVLM with (for $p_F = 12$, $N_q = 2$, and $s = 300$) and without the FMM for the individual timesteps. With dashed line, the author shows quadratic dependence for the individual timesteps of the UVLM, and with dotted line, the author shows the linear dependence of FMM accelerated UVLM.

computational workload of the computational aerodynamic model, which in turn is expected to accelerate the computational aeroelastic model of the joined-wing SensorCraft.

These results show the improvements gained from implementing the FMM algorithm only into the evaluation of the velocity fields for the wake convection process. The FMM algorithm has also been implemented for the evaluation of the velocity fields in the formulation of the right hand side (RHS) vector process and the calculation of the aerodynamic loads process for the joined-wing aircraft aerodynamic model. Since the number of elements in the wake is growing, the number of velocity fields that need to be evaluated also grows. The FMM algorithm is capable of handling the evaluation of the velocity fields as the problem grows. It should also be noted that the FMM code used for this work has been modified for

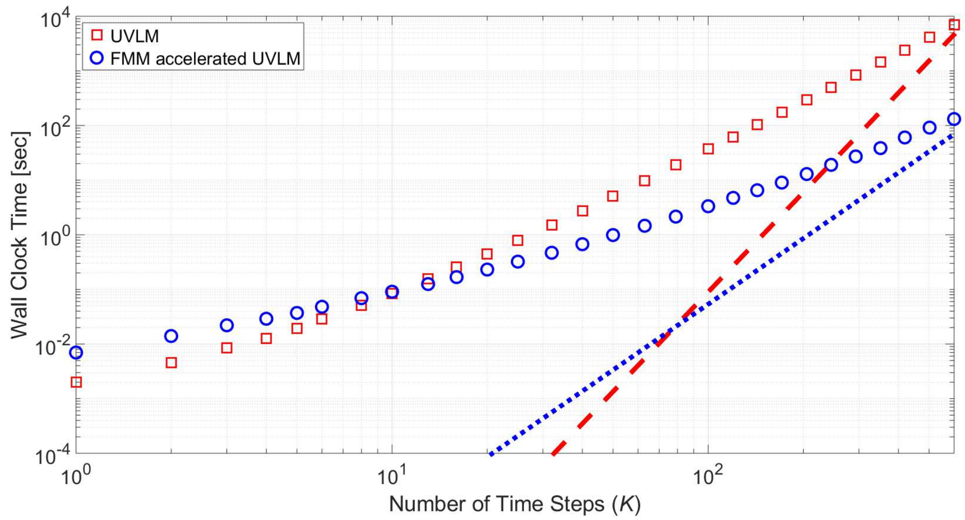

Figure 2.14: Wall clock time for evaluation of wake velocity in UVLM with (for $p_F = 12$, $N_q = 2$, and $s = 300$) and without FMM for the cumulative timesteps. With dashed line, the author shows cubic dependence for the cumulative timesteps of the UVLM, and with dotted line, the author shows quadratic dependence of the FMM accelerated UVLM.

parallel computing [40].

2.3 Computational Aerodynamic Model

A flowchart of the aerodynamic model is shown in Figure 2.15. In the model used, the wake is convected at the first iteration of each timestep and then held stationary for the remaining iterations. The computation of the aerodynamic coefficient influence matrix, ${}^t\mathbf{A}$, and the RHS vector, ${}^t\mathbf{b}$, are not dependent on each other but the RHS vector relies on the convected wake information. After using the aerodynamic influence matrix and the RHS vector, the circulations, ${}^t\mathbf{G}$, are solved for using equation (2.5). Finally, with the circulations, the aerodynamic loads, $\mathbf{F}_A(t)$, are calculated and transferred to the structural model to solve for the structural displacements. This whole process is repeated in the timestep until there

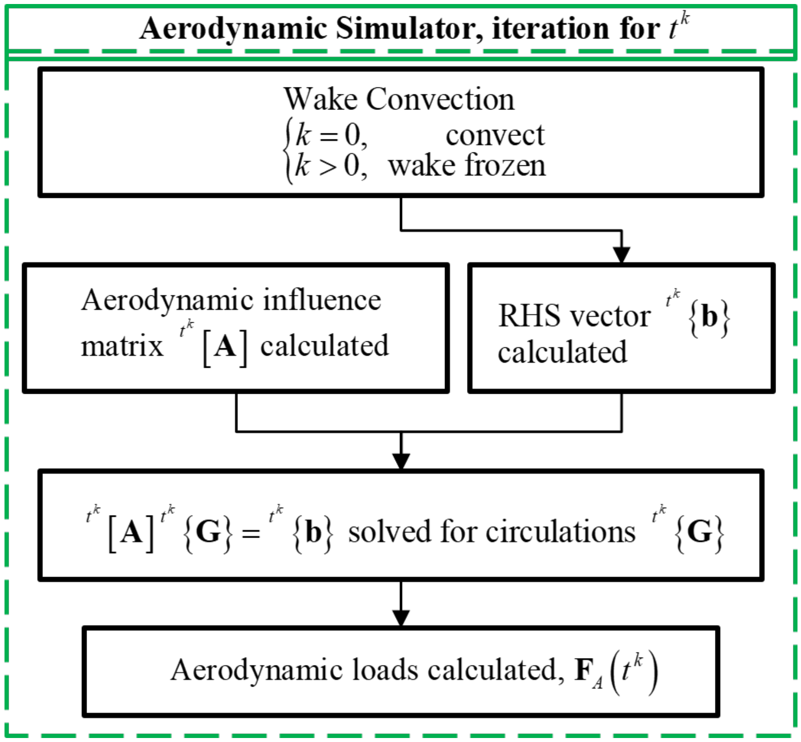

Figure 2.15: Flowchart of UVLM aerodynamic simulator.

is convergence in the solution for the structural displacements.

2.3.1 Joined-Wing SensorCraft

In Figure 2.16, the seven components of the aerodynamic model mesh are shown as follows: 1) right forward wing, 2) right aft wing, 3) right half of fuselage, 4) left forward wing, 5) left aft wing, 6) left half of fuselage, and 7) vertical tail. In previous versions of the aerodynamic model, only the mesh of the right forward wing, right aft wing, and right fuselage data of the joined-wing aircraft were needed. In the calculation of the wake velocities, it was assumed that the data for the left forward wing, left aft wing, and left fuselage was available via modifications in the Biot-Savart law calculations. Thus, simulations were limited to only cases of symmetric flows for the no-penetration condition to be satisfied around the vertical tail. The

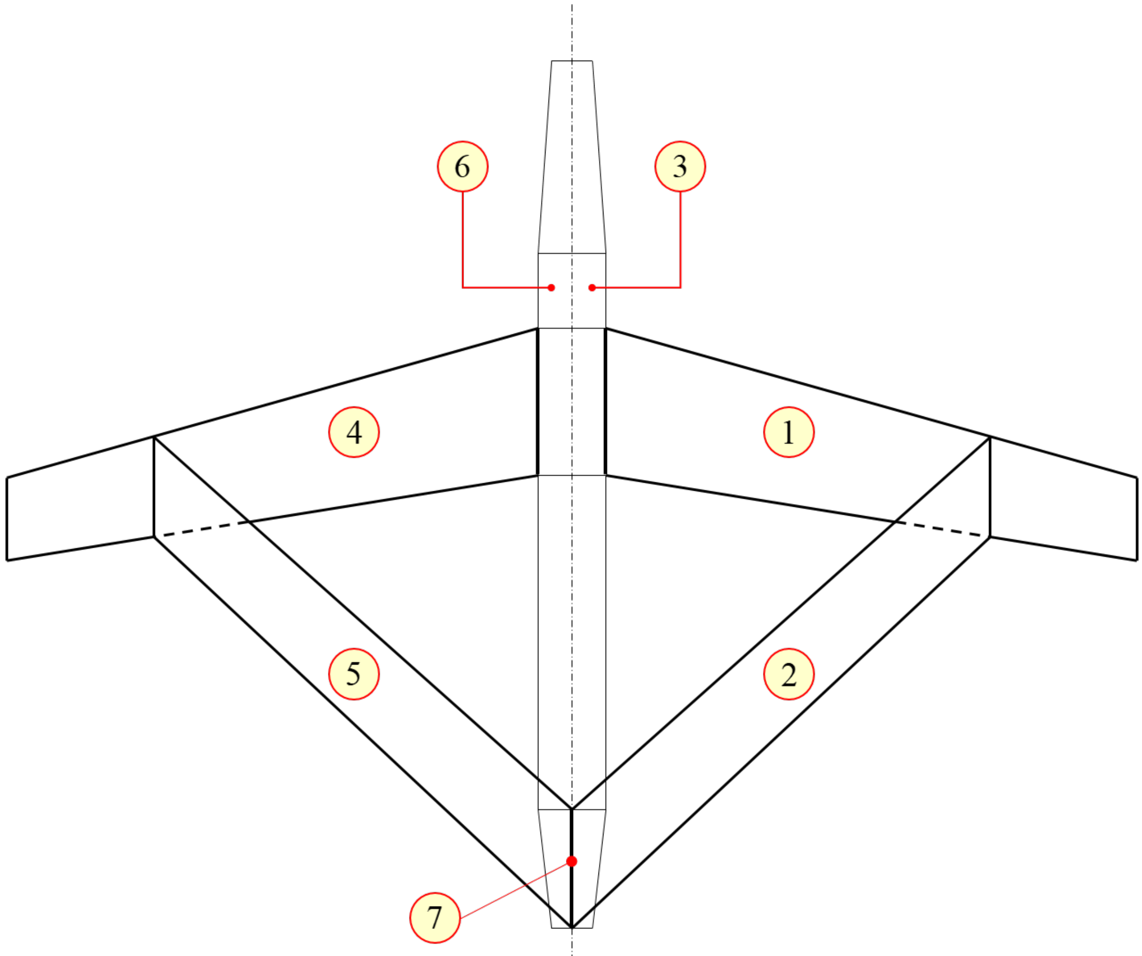

Figure 2.16: Topview of the joined-wing SensorCraft aerodynamic mesh components.

aerodynamic mesh of the joined-wing aircraft configuration used for this dissertation work is displayed in Figure 2.17. In this configuration, the joint connecting the forward and aft wing is located closer to the root of the forward wing that is attached to the fuselage. The inclusion of the full aerodynamic mesh geometry allows for scenarios of flow with variations in pitch, roll, and yaw angles as opposed to just the pitch angle in the previous model. From Figure 2.18, the yaw, pitch, and roll angles of the freestream direction are represented by α, β, and ϕ. Based on the Figure 2.18, the freestream direction is given by (α, β, ϕ).

With the integration of the FMM and the UVLM based aerodynamic model,

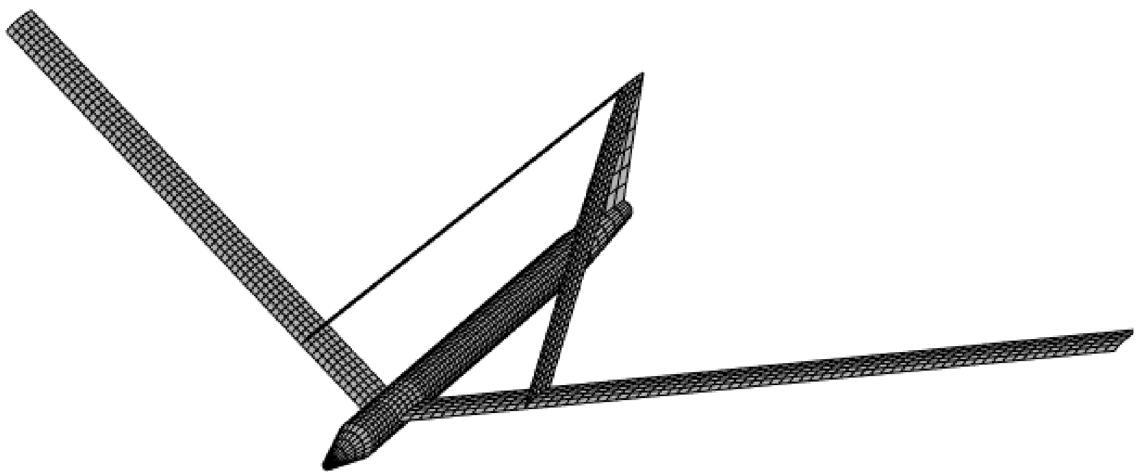

Figure 2.17: Aerodynamic mesh of joined-wing aircraft used in this work.

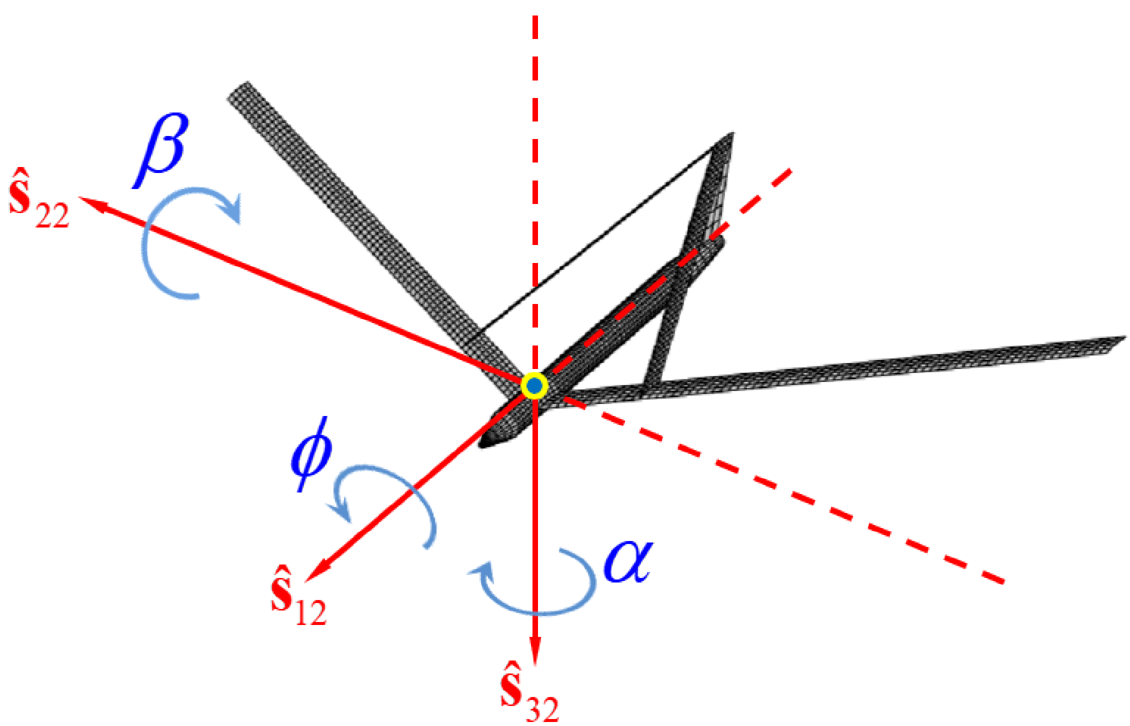

Figure 2.18: Angles of freestream direction.

the mesh data of the full joined-wing aircraft is required for all computations. Given the symmetry of the model, the left half of the joined-wing aircraft is generated by reflecting the right half mesh data along the symmetric axis. From Table 2.1, the computational complexity for forming the aerodynamic influence matrix, evaluating the RHS vector, evaluating the wake velocity, and evolving the mesh would be more than squared compared to the original half joined-wing aircraft model. Expanding equation (2.5) to account for the full joined-wing aircraft yields

$$\left[\begin{array}{ccc:ccc:c} {}^t\mathbf{A}_{11} & {}^t\mathbf{A}_{12} & {}^t\mathbf{A}_{13} & {}^t\mathbf{A}_{14} & {}^t\mathbf{A}_{15} & {}^t\mathbf{A}_{16} & {}^t\mathbf{A}_{17} \\ {}^t\mathbf{A}_{21} & {}^t\mathbf{A}_{22} & {}^t\mathbf{A}_{23} & {}^t\mathbf{A}_{24} & {}^t\mathbf{A}_{25} & {}^t\mathbf{A}_{26} & {}^t\mathbf{A}_{27} \\ {}^t\mathbf{A}_{31} & {}^t\mathbf{A}_{32} & {}^t\mathbf{A}_{33} & {}^t\mathbf{A}_{34} & {}^t\mathbf{A}_{35} & {}^t\mathbf{A}_{36} & {}^t\mathbf{A}_{37} \\ \hdashline {}^t\mathbf{A}_{41} & {}^t\mathbf{A}_{42} & {}^t\mathbf{A}_{43} & {}^t\mathbf{A}_{44} & {}^t\mathbf{A}_{45} & {}^t\mathbf{A}_{46} & {}^t\mathbf{A}_{47} \\ {}^t\mathbf{A}_{51} & {}^t\mathbf{A}_{52} & {}^t\mathbf{A}_{53} & {}^t\mathbf{A}_{54} & {}^t\mathbf{A}_{55} & {}^t\mathbf{A}_{56} & {}^t\mathbf{A}_{57} \\ {}^t\mathbf{A}_{61} & {}^t\mathbf{A}_{62} & {}^t\mathbf{A}_{63} & {}^t\mathbf{A}_{64} & {}^t\mathbf{A}_{65} & {}^t\mathbf{A}_{66} & {}^t\mathbf{A}_{67} \\ \hdashline {}^t\mathbf{A}_{71} & {}^t\mathbf{A}_{72} & {}^t\mathbf{A}_{73} & {}^t\mathbf{A}_{74} & {}^t\mathbf{A}_{75} & {}^t\mathbf{A}_{76} & {}^t\mathbf{A}_{77} \end{array}\right] \left\{\begin{array}{c} {}^t\mathbf{G}_1 \\ {}^t\mathbf{G}_2 \\ {}^t\mathbf{G}_3 \\ \hdashline {}^t\mathbf{G}_4 \\ {}^t\mathbf{G}_5 \\ {}^t\mathbf{G}_6 \\ \hdashline {}^t\mathbf{G}_7 \end{array}\right\} = \left\{\begin{array}{c} {}^t\mathbf{b}_1 \\ {}^t\mathbf{b}_2 \\ {}^t\mathbf{b}_3 \\ \hdashline {}^t\mathbf{b}_4 \\ {}^t\mathbf{b}_5 \\ {}^t\mathbf{b}_6 \\ \hdashline {}^t\mathbf{b}_7 \end{array}\right\} \tag{2.21}$$

where ${}^t\mathbf{A}_{ij}$, for $i, j = 1, 2, \cdots, 7$, is the aerodynamic influence matrix between the components i and j of the aerodynamic model mesh shown in Figure 2.16 at timestep t. ${}^t\mathbf{G}_i$ and ${}^t\mathbf{b}_i$ are the circulation and RHS vectors corresponding to component i, respectively. Considering that only the wings are deforming in the aeroelastic simulator, the aerodynamic influence matrix for any pair combination involving the vertical and the right and left fuselage are not time dependent. This means $\mathbf{A}_{33}$, $\mathbf{A}_{36}$, $\mathbf{A}_{37}$, $\mathbf{A}_{63}$, $\mathbf{A}_{66}$, $\mathbf{A}_{67}$, $\mathbf{A}_{73}$, $\mathbf{A}_{76}$, and $\mathbf{A}_{77}$ are constant throughout the whole simulation runtime. Due to the symmetry of the aerodynamic mesh, the equations

$$\begin{Bmatrix} {}^{t}\mathbf{G}_1 \\ \hdashline {}^{t}\mathbf{G}_2 \\ \hdashline {}^{t}\mathbf{G}_3 \end{Bmatrix} \simeq \begin{Bmatrix} {}^{t}\mathbf{G}_4 \\ \hdashline {}^{t}\mathbf{G}_5 \\ \hdashline {}^{t}\mathbf{G}_6 \end{Bmatrix} \tag{2.22}$$

$$\begin{Bmatrix} {}^{t}\mathbf{b}_1 \\ \hdashline {}^{t}\mathbf{b}_2 \\ \hdashline {}^{t}\mathbf{b}_3 \end{Bmatrix} \simeq \begin{Bmatrix} {}^{t}\mathbf{b}_4 \\ \hdashline {}^{t}\mathbf{b}_5 \\ \hdashline {}^{t}\mathbf{b}_6 \end{Bmatrix} \tag{2.23}$$

must hold true for the cases of symmetric flow in the purely aerodynamic model. Furthermore, the positioning and orientation of the vertical tail requires that

$${}^{t}\mathbf{G}_7 \simeq \mathbf{0}. \tag{2.24}$$

2.3.1.1 Global Mesh Data Numbering

Depending on the component of the aerodynamic mesh, the global numbering of the panels and nodal points can be different. The forward wing aerodynamic meshes are composed of 350 panels constructed from 432 nodal points as can be seen in Figure 2.19. For the right forward wing presented in Figure 2.19(a), the global nodal points and panels are numbered from top to bottom and left to right. For the left forward wing presented in Figure 2.19(b), the global nodal points and panels are numbered from top to bottom and right to left. It should be noted that the nodes in the forward wings that intersect with the aft wings are counted twice in the model.

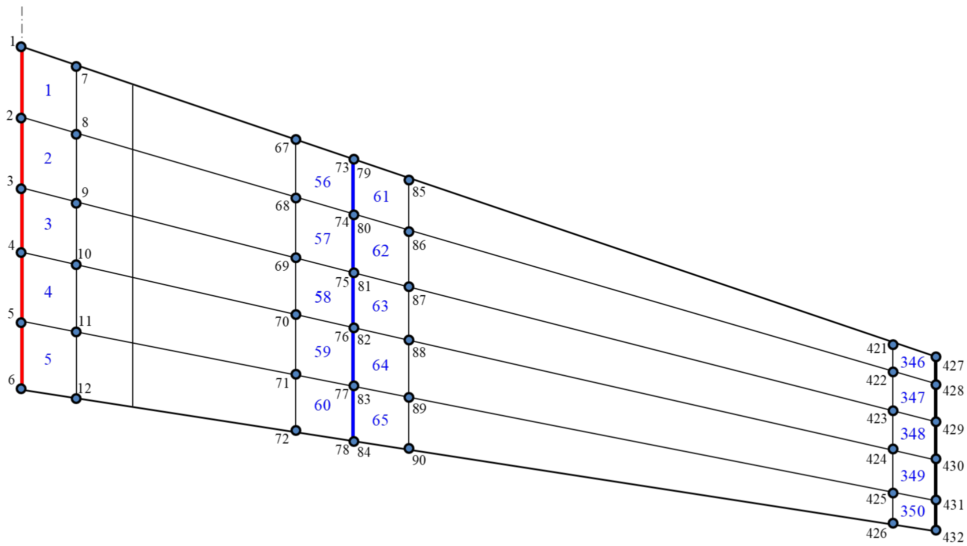

(a)

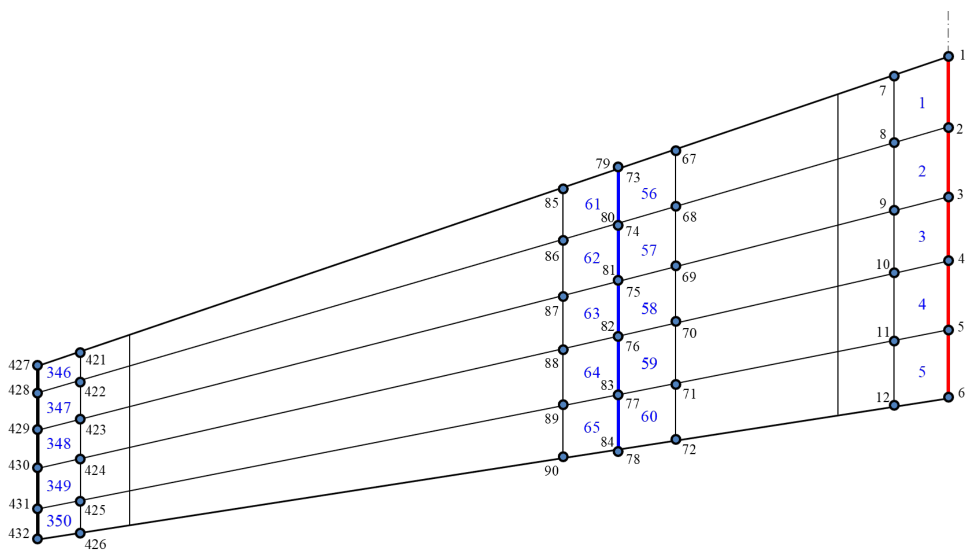

(b)

Figure 2.19: Global nodal point and element numbering: (a) right forward wing [1] and (b) left forward wing [4].

The aft wing aerodynamic meshes are composed of 220 panels constructed from 270 nodal points as can be seen in Figure 2.20. For the right aft wing presented in Figure 2.20(a), the global nodal points and panels are numbered from top to bottom and left to right. For the left aft forward wing presented in Figure 2.20(b), the global nodal points and panels are numbered from top to bottom and right to left.

The fuselage aerodynamic meshes are composed of 810 panels constructed from 902 nodal points as can be seen in Figure 2.21. For the right half of the fuselage presented in Figure 2.21(a), the global nodal points and panels are numbered from left to right and top to bottom. For the left half of the fuselage presented in Figure 2.21(b), the global nodal points and panels are numbered from right to left and top to bottom.

The vertical tail aerodynamic mesh is composed of 35 panels constructed from 48 nodal points as can be seen in Figure 2.22. For the vertical tail, the global nodal points and panels are numbered from left to right and bottom to top.

In total, over 3,200 nodal points are used to create the almost 2,800 elements in the aerodynamic mesh. There are five elements along the chordwise direction of the each of the lifting surfaces (i.e., the right and left forward and aft wings). This ensured that there were enough elements on the wing-tips to capture the formation of tip roll-up of vortices as investigated by Ceballos [63]. In the future, further refinement of the aerodynamic mesh can be considered.

2.3.1.2 Local Mesh Data Numbering

For the seven components of the aerodynamic mesh, the local numbering of the nodal points are consistent. With the local nodal points numbering system established, the ordering and numbering of the vortex segments can be defined. As shown in Figure 2.23, each panel is constructed from four nodal points numbered in clockwise orientation starting from the top left nodal point. The vortex segments, $\mathbf{L}_i$, of the panel, along with their corresponding circulation strength Γ_i, are also numbered in clockwise orientation starting from the topmost segment.

In Figure 2.24, vector $\mathbf{v}_1$ is obtained as the difference between node 1 and node 3, while vector $\mathbf{v}_2$ is obtained as the difference between node 2 and node 4. Given these vectors $\mathbf{v}_1$ and $\mathbf{v}_2$, the normals to each panel are defined by normalizing the vector that results from the vector product:

$$\hat{\mathbf{n}} = \mathbf{v}_1 \times \mathbf{v}_2. \tag{2.25}$$

Note that location of the control point of the panel will coincide with the normal vector at the intersection of the vectors $\mathbf{v}_1$ and $\mathbf{v}_2$.

2.4 Summary

In this chapter, the construction of the FMM accelerated UVLM based aerodynamic model used for the joined-wing aircraft aeroelastic simulator has been discussed. This included the implementation of the FMM accelerated UVLM based aerodynamic model. For a rectangular flat plate, the procedure used to do the numerical tradeoff study and computational cost reduction for the FMM accelerated UVLM were presented. The chapter ended with the description of the computational aerodynamic model for the joined-wing system.

In the next chapter, the structural model utilized for this dissertation work is discussed in detail.

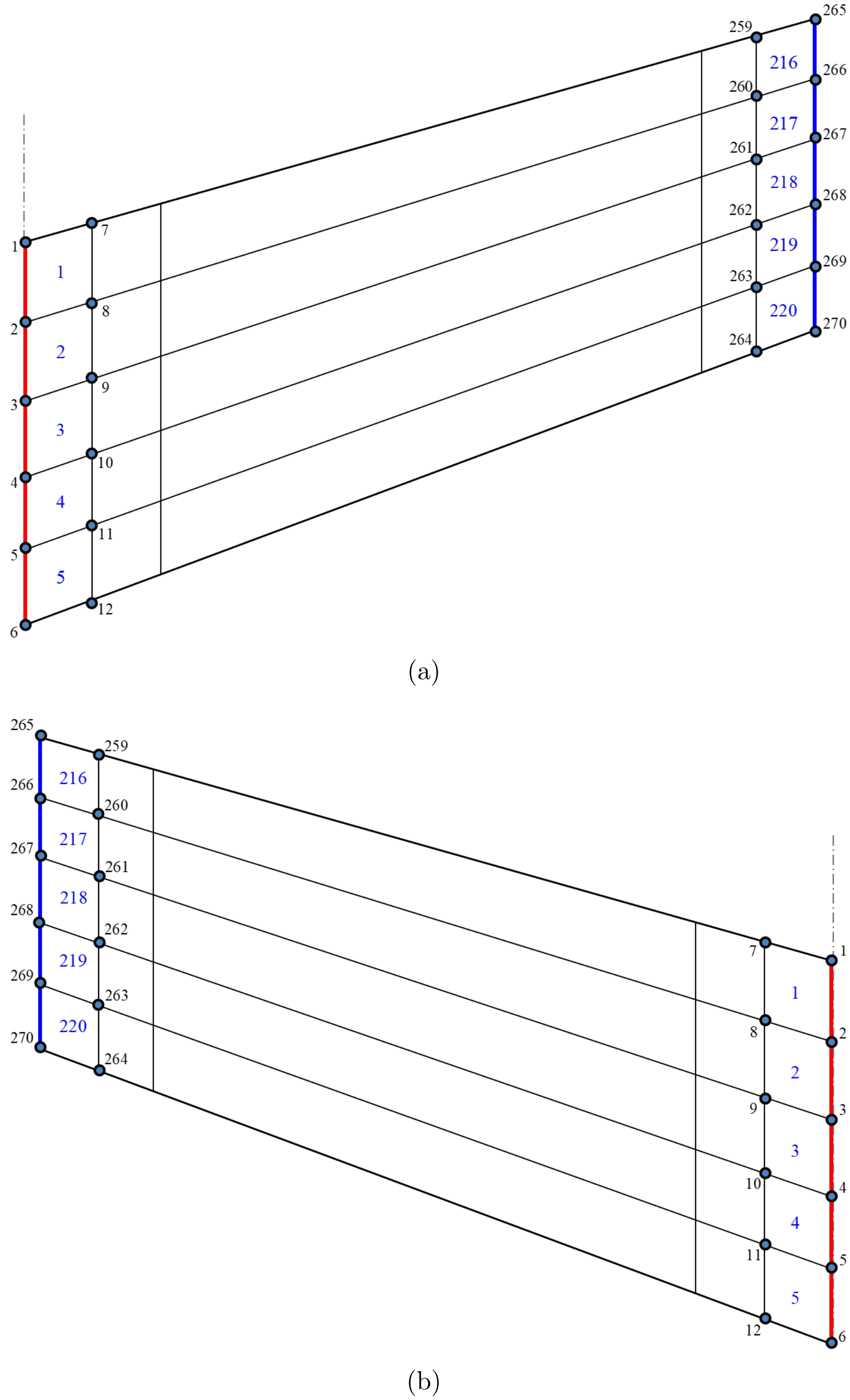

Figure 2.20: Global nodal point and element numbering: (a) right aft forward wing [2] and (b) left aft forward wing [5].

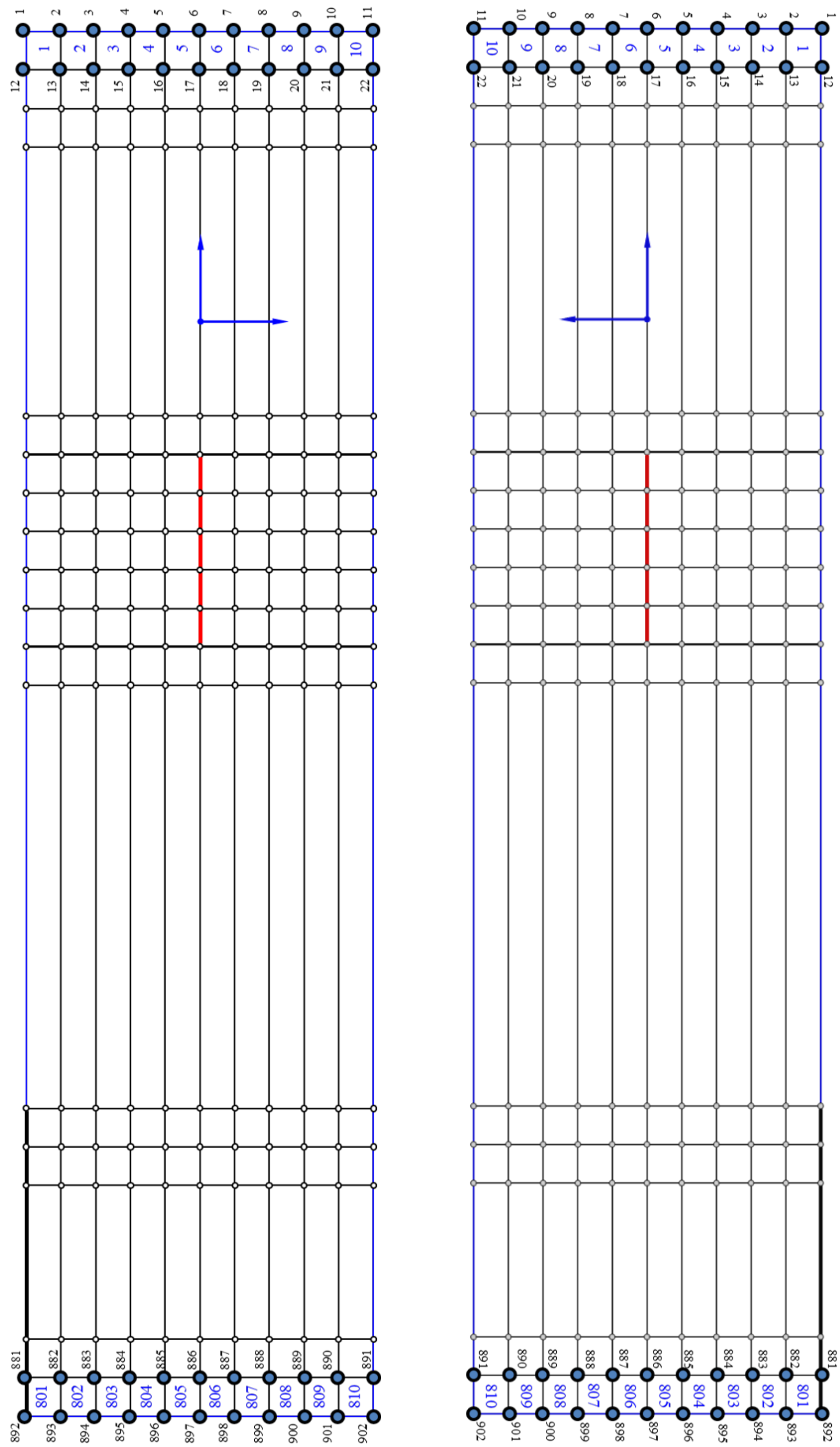

(a)

(b)

Figure 2.21: Global nodal point and element numbering: (a) right half of the fuselage [3] and (b) left half of the fuselage [6].

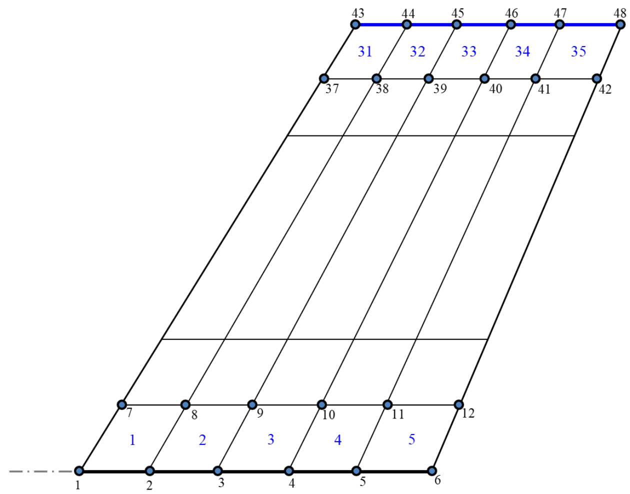

Figure 2.22: Global nodal point and element numbering for the vertical tail [7].

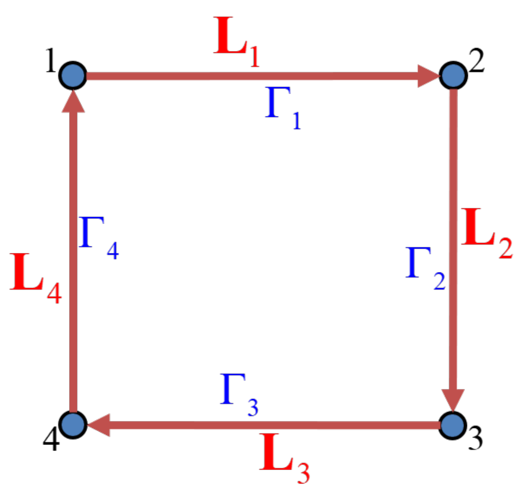

Figure 2.23: Local nodal point numbering with vortex segments and circulations.

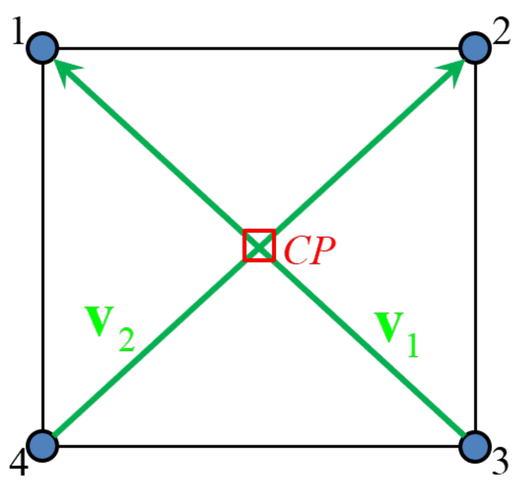

Figure 2.24: Control point and normal vector location of each panel.

Chapter 3: Structural Dynamics: FE Model

In this chapter, the FE based structural dynamics model used in the aeroelastic simulations is presented. Some of the work presented in this chapter is based on the author's contributions in reference [48]. This chapter is used to answer research question **RQ2**. The structural model is constructed via the FE method to describe the motions of the representative joined-wing SensorCraft's wings using non-prismatic, linearly elastic, undamped cantilevered beams with rigid constraints at the roots. The beams satisfy the Euler-Bernoulli beam theory. The fuselage and the vertical tail of the joined-wing SensorCraft are assumed to be completely rigid.

The structural model is composed of four beam structures: 1) the right forward wing, 2) the left forward wing, 3) the right aft wing, and 4) the left aft wing. The right and left forward and aft wings share a joint node, respectively, and the right and left aft wings share a joint node at the vertical tail. A topview of these connections can be seen in Figure 3.1.

The reference systems used for the structural model are presented in Section 3.1. The multi-freedom constraints (MFCs) used to model the rigid-body nature of the fuselage and vertical tail is explained in Section 3.2. Consideration of structural damage on the joined-wings is represented is presented in Section 3.3

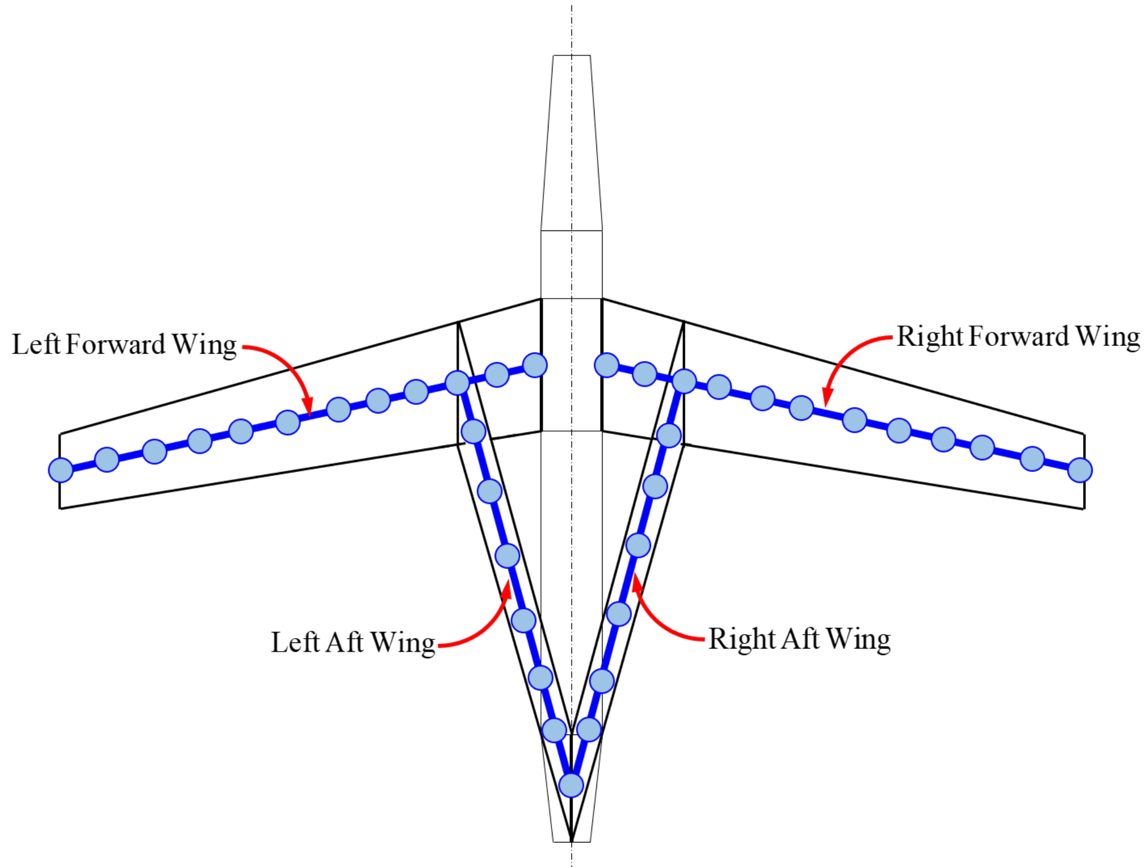

Figure 3.1: Topview of beams used for joined-wings.

and the equations of motion of the system in nodal and modal space are reported in Section 3.4, along with the nondimensionalized equations. In Section 3.5, the structural computational model for the joined-wing SensorCraft is introduced and this is accompanied by a flowchart of the structural simulation procedure; Finally, Section 3.6, is used for the chapter summary.

3.1 Reference Systems

There are six reference systems used in this work: an inertial system that is fixed to the ground, N, and five mobile systems that are fixed to the UAV at all times. The first mobile system, S_2, is fixed to the fuselage and the remaining four are positioned on the left and right forward and aft wings with the right forward wing in the S_3 reference frame, the right aft wing in the S_4 reference frame, the left forward wing in the S_5 reference frame, and the left aft wing in the S_6 reference frame. The S_3 and S_4 reference systems have the associated systems of orthonormal vectors. The S_5 and S_6 reference systems are constructed from the S_3 and S_4 reference systems using the improper orthogonal tensor

$$\mathbf{Q} = \begin{bmatrix} 1 & 0 & 0 \\ 0 & -1 & 0 \\ 0 & 0 & 1 \end{bmatrix}, \tag{3.1}$$

corresponding to a reflection about the xz-plane. The tensor is improper orthogonal because it has a determinant that is equal to -1. The base vectors associated with the reference systems N, S_2, S_3, S_4, S_5, and S_6 are denoted, respectively, as $\left(\hat{\mathbf{i}},\ \hat{\mathbf{j}},\ \hat{\mathbf{k}}\right)$, $\left(\hat{\mathbf{S}}_{12},\ \hat{\mathbf{S}}_{22},\ \hat{\mathbf{S}}_{32}\right)$, $\left(\hat{\mathbf{S}}_{13},\ \hat{\mathbf{S}}_{23},\ \hat{\mathbf{S}}_{33}\right)$, $\left(\hat{\mathbf{S}}_{14},\ \hat{\mathbf{S}}_{24},\ \hat{\mathbf{S}}_{34}\right)$, $\left(\hat{\mathbf{S}}_{15},\ \hat{\mathbf{S}}_{25},\ \hat{\mathbf{S}}_{35}\right)$, and $\left(\hat{\mathbf{S}}_{16},\ \hat{\mathbf{S}}_{26},\ \hat{\mathbf{S}}_{36}\right)$.

In Figure 3.2, a three-dimensional sideview of the beams of the right forward wing and the right aft wing of the joined-wing SensorCraft are shown with the N and S_2 reference systems labeled. The mobile reference systems of the four wings are depicted in Figure 3.3.

Each nodal point in the beam has six degrees of freedom (DOF) representing three structural nodal translations, $u_{1,2,3}$, and three rotations, $\theta_{1,2,3}$. The beam elements are constructed from two neighboring nodal points as shown in Figure 3.4.

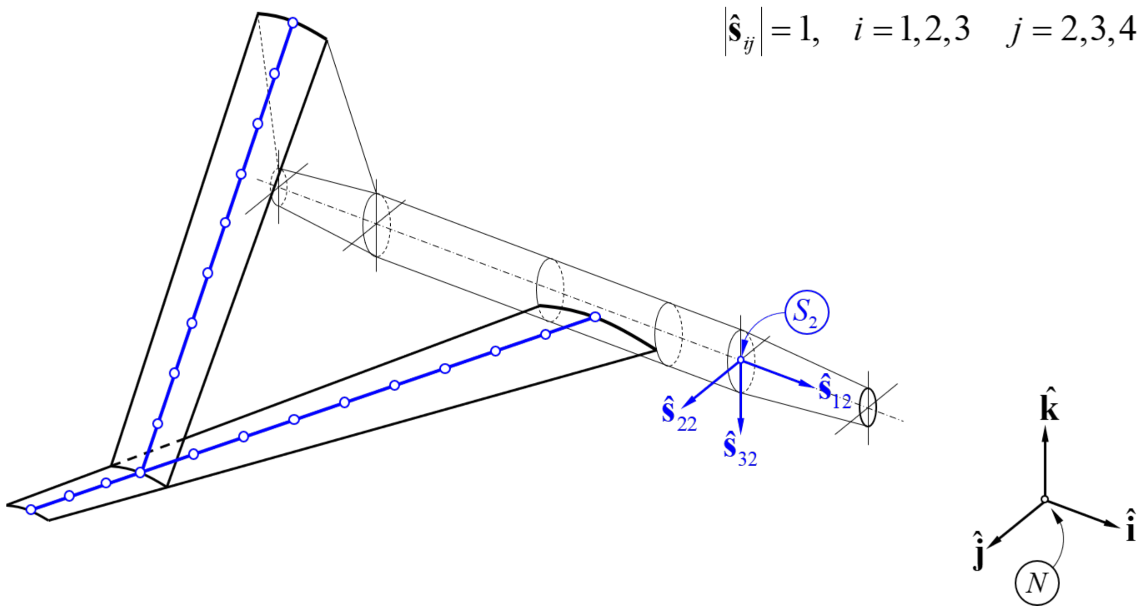

Figure 3.2: Three-dimensional sideview of right half of joined-wing aircraft.

Here, the element has a length of h_e, material density ρ_m, Young's modulus E, and shear modulus G.

3.2 Multi-Freedom Constraints via Master-Slave Elimination

In this work, the fuselage and vertical tail are assumed to be rigid. Given the rigid body motion of the fuselage and vertical, rigid-links need to be established between the rigid bodies and the flexible bodies. To enforce this relation between the two types of bodies, multi-freedom constraints (MFCs) are utilized. MFCs [64] can be implemented through one of three methods: penalty functions, Lagrange multipliers, or master-slave elimination. The Lagrange multiplier method adds to the total number of equations but requires less manipulation. The penalty method leaves the number of unknowns unchanged but may produce an ill-conditioned set of equations. For these reasons, the master-slave elimination method is employed in

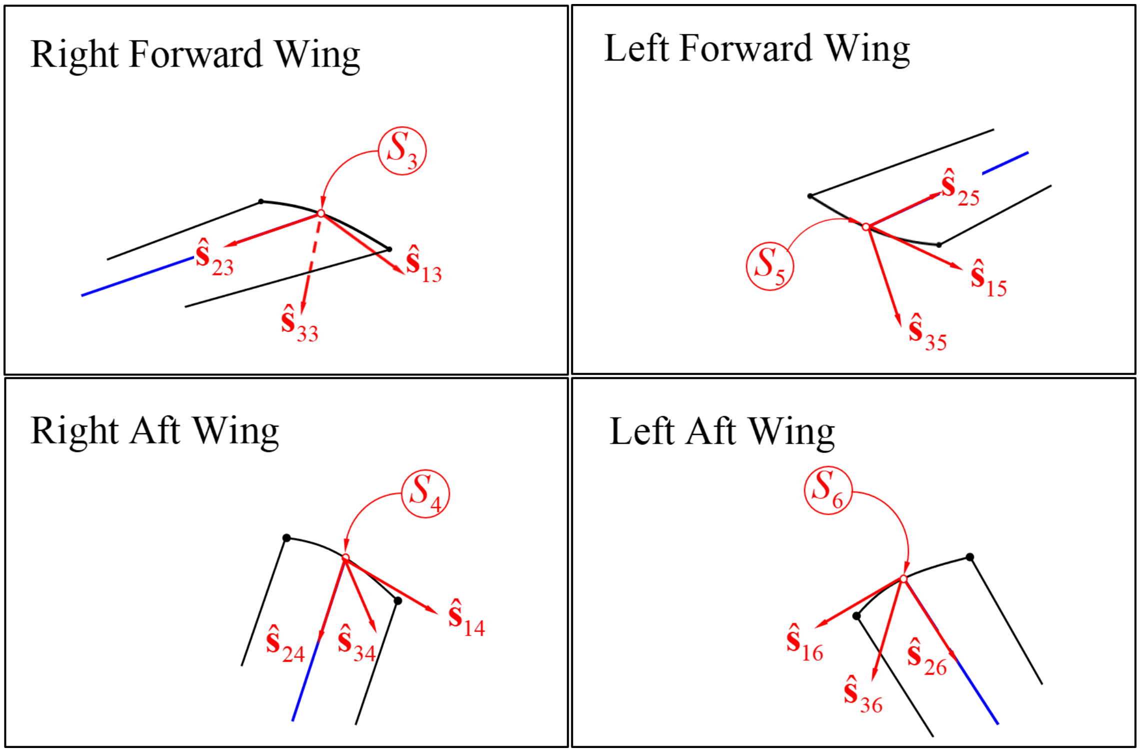

Figure 3.3: Mobile reference systems of wings.

this work.

With the master-slave elimination, the DOF in the structural model are classified into three types: independent, master, and slave. The independent DOF are those that do not appear in any MFCs. The slave DOF are then explicitly eliminated and the modified equations do not contain the slave DOF.

For each constraint a slave DOF is chosen. The DOF remaining in that constraint are labeled master. A new set of DOF is established by removing all slave DOF from the original set of degrees of freedom. This new vector contains master freedoms as well as those that do not appear in the MFCs. A matrix transformation equation that relates the two sets of DOF is generated. The transformation matrix

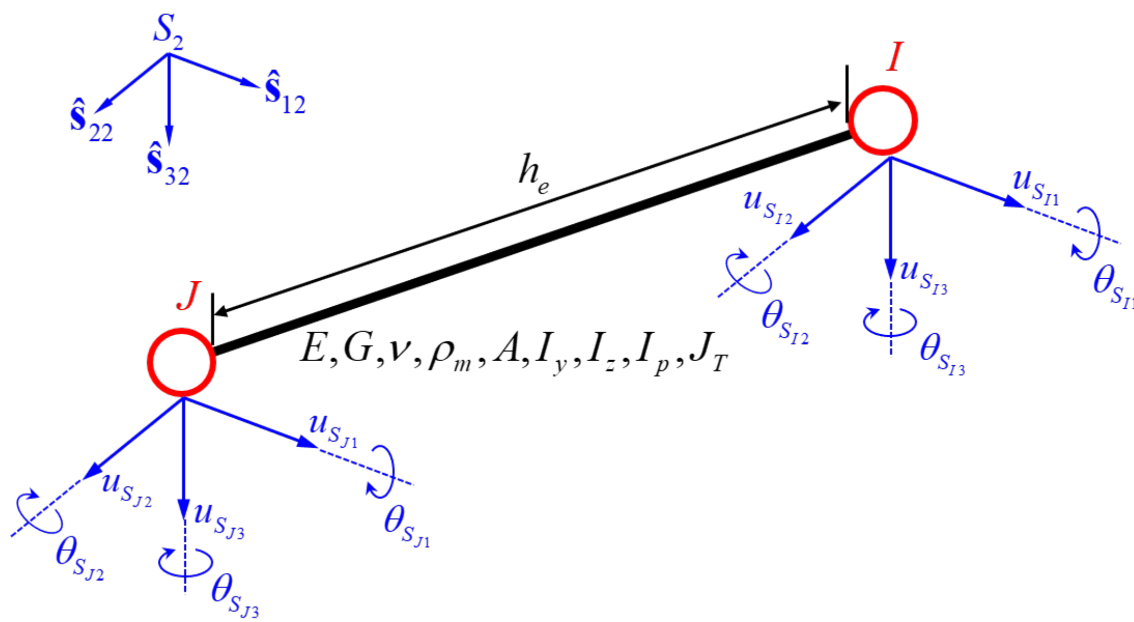

Figure 3.4: Element constructed from node I and node J in the global reference frame, S_2.

equation relating the slave DOF to the master DOF is given by

$$\mathbf{v}_S = \left[\begin{array}{c|c} \mathbf{I}_{3\times 3} & \mathbf{T} \\ \hline \mathbf{0}_{3\times 3} & \mathbf{I}_{3\times 3} \end{array}\right] \mathbf{v}_M \tag{3.2}$$

or

$$\left\{\begin{array}{c} u_{S_1} \\ u_{S_2} \\ u_{S_3} \\ \hline \theta_{S_1} \\ \theta_{S_2} \\ \theta_{S_3} \end{array}\right\} = \left[\begin{array}{ccc|ccc} 1 & 0 & 0 & 0 & r_3 & -r_2 \\ 0 & 1 & 0 & -r_3 & 0 & r_1 \\ 0 & 0 & 1 & r_2 & -r_1 & 0 \\ \hline 0 & 0 & 0 & 1 & 0 & 0 \\ 0 & 0 & 0 & 0 & 1 & 0 \\ 0 & 0 & 0 & 0 & 0 & 1 \end{array}\right] \left\{\begin{array}{c} u_{M_1} \\ u_{M_2} \\ u_{M_3} \\ \hline \theta_{M_1} \\ \theta_{M_2} \\ \theta_{M_3} \end{array}\right\}. \tag{3.3}$$

Here r_i (for $i = 1, 2, 3$) are the components of the vector $\mathbf{r}$ that connects the master node to the slave node. u_{M_i}, θ_{M_i}, u_{S_i}, and θ_{S_i} (for $i = 1, 2, 3$) are the components of the translation and rotation of the master node and slave node, respectively. The global transformation matrix $\mathbf{T}_G$ is used to apply a congruent transformation to the full stiffness and mass matrices, $\mathbf{K}_\mathrm{f}$ and $\mathbf{M}_\mathrm{f}$. This can be done in the following way

$$\mathbf{K} = \mathbf{T}_G^T \mathbf{K}_\mathrm{f} \mathbf{T}_G \tag{3.4}$$

$$\mathbf{M} = \mathbf{T}_G^T \mathbf{M}_\mathrm{f} \mathbf{T}_G \tag{3.5}$$

through which the reduced stiffness and mass matrices are obtained. This procedure yields a set of modified stiffness and mass matrices, $\mathbf{K}$ and $\mathbf{M}$, that are expressed in terms of the new DOF set. Because the modified system does not contain the slave DOF, these have been effectively eliminated.

In this work, the master node is assumed to be at the origin between the vertical tail and the fuselage as shown in Figure 3.5. The slave nodes are the root nodes of the left and right forward wing beams and the root node shared by the left and right aft wing beams. All other nodes in the structural model are assumed to be independent.

3.3 Structural Damage

As shown in Figure 3.4, each element in the structural model has defined material properties (i.e., material density ρ_m, Young's modulus E, Poisson's ratio ν, and shear modulus G) and geometric cross-sectional properties (i.e., area A, planar moments of inertia I_y and I_z, polar moment of inertia I_p, and torsion constant J_T). In this dissertation, structural damage is defined by *reductions* in the stiffness and/or

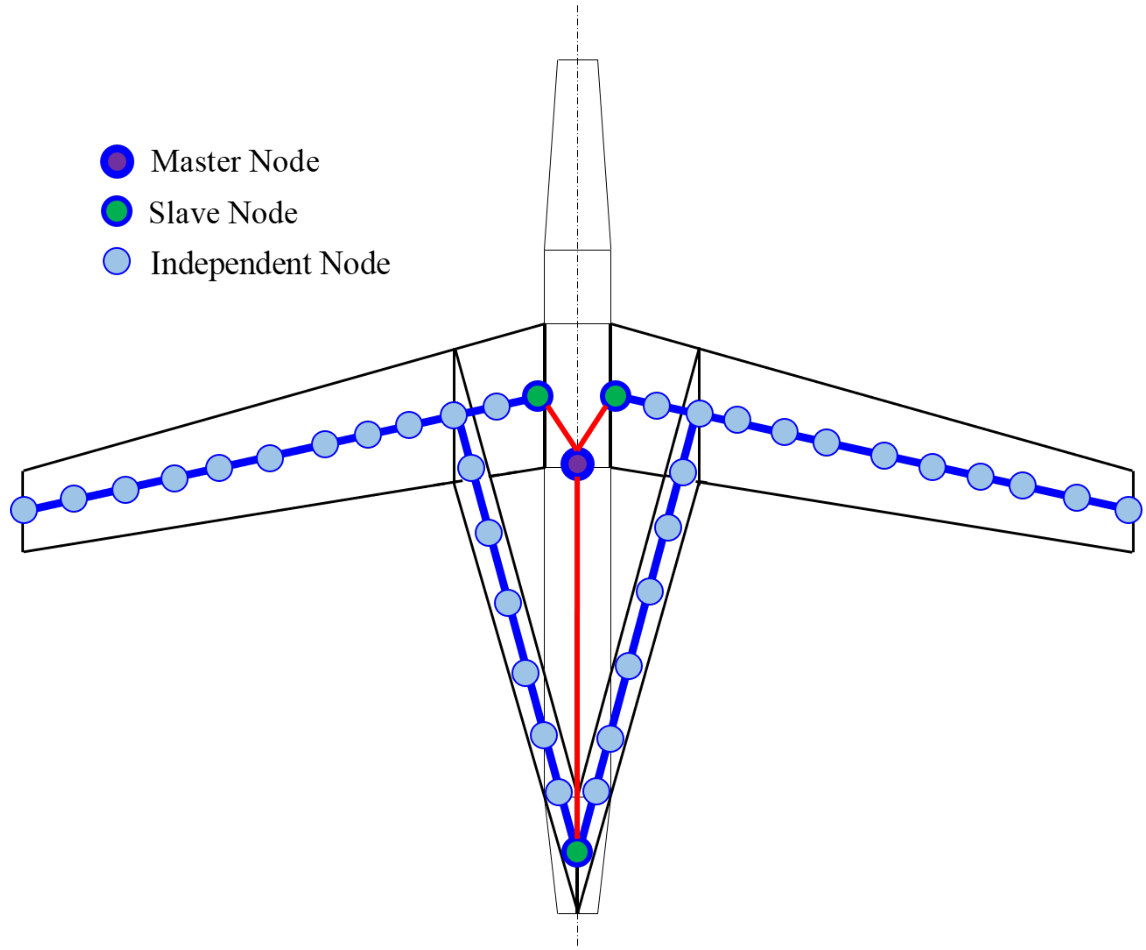

Figure 3.5: Structural node specifications for MFCs via master-slave elimination.

mass properties. This is possible by altering the material properties and/or the cross-sectional properties. In the damage case studies to be presented in Chapter 5, reductions in the polar moment of inertia and torsion constant are used to represent bending and torsional wing damage on specific elements, respectively. While the damage case studies in this dissertation only accounted for damage at one region, it should be noted that the joined-wing structure can have prescribed damage at more than one region in the system.

In this dissertation, damage is prescribed at the beginning of the simulations and cannot be incurred while the simulation is running. In an operating scenario, one can envision the use of sensors to detect damage and use that information to conduct offline and/or online simulations to examine the system performance.

3.4 Equations of Motion

The structural model used in this dissertation work is based on a non-prismatic, linearly elastic model presented in the work of Preidikman [5] and Ceballos [63]. The semi-discrete version of the equations of motion of the wings in terms of dimensional physical variables have the form:

$$[\mathbf{M}^*] \frac{d^2}{dt^{*2}} \mathbf{v}_S^*(t^*) + [\mathbf{K}^*] \, \mathbf{v}_S^*(t^*) = \mathbf{F}_S^*(t^*) \tag{3.6}$$

where $[\mathbf{M}^*]$ is the mass matrix, $[\mathbf{K}^*]$ is the stiffness matrix, $\mathbf{F}_S^*(t)$ is the vector of generalized structural nodal forces, and $\mathbf{v}_S^*(t^*)$ is the vector of generalized structural nodal displacements from generalized nodal translations and rotations. Here, $[\mathbf{M}^*]$ and $[\mathbf{K}^*]$ are $\left(n_S^{dof} \times n_S^{dof}\right)$ matrices and $\mathbf{F}_S^*(t^*)$ and $\mathbf{v}_S^*(t^*)$ are $\left(n_S^{dof} \times 1\right)$ vectors, where n_S^{dof} is the number of DOF of the FE structural element. Let it be noted that $n_S^{dof} = 6n_S$ since the structural model has n_S nodal points with six degrees of freedom per node.

An expansion in terms of the free-vibration modes of the undamped beams is used to describe the motions of the wings. The generalized coordinates of the dynamical system are the time dependent coefficients in the expansions. The free-vibration modes of the structure are obtain by solving the generalized eigenvalue problem:

$$[\mathbf{K}^*]\left[\tilde{\mathbf{\Phi}}^*\right] = [\mathbf{M}^*]\left[\tilde{\mathbf{\Phi}}^*\right]\left[\tilde{\mathbf{\Lambda}}^*\right] \tag{3.7}$$

where

$$\tilde{\mathbf{\Phi}}^* = [\phi_1^* \,|\, \phi_2^* \,|\, \cdots \,|\, \phi_m^*] \tag{3.8}$$

is an $\left(n_S^{dof} \times n_S^{dof}\right)$ matrix with its columns being the n_S^{dof} eigenvectors or mode shape vectors, and

$$\tilde{\mathbf{\Lambda}}^* = \mathrm{diag}\left(\omega_j^{*2}\right) = \begin{bmatrix} \omega_1^{*2} & & & \\ & \omega_2^{*2} & & \\ & & \ddots & \\ & & & \omega_{n_S^{dof}}^{*2} \end{bmatrix} \tag{3.9}$$

is an $\left(n_S^{dof} \times n_S^{dof}\right)$ diagonal matrix with the diagonal elements being the corresponding n_S^{dof} eigenvalues ω_k^{*2}; where the ω_k^* are the natural frequencies of the structure.

The generalized structural nodal displacements $\mathbf{v}_S^*(t^*)$ can be expanded as

$$\mathbf{v}_S^*(t^*) \simeq \sum_{k=1}^{n_m} q_k(t^*)\phi_k^* = [\mathbf{\Phi}^*]\,\mathbf{q}(t^*) \tag{3.10}$$

where

$$\tilde{\mathbf{\Phi}} = \left[\phi_1^* \middle| \phi_2^* \middle| \cdots \middle| \phi_{n_S^{dof}}^*\right] \tag{3.11}$$

is an $\left(n_S^{dof} \times n_m\right)$ matrix with its columns equal to the first-n_m mode shape vectors

and

$$\mathbf{q}(t^*) = \left[q_1(t^*),\ q_2(t^*),\ \cdots,\ q_{n_m}(t^*)\right]^T \tag{3.12}$$

is the $(n_m \times 1)$ nondimensional vector of the generalized coordinates $q_i(t^*)$, and $n_m < n_S^{dof}$. In the numerical simulations performed for this work, 20 modes are used; that is, $n_m = 20$.

After substituting equations (3.10) into equation (3.6), the result is

$$[\mathbf{M}^*]\,[\mathbf{\Phi}^*]\,\frac{d^2}{dt^{*2}}\mathbf{q}(t^*) + [\mathbf{K}^*]\,[\mathbf{\Phi}^*]\,\mathbf{q}(t^*) = \mathbf{F}_S^*(t^*). \tag{3.13}$$

Subsequently, left multiplying this equation by $[\mathbf{\Phi}^*]^T$ leads to

$$[\mathbf{\Phi}^*]^T\,[\mathbf{M}^*]\,[\mathbf{\Phi}^*]\,\frac{d^2}{dt^{*2}}\mathbf{q}(t^*) + [\mathbf{\Phi}^*]^T\,[\mathbf{K}^*]\,[\mathbf{\Phi}^*]\,\mathbf{q}(t^*) = [\mathbf{\Phi}^*]^T\,\mathbf{F}_S^*(t^*). \tag{3.14}$$

Due to the orthogonality properties of $[\mathbf{\Phi}^*]$ with respect to the mass and stiffness matrices, one has

$$[\mathbf{\Phi}^*]^T\,[\mathbf{M}^*]\,[\mathbf{\Phi}^*] = \operatorname{diag}\left(m_j^*\right) = \begin{bmatrix} m_1^* & & & \\ & m_2^* & & \\ & & \ddots & \\ & & & m_{n_m}^* \end{bmatrix} \tag{3.15}$$

and

$$[\mathbf{\Phi}^*]^T [\mathbf{K}^*] [\mathbf{\Phi}^*] = \mathrm{diag}\left(k_j^*\right) = \begin{bmatrix} k_1^* & & & \\ & k_2^* & & \\ & & \ddots & \\ & & & k_{n_m}^* \end{bmatrix}. \tag{3.16}$$

Equations (3.14) can be written as

$$\mathrm{diag}\left(k_j^*\right) \frac{d^2}{dt^{*2}}\mathbf{q}(t^*) + \mathrm{diag}\left(k_j^*\right) \mathbf{q}(t^*) = [\mathbf{\Phi}^*]^T \mathbf{F}_S^*(t^*). \tag{3.17}$$

where $\mathrm{diag}\left(m_j^*\right)$ is the $(n_m \times n_m)$ diagonal matrix with the diagonal entries being the modal masses and $\mathrm{diag}\left(k_j^*\right)$ is the $(n_m \times n_m)$ diagonal matrix listing the modal stiffnesses. $\mathrm{diag}\left(m_j^*\right)$ being positive definite means that equations (3.17) can be left multiplied by $\mathrm{diag}\left(m_j^*\right)^{-1}$ to get

$$\frac{d^2}{dt^{*2}}\mathbf{q}(t^*) + [\mathbf{\Lambda}^*] \mathbf{q}(t^*) = \mathrm{diag}\left(m_j^*\right)^{-1} [\mathbf{\Phi}^*]^T \mathbf{F}_S^*(t^*) \tag{3.18}$$

with

$$\mathrm{diag}\left(m_j^*\right)^{-1} \mathrm{diag}\left(k_j^*\right) = \mathrm{diag}\left(\frac{k_j^*}{m_j^*}\right) = \mathrm{diag}\left(\omega_j^{*2}\right) = [\mathbf{\Lambda}^*] \tag{3.19}$$

where $[\mathbf{\Lambda}^*]$ is a $(n_m \times n_m)$ diagonal matrix listing the squares of the first-n_m natural frequencies of the structure.

From here, the characteristic variables can be used to nondimensionalize the equations of motion. The nondimensional or computational time t, which is related to the physical time t^*, is introduced as

$$t^* = T_C\, t \tag{3.20}$$

where T_C is the characteristic time defined as:

$$T_C = \frac{L_C}{V_C} \tag{3.21}$$

where L_C is the chordwise length of one element of the bound lattice and V_C is the magnitude of the freestream velocity of the fluid.

Also a new set of modal coordinates $\mathbf{q}(t) = [q_1(t),\ q_2(t),\ \cdots,\ q_{n_m}(t)]^T$, a function of the computational time, is introduced as follows

$$\mathbf{q}(t) = \mathbf{q}\left[t^*(t)\right] = \left(\mathbf{q} \circ t^*\right)(t). \tag{3.22}$$

By using the chain rule, the following derivatives are evaluated

$$\begin{aligned}
\dot{\mathbf{q}}(t) &= \frac{d}{dt}\mathbf{q}(t) \\
&= \frac{d}{dt}\left(\mathbf{q} \circ t^*\right)(t) \\
&= \frac{d}{dt^*}\mathbf{q}\left[t^*(t)\right]\frac{d}{dt}t^*(t) \\
&= T_C\frac{d}{dt^*}\mathbf{q}\left[t^*(t)\right] \\
&= T_C\frac{d}{dt^*}\mathbf{q}(t^*)
\end{aligned} \tag{3.23}$$

and

$$\begin{aligned}
\ddot{\mathbf{q}}(t) &= \frac{d^2}{dt^2}\mathbf{q}(t) \\
&= \frac{d^2}{dt^2}\left(\mathbf{q} \circ t^*\right)(t) \\
&= \frac{d}{dt}\left\{T_C \frac{d}{dt^*}\mathbf{q}\left[t^*(t)\right]\right\} \\
&= \frac{d}{dt^*}\left\{T_C \frac{d}{dt^*}\mathbf{q}\left[t^*(t)\right]\right\}\frac{d}{dt}t^*(t) \\
&= T_C^2 \frac{d^2}{dt^{*2}}\mathbf{q}\left[t^*(t)\right] \\
&= T_C^2 \frac{d^2}{dt^{*2}}\mathbf{q}(t^*).
\end{aligned} \tag{3.24}$$

Hence, equations (3.18) can be rewritten as follows:

$$\frac{1}{T_C^2}\ddot{\mathbf{q}}(t) + \left[\mathbf{\Lambda}^*\right]\mathbf{q}(t) = \mathrm{diag}\left(m_j^*\right)^{-1}\left[\mathbf{\Phi}^*\right]^T \mathbf{F}_S^*(t^*) \tag{3.25}$$

or

$$\ddot{\mathbf{q}}(t) + T_C^2\ \left[\mathbf{\Lambda}^*\right]\mathbf{q}(t) = T_C^2\ \mathrm{diag}\left(m_j^*\right)^{-1}\left[\mathbf{\Phi}^*\right]^T \mathbf{F}_S^*(t^*). \tag{3.26}$$

It is noted that

$$\begin{aligned}
T_C^2\ \left[\mathbf{\Lambda}^*\right] &= \mathrm{diag}\left(T_C^2\ \omega_j^{*2}\right) \\
&= \mathrm{diag}\left(\left(\frac{L_C\ \omega_j^*}{V_C}\right)^2\right) \\
&= \mathrm{diag}\left(\omega_j^2\right) \\
&= \left[\mathbf{\Lambda}\right]
\end{aligned} \tag{3.27}$$

where $[\mathbf{\Lambda}]$ is a $(n_m \times n_m)$ diagonal matrix listing the squares of the first-n_m dimensionless or reduced frequencies, $\omega_j = \frac{L_C\, \omega_j^*}{V_C}$, $j = 1, \cdots, n_m$, of the structure. Hence, the equationx of motion of the joined-wings is given by

$$\ddot{\mathbf{q}}(t) + [\mathbf{\Lambda}]\, \mathbf{q}(t) = T_C^2 \,\mathrm{diag}\left(m_j^*\right)^{-1} [\mathbf{\Phi}^*]^T\, \mathbf{F}_S^*(t^*) \tag{3.28}$$

3.5 Computational Structural Dynamics Model

A flowchart of the structural dynamics model is shown in Figure 3.6. In the model used, the mass matrix, $[\mathbf{M}]$, and elastic stiffness matrix, $[\mathbf{K}]$, are computed from the material and geometric properties of the aircraft wings. The structural load vector $\mathbf{F}_S(t)$, can be obtained from the UVLM aerodynamic model. The nodal displacements, $\mathbf{v}_S(t)$, are computed by using the equation of motion and used to update the aerodynamic mesh. The procedure of correcting for the displacements and updating the aerodynamic mesh is repeated until the solution convergence it achieved. The structural model is capable of taking into account wing structural degradation and rigid-body body motion of the fuselage.

As stated earlier, the structural model is composed of four beams representing the left and right forward and aft wings of the joined-wing aircraft. The left and right forward wing beams contain 11 elements made from 12 nodal points each. The left and right aft wing beams contain seven elements made from eight nodal points each. The left and right aft wing beams share one nodal point between each other and share a nodal point with their respective forward wing beams. For the joined-

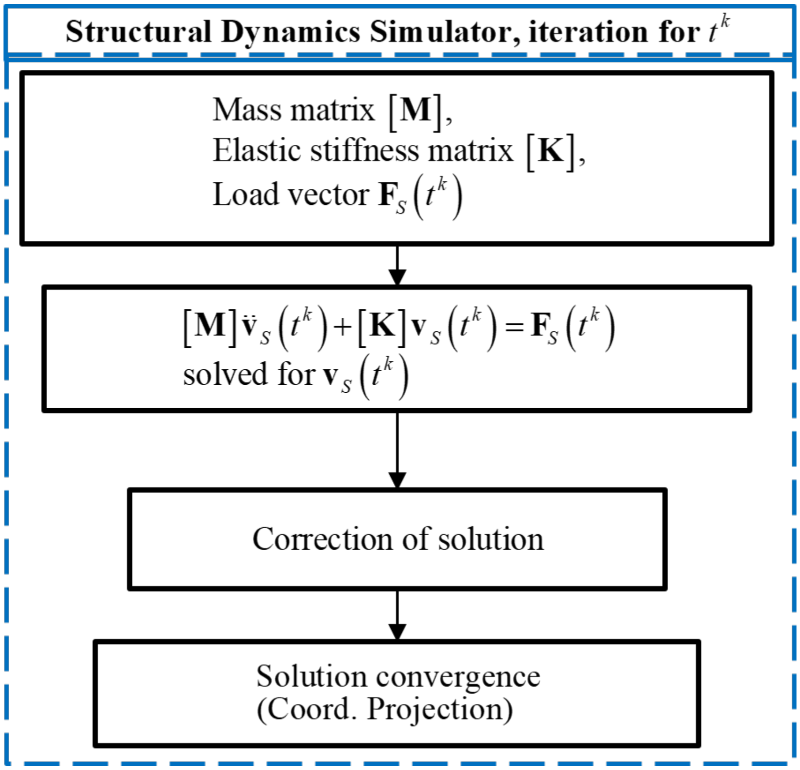

Figure 3.6: Flowchart of FE structural dynamics simulator.

wing aircraft utilized for this dissertation work, the joint connecting the aft wing with the forward wing is located closer to the root of the forward wing attached to the fuselage. This can all be seen in Figure 3.7, where the structural beam model (in blue) is superimposed on the aerodynamic mesh. The element size has been chosen to determine upto the first 20 modes of vibrations, which are discussed in the next section.

3.5.1 Modes of Vibration

The material properties and geometric cross-sectional properties used for the computational structural model are listed in Tables 3.1 and 3.2, respectively. With these properties, the natural frequencies and mode shapes of the structural can

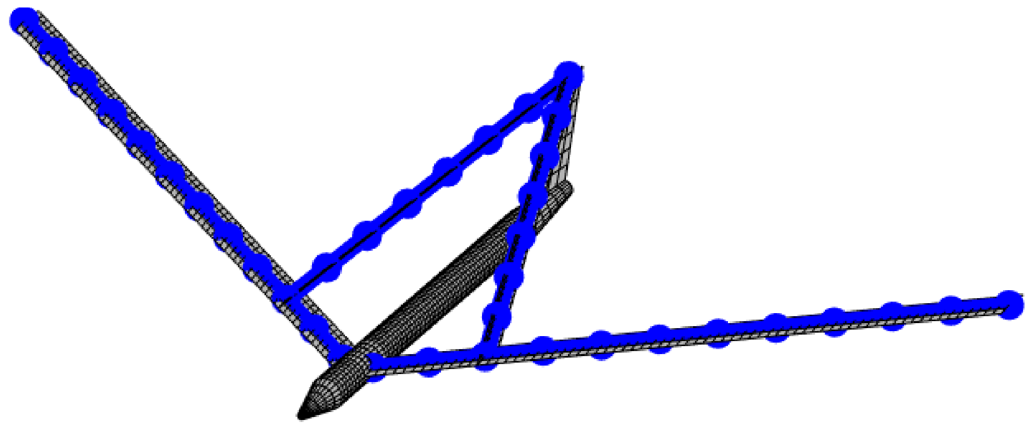

Figure 3.7: Structural beam model superimposed on aerodynamic mesh.

obtained. The first 20 natural frequencies, which are required for the aeroelastic model, are listed in Table 3.3 and the corresponding mode shapes for the first four natural frequencies are shown in Figures 3.8, 3.9, 3.10, and 3.11. From the natural frequencies and the mode shapes, a pattern can be detected. Note that starting from the first two modes of vibration, subsequent pairs of natural frequencies are nearly identical (e.g., Modes 1 and 2, Modes 3 and 4, Modes 5 and 6, and so on.). In the mode, it is seen that each mode from a pair corresponds to a bending or torsional motion on one half of the joined-wing. For example, the first bending vibration mode of the left forward wing can be seen in Figure 3.8 while the first bending vibration mode of the right forward wing can be seen in Figure 3.9. The first torsional vibration modes can be seen in Figures 3.10 and 3.11 with the third mode corresponding to twisting in the right forward wing and the fourth mode corresponding to the twisting in the left forward wing. Even though the motions of the vibrations are represented on opposite wings, the motions are identical (similar to how the natural frequencies are identical). The mode shapes corresponding to

Table 3.1: Material properties of computational structural model with no damage.

E [N/m^2]	G [N/m^2]	ν	ρ_m [kg/m^3]
7.310×10^{10}	2.800×10^{10}	0.33	2.780×10^{3}

Table 3.2: Geometric cross-sectional properties of computational structural model with no damage.

A [m^2]	I_y [m^4]	I_z [m^4]	I_p [m^4]	J_T [m^4]
1.744×10^{-2}	3.303×10^{-4}	7.576×10^{-3}	7.907×10^{-1}	1.055×10^{-3}

the last 16 natural frequencies are displayed in Appendix B.

3.6 Summary

In this chapter, the reference systems required for describing the motions of the four flexible wings is presented along with the structural damage and MFCs. Also, how the equations of motion are converted from nodal space to modal space and the nondimensionalized form is discussed. The computational structural dynamics model along with the mode shapes corresponding with the material and geometric cross-sectional properties used in this work are presented.

In the next chapter, the method used to integrate the structural dynamic and

Table 3.3: First 20 natural frequencies of structural system with no damage.

Mode i	Frequency f_i [Hz]	Mode i	Frequency f_i [Hz]
1	0.370	2	0.370
3	0.868	4	0.868
5	1.548	6	1.548
7	2.215	8	2.215
9	2.530	10	2.530
11	2.666	12	2.666
13	3.769	14	3.769
15	4.583	16	4.583
17	5.047	18	5.047
19	6.057	20	6.057

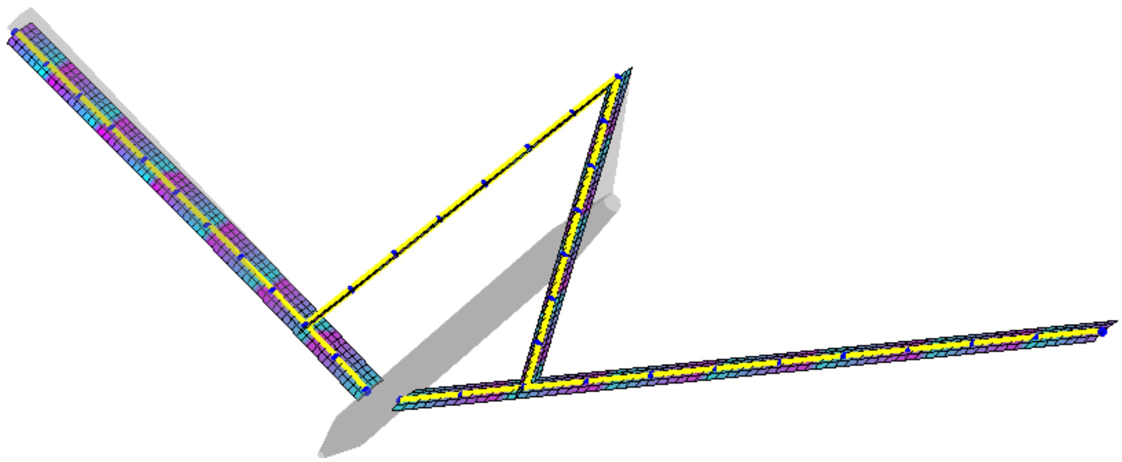

Figure 3.8: First mode corresponding to natural frequency $f_1 = 0.370\,\text{Hz}$.

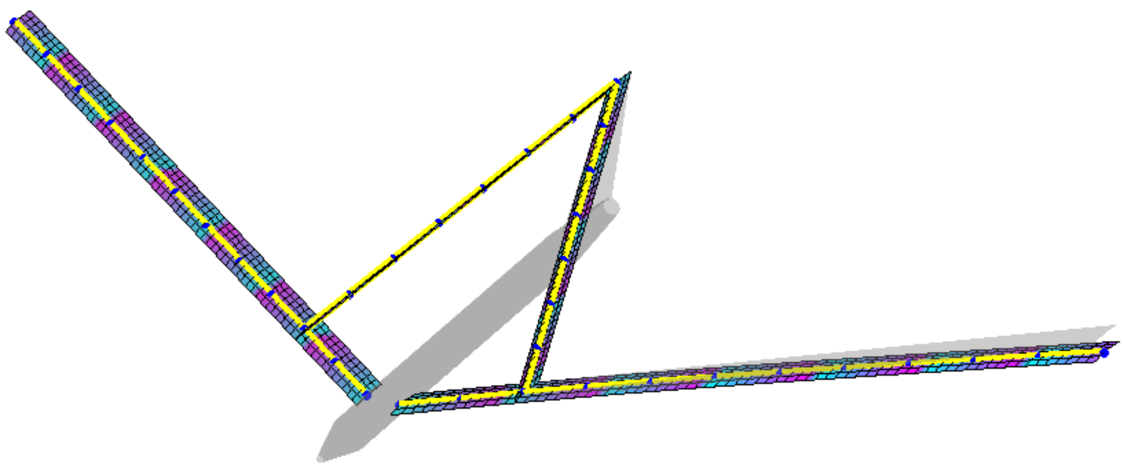

Figure 3.9: Second mode corresponding to natural frequency $f_2 = 0.370\,\text{Hz}$.

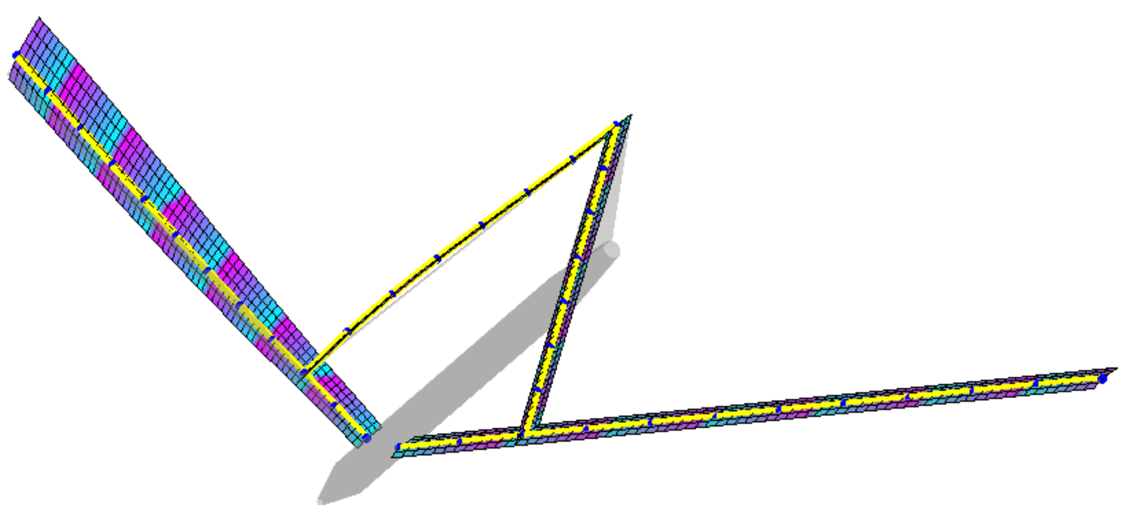

Figure 3.10: Third mode corresponding to natural frequency $f_3 = 0.868\,\text{Hz}$.

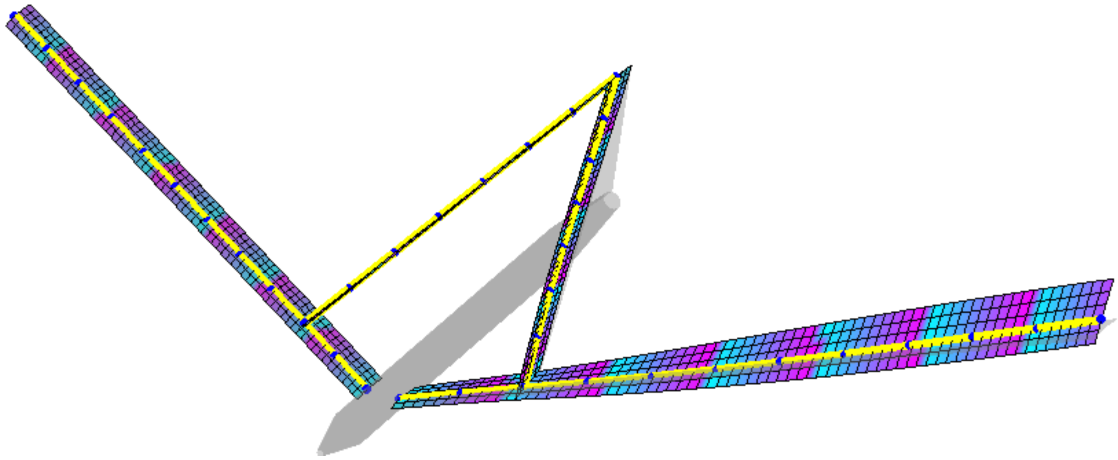

Figure 3.11: Fourth mode corresponding to natural frequency $f_4 = 0.868\,\mathrm{Hz}$.

aerodynamic models is addressed.

Chapter 4: Integration of Aerodynamics and Structural Dynamics

In this chapter, the co-simulation process is expanded upon to describe the integration of the aerodynamic and structural dynamic models, which produces the aeroelastic model. Some of the work presented in this chapter is based on the author's contributions in reference [48]. This chapter is used to answer research question **RQ3**. A flowchart for the aeroelastic simulations is shown in Figure 4.1. Based on the initial conditions obtained with the structural response, the wake velocities are computed, which tends to be the most computationally expensive process, in the aerodynamic model. With the newly computed wake velocities in the aerodynamic model, the RHS vector and the aerodynamic influence matrix, which are required in solving for the circulations for the vortex panels, are evaluated. After the aerodynamic loads are calculated, the aerodynamic loads are transferred to the structural model to get the displacements and velocities needed to update the models. If the structural solution does not converge after two sequential iterations, the aerodynamic influence matrix and RHS vector need to to reevaluated with the updated aerodynamic mesh geometry. This is repeated until the solution convergence is reached. It is assumed that a solution cannot be reached if the solution does not converge after a specified amount of iterations.

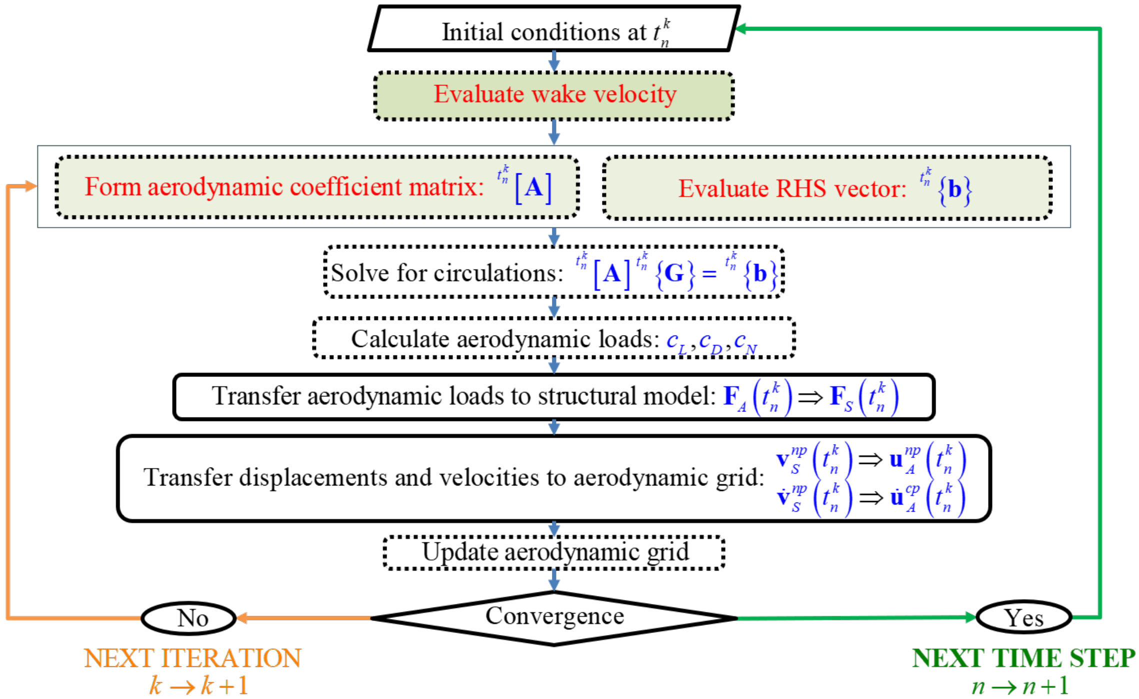

Figure 4.1: Flowchart of aeroelastic simulations via integration of UVLM aerodynamic model and FE method structural model.

In Section 4.1, the co-simulation framework is described in detail. The methodology used to transfer displacements, velocities, and forces between the aerodynamic and structural models is presented in Section 4.2. In Section 4.3, the author has discussed the transferring of model information methodology and the integration of the equations of motion. In Section 4.4, the numerical integration scheme used to solve the equations of motion of the system is discussed. The incorporated of the aerodynamic model into the numerical integration scheme is presented in Section 4.5. Finally, in Section 4.6, the author provides a summary of the chapter.

4.1 Co-simulation Framework

Co-simulation refers to the partitioning of a coupled system into subsystems that are separately simulated (but numerically integrated) with a suitable exchange of states at predefined time instances to account for the coupling.

In Figure 4.2, the steps involved in the co-simulation process for a joined-wing SensorCraft wing in airflow are depicted. At the initial stage, the coupled system (structure in airflow) is represented by the continuous system, wherein the state vector is given by

$$\mathbf{z}(t) = \begin{pmatrix} \mathbf{v}_S(t) \\ \mathbf{F}_A(t) \end{pmatrix} \tag{4.1}$$

where $\mathbf{v}_S(t)$ is the state vector associated with the wing structures and $\mathbf{F}_A(t)$ is the aerodynamic loads generated from the velocity/pressure fields of airflow. The next stage in the co-simulation process involves the partitioning of the dynamic system into two subsystems as follows:

$$\frac{d}{dt}\mathbf{z}(t) = \frac{d}{dt}\begin{pmatrix} \mathbf{v}_S(t) \\ \mathbf{F}_A(t) \end{pmatrix} = \begin{pmatrix} f_1\left(\mathbf{v}_S(t), \mathbf{F}_A(t)\right) \\ f_2\left(\mathbf{v}_S(t), \mathbf{F}_A(t)\right) \end{pmatrix} \tag{4.2}$$

or

$$\begin{aligned} \dot{\mathbf{v}}_S(t) &= f_1\left(\mathbf{v}_S(t), \mathbf{F}_A(t)\right) \\ \dot{\mathbf{F}}_A(t) &= f_2\left(\mathbf{v}_S(t), \mathbf{F}_A(t)\right) \end{aligned} \tag{4.3}$$

The final stage of the co-simulation process involves exchanging information bi-directionally between the two subsystems. This is accomplished by using a predic-

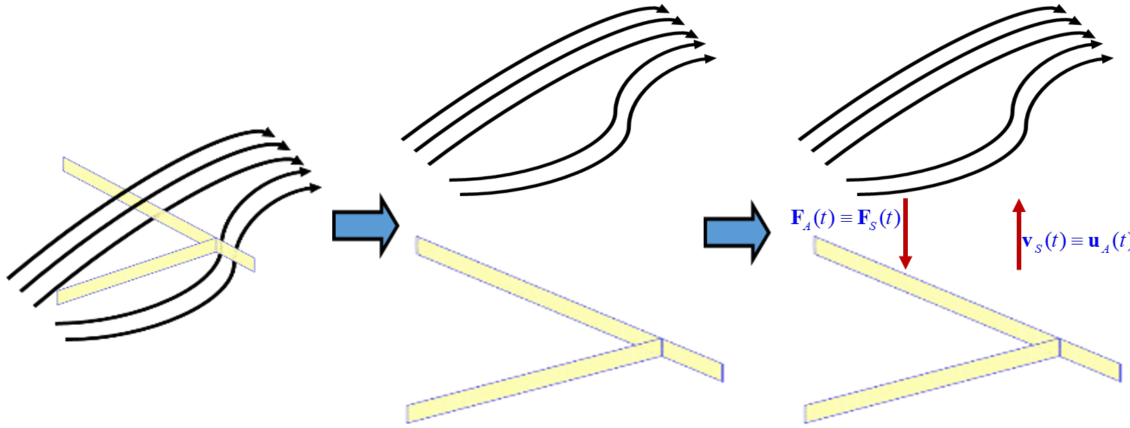

Figure 4.2: Co-simulation process for a system in airflow.

tion to represent the unknown state vector in the opposite subsystems. Therefore, to simulate the $\dot{\mathbf{v}}_S(t)$ subsystem, a prediction $\mathbf{F}_S(t)$ is needed for its $\mathbf{F}_A(t)$ input. Similarly, to simulate the $\dot{\mathbf{F}}_A(t)$ system, a prediction $\mathbf{u}_A(t)$ is needed for the $\mathbf{v}_S(t)$ input. The system can be written as

$$\begin{aligned} \dot{\mathbf{v}}_S(t) &= \mathbf{f}_1\left(\mathbf{v}_S(t), \mathbf{F}_S(t)\right) \\ \dot{\mathbf{F}}_A(t) &= \mathbf{f}_2\left(\mathbf{u}_A(t), \mathbf{F}_A(t)\right) \end{aligned} \tag{4.4}$$

in which the structure's state is simulated by using the predicted airflow states and the airflow state is simulated by using the predicted structure states. More information on co-simulation of complex systems can be found in references [6–8].

The last stage of the co-simulation process can be summarized as a three-step procedure:

1. Mapping of the structural motion onto the aerodynamic grid;

2. Mapping of the aerodynamic forces onto the structural grid;

3. Numerical integration of all of the governing equations simultaneously and

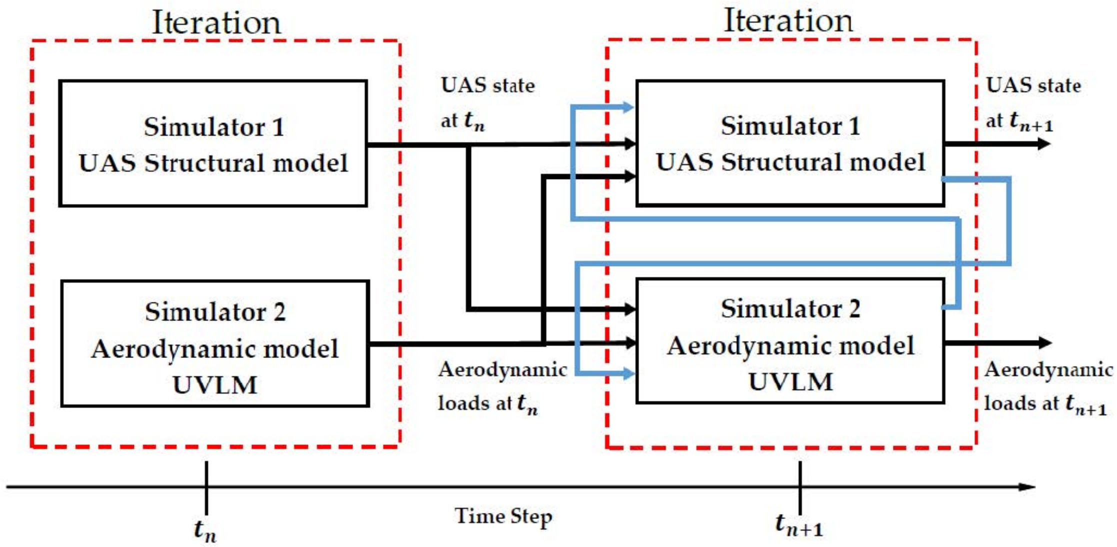

Figure 4.3: Strong coupling scheme between structural dynamic and aerodynamic models.

interactively in the time domain.

This procedure can be observed in Figure 4.3.

4.2 Transferring Generalized Displacements and Forces

The development of an aeroelastic simulator requires the transfer of displacements from the structural grid to the aerodynamic grid and the transfers of forces from the aerodynamic grid to the structural grid. The methodology used in this work to exchange information between the two models will be described in detail in this section.

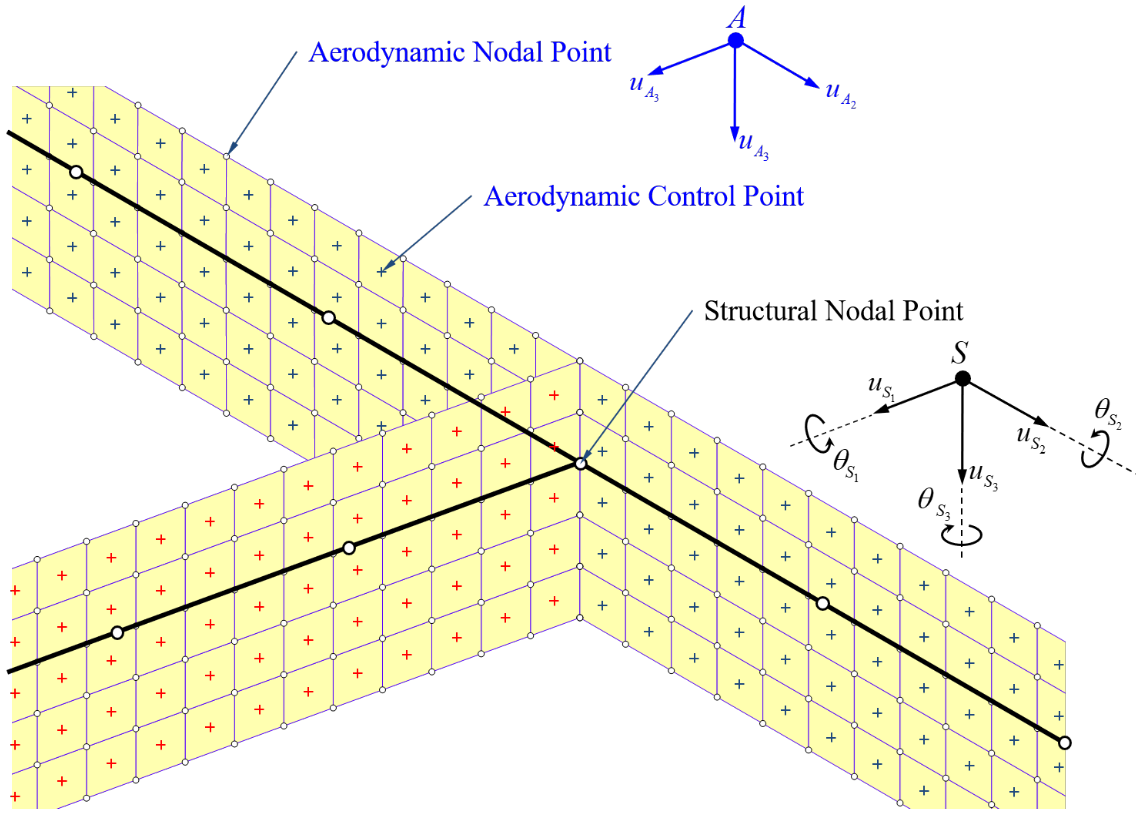

Figure 4.4: Structural nodal grids aligned with aerodynamic nodal and control points.

4.2.1 Generalized Displacements in Structural Grid to Translations in Aerodynamic Grid

A representation of the alignment of the joined-wing configuration structural grid along the aerodynamic grid is shown in Figure 4.4.In this figure, the author shows the structural nodal points, aerodynamic nodal points, and aerodynamic control points along with the DOF corresponding to the nodal points in both meshes.

Transfer of information between the two models is achieved through the use of an interpolation matrix. This matrix makes explicit the relationship between the DOF of the structural model and the aerodynamic model. In dimensional physical variables, The displacements of arbitrary points in the aerodynamic grid are connected to the generalized structural nodal displacements through the following linear transformation:

$$\mathbf{u}_A^*(t^*) = [\mathbf{G}_{AS}^*]\ \mathbf{v}_S^*(t^*), \tag{4.5}$$

where $\mathbf{u}_A^*(t^*)$ is a $(3n_A \times 1)$ vector containing the components of the displacements of the selected points in the aerodynamic grid, $\mathbf{v}_S^*(t^*)$ is a $(6n_S \times 1)$ vector containing the components of generalized nodal displacements, n_A is the number of selected points in the aerodynamic grid, n_S is the number of nodes in the structural grid, and $[\mathbf{G}_{AS}^*]$ is the $(3n_A \times 6n_S)$ interpolation matrix that relates the generalized displacements of the structural grid nodal points to the displacements of the aerodynamic grid selected points. The construction of the interpolation matrix, $[\mathbf{G}_{AS}^*]$, depends on the following

1. the geometry of both the aerodynamic and structural grid,

2. the particular points selected in the aerodynamic grid, and

3. the particular kind of finite element selected to discretize the structure.

4.2.2 Calculation of Interpolation Matrix

In this subsection, the calculation of the elements that constitute the interpolation matrix that relates the displacements and rotations on the structural grid nodal points with the translations on the aerodynamic grid selected points is discussed. In developing these elements, point B in considered to lie in a plane perpendicular to the undeformed axis of the beam. There are three cases:

1. the plane containing point B intersects the beam axis and is an "internal point"

2. the plane containing point B intersects an imaginary extension near the beginning of the beam and is an "initial point"

3. the plane containing point B intersects an imaginary extension near the end of the beam and is an "end point."

Case I: Connection with an Internal Point

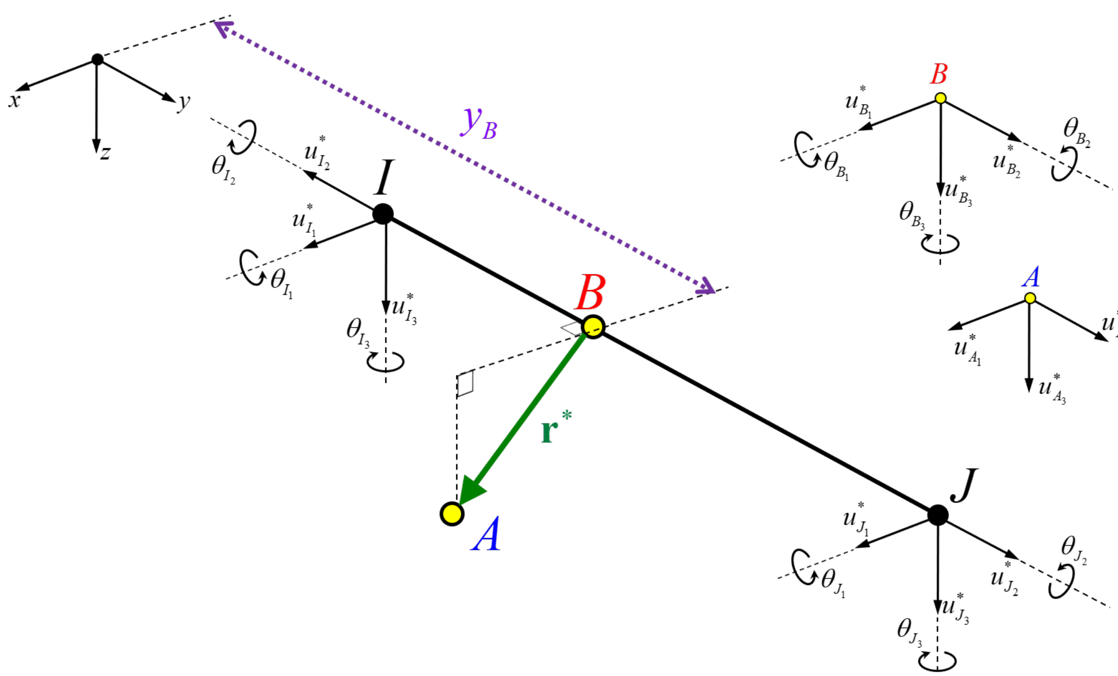

Figure 4.5: Connection with an internal point.

First, point A is selected on the aerodynamic grid and then find point B on the elastic axis of the beam between the structural grid nodal points I and J such that A and B lie in same plane perpendicular to the undeformed axis of the beam. As shown in Figure 4.5, the relative position of point A with respect to point B is given by the vector $\mathbf{r}^*$.

To be consistent with the Euler-Bernoulli theory, it is assumed that the flat section normal to the undeformed axis of the beam remains flat after deformation and it is further assumed that the cross section maintains its shape. Hence, the vector $\mathbf{r}^*$ that connects the points A and B is rigid. The displacements of nodal point A are related to the generlaized displacements of point B by the following relationship:

$$\mathbf{u}_A^* = \left[\begin{array}{c|c} \mathbf{I}_{3\times 3} & \mathbf{T}_1 \end{array} \right] \left\{ \begin{array}{c} \mathbf{u}_B^* \\ \boldsymbol{\theta}_B^* \end{array} \right\} \tag{4.6}$$

or

$$\left\{ \begin{array}{c} u_{A_1}^* \\ u_{A_2}^* \\ u_{A_3}^* \end{array} \right\} = \left[\begin{array}{ccc|ccc} 1 & 0 & 0 & 0 & r_3^* & 0 \\ 0 & 1 & 0 & -r_3^* & 0 & r_1^* \\ 0 & 0 & 1 & 0 & -r_1^* & 0 \end{array} \right] \left\{ \begin{array}{c} u_{B_1}^* \\ u_{B_2}^* \\ u_{B_3}^* \\ \theta_{B_1} \\ \theta_{B_2} \\ \theta_{B_3} \end{array} \right\} \tag{4.7}$$

where (r_1^*, r_2^*, r_3^*) are the components of the $\mathbf{r}^*$, $(u_{A_1}^*, u_{A_2}^*, u_{A_3}^*)$ are the components of the translation of point A on the aerodynamic grid, and $(u_{B_1}^*, u_{B_2}^*, u_{B_3}^*, \theta_{B_1}, \theta_{B_2}, \theta_{B_3})$ are the components of the displacement and rotation of point B on the structural grid. All of these components are referenced in the (x, y, z) coordinate system are shown in Figure 4.5.

After using the characteristic length L_C, $\mathbf{r}^*$ is rewritten as follows

$$\mathbf{r}^* = L_C\, \mathbf{r} \tag{4.8}$$

and equation (4.7) becomes

$$\begin{Bmatrix} u^*_{A_1} \\ u^*_{A_2} \\ u^*_{A_3} \end{Bmatrix} = \left[\begin{array}{ccc|ccc} 1 & 0 & 0 & 0 & L_C\, r_3 & 0 \\ 0 & 1 & 0 & -L_C\, r_3 & 0 & L_C\, r_1 \\ 0 & 0 & 1 & 0 & -L_C\, r_1 & 0 \end{array} \right] \begin{Bmatrix} u^*_{B_1} \\ u^*_{B_2} \\ u^*_{B_3} \\ \theta_{B_1} \\ \theta_{B_2} \\ \theta_{B_3} \end{Bmatrix} \tag{4.9}$$

Note that the displacement field within each finite element depends on the type of finite element used in the discretization process. In general, these fields may be written as linear combinations of the shape functions and the nodal displacements. For the finite element used in this work, the displacement and rotation fields are obtained as linear combinations of the shape functions $\bar{N}_1$ through $\bar{N}_6$, the displacements $u^*_{I_i}$ and $u^*_{J_i}$, as well as the rotations θ_{I_i} and θ_{J_i} of the nodal points I and J, for $i = 1, 2, 3$, as follows:

$$u^*_1(\eta^*) = u^*_{I_1}\, \bar{N}_3(\eta^*) + u^*_{J_1}\, \bar{N}_4(\eta^*) - \theta_{I_3}\, \bar{N}_5(\eta^*) - \theta_{J_3}\, \bar{N}_6(\eta^*) \tag{4.10}$$

$$u^*_2(\eta^*) = u^*_{I_2}\, \bar{N}_1(\eta^*) + u^*_{J_2}\, \bar{N}_2(\eta^*) \tag{4.11}$$

$$u^*_3(\eta^*) = u^*_{I_3}\, \bar{N}_3(\eta^*) + u^*_{J_3}\, \bar{N}_4(\eta^*) + \theta_{I_1}\, \bar{N}_5(\eta^*) + \theta_{J_1}\, \bar{N}_6(\eta^*) \tag{4.12}$$

and

$$
\begin{aligned}
\theta_1(\eta^*) &= \frac{d}{d\eta^*} u_3^*(\eta^*) \\
&= u_{I_3}^* \ \frac{d}{d\eta^*} \bar{N}_3(\eta^*) + u_{J_3}^* \ \frac{d}{d\eta^*} \bar{N}_4(\eta^*) + \theta_{I_1} \ \frac{d}{d\eta^*} \bar{N}_5(\eta^*) + \theta_{J_1} \ \frac{d}{d\eta^*} \bar{N}_6(\eta^*) \quad (4.13) \\
\theta_2(\eta^*) &= \theta_{I_2} \ \bar{N}_1(\eta^*) - \theta_{J_2} \ \bar{N}_2(\eta^*) \quad (4.14) \\
\theta_3(\eta^*) &= -\frac{d}{d\eta^*} u_1^*(\eta^*) \\
&= -u_{I_1}^* \ \frac{d}{d\eta^*} \bar{N}_3(\eta^*) - u_{J_1}^* \ \frac{d}{d\eta^*} \bar{N}_4(\eta^*) + \theta_{I_3} \ \frac{d}{d\eta^*} \bar{N}_5(\eta^*) + \theta_{J_3} \ \frac{d}{d\eta^*} \bar{N}_6(\eta^* \quad (4.15)
\end{aligned}
$$

where

$$
\begin{aligned}
\bar{N}_1(\eta^*) &= \frac{\eta_J^* - \eta^*}{h_e^*} \quad (4.16) \\
\bar{N}_2(\eta^*) &= \frac{\eta^* - \eta_I^*}{h_e^*} \quad (4.17) \\
\bar{N}_3(\eta^*) &= 1 - 3\left(\frac{\eta^* - \eta_I^*}{h_e^*}\right)^2 + 2\left(\frac{\eta^* - \eta_I^*}{h_e^*}\right)^3 \quad (4.18) \\
\bar{N}_4(\eta^*) &= 3\left(\frac{\eta^* - \eta_I^*}{h_e^*}\right)^2 - 2\left(\frac{\eta^* - \eta_I^*}{h_e^*}\right)^3 \quad (4.19) \\
\bar{N}_5(\eta^*) &= (\eta^* - \eta_I^*) - \frac{2}{h_e^*}(\eta^* - \eta_I^*)^2 + \frac{1}{{h_e^*}^2}(\eta^* - \eta_I^*)^3 \quad (4.20) \\
\bar{N}_6(\eta^*) &= -\frac{1}{h_e^*}(\eta^* - \eta_I^*)^2 + \frac{1}{{h_e^*}^2}(\eta^* - \eta_I^*)^3 \quad (4.21)
\end{aligned}
$$

and

$$
\begin{aligned}
\bar{N}_7(\eta^*) &\equiv \frac{d}{d\eta^*} \bar{N}_3(\eta^*) = -\frac{6}{{h_e^*}^2}(\eta^* - \eta_I^*) + \frac{1}{{h_e^*}^3}(\eta^* - \eta_I^*)^2 \quad (4.22) \\
\bar{N}_8(\eta^*) &\equiv \frac{d}{d\eta^*} \bar{N}_4(\eta^*) = \frac{6}{{h_e^*}^2}(\eta^* - \eta_I^*) - \frac{6}{{h_e^*}^3}(\eta^* - \eta_I^*)^2 \quad (4.23)
\end{aligned}
$$

$$\bar{N}_9(\eta^*) \equiv \frac{d}{d\eta^*}\bar{N}_5(\eta^*) = 1 - \frac{4}{h_e^*}(\eta^* - \eta_I^*) + \frac{3}{h_e^{*2}}(\eta^* - \eta_I^*)^2 \tag{4.24}$$

$$\bar{N}_{10}(\eta^*) \equiv \frac{d}{d\eta^*}\bar{N}_6(\eta^*) = -\frac{2}{h_e^*}(\eta^* - \eta_I^*) + \frac{3}{h_e^{*2}}(\eta^* - \eta_I^*)^2 \tag{4.25}$$

where η_I^* is the coordinate along the elastic axis of the structural node I, η_J^* is the coordinate along the elastic axis of the structural node J, and

$$h_e^* = \eta_J^* - \eta_I^* \tag{4.26}$$

is the length between structural nodes I and J.

By using matrix rotation, the translation $\mathbf{u}_B^*$ and rotation $\boldsymbol{\theta}_B^*$ of point B, whose coordinates in the elastic axis system are $(0, y_B, 0)$, are written in terms of the displacements $\mathbf{u}_I^*$ and $\mathbf{u}_J^*$ as well as the rotations $\boldsymbol{\theta}_I^*$ and $\boldsymbol{\theta}_J^*$ of the nodal points I and J as follows:

$$\begin{Bmatrix} \mathbf{u}_B^* \\ \boldsymbol{\theta}_B^* \end{Bmatrix} = \left[\begin{array}{cc|cc} \bar{\mathbf{N}}_{11} & \bar{\mathbf{N}}_{12} & \bar{\mathbf{N}}_{13} & \bar{\mathbf{N}}_{14} \\ \bar{\mathbf{N}}_{21} & \bar{\mathbf{N}}_{22} & \bar{\mathbf{N}}_{23} & \bar{\mathbf{N}}_{24} \end{array}\right] \left\{\begin{array}{c} \mathbf{u}_I^* \\ \boldsymbol{\theta}_I^* \\ \hline \mathbf{u}_J^* \\ \boldsymbol{\theta}_J^* \end{array}\right\}. \tag{4.27}$$

Here, the submatrices $\bar{\mathbf{N}}_{11}$ through $\bar{\mathbf{N}}_{24}$ are given by

$$\bar{\mathbf{N}}_{11} = \begin{bmatrix} \bar{N}_3(\eta_B^*) & 0 & 0 \\ 0 & \bar{N}_1(\eta_B^*) & 0 \\ 0 & 0 & \bar{N}_3(\eta_B^*) \end{bmatrix} \tag{4.28}$$

$$\bar{\mathbf{N}}_{12} = \begin{bmatrix} 0 & 0 & -\bar{N}_5(\eta_B^*) \\ 0 & 0 & 0 \\ \bar{N}_5(\eta_B^*) & 0 & 0 \end{bmatrix} \tag{4.29}$$

$$\bar{\mathbf{N}}_{13} = \begin{bmatrix} \bar{N}_4(\eta_B^*) & 0 & 0 \\ 0 & \bar{N}_2(\eta_B^*) & 0 \\ 0 & 0 & \bar{N}_4(\eta_B^*) \end{bmatrix} \tag{4.30}$$

$$\bar{\mathbf{N}}_{14} = \begin{bmatrix} 0 & 0 & -\bar{N}_6(\eta_B^*) \\ 0 & 0 & 0 \\ \bar{N}_6(\eta_B^*) & 0 & 0 \end{bmatrix} \tag{4.31}$$

$$\bar{\mathbf{N}}_{21} = \begin{bmatrix} 0 & 0 & \bar{N}_7(\eta_B^*) \\ 0 & 0 & 0 \\ -\bar{N}_7(\eta_B^*) & 0 & 0 \end{bmatrix} \tag{4.32}$$

$$\bar{\mathbf{N}}_{22} = \begin{bmatrix} \bar{N}_9(\eta_B^*) & 0 & 0 \\ 0 & \bar{N}_1(\eta_B^*) & 0 \\ 0 & 0 & \bar{N}_9(\eta_B^*) \end{bmatrix} \tag{4.33}$$

$$\bar{\mathbf{N}}_{23} = \begin{bmatrix} 0 & 0 & \bar{N}_8(\eta_B^*) \\ 0 & 0 & 0 \\ -\bar{N}_8(\eta_B^*) & 0 & 0 \end{bmatrix} \tag{4.34}$$

$$\bar{\mathbf{N}}_{24} = \begin{bmatrix} \bar{N}_{10}(\eta_B^*) & 0 & 0 \\ 0 & \bar{N}_2(\eta_B^*) & 0 \\ 0 & 0 & \bar{N}_{10}(\eta_B^*) \end{bmatrix}. \tag{4.35}$$

After substituting the expressions for $\mathbf{u}_B^*$ and $\boldsymbol{\theta}_B^*$ given by equations (4.27) into equation (4.6), the following expression for the translation of point B in terms of the displacements $\mathbf{u}_I^*$ and $\mathbf{u}_J^*$ are otained as well as the rotations $\boldsymbol{\theta}_I^*$ and $\boldsymbol{\theta}_J^*$ of the nodal points I and J:

$$\mathbf{u}_A^* = \left[\begin{array}{c|c} \mathbf{I}_{3\times 3} & \mathbf{T}_1 \end{array}\right] \left[\begin{array}{cc|cc} \bar{\mathbf{N}}_{11} & \bar{\mathbf{N}}_{12} & \bar{\mathbf{N}}_{13} & \bar{\mathbf{N}}_{14} \\ \bar{\mathbf{N}}_{21} & \bar{\mathbf{N}}_{22} & \bar{\mathbf{N}}_{23} & \bar{\mathbf{N}}_{24} \end{array}\right] \left\{\begin{array}{c} \mathbf{u}_I^* \\ \boldsymbol{\theta}_I^* \\ \hline \mathbf{u}_J^* \\ \boldsymbol{\theta}_J^* \end{array}\right\} \tag{4.36}$$

$$= \left[\begin{array}{cc|cc} \mathbf{G}_{AS_1}^* & \mathbf{G}_{AS_2}^* & \mathbf{G}_{AS_3}^* & \mathbf{G}_{AS_4}^* \end{array}\right] \left\{\begin{array}{c} \mathbf{u}_I^* \\ \boldsymbol{\theta}_I^* \\ \hline \mathbf{u}_J^* \\ \boldsymbol{\theta}_J^* \end{array}\right\} \tag{4.37}$$

Here, the submatrices $\mathbf{G}_{AS_1}^*$ through $\mathbf{G}_{AS_4}^*$ are given by

$$\mathbf{G}_{AS_1}^* = \bar{\mathbf{N}}_{11} + \mathbf{T}_1\bar{\mathbf{N}}_{21} \tag{4.38}$$

$$= \begin{bmatrix} \bar{N}_3(\eta_B^*) & 0 & 0 \\ -r_1^*\,\bar{N}_7(\eta_B^*) & \bar{N}_1(\eta_B^*) & -r_3^*\,\bar{N}_7(\eta_B^*) \\ 0 & 0 & \bar{N}_3(\eta_B^*) \end{bmatrix} \tag{4.39}$$

$$\mathbf{G}_{AS_2}^* = \bar{\mathbf{N}}_{12} + \mathbf{T}_1\bar{\mathbf{N}}_{22} \tag{4.40}$$

$$= \begin{bmatrix} 0 & r_3^*\,\bar{N}_1(\eta_B^*) & -\bar{N}_5(\eta_B^*) \\ -r_3^*\,\bar{N}_9(\eta_B^*) & 0 & r_1^*\,\bar{N}_9(\eta_B^*) \\ \bar{N}_5(\eta_B^*) & -r_1^*\,\bar{N}_1(\eta_B^*) & 0 \end{bmatrix} \tag{4.41}$$

$$\mathbf{G}_{AS_3}^* = \bar{\mathbf{N}}_{13} + \mathbf{T}_1\bar{\mathbf{N}}_{23} \tag{4.42}$$

$$= \begin{bmatrix} \bar{N}_4(\eta_B^*) & 0 & 0 \\ -r_1^*\,\bar{N}_8(\eta_B^*) & \bar{N}_2(\eta_B^*) & -r_3^*\,\bar{N}_8(\eta_B^*) \\ 0 & 0 & \bar{N}_4(\eta_B^*) \end{bmatrix} \tag{4.43}$$

$$\mathbf{G}_{AS_4}^* = \bar{\mathbf{N}}_{14} + \mathbf{T}_1\bar{\mathbf{N}}_{24} \tag{4.44}$$

$$= \begin{bmatrix} 0 & r_3^*\,\bar{N}_2(\eta_B^*) & -\bar{N}_6(\eta_B^*) \\ -r_3^*\,\bar{N}_{10}(\eta_B^*) & 0 & r_1^*\,\bar{N}_{10}(\eta_B^*) \\ \bar{N}_6(\eta_B^*) & -r_1^*\,\bar{N}_2(\eta_B^*) & 0 \end{bmatrix} \tag{4.45}$$

After using the characteristic variable L_C, the dimensionless form of the interpolation matrix $[\mathbf{G}_{AS}^*]$ can be obtained through the following dimensionless variables and shape functions:

$$\eta^*(\eta) = L_C\,\eta \tag{4.46}$$

$$h_e^*(h_e) = L_C\,h_e \tag{4.47}$$

$$N_1(\eta) = \bar{N}_1(\eta^*(\eta)) = \frac{\eta_J - \eta}{h_e} \tag{4.48}$$

$$N_2(\eta) = \bar{N}_2(\eta^*(\eta)) = \frac{\eta - \eta_I}{h_e} \tag{4.49}$$

$$N_3(\eta) = \bar{N}_3(\eta^*(\eta)) = 1 - 3\left(\frac{\eta - \eta_I}{h_e}\right)^2 + 2\left(\frac{\eta - \eta_I}{h_e}\right)^3 \tag{4.50}$$

$$N_4(\eta) = \bar{N}_4(\eta^*(\eta)) = 3\left(\frac{\eta - \eta_I}{h_e}\right)^2 - 2\left(\frac{\eta - \eta_I}{h_e}\right)^3 \tag{4.51}$$

$$N_5(\eta) = \bar{N}_5(\eta^*(\eta)) = L_C\left[(\eta - \eta_I) - \frac{2}{h_e}(\eta - \eta_I)^2 + \frac{1}{h_e^2}(\eta - \eta_I)^3\right] \tag{4.52}$$

$$N_6(\eta) = \bar{N}_6(\eta^*(\eta)) = L_C\left[-\frac{1}{h_e}(\eta - \eta_I)^2 + \frac{1}{h_e^2}(\eta - \eta_I)^3\right] \tag{4.53}$$

$$N_7(\eta) = \bar{N}_7(\eta^*(\eta)) = -\frac{6}{h_e^2}(\eta - \eta_I) + \frac{6}{h_e^3}(\eta - \eta_I)^2 \tag{4.54}$$

$$N_8(\eta) = \bar{N}_8(\eta^*(\eta)) = \frac{6}{h_e^2}(\eta - \eta_I) - \frac{6}{h_e^3}(\eta - \eta_I)^2 \tag{4.55}$$

$$N_9(\eta) = \bar{N}_9(\eta^*(\eta)) = L_C\left[1 - \frac{4}{h_e}(\eta - \eta_I) + \frac{3}{h_e^2}(\eta - \eta_I)^2\right] \tag{4.56}$$

$$N_{10}(\eta) = \bar{N}_{10}(\eta^*(\eta)) = L_C\left[-\frac{2}{h_e}(\eta - \eta_I) + \frac{3}{h_e^2}(\eta - \eta_I)^2\right] \tag{4.57}$$

Introducing the expressions for the dimensionless shape functions $N_1(\eta)$ through $N_{10}(\eta)$, given by equations (4.48)-(4.57), into equations (4.38)-(4.45), the components of the interpolation matrix $[\mathbf{G}^*_{AS}]$ are rewritten in terms of the dimensionless variables and the characteristic length as:

$$\mathbf{G}^*_{AS_1} = \bar{\mathbf{N}}_{11} + \mathbf{T}_1\bar{\mathbf{N}}_{21} \tag{4.58}$$

$$= \begin{bmatrix} N_3(\eta_B) & 0 & 0 \\ -r_1\,N_7(\eta_B) & N_1(\eta_B) & -r_3\,N_7(\eta_B) \\ 0 & 0 & N_3(\eta_B) \end{bmatrix} \tag{4.59}$$

$$\mathbf{G}^*_{AS_2} = \bar{\mathbf{N}}_{12} + \mathbf{T}_1\bar{\mathbf{N}}_{22} \tag{4.60}$$

$$= \begin{bmatrix} 0 & L_C\, r_3\, N_1(\eta_B) & -N_5(\eta_B) \\ -r_3\, N_9(\eta_B) & 0 & r_1\, N_9(\eta_B) \\ N_5(\eta_B) & -r_1\, N_1(\eta_B) & 0 \end{bmatrix} \tag{4.61}$$

$$\mathbf{G}^*_{AS_3} = \bar{\mathbf{N}}_{13} + \mathbf{T}_1 \bar{\mathbf{N}}_{23} \tag{4.62}$$

$$= \begin{bmatrix} N_4(\eta_B) & 0 & 0 \\ -r_1\, N_8(\eta_B) & N_2(\eta_B) & -r_3\, N_8(\eta_B) \\ 0 & 0 & N_4(\eta_B) \end{bmatrix} \tag{4.63}$$

$$\mathbf{G}^*_{AS_4} = \bar{\mathbf{N}}_{14} + \mathbf{T}_1 \bar{\mathbf{N}}_{24} \tag{4.64}$$

$$= \begin{bmatrix} 0 & L_C\, r_3\, N_2(\eta_B) & -N_6(\eta_B) \\ -r_3\, N_{10}(\eta_B) & 0 & r_1\, N_{10}(\eta_B) \\ N_6(\eta_B) & -L_C\, r_1\, N_2(\eta_B) & 0 \end{bmatrix}. \tag{4.65}$$

Case II: Connection with an Initial Point

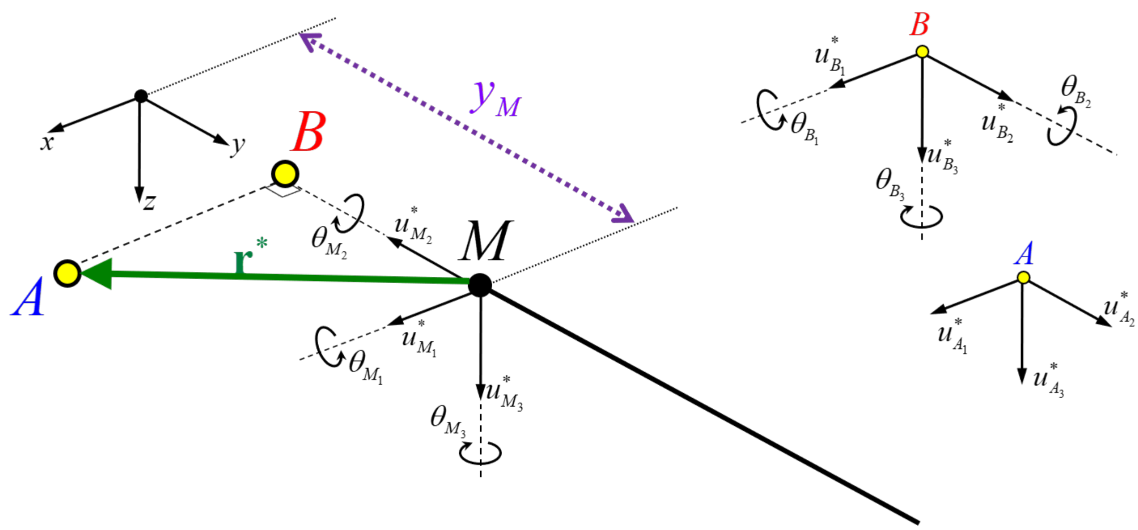

Figure 4.6: Connection with an initial point.

Next, select point A on the aerodynamic grid and then find point B on an imaginary extension of the elastic axis of the beam that comes before the structural grid nodal points M, which is the first node (root) of the beam, such that A and B lie in same plane perpendicular to the undeformed axis of the beam. As shown in Figure 4.6, the relative position of point A with respect to point B is given by the vector $\mathbf{r}^*$. The displacements of nodal point A are related to the generlized displacements of point M by the following relationship:

$$\mathbf{u}_A^* = \left[\begin{array}{c|c} \mathbf{I}_{3\times 3} & \mathbf{T}_2 \end{array} \right] \begin{Bmatrix} \mathbf{u}_M^* \\ \boldsymbol{\theta}_M^* \end{Bmatrix}. \tag{4.66}$$

In expanded form, this relationship is given by

$$\begin{Bmatrix} u_{A_1}^* \\ u_{A_2}^* \\ u_{A_3}^* \end{Bmatrix} = \left[\begin{array}{ccc|ccc} 1 & 0 & 0 & 0 & r_3^* & -r_2^* \\ 0 & 1 & 0 & -r_3^* & 0 & r_1^* \\ 0 & 0 & 1 & r_2^* & -r_1^* & 0 \end{array} \right] \begin{Bmatrix} u_{M_1}^* \\ u_{M_2}^* \\ u_{M_3}^* \\ \theta_{M_1} \\ \theta_{M_2} \\ \theta_{M_3} \end{Bmatrix} \tag{4.67}$$

where (r_1^*, r_2^*, r_3^*) are the components of the $\mathbf{r}^*$, $(u_{A_1}^*, u_{A_2}^*, u_{A_3}^*)$ are the components of the translation of point A on the aerodynamic grid, and $(u_{M_1}^*, u_{M_2}^*, u_{M_3}^*, \theta_{M_1}, \theta_{M_2}, \theta_{M_3})$ are the components of the displacement and rotation of point M on the structural grid. All of these components are with respect to the (x, y, z) coordinate system shown in Figure 4.6. By using the dimensionless expression for $\mathbf{r}^*$ given by equation (4.8), equation (4.67) can be rewritten in terms of the dimensionless variables and the characteristic length as

$$\begin{Bmatrix} u^*_{A_1} \\ u^*_{A_2} \\ u^*_{A_3} \end{Bmatrix} = \left[\begin{array}{ccc|ccc} 1 & 0 & 0 & 0 & L_C\, r_3 & -L_C\, r_2 \\ 0 & 1 & 0 & -L_C\, r_3 & 0 & L_C\, r_1 \\ 0 & 0 & 1 & L_C\, r_2 & -L_C\, r_1 & 0 \end{array}\right] \begin{Bmatrix} u^*_{M_1} \\ u^*_{M_2} \\ u^*_{M_3} \\ \theta_{M_1} \\ \theta_{M_2} \\ \theta_{M_3} \end{Bmatrix} \tag{4.68}$$

or

$$\mathbf{u}^*_A = \begin{bmatrix} \mathbf{G}^*_{AS_1} & \mathbf{G}^*_{AS_2} \end{bmatrix} \begin{Bmatrix} \mathbf{u}^*_M \\ \boldsymbol{\theta}_M \end{Bmatrix}. \tag{4.69}$$

Case III: Connection with an End Point

Now, select point A on the aerodynamic grid and then find point B on an imaginary extension of the elastic axis of the beam that comes after the structural grid nodal points N, which is the last node (tip) of the beam, such that A and B lie in same plane perpendicular to the undeformed axis of the beam. As shown in Figure 4.7, the relative position of point A with respect to point B is given by the vector $\mathbf{r}^*$. The displacements of nodal point A are related to the generlaized

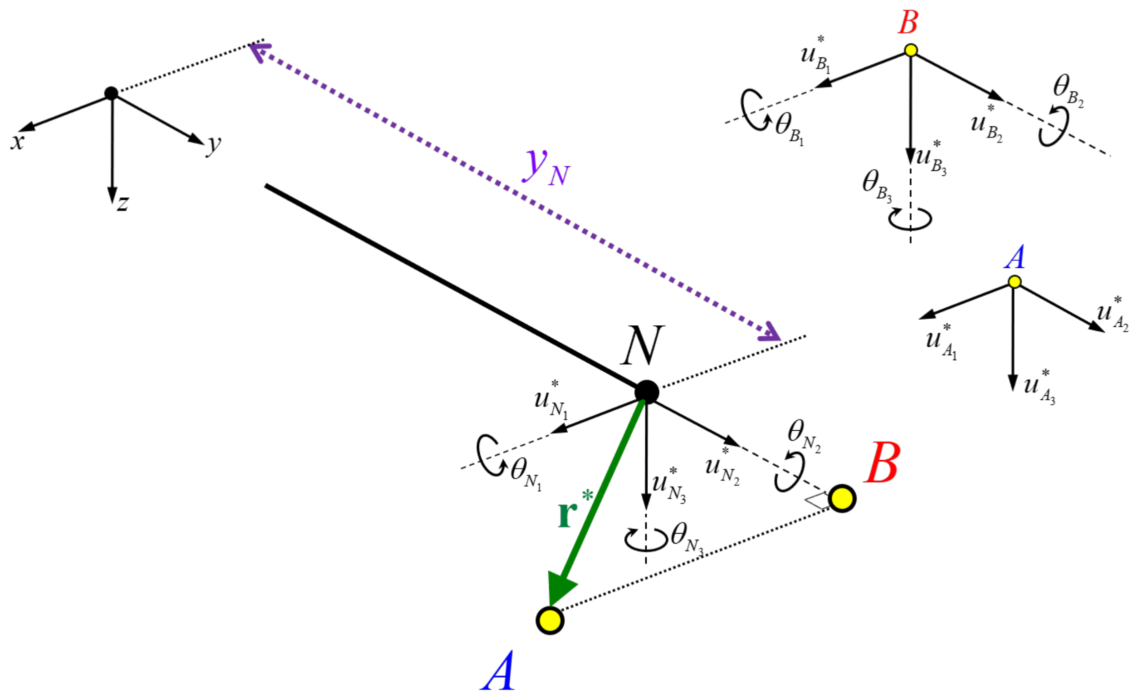

Figure 4.7: Connection with an end point.

displacements of point N by the following relationship:

$$\mathbf{u}_A^* = \left[\begin{array}{c|c} \mathbf{I}_{3\times 3} & \mathbf{T}_2 \end{array}\right] \begin{Bmatrix} \mathbf{u}_N^* \\ \boldsymbol{\theta}_N^* \end{Bmatrix} \tag{4.70}$$

or

$$\begin{Bmatrix} u^*_{A_1} \\ u^*_{A_2} \\ u^*_{A_3} \end{Bmatrix} = \left[\begin{array}{ccc|ccc} 1 & 0 & 0 & 0 & r_3^* & -r_2^* \\ 0 & 1 & 0 & -r_3^* & 0 & r_1^* \\ 0 & 0 & 1 & r_2^* & -r_1^* & 0 \end{array}\right] \begin{Bmatrix} u^*_{N_1} \\ u^*_{N_2} \\ u^*_{N_3} \\ \theta_{N_1} \\ \theta_{N_2} \\ \theta_{N_3} \end{Bmatrix} \tag{4.71}$$

where (r_1^*, r_2^*, r_3^*) are the components of the $\mathbf{r}^*$, $(u_{A_1}^*, u_{A_2}^*, u_{A_3}^*)$ are the components of the translation of point A on the aerodynamic grid, and $(u_{N_1}^*, u_{N_2}^*, u_{N_3}^*, \theta_{N_1}, \theta_{N_2}, \theta_{N_3})$ are the components of the displacement and rotation of point N on the structural grid. All of these components are reference in the (x, y, z) coordinate system shown in Figure 4.7. Using the dimensionless expression for $\mathbf{r}^*$ given by equation (4.8), equation (4.71) can be rewritten in terms of the dimensionless variables and the characteristic length as

$$\begin{Bmatrix} u_{A_1}^* \\ u_{A_2}^* \\ u_{A_3}^* \end{Bmatrix} = \left[\begin{array}{ccc|ccc} 1 & 0 & 0 & 0 & L_C\, r_3 & -L_C\, r_2 \\ 0 & 1 & 0 & -L_C\, r_3 & 0 & L_C\, r_1 \\ 0 & 0 & 1 & L_C\, r_2 & -L_C\, r_1 & 0 \end{array}\right] \begin{Bmatrix} u_{N_1}^* \\ u_{N_2}^* \\ u_{N_3}^* \\ \theta_{N_1} \\ \theta_{N_2} \\ \theta_{N_3} \end{Bmatrix} \tag{4.72}$$

or in compact form by

$$\mathbf{u}_A^* = \begin{bmatrix} \mathbf{G}_{AS_1}^* & \mathbf{G}_{AS_2}^* \end{bmatrix} \begin{Bmatrix} \mathbf{u}_N^* \\ \boldsymbol{\theta}_N \end{Bmatrix} . \tag{4.73}$$

After the procedures explained above are repeated for every selected point in the aerodynamic grid, then a global interpolation matrix $\left[{}^{n_{A_n}}\mathbf{G}_{AS}^{n_{S_n}\,*}\right]$ for mapping the generalized displacements of all the structural nodes into the deflections of all the selected points in the aerodynamic grid is assembled. In regards to the global interpolation matrix $\left[{}^{n_{A_n}}\mathbf{G}_{AS}^{n_{S_n}*}\right]$, n_{A_n} is the number of aerodynamic grid nodal points and n_{S_n} is the number of structural grid nodal points,

4.2.3 Transfer of Forces from Aerodynamic Grid to Structural Grid

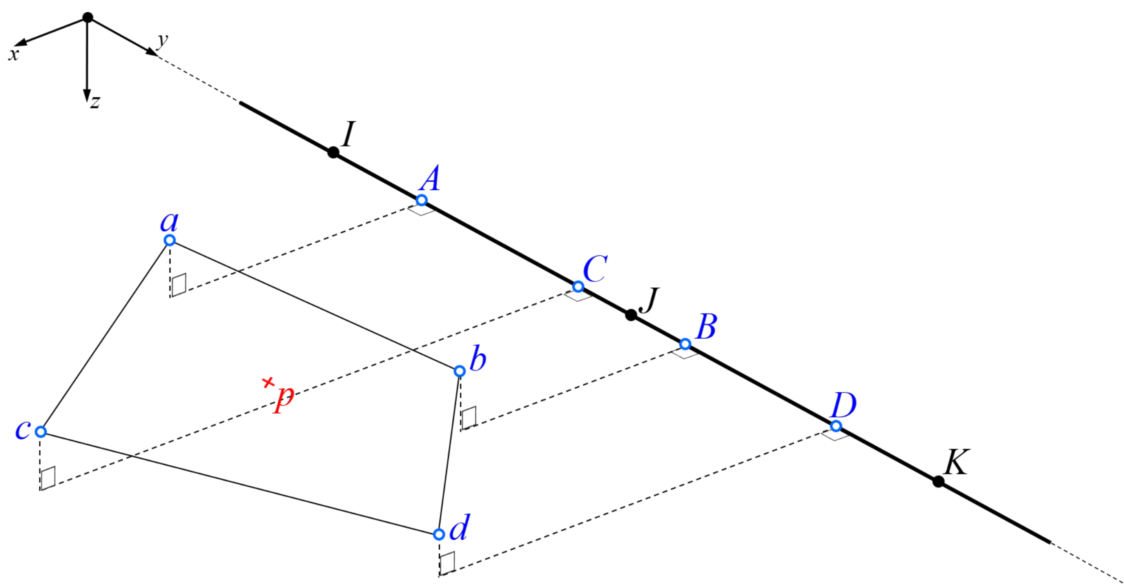

Figure 4.8: Control point of aerodynamic grid.

After using the global interpolation matrix $\left[{}^{n_{A_n}}\mathbf{G}_{AS}^{n_{S_n}*}\right]$ for mapping the generalized displacements of all the structural nodes into the deflections of all the selected points in the aerodynamic grid, the global interpolation matrix $\left[{}^{n_{S_n}}\mathbf{G}_{SA}^{n_{A_c}*}\right] = \left[{}^{n_{A_c}}\mathbf{G}_{AS}^{n_{S_n}*}\right]^T$ that maps the aerodynamics forces into structural nodal forces is obtained, where n_{A_c} is the number of aerodynamic grid control points, n_{A_n} is the number of aerodynamic grid nodal points and n_{S_n} is the number of structural grid nodal points.

For any element in the aerodynamic grid, the position of the control point is the average of the positions of its corners, as shown in Figure (4.8). This definition is used to compute $\left[{}^{n_{A_c}}\mathbf{G}_{AS}^{n_{S_n}*}\right]$ from $\left[{}^{n_{A_n}}\mathbf{G}_{AS}^{n_{S_n}*}\right]$ as follows:

$$\mathbf{u}_p^* = \frac{1}{4}\left(\mathbf{u}_a^* + \mathbf{u}_b^* + \mathbf{u}_c^* + \mathbf{u}_d^*\right) \tag{4.74}$$

or equivalently

$$\left\{\begin{array}{c} u_{p_1}^* \\ u_{p_2}^* \\ u_{p_3}^* \end{array}\right\} = \left[\begin{array}{ccc|ccc|ccc|ccc} \frac{1}{4} & 0 & 0 & \frac{1}{4} & 0 & 0 & \frac{1}{4} & 0 & 0 & \frac{1}{4} & 0 & 0 \\ 0 & \frac{1}{4} & 0 & 0 & \frac{1}{4} & 0 & 0 & \frac{1}{4} & 0 & 0 & \frac{1}{4} & 0 \\ 0 & 0 & \frac{1}{4} & 0 & 0 & \frac{1}{4} & 0 & 0 & \frac{1}{4} & 0 & 0 & \frac{1}{4} \end{array}\right] \left\{\begin{array}{c} u_{a_1}^* \\ u_{a_2}^* \\ u_{a_3}^* \\ \hline u_{b_1}^* \\ u_{b_2}^* \\ u_{b_3}^* \\ \hline u_{c_1}^* \\ u_{c_2}^* \\ u_{c_3}^* \\ \hline u_{d_1}^* \\ u_{d_2}^* \\ u_{d_3}^* \end{array}\right\} \tag{4.75}$$

where $(u_{p_1}^*, u_{p_2}^*, u_{p_3}^*)$ are the components of the translation of the control point p, $(u_{a_1}^*, u_{a_2}^*, u_{a_3}^*)$, $(u_{b_1}^*, u_{b_2}^*, u_{b_3}^*)$, $(u_{c_1}^*, u_{c_2}^*, u_{c_3}^*)$, and $(u_{d_1}^*, u_{d_2}^*, u_{d_3}^*)$ are the components of the translation of the aerodynamic nodes a, b, c, and d, respectively. All components are expressed in the elastic axis coordinate system. By using matrix notation, equation (4.75) is rewritten as follows:

$$\mathbf{u}_p^* = [\mathbf{T}_3] \left\{ \begin{array}{c} \mathbf{u}_a^* \\ \hline \mathbf{u}_b^* \\ \hline \mathbf{u}_c^* \\ \hline \mathbf{u}_d^* \end{array} \right\}. \tag{4.76}$$

This relationship among the translation of a control point and the translations of all four corners is written for every element in the aerodynamic grid. Then a global matrix $[\mathbf{T}_3]$ for mapping the translations of all nodal points into the translations of all control points in the aerodynamic grid is obtained. Hence, using this global matrix $\left[{}^{n_{A_c}}\mathbf{T}_3^{n_{A_n}}\right]$,

$$\mathbf{u}_A^{n_{A_c}*} = \left[{}^{n_{A_c}}\mathbf{T}_3^{n_{A_n}}\right] \mathbf{u}_A^{n_{A_n}*}. \tag{4.77}$$

Taking into account equation (4.5), equation (4.77) leads to

$$\begin{aligned} \mathbf{u}_A^{n_{A_c}*} &= \left[{}^{n_{A_c}}\mathbf{T}_3^{n_{A_n}}\right] \mathbf{u}_A^{n_{A_n}*} \\ &= \left[{}^{n_{A_c}}\mathbf{T}_3^{n_{A_n}}\right] \left[{}^{n_{A_n}}\mathbf{G}_{AS}^{n_{S_n}*}\right] \mathbf{v}_S^{n_{S_n}*} \\ &= \left[{}^{n_{A_c}}\mathbf{G}_{AS}^{n_{S_n}*}\right] \mathbf{v}_S^{n_{S_n}*}. \end{aligned} \tag{4.78}$$

Let's also note that the same procedure used to find the translations of the aerodynamic grid nodal points could have been used to find the translations of the aerodynamic grid control points.

4.3 Equations of Motion for Numerical Integration Scheme

4.3.1 Relationship Between Forces in Aerodynamic Model and Structural Model

To relate the structural forces F_S^* to the aerodynamic forces F_A^*, it is required that the two systems of forces be structurally equivalent. This means that the two force systems will do the same work for any virtual displacement, that is,

$$\delta \bar{W}_A^* = \delta \bar{W}_S^*, \tag{4.79}$$

where the bar over δW_A^* and δW_S^* indicates that these quantities represent infinitesimal increments and not true variations; the virtual work is given by

$$\delta \bar{W}_A^* = \left(\delta \mathbf{u}_A^*\right)^T \; \mathbf{F}_A^* \tag{4.80}$$

$$\delta \bar{W}_S^* = \left(\delta \mathbf{v}_S^*\right)^T \; \mathbf{F}_S^*, \tag{4.81}$$

where $\delta \bar{W}_A^*$ is the virtual work performed by the aerodynamic forces over the virtual displacement $\delta \mathbf{u}_A^*$ and $\delta \bar{W}_S^*$ is the virtual work performed by the structural forces over the virtual displacement $\delta \mathbf{v}_S^*$. From here, equation (4.78) is used to relate the virtual displacements in the aerodynamic grid to those in the structural grid as follows:

$$\delta \mathbf{u}_A^{n_{A_c}*} = \left[{}^{n_{A_c}}\mathbf{G}_{AS}^{n_{S_n}*}\right] \; \delta \mathbf{v}_S^*. \tag{4.82}$$

Then the requirement that work done by the two force systems be equal leads to

$$\delta \bar{W}_A^* = \left(\delta \mathbf{u}_A^*\right)^T \ \mathbf{F}_A^* = \left(\delta \mathbf{v}_S^*\right)^T \ \left[{}^{n_{A_c}}\mathbf{G}_{AS}^{n_{S_n}*}\right]^T \ \mathbf{F}_A^* \tag{4.83}$$

$$= \delta \bar{W}_S^* = \left(\delta \mathbf{v}_S^*\right)^T \ \mathbf{F}_S^*. \tag{4.84}$$

Due to the arbitrariness of the virtual displacement $\delta \mathbf{v}_S^*$, the result is

$$\mathbf{F}_S^* = \left[{}^{n_{A_c}}\mathbf{G}_{AS}^{n_{S_n}*}\right]^T \ \mathbf{F}_A^* \tag{4.85}$$

$$= \left[{}^{n_{S_n}}\mathbf{G}_{SA}^{n_{A_c}*}\right] \ \mathbf{F}_A^*. \tag{4.86}$$

On substituting the expression for $\mathbf{F}_S^*$ given by equation (4.86) into the equations of motion for the joined-wings, equation (3.28), gives

$$\ddot{\mathbf{q}}(t) + [\mathbf{\Lambda}]\,\mathbf{q}(t) = T_C^2 \ \mathrm{diag}\left(m_j^*\right)^{-1} [\mathbf{\Phi}^*]^T \ \left[{}^{n_{S_n}}\mathbf{G}_{SA}^{n_{A_c}*}\right] \ \mathbf{F}_A^*(t^*). \tag{4.87}$$

A new matrix $\left[{}^{n_m}\mathbf{G}_{MA}^{n_{A_c}*}\right]$ is defined to relate the aerodynamic forces to the modal forces:

$$\left[{}^{n_m}\mathbf{G}_{MA}^{n_{A_c}*}\right] = \left\{\left[{}^{n_{A_c}}\mathbf{G}_{AS}^{n_{S_n}*}\right] \ [\mathbf{\Phi}^*] \ \mathrm{diag}\left(m_j^*\right)^{-1}\right\}^T. \tag{4.88}$$

Equation (4.87) can be rewritten as follows

$$\ddot{\mathbf{q}}(t) + [\mathbf{\Lambda}]\,\mathbf{q}(t) = T_C^2 \ \left[{}^{n_m}\mathbf{G}_{MA}^{n_{A_c}*}\right] \mathbf{F}_A^*(t^*). \tag{4.89}$$

4.3.1.1 Nondimensionalization of $\mathbf{F}_A^*$

In nondimensionalizing the aerodynamic forces, the aerodynamic force $\{\mathbf{F}_k^*\}_A$ acting on panel k is taken into consideration. This force is considered to be applied at the control point and is given by

$$\{\mathbf{F}_k^*\}_A = \Delta p_k^* \, A_k^* \, \hat{\mathbf{n}}_k, \tag{4.90}$$

where $\Delta p_k^* = (p_L^*)_k - (p_U^*)_k$ is the pressure jump across the panel at the control point k, and is defined as the pressure below the panel (point L) minus the pressure above the panel (point U). This pressure jump is found from Bernoulli's equation, equation (2.8), from unsteady flows as described in Chapter 2. A_k^* is the area of the panel k, and $\hat{\mathbf{n}}_k$ is the unit vector normal to panel k.

Making use of the definition of the pressure coefficient C_p, the pressure jump is rewritten as follows:

$$\Delta p_k^* = (\Delta C_p)_k \, \frac{1}{2} \, \rho_C \, V_C^2, \tag{4.91}$$

After using the characteristic length L_C, the area of the panel A_k^* can be written in terms of the dimensionless area A_k as

$$A_k^* = L_C^2 \, A_k. \tag{4.92}$$

Introducing equations (4.91) and (4.92) into equation (4.90), leads to

$$\{\mathbf{F}_k^*\}_A = \frac{1}{2}\,\rho_C\,V_C^2\,L_C^2\,(\Delta C_p)_k\,A_k\,\hat{\mathbf{n}}_k. \tag{4.93}$$

The dimensionless aerodynamic force $\{\mathbf{F}_k\}_A$ are defined as

$$\{\mathbf{F}_k\}_A = (\Delta C_p)_k\,A_k\,\hat{\mathbf{n}}_k. \tag{4.94}$$

One can rewrite equation (4.93) as

$$\{\mathbf{F}_k^*\}_A = \frac{1}{2}\,\rho_C\,V_C^2\,L_C^2\,\{\mathbf{F}_k\}_A. \tag{4.95}$$

By extending this idea to all the panels that form the aerodynamic mesh, one obtains

$$\mathbf{F}_A^* = \begin{Bmatrix} \mathbf{F}_1^* \\ \mathbf{F}_2^* \\ \vdots \\ \mathbf{F}_{n_{A_n}}^* \end{Bmatrix}_A = \frac{1}{2}\,\rho_C\,V_C^2\,L_C^2 \begin{Bmatrix} \mathbf{F}_1 \\ \mathbf{F}_2 \\ \vdots \\ \mathbf{F}_{n_{A_n}} \end{Bmatrix}_A \tag{4.96}$$

$$= \left(\frac{1}{2}\,\rho_C\,V_C^2\,L_C^2\right)\,\mathbf{F}_A \tag{4.97}$$

where n_{A_c} is the number of panels in the aerodynamic mesh.

Then substituting the expression for $\mathbf{F}_A^*$ given by equation (4.97) into the equations of motion for the joined-wings, equation (4.89), the result is

$$\ddot{\mathbf{q}}(t) + [\mathbf{\Lambda}]\,\mathbf{q}(t) = T_C^2 \ \left[{}^{n_m}\mathbf{G}_{MA}^{n_{A_c}*}\right] \left(\frac{1}{2}\,\rho_C\, V_C^2\, L_C^2\right)\ \mathbf{F}_A(t). \tag{4.98}$$

Taking into account that $L_C = V_C\, T_C$, leads to

$$\ddot{\mathbf{q}}(t) + [\mathbf{\Lambda}]\,\mathbf{q}(t) = \left(\frac{1}{2}\,\rho_C\ \ L_C^4\right)\ \left[{}^{n_m}\mathbf{G}_{MA}^{n_{A_c}*}\right]\mathbf{F}_A(t). \tag{4.99}$$

4.3.2 Integrating Equations of Motion

To numerically integrate the equations of motion, equation (4.99), it is necessary first to rewrite them as a system of first-order ordinary differential equations. To do this, the state vector is introduced

$$\mathbf{y}(t) = \begin{Bmatrix} \mathbf{y}_1(t) \\ \\ \mathbf{y}_2(t) \end{Bmatrix} \tag{4.100}$$

where $\mathbf{y}(t)$ is a $(2n_m \times 1)$ vector (with n_m being the number of modes of the system), and the state variables $\mathbf{y}_1(t)$ and $\mathbf{y}_2(t)$ are given by

$$\mathbf{y}_1(t) = \mathbf{q}(t) \tag{4.101}$$

$$\mathbf{y}_2(t) = \dot{\mathbf{q}}(t). \tag{4.102}$$

After using equation (4.99) and taking the derivatives of the state variables with respect to time t, one obtains

$$\dot{\mathbf{y}}_1(t) = \mathbf{y}_2(t) \tag{4.103}$$

$$\dot{\mathbf{y}}_2(t) = -\left[\mathbf{\Lambda}\right]\ \mathbf{y}_1(t) + \left(\frac{1}{2}\,\rho_C\ \ L_C^4\right)\ \left[{}^{n_m}\mathbf{G}_{MA}^{n_{A_c}*}\right]\mathbf{F}_A. \tag{4.104}$$

which in state form can be written as

$$\begin{Bmatrix} \dot{\mathbf{y}}_1(t) \\ \dot{\mathbf{y}}_2(t) \end{Bmatrix} = \begin{bmatrix} \mathbf{0}_{n_m \times n_m} & \mathbf{I}_{n_m \times n_m} \\ -\left[\mathbf{\Lambda}\right] & \mathbf{0}_{n_m \times n_m} \end{bmatrix} \begin{Bmatrix} \mathbf{y}_1(t) \\ \mathbf{y}_2(t) \end{Bmatrix} + \begin{Bmatrix} \mathbf{0}_{n_m \times 1} \\ \left(\frac{1}{2}\,\rho_C\ \ L_C^4\right)\ \left[{}^{n_m}\mathbf{G}_{MA}^{n_{A_c}*}\right]\mathbf{F}_A \end{Bmatrix}. \tag{4.105}$$

Here, $\mathbf{0}_{n_m \times n_m}$ is matrix of zeros with dimension $(n_m \times n_m)$, $\mathbf{0}_{n_m \times 1}$ is matrix of zeros with dimension $(n_m \times 1)$, and $\mathbf{I}_{n_m \times n_m}$ is the identity matrix of dimension $(n_m \times n_m)$.

Finally, equations (4.105) will be integrated by using the numerical integration scheme that is described in the next section.

4.4 Numerical Integration Scheme

During a timestep, the moving of the wake and the structure to their new positions are occurring simultaneously. For this reason, Hamming's fourth-order predictor-corrector scheme [65] is used for time domain numerical integration. This scheme was chosen because the aerodynamic model works better when the loads are only evaluated at integral timesteps and the aerodynamic loads contain contributions that are proportional to the acceleration. These contributions come from $\dfrac{\partial \Phi}{\partial t}$, where $\Phi(R, t)$ is proportional to the velocity.

Equation (4.105) can be written as a system of $2n_m$ first-order ordinary differential equations by redefining the modal displacements and modal velocities vectors:

$$\dot{\mathbf{y}}(t) = \mathbf{F}[y(t)] \tag{4.106}$$

where half of the vector $\mathbf{F}$ represents the generalized velocities and the other half represents the generalized forces divided by the corresponding inertias. In general, the loads depend explicitly on $\mathbf{y}$, and implicitly on the history of the motion and acceleration through the term $\dfrac{\partial \Phi}{\partial t}$.

In equation (4.106), $\dot{\mathbf{y}}(t) = \dfrac{d}{dt}\mathbf{y}(t)$ is a vector of size $(2n_m \times 1)$ along with the $F_i[\mathbf{y}(t)]$ components in $\mathbf{F}[\mathbf{y}(t)]$ and the $y_i(t)$ components in $\mathbf{y}(t)$ for $i = 1, 2, \cdots, 2n_m$. Let $t_j = j\Delta t$ denote the time at the j-th timestep, where Δt is the timestep size used to obtain the numerical solution, and

$$\mathbf{y}^j = \mathbf{y}(t_j) \tag{4.107}$$

$$\dot{\mathbf{y}}^j = \dot{\mathbf{y}}(t_j) \tag{4.108}$$

$$\mathbf{F}^j = \mathbf{F}[\mathbf{y}(t_j)]. \tag{4.109}$$

The details of the basic numerical procedure used to determine the current value of the vector $\mathbf{y}$ are given next:

A.1 At t_0 (i.e. $t = 0$), the initial conditions of the problem are given, that is, $\mathbf{y}^0 = \mathbf{y}(t_0)$ is known. Hence, after using equation (4.106), the value of $\dot{\mathbf{y}}^0$ is obtained as

$$\dot{\mathbf{y}}^0 = \mathbf{F}^0 = \mathbf{F}\left(\mathbf{y}^0\right). \tag{4.110}$$

A.2 At t_1 (i.e., $t = \Delta t$), the predicted solution, ${}^p\mathbf{y}^1$, is computed by using the Euler Method scheme

$${}^p\mathbf{y}^1 = \mathbf{y}^0 + \Delta t\, \mathbf{F}^0. \tag{4.111}$$

A.3 The predicted solution is corrected by using the Modified Euler Method scheme

$${}^{k+1}\mathbf{y}^1 = \mathbf{y}^0 + \frac{\Delta t}{2}\left({}^k\mathbf{F}^1 + \mathbf{F}^0\right) \tag{4.112}$$

$${}^k\mathbf{F}^1 = \mathbf{F}\left({}^k\mathbf{y}^1\right) \tag{4.113}$$

where k is the iteration number and ${}^1\mathbf{y}^1 = {}^p\mathbf{y}^1$. This step is repeated until the iteration error

$$e^1 = \left\|{}^{k+1}\mathbf{y}^1 - {}^k\mathbf{y}^1\right\|_\infty \tag{4.114}$$

is less than a prescribed error tolerance ε. If $e^1 > \varepsilon$, then one sets

$${}^k\mathbf{y}^1 = {}^{k+1}\mathbf{y}^1 \tag{4.115}$$

$${}^k\dot{\mathbf{y}}^1 = {}^{k+1}\dot{\mathbf{y}}^1 \tag{4.116}$$

and goes to equation (4.112); if $e^1 \leq \varepsilon$, then one sets

$$\mathbf{y}^1 = {}^{k+1}\mathbf{y}^1 \tag{4.117}$$

$$\dot{\mathbf{y}}^1 = {}^{k+1}\dot{\mathbf{y}}^1 \tag{4.118}$$

and computes the response at $t_2 = t_1 + \Delta t = 2\Delta t$.

A.4 At t_2 (i.e., $t = 2\Delta t$), the predicted solution, ${}^p\mathbf{y}^2$, is computed by the Adams-Bashforth Two-Step Predictor Method scheme

$${}^p\mathbf{y}^2 = \mathbf{y}^1 + \frac{\Delta t}{2}\left(3\mathbf{F}^1 - \mathbf{F}^0\right). \tag{4.119}$$

A.5 The predicted solution is corrected by using the Adams-Moulton Two-Step Method scheme

$${}^{k+1}\mathbf{y}^2 = \mathbf{y}^1 + \frac{\Delta t}{12}\left(5\,{}^k\mathbf{F}^2 + 8\mathbf{F}^1 - \mathbf{F}^0\right) \tag{4.120}$$

$${}^k\mathbf{F}^2 = \mathbf{F}\left({}^k\mathbf{y}^2\right) \tag{4.121}$$

and ${}^1\mathbf{y}^2 = {}^p\mathbf{y}^2$. This step is repeated until the iteration error

$$e^2 = \left\|{}^{k+1}\mathbf{y}^2 - {}^k\mathbf{y}^2\right\|_\infty \tag{4.122}$$

is less than a prescribed error tolerance ε. If $e^2 > \varepsilon$, then one sets

$${}^k\mathbf{y}^2 = {}^{k+1}\mathbf{y}^2 \tag{4.123}$$

$${}^k\dot{\mathbf{y}}^2 = {}^{k+1}\dot{\mathbf{y}}^2 \tag{4.124}$$

and goes to equation (4.120); if $e^2 \leq \varepsilon$, then one sets

$$\mathbf{y}^2 = {}^{k+1}\mathbf{y}^2 \tag{4.125}$$

$$\dot{\mathbf{y}}^2 = {}^{k+1}\dot{\mathbf{y}}^2 \tag{4.126}$$

and computes the response at $t_3 = t_2 + \Delta t = 3\Delta t$.

A.6 At t_3 (i.e., $t = 3\Delta t$), the predicted solution, ${}^{p}\mathbf{y}^3$, is computed by using the Adams-Bashforth Three-Step Predictor Method scheme

$${}^{p}\mathbf{y}^3 = \mathbf{y}^2 + \frac{\Delta t}{12}\left(23\mathbf{F}^2 - 16\mathbf{F}^1 + 5\mathbf{F}^0\right). \tag{4.127}$$

A.7 The predicted solution is corrected by using the Adams-Moulton Three-Step Method scheme

$${}^{k+1}\mathbf{y}^3 = \mathbf{y}^2 + \frac{\Delta t}{24}\left(9\,{}^{k}\mathbf{F}^3 + 19\mathbf{F}^2 - 5\mathbf{F}^1 + \mathbf{F}^0\right) \tag{4.128}$$

$${}^{k}\mathbf{F}^3 = \mathbf{F}\left({}^{k}\mathbf{y}^3\right) \tag{4.129}$$

and ${}^{1}\mathbf{y}^3 = {}^{p}\mathbf{y}^3$. This step is repeated until the iteration error

$$e^3 = \left\|{}^{k+1}\mathbf{y}^3 - {}^{k}\mathbf{y}^3\right\|_\infty \tag{4.130}$$

is less than a prescribed error tolerance ε. If $e^3 > \varepsilon$, then one sets

$$^{k}\mathbf{y}^3 = {}^{k+1}\mathbf{y}^3 \tag{4.131}$$

$$^{k}\dot{\mathbf{y}}^3 = {}^{k+1}\dot{\mathbf{y}}^3 \tag{4.132}$$

and goes to equation (4.128); if $e^3 \leq \varepsilon$, then, for the first time, one evaluates the local truncation error

$$\mathbf{e}^3 = {}^{k+1}\mathbf{y}^3 - {}^{1}\mathbf{y}^3. \tag{4.133}$$

Next, one sets

$$\mathbf{y}^3 = {}^{k+1}\mathbf{y}^3 \tag{4.134}$$

$$\dot{\mathbf{y}}^3 = {}^{k+1}\dot{\mathbf{y}}^3 \tag{4.135}$$

and computes the response at $t_4 = t_3 + \Delta t = 4\Delta t$.

A.8 For t_4 and higher (i.e., $t = 4\Delta t, 5\Delta t, 6\Delta t, \cdots$), the solution is computed by using the Hamming's Fourth-Order Modified Predictor-Corrector Method scheme. The predicted solution, ${}^{p}\mathbf{y}^j$, is computed from the predictor equation

$$^{p}\mathbf{y}^j = \mathbf{y}^{j-4} + \frac{4}{3}\Delta t\left(2\mathbf{F}^{j-1} - \mathbf{F}^{j-2} + 2\mathbf{F}^{j-3}\right). \tag{4.136}$$

A.9 The predicted solution is modified by using the local truncation error from the previous timestep

$$ {}^{1}\mathbf{y}^{j} = {}^{p}\mathbf{y}^{j} + \frac{112}{9}\,\mathbf{e}^{j-1}. \tag{4.137} $$

A.10 The modified-predicted solution is corrected by using the correction equation

$$ {}^{k+1}\mathbf{y}^{j} = \frac{1}{8}\left[9\mathbf{y}^{j-1} - \mathbf{y}^{j-3} + 3\Delta t\left({}^{k}\mathbf{F}^{j} + 2\mathbf{F}^{j-1} - \mathbf{F}^{j-2}\right)\right] \tag{4.138} $$

$$ {}^{k}\mathbf{F}^{j} = \mathbf{F}\left({}^{k}\mathbf{y}^{j}\right) \tag{4.139} $$

and ${}^{1}\mathbf{y}^{j} = {}^{p}\mathbf{y}^{j}$. This step is repeated until the iteration error

$$ e^{j} = \left\| {}^{k+1}\mathbf{y}^{j} - {}^{k}\mathbf{y}^{j} \right\|_{\infty} \tag{4.140} $$

is less than a prescribed error tolerance ε. If $e^{j} > \varepsilon$, then one sets

$$ {}^{k}\mathbf{y}^{j} = {}^{k+1}\mathbf{y}^{j} \tag{4.141} $$

$$ {}^{k}\dot{\mathbf{y}}^{3} = {}^{k+1}\dot{\mathbf{y}}^{j} \tag{4.142} $$

and goes to equation (4.138).

A.11 When $e^{j} \leq \varepsilon$, one estimates the local truncation error for the use in the current and next timesteps

$$ \mathbf{e}^{j} = \frac{9}{121}\left({}^{k+1}\mathbf{y}^{j} - {}^{p}\mathbf{y}^{j}\right). \tag{4.143} $$

A.12 The final solution at step j is

$$\mathbf{y}^j = {}^{k+1}\mathbf{y}^j - \mathbf{e}^j. \tag{4.144}$$

A.13 To calculate the solution at the next timestep, one sets

$$\mathbf{y}^{j-4} = \mathbf{y}^{j-3} \tag{4.145}$$

$$\mathbf{y}^{j-3} = \mathbf{y}^{j-2} \tag{4.146}$$

$$\mathbf{y}^{j-2} = \mathbf{y}^{j-1} \tag{4.147}$$

$$\mathbf{y}^{j-1} = \mathbf{y}^{j} \tag{4.148}$$

$$\mathbf{e}^{j-1} = \mathbf{e}^{j} \tag{4.149}$$

and repeats steps A.8 to A.13 as many times as required. If $e^j > \varepsilon$ for more than a specified amount of iterations, the program stops and it is assumed that a solution cannot be reached.

4.5 Integrating Aerodynamic Model into the Numerical Scheme

During a timestep Δt, the wakes convect to their new positions consistent with the requirement that vorticity moves with the fluid particles and, simultaneously, the structure moves to a new position consistent with the current forces and equations of motion. This concept is implemented through the following sequence of steps to calculate the solution at time $t + \Delta t$ when the solution is known at time t, $t - \Delta t$,

$t - 2\Delta t$, and $t - 3\Delta t$:

B.1 The wakes are convected to their positions. A fluid particle in a wake is moved to its new position $\mathbf{R}(t + \Delta t)$ from its current position according to $\mathbf{R}(t)$

$$\mathbf{R}(t + \Delta t) = \mathbf{R}(t) + \mathbf{V}\left(\mathbf{R}(t)\right)\ \Delta t, \tag{4.150}$$

where $\mathbf{V}\left(\mathbf{R}(t)\right)$ is the local velocity of the fluid. During the remainder of the procedure for this timestep, the wake is not moved. Numerical experiments with more precise algorithms for convecting the wake have shown that equation (4.150) is adequate [66].

B.2 The current loads (i.e., those at the beginning of the timestep) are used to predict the state of the structure by using equation (4.136).

B.3 The predicted solution is modified by using the local truncation error from the previous timestep by using equation (4.137).

B.4 The modified-predicted solution is corrected by the iterative procedure that makes use of the corrector equation (4.138). The loads are recalculated for each iteration while the wake remains frozen. A great effort is required for the calculating of aerodynamic forces since the aerodynamic model must be used to completely recalculate the flowfield. This step is repeated until convergence is reached; that is, until the iteration error given by equation (4.139) is less than a prescribed error tolerance value). Typically, three to six iterations are required to reduce the value of the iteration error to 10^{-6}.

B.5 After convergence, the local truncation error given by equation (4.143) is obtained for the next timestep and for the final evaluation of the loads at the current timestep.

B.6 Then equation (4.144) is used to evaluate that final position and velocity of the structure, and these are used to recalculate the flowfield and to obtain the final estimate of the aerodynamic loads.

At this point in time, $(t + \Delta t)$, the position and velocity of the structure, the distribution of the vorticity and the aerodynamic loads on the lifting surface, and the distribution of vorticity are known as well as the positions of the wakes. This information is used in the calculation of the solution for the next timestep. Begin by shifting the information according to equations (4.145)-(4.149) and then repeat steps B.1 though B.6 in this section.

The procedures described above requires information from the four previous timesteps. In the beginning, this information does not exist so a special starting scheme, which is described in steps A.8 through A.7 of Section 4.4, is used:

C.1 At $t = 0$, the initial conditions are used to calculate the aerodynamic loads ignoring the contribution of $\dfrac{\partial \Phi}{\partial t}$. It is not important to capture this contribution precisely at this timestep because the response of the structure to an arbitrary initial disturbance is being determined. Then equation (4.110) is used to calculate $\mathbf{F}^0$ and the wake is convected to its position for the next timestep. Next, the state of the structure is predicted at time Δt by using the first-order Euler method scheme given by equation (4.111). Then, the predicted state is iteratively corrected using the modified Euler method scheme given by equation (4.112), recalculating the loads in each iteration. As previously mentioned, the position of the wake is not recalculated.

C.2 After convergence, time is advanced and the wake is convected. The solution is predicted at time $2\Delta t$ by using the second-order Adams-Bashforth two-step predictor method scheme given by equation (4.119). Then, the prediction is iteratively corrected using the Adams-Moulton two-step method scheme given by equation (4.120), recalculating the loads in each iteration.

C.3 After convergence, time is advanced and the wake is convected. The solution is predicted at time $3\Delta t$ by using the third-order Adams-Bashforth three-step predictor method scheme given by equation (4.127). Then, the predicted is iteratively corrected by using the Adams-Moulton three-step method scheme given by equation (4.128), recalculating the loads in each iteration. After convergence, the local truncation error is calculated for the first time and then, the procedure described at the beginning of this section is followed.

4.6 Summary

In this chapter, the co-simulation framework required for integrating the structural and aerodynamic model has been presented. It should be noted the co-simulation approach is broad and can be used with different aerodynamics and structural aerodynamics models. How the displacements and forces are transferred between the two models is described in this chapter along with the methodology for solving the equations of motion of the system. In the next chapter, the results obtained by using the aeroelastic simulator to predict the critical flutter speed of a joined-wing aircraft is discussed.

Chapter 5: Simulation Results

In this chapter, the simulation results obtained for a flat plate and a joined-wing aircraft aeroelastic model are presented. The flat plate aeroelastic model is used to verify the validity of the model to predict the critical flutter speed. For different freestream directions, the critical flutter speed of the joined-wing aircraft is predicted by using the aeroelastic model. With damage present on a specific location of the joined-wing, the change in the critical flutter speed at a specific freestream direction is investigated.

The verification of the aeroelastic model using an example for a flat plate from the literature is presented in Section 3.1. The critical flutter speed of the joined-wing aircraft with and without structural wing damage is discussed in Section 3.2. Finally, Section 5.3, has a summary of the chapter. This body of work answers research question **RQ4**.

5.1 Verification: Flat Plate Aeroelastic Model

To verify the flutter predictive capabilities of the accelerated aeroelastic simulator, a classic problem provided by Fung [67] to determine the torsion-bending flutter for a suspension bridge is used. Fung modeled the bridge as a system with

Table 5.1: Geometrical and material properties of Fung's model.

b [ft]	m $\left[\frac{\text{slug}}{\text{ft}}\right]$	r_β^2	ω_h^2 $\left[\frac{\text{rad}}{\text{s}^2}\right]$	ω_β^2 $\left[\frac{\text{rad}}{\text{s}^2}\right]$
30	269	0.6222	0.775	2.410

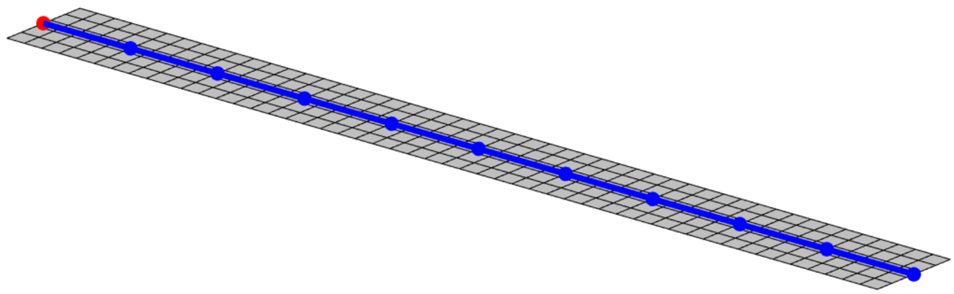

Figure 5.1: Computation model used to verify aeroelastic simulation results.

two degrees of freedom. This system had the geometrical and material properties shown in Table 5.1. In Table 5.1, $2b$ is the width of the bridge, m is the mass per unit length, r_β^2 is the radius of gyration around the elastic axis, ω_h is the natural bending frequency, and ω_β is the natural torsional frequency. The elastic axis lies at the center of the chord, the mass distribution is symmetrical, and the air density is $\rho = 2.378 \times 10^{-4}$ slug/ft^3. Fung [67] reported a flutter speed of 162 ft/s with a corresponding frequency of 1.25 rad/s.

To perform the verification test for the aeroelastic simulator, an aerodynamic mesh with an aspect ratio of 10, with five panels along the chord length, and 50 panels along the span length, was utilized. The chord and span of the mesh are 60 ft and 600 ft, respectively. The computational model used can be seen in Figure 5.1. The structural beam is composed of 10 elements constructed from 11 nodes. A rectangular cross-section with a width of 60 ft and thickness of 1 ft was used. To ensure that the same natural bending and torsion frequencies are obtained, the material and geometrical properties used for the simulations, with regard to Figure 3.4, are

Table 5.2: Material properties of computational structural model used for verification case.

$E\ \left[\frac{\text{slug}}{\text{ft s}^2}\right]$	$G\ \left[\frac{\text{slug}}{\text{ft s}^2}\right]$	ν	$\rho_m\ \left[\frac{\text{slug}}{\text{ft}^3}\right]$
1.482×10^9	2.671×10^9	0.33	4.483

Table 5.3: Geometric cross-sectional properties of computational structural model used for verification case.

A [ft^2]	I_y [ft^4]	I_z [ft^4]	I_p [ft^4]	J_T [ft^4]
60	5	18000	18005	19.790

given in Tables 5.2 and 5.3.

The first two vibration modes are shown in Figure 5.2 and their corresponding natural bending and torsion frequencies closely match those provided by Fung

$$\omega_h = 0.8804\,\text{rad/s} \tag{5.1}$$

$$\omega_\beta = 1.5524\,\text{rad/s}. \tag{5.2}$$

The simulations were run for 240 seconds in realtime. Depending on the freestream speed, the number of timesteps needed to run each individual simulation ranged from 1,000 to 3,600. A freestream air density of $\rho = 0.0002378$ slug/ft^3 and freestream direction of $(0°, 0°, 0°)$ was used with initial conditions

$$q_1(0) = 0 \qquad \dot{q}_1(0) = 0 \tag{5.3}$$

$$q_2(0) = 0.1 \qquad \dot{q}_2(0) = 0 \tag{5.4}$$

The responses of the aeroelastic behavior of the flat plate for a freestream speed of 110 ft/s are shown in Figure 5.3. This freestream speed is called a *subcritical speed*

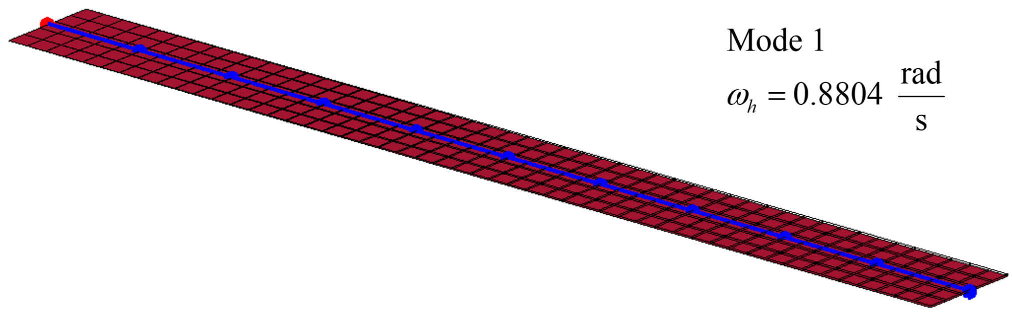

(a)

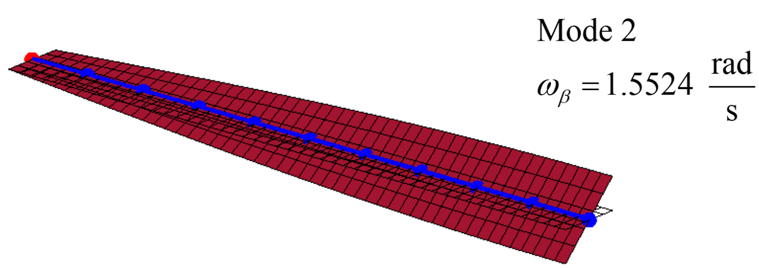

(b)

Figure 5.2: Vibration modes of structure: (a) first mode and (b) second mode.

since the amplitude of the oscillatory behavior of the q_1 and q_2 responses decay over time, as can be seen in Figure 5.3(a). This is caused by the presence of just aerodynamic damping.

The normalized fast Fourier transforms (FFTs) of q_1 and q_2 superimposed on the same plot are shown in Figure 5.3(b). The entire response of the aeroelastic behavior is used to obtain the FFT plots. To have a better view of the frequency responses around the natural frequencies of the system, the signals ranging between 0 rad/s and 5 rad/s are shown in the FFT plots. It can be seen that a frequency of 1.412 rad/s can be observed in both the q_1 and q_2 responses. It should also be noted that the q_1 response has an additional frequency of 0.890 rad/s. Both notable frequencies are bound between the natural frequencies (equations 5.1 and 5.2) of the structure during free oscillation (i.e., $V_\infty = 0$). These natural frequencies are indicated by the dotted vertical black lines in Figure 5.3(b).

The projected responses in the phase planes are shown in Figure 5.3(c). In the two projections shown, it can be observed that spirals are converging to an equilibrium point, typical of a stable focus.

The responses of the aeroelastic behavior of the flat plate for a freestream speed of 124 ft/s, which is close to the *critical speed*, are shown in Figure 5.4. It can be observed that after the transient, an oscillatory behavior of constant amplitude develops in the responses of q_1 and q_2.

The normalized FFTs of q_1 and q_2 superimposed on the same plot are shown in Figure 5.4(b). It can be seen that both the q_1 and q_2 responses oscillate at a frequency of 1.361 rad/s. The observed frequency is bounded between the natural frequencies of the structure during free oscillation, which is also indicated by the dotted vertical black lines in Figure 5.4(b).

The projected responses in the phase planes are shown in Figure 5.4(c). In the two projections shown, it can be observed that there is a tendency to establish a closed path with constant amplitude. This is illustrated through the presence of a limit cycle.

The responses of the aeroelastic behavior of the flat plate for a freestream speed of 140 ft/s, which is called a *supercritical speed*, are shown in Figure 5.5. This is because this velocity is past the critical fluttter speed. The amplitudes of the oscillatory behavior of the responses q_1 and q_2 increases over time before reaching a steady state, as can be seen in Figure 5.5(a).

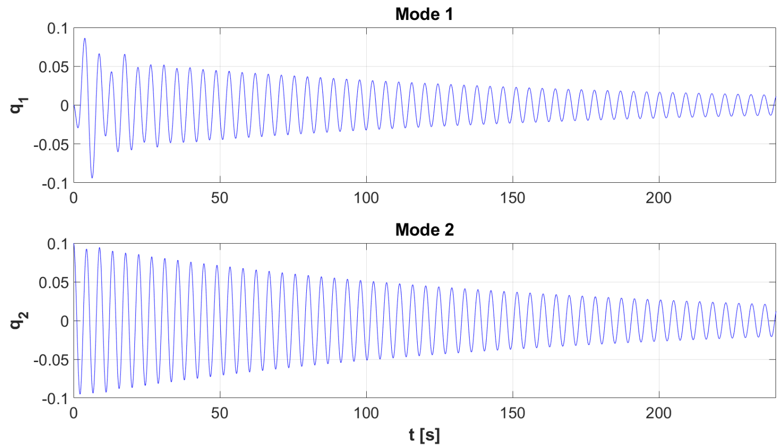

(a)

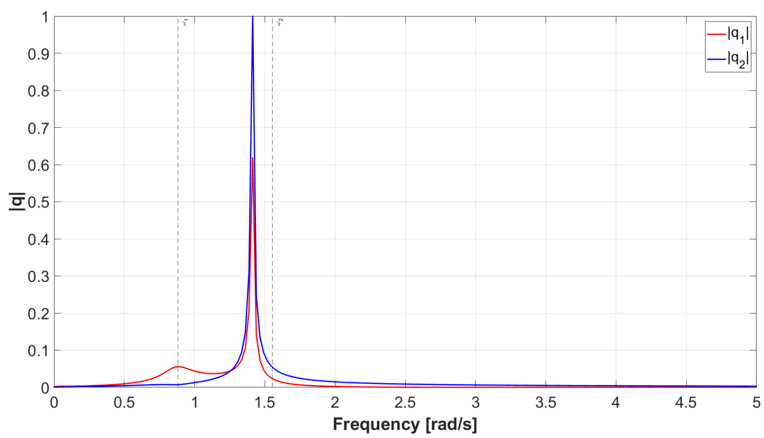

(b)

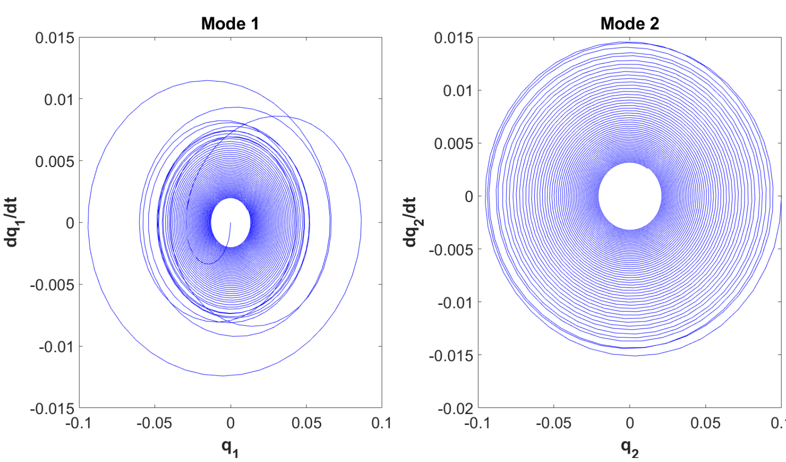

(c)

Figure 5.3: Aeroelastic response at subcritical speed, $V_\infty = 110$ ft/s. (a) Time responses of q_1 and q_2, (b) response in the frequency domain, and (c) projections in the state space.

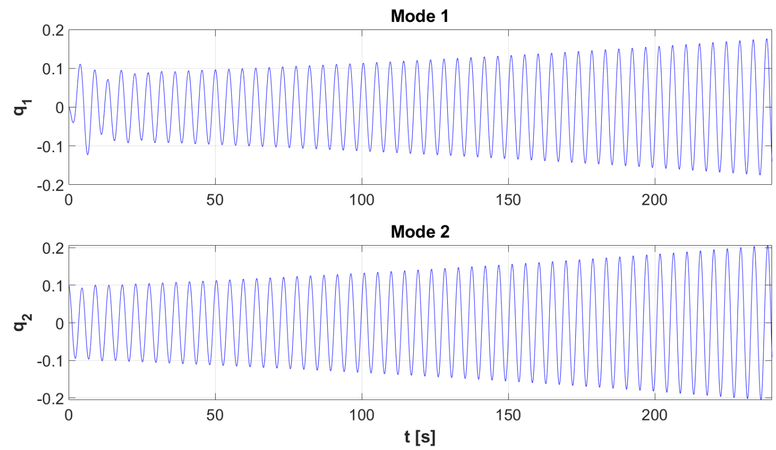

(a)

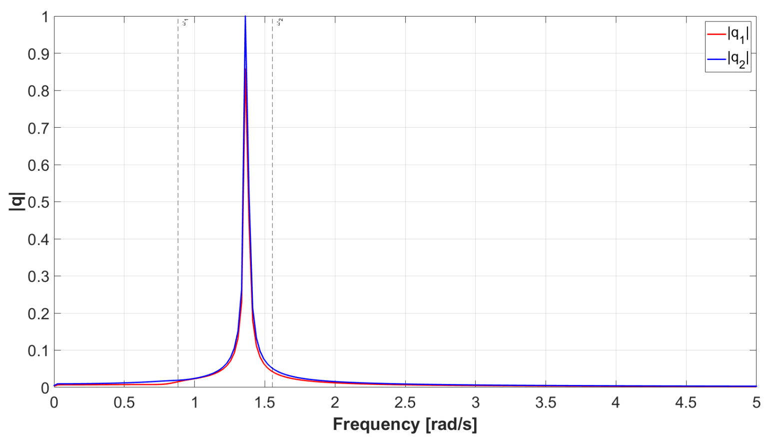

(b)

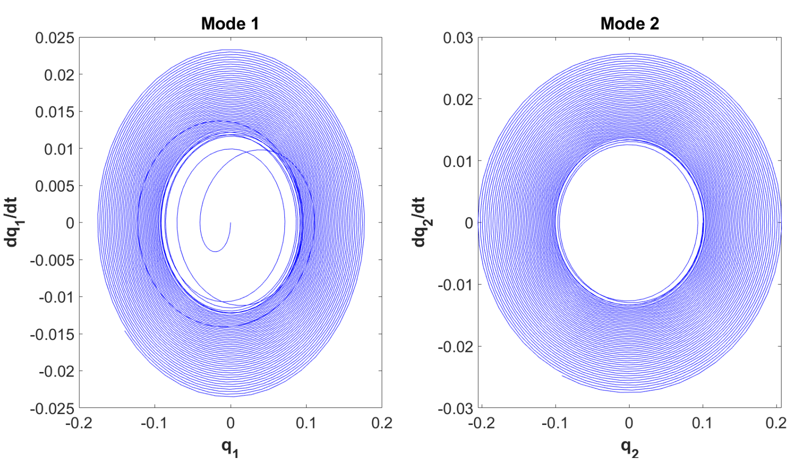

(c)

Figure 5.4: Aeroelastic response at critical speed, $V_\infty = 124\,\text{ft/s}$. (a) Time responses of q_1 and q_2, (b) response in the frequency domain, and (c) projections in the state space.

The normalized FFTs of q_1 and q_2 superimposed on the same plot are shown in Figure 5.5(b). It can be seen that both the q_1 and q_2 responses oscillate at a frequency of 1.309 rad/s. The observed frequency is bounded between the natural frequencies of the structure during free oscillation, which is also indicated by the dotted vertical black lines in Figure 5.5(b).

The projected responses in the phase planes are shown in Figure 5.5(c). In the two projections shown, it can be observed that trajectories are diverging in a spiral from the initial conditions and will eventually converge towards a closed curve of constant amplitude.

Fung [67] predicted a critical flutter speed of 162 ft/s with a corresponding frequency of 1.25 rad/s. Based on the developed aeroelastic computational tool, a critical flutter speed of 124 ft/s with a corresponding frequency of 1.36 rad/s was obtained. The predicted critical flutter speed can be observed in the bifurcation diagrams of Figure 5.6 based on responses of q_1, in Figure 5.6(a), and q_2, in Figure 5.6(b). After the critical flutter speed (indicated by the red marker), the amplitudes of the limit cycles start to grow gradually. These numerical approximations differ from Fung's predictions by 23.5% for the speed and 8.8% frequency, respectively. The differences in the predicted critical flutter speed are attributed to the following:

- Fung [67] considered a plate with an infinite aspect ratio (i.e., plate of infinite length), while the current model has an aspect ratio of ten;
- Fung [67] utilized a two-dimensional, linear theory based aerodynamic model,

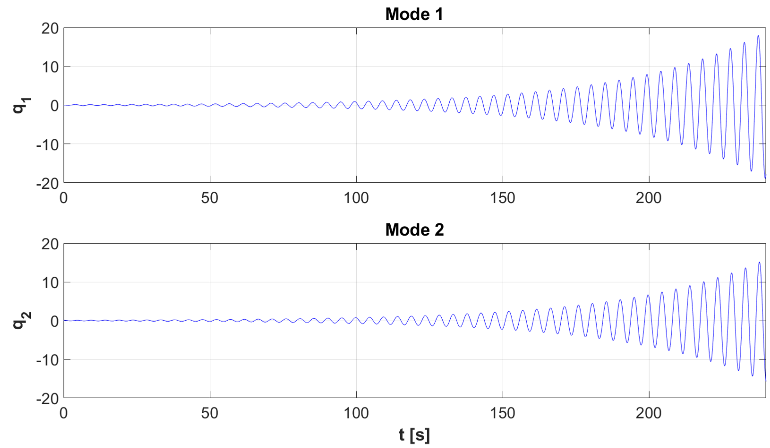

(a)

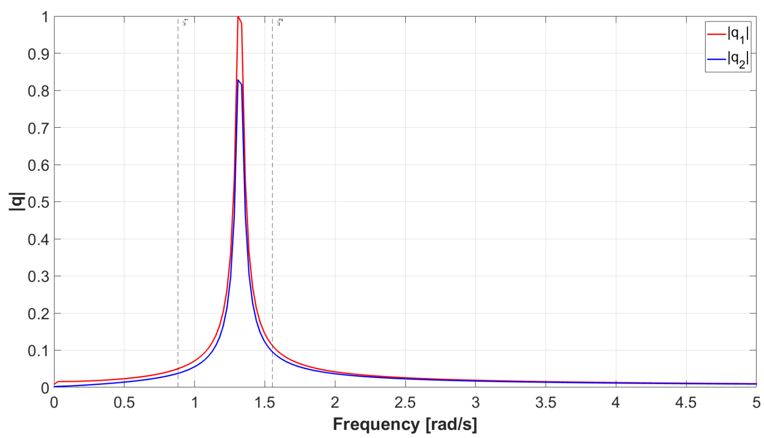

(b)

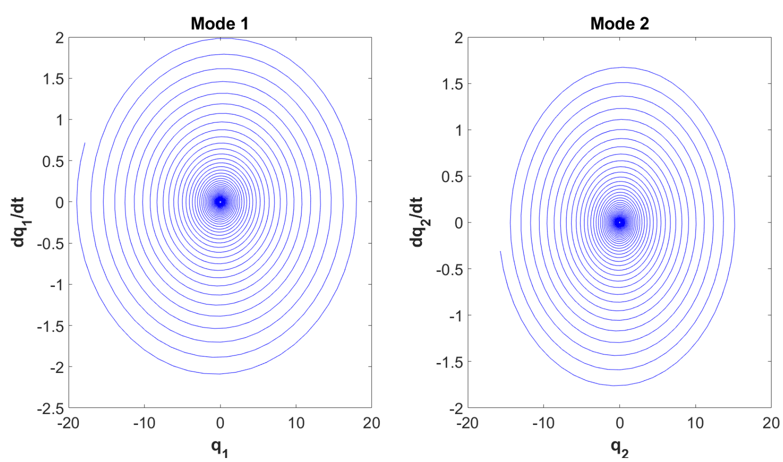

(c)

Figure 5.5: Aeroelastic response at supercritical speed, $V_\infty = 140$ ft/s. (a) Time responses of q_1 and q_2, (b) response in the frequency domain, and (c) projections in the state space.

while in the current work, the author has utilized the UVLM based aerodynamic model.

The predicted results match closely with those predicted by Strganac [68], who predicted a critical flutter speed of 125 ft/s. It should be noted that Strganac also implemented Fung's aeroelastic model with a three-dimensional UVLM based aerodynamic model. In the present case, the author has used an accelerated aeroelastic model.

5.2 Joined-Wing SensorCraft Aeroelastic Model

The simulations for the joined-wing aircraft aeroelastic model were run for 180 seconds in real-time. Depending on the freestream speed, the number of timesteps needed to run each individual simulations ranges from 18,000 to 60,000. The freestream air density is $\rho = 0.1152$ kg/m^3. This is a reasonable air density for a surveillance drone, such as the joined-wing SensorCraft, flying at an altitude that is between 15,000 to 20,000 ft above sea level. Tilmann [2] suggested that a different joined-wing SensorCraft configuration could cruise at an altitude between 60,000 to 70,000 ft above sea level. The initial conditions were chosen as

$$q_i(0) = 0 \qquad \dot{q}_i(0) = 0 \tag{5.5}$$

for $i = 1, 2, \cdots, 20$. The wake in the aerodynamic model is truncated after six chord lengths or 30 timesteps. More details about the simulation setup for the joined-wing

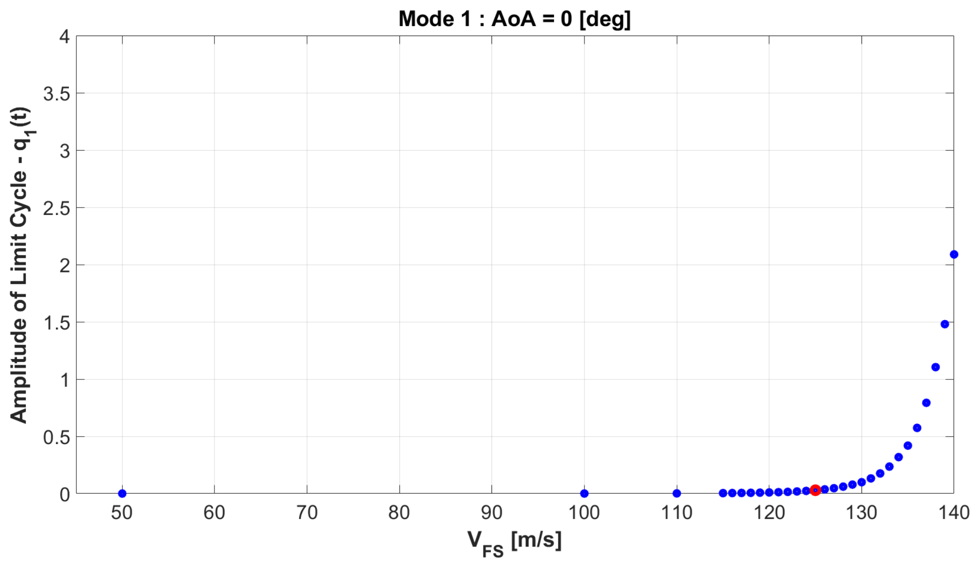

(a)

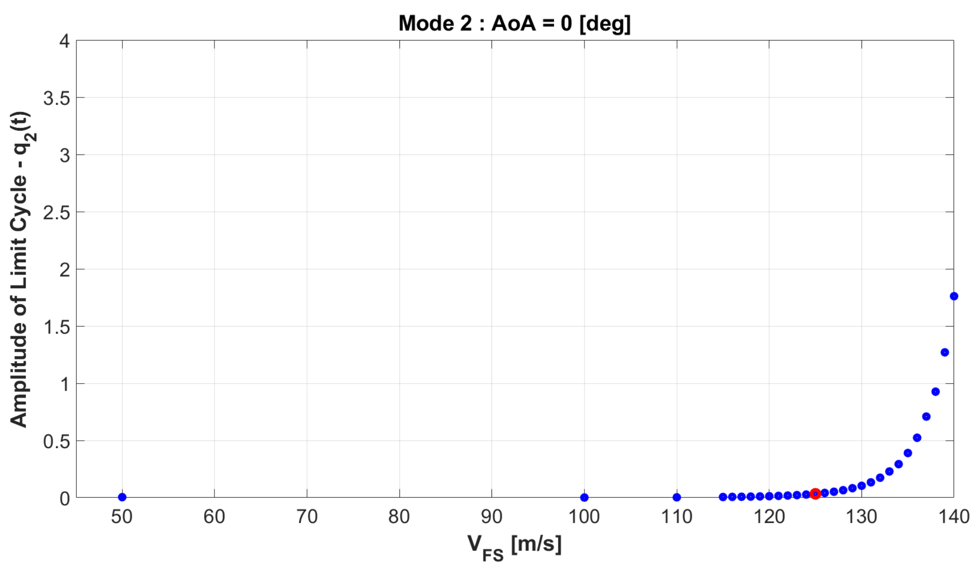

(b)

Figure 5.6: Bifurcation diagram constructed with freestream speed as a control parameter: (a) q_1 versus freestream speed and (b) q_2 versus freestream speed.

aircraft is presented in Appendix C. On an Intel® Xeon® CPU E3-1245 v5 (3.50 GHz) eight-core PC with 16 GB of RAM, each simulation ran from approximately two to fours days. A majority of the simulations were ran on the Deepthought High-Performance Computing (HPC) cluster. On the HPC clusters, each simulation ran from approximately one to two days, essentially cutting the runtime in half. It should be noted that the simulations of the joined-wing computational aeroelastic model developed in reference [63], where only half of the geometry for the aerodynamic mesh ws used, ran on average for about three days on a desktop with a dual-core processor and support for *Hyper-Threading Technology*®.

5.2.1 Cases with No Damage

5.2.1.1 Freestream Direction: $(0°, 5°, 0°)$

In the first case of no damage to the structure, the freestream direction is given by a yaw angle of 0°, a pitch angle of 5°, and a roll angle of 0°. Over 20 different simulations were run to determine the critical flutter speed. For this case, the critical flutter speed was predicted to be 156 m/s. This can be observed in the bifurcation diagrams of of the modes representing vibrations of the right joined-wing, shown in Figure 5.7, and the modes representing vibrations of the left joined-wing, shown in Figure 5.8. After the critical flutter speed (indicated by the red marker), the amplitudes of the limit cycles start to grow gradually with increase in the freestream speed. This is an example of emphsupercritical flutter or emphsupercritical Hopf bifurcation [69, 70].

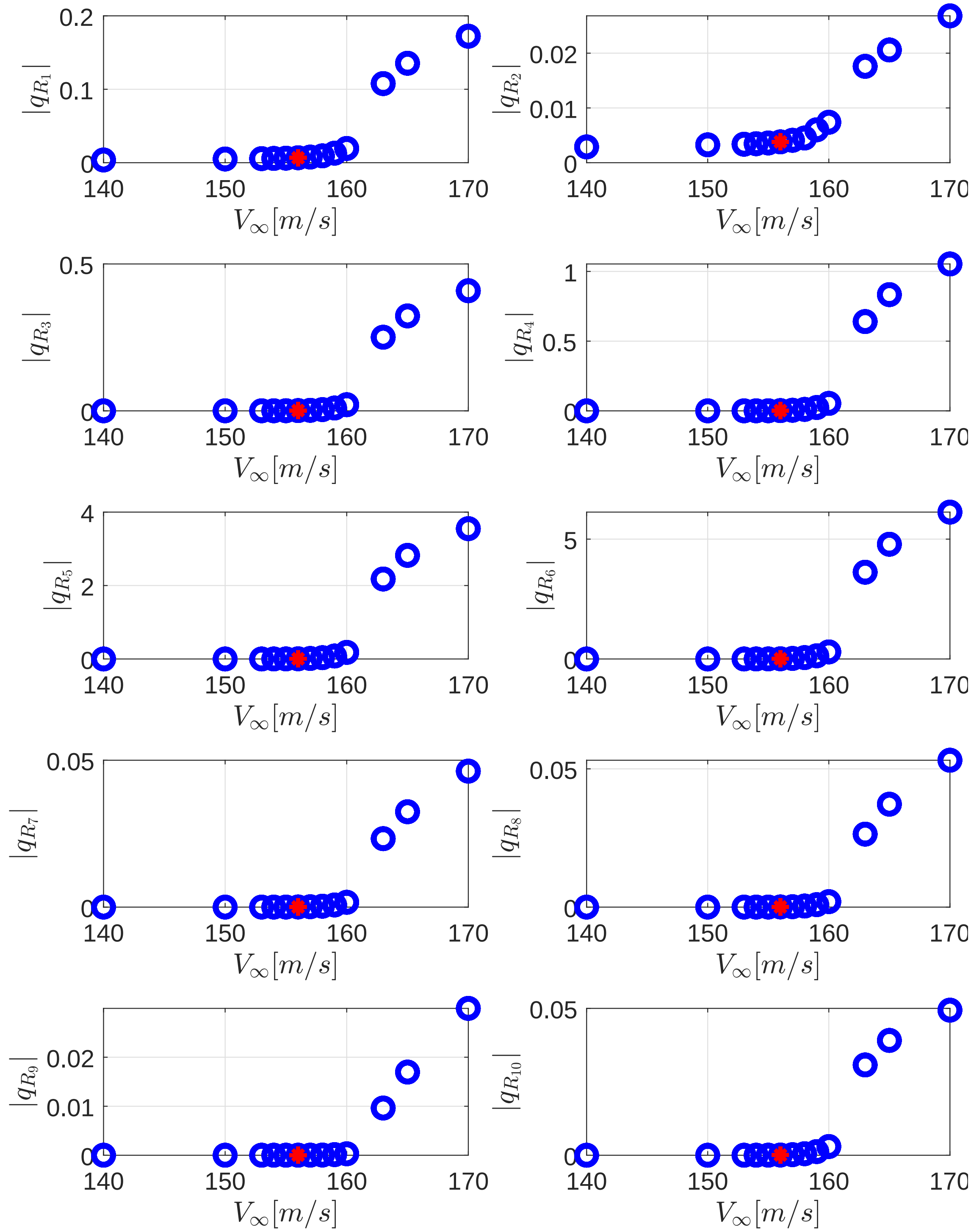

Figure 5.7: Bifurcation diagram constructed with $(0°, 5°, 0°)$ freestream direction and freestream speed as a control parameter. Responses of modes corresponding to the right joined-wing of the undamaged structure are shown.

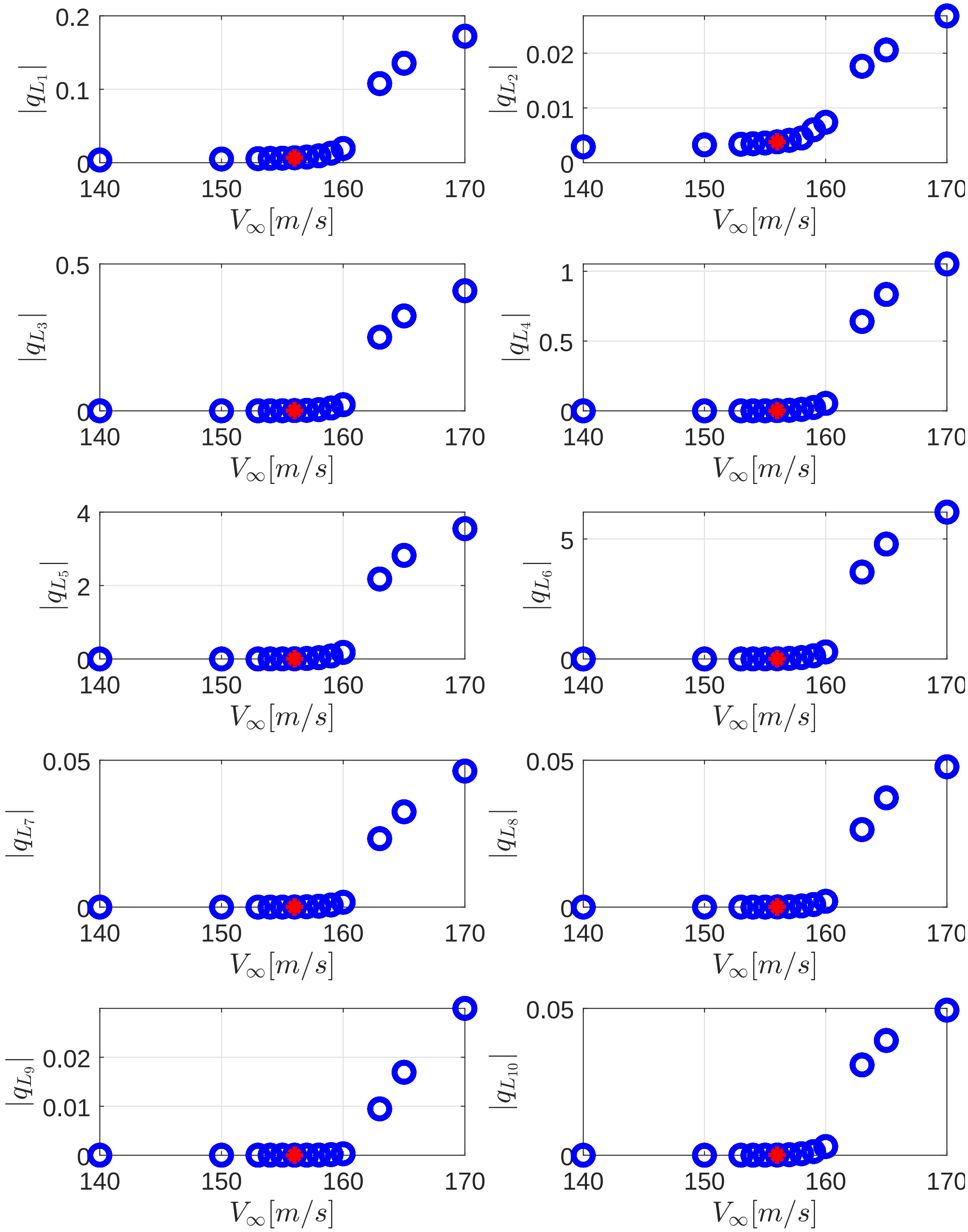

Figure 5.8: Bifurcation diagram constructed with $(0°, 5°, 0°)$ freestream direction and freestream speed as a control parameter. Responses of modes corresponding to the left joined-wing of the undamaged structure are shown.

The results shown in Figures 5.9 and 5.10 correspond to a case where the freestream speed is 120 m/s, which is below the critical flutter speed. The time responses of all modes corresponding to the right joined-wing are shown in Figures 5.9 and the time responses of all modes corresponding to the left joined-wing are shown in 5.10. In the two figures, it can be observed that after a brief transient, all modes exhibit an oscillatory behavior that decreases in amplitude as time passes. This is caused by the presence of just aerodynamic damping.

The projected responses in the phase planes of the right joined-wing and the left joined-wing are shown in Figures 5.11 and 5.12, respectively. Stable focus type of characteristics can be observed in all modes as the spirals converge to an equilibrium point.

In Figures 5.13 and 5.14, the normalized FFTs of the modes corresponding to the right joined-wing and the left joined-wing, respectively, are presented. To have a better view of the frequency responses around the free vibration frequencies of the system, the signals ranging between 0 Hz and 6.5 Hz are shown in the FFT plots of joined-wing aircraft. The free vibration frequencies are marked in the figures by dashed red lines. In all cases, a dominant frequency can be observed from a composition of two or more frequency components.

The results shown in Figures 5.15 and 5.16 correspond to a case where the freestream speed is 156 m/s, which is close to the critical flutter speed. The time responses of all modes corresponding to the right joined-wing are shown in Figures 5.15 and the time responses of all modes corresponding to the left joined-wing are shown in 5.16. In the two figures, it can be observed that after the transient

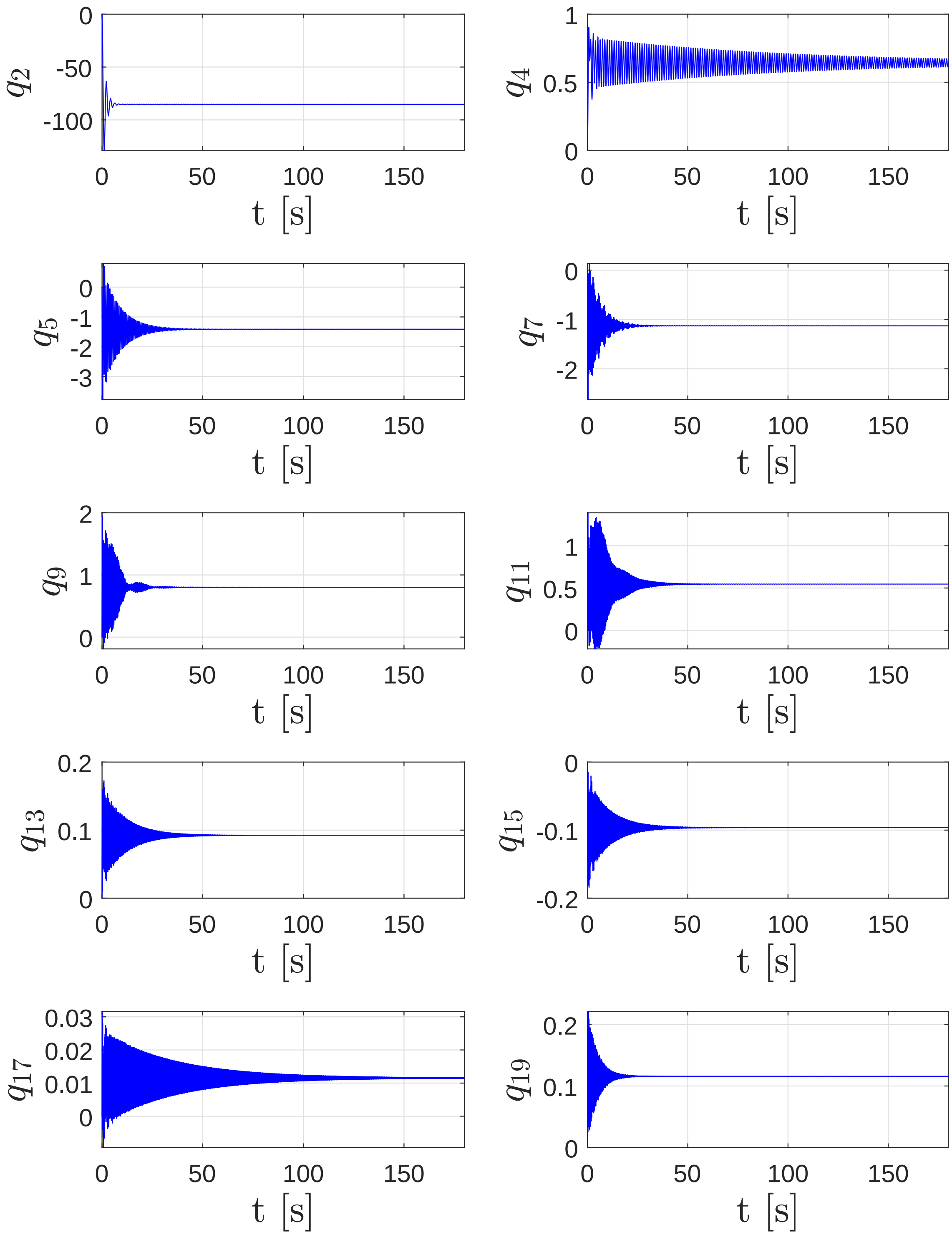

Figure 5.9: Time responses of modes corresponding to the right joined-wing for the case with no structural damage at subcritical speed $V_\infty = 120$ m/se case and freestream direction $(0°, 5°, 0°)$.

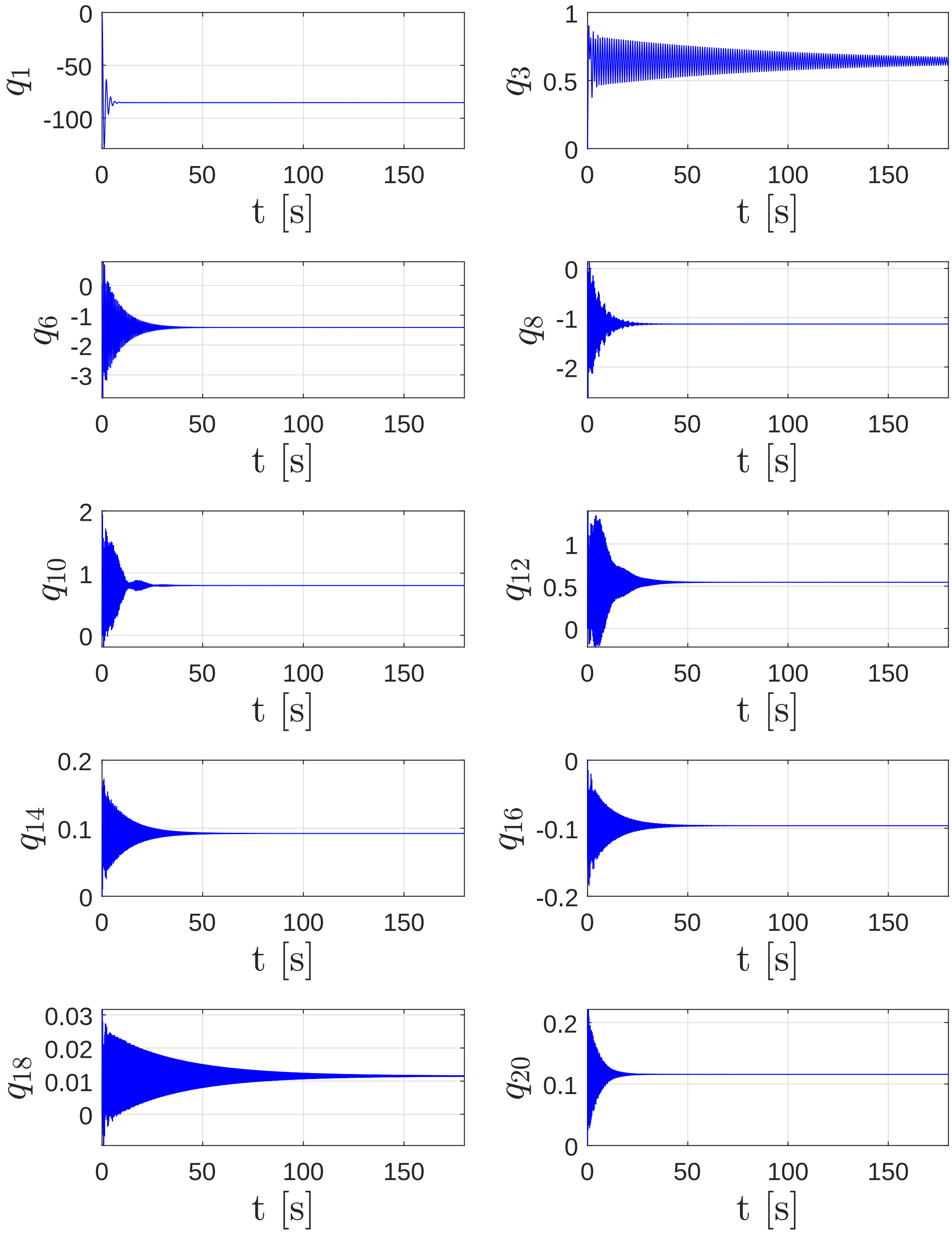

Figure 5.10: Time responses of modes corresponding to the left joined-wing for the case with no structural damage at subcritical speed $V_\infty = 120\,\mathrm{m/s}$ and freestream direction $(0°, 5°, 0°)$.

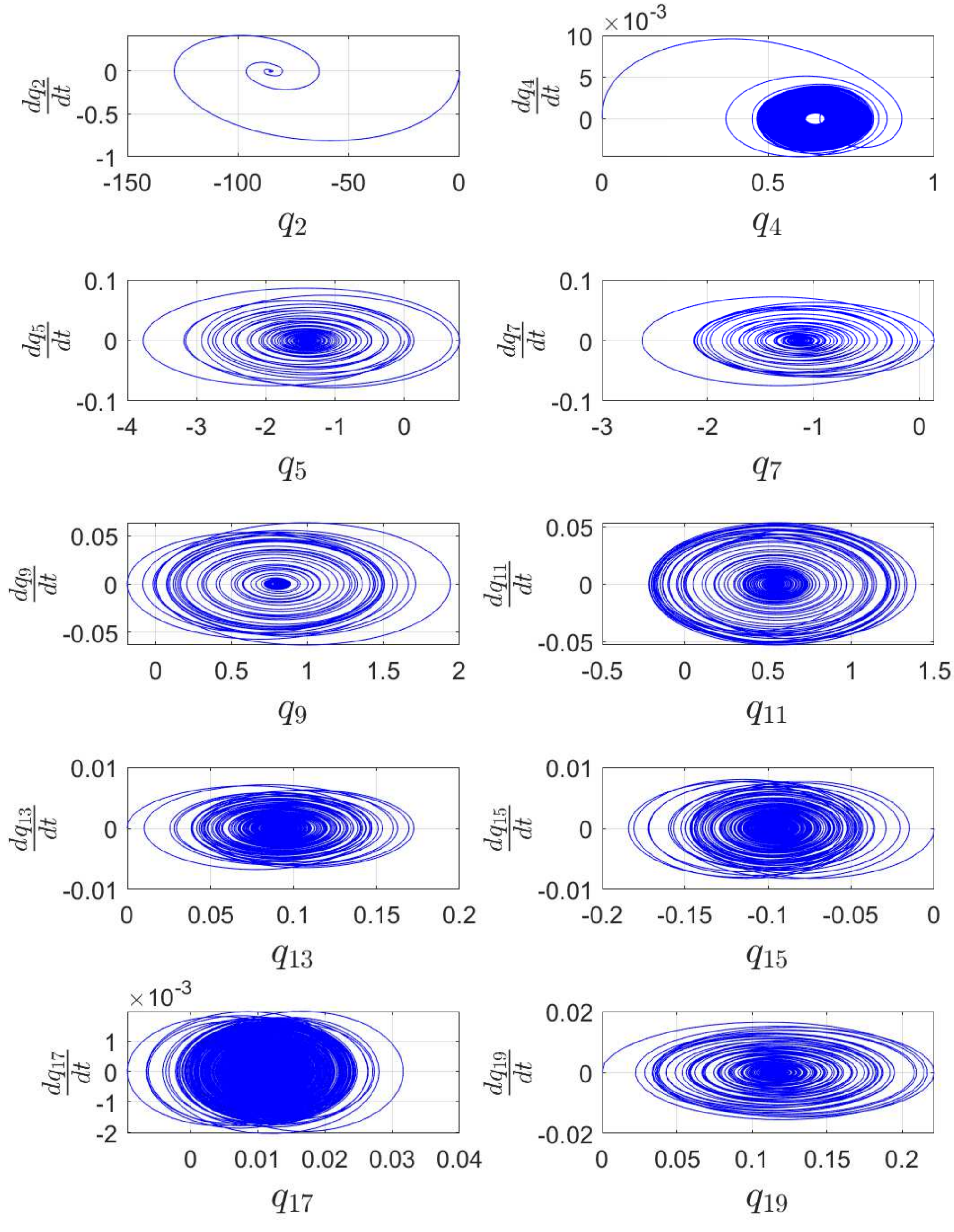

Figure 5.11: At subcritical speed $V_\infty = 120$m/s, projections in phase planes of modes corresponding to the right joined-wing for the case with no structural damage case and freestream direction $(0°, 5°, 0°)$.

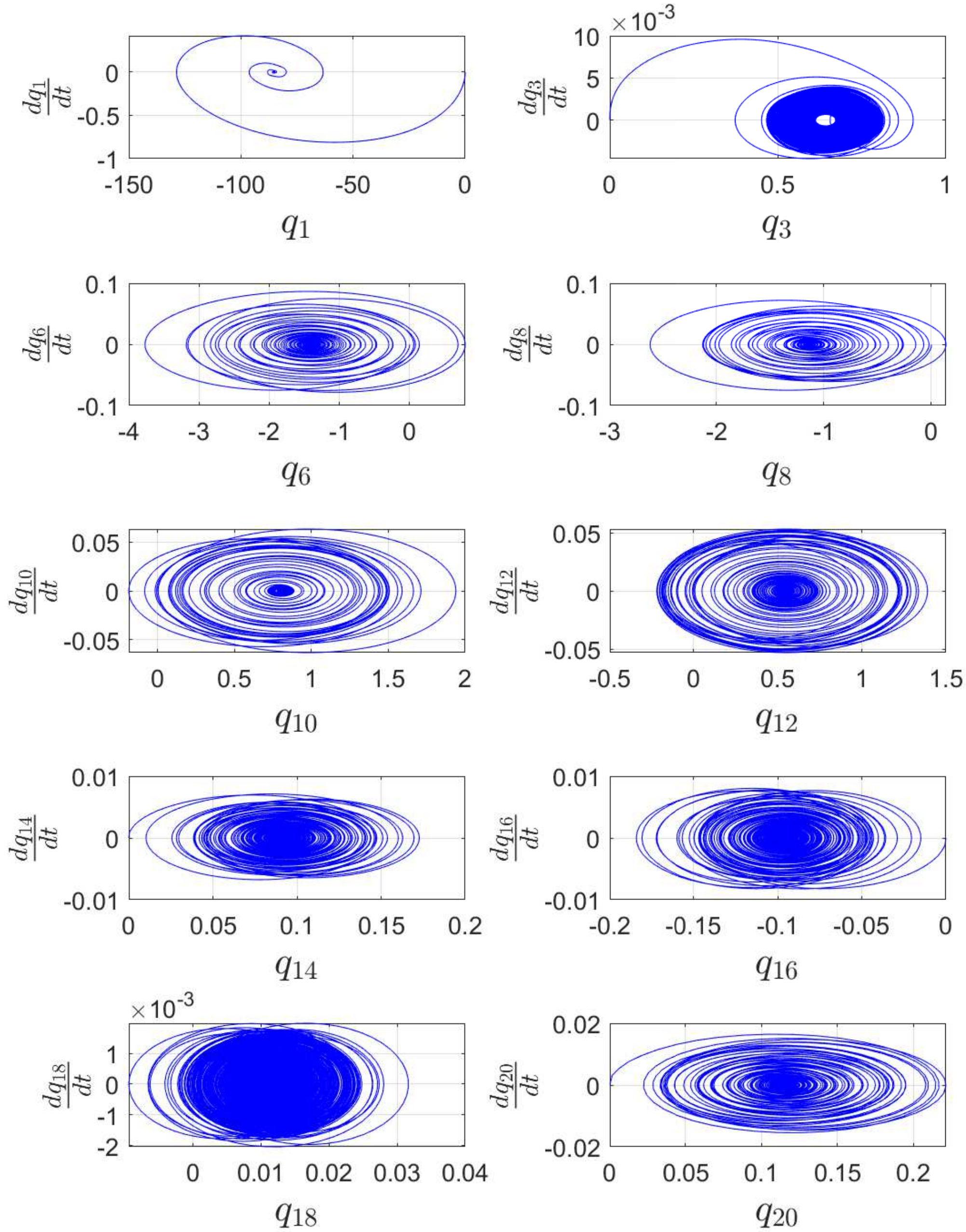

Figure 5.12: At subcritical speed $V_\infty = 120$ m/s, projections in phase planes of modes corresponding to the left joined-wing for the case with no structural damage and freestream direction $(0°, 5°, 0°)$.

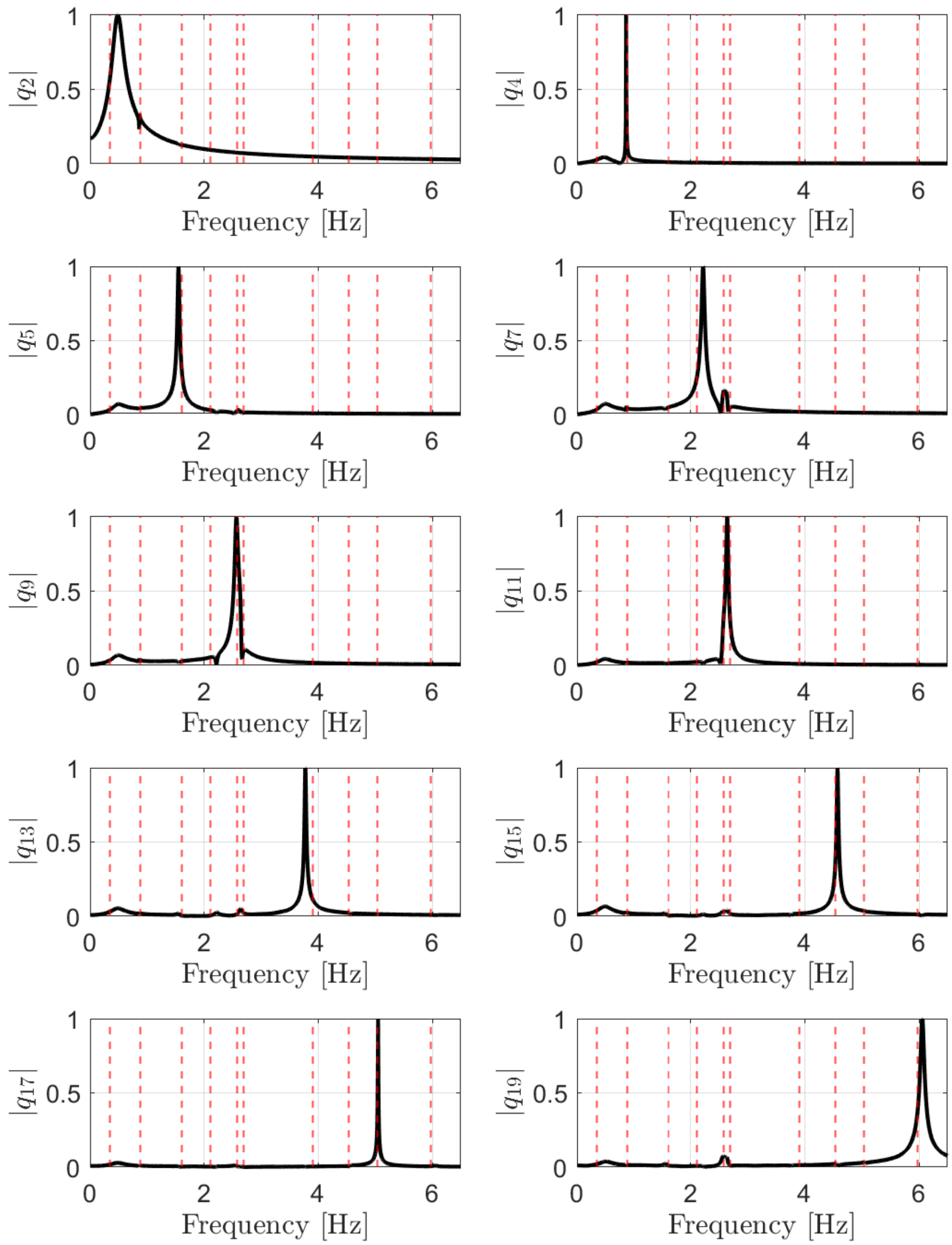

Figure 5.13: At subcritical speed $V_\infty = 120\,\mathrm{m/s}$, responses in the frequency domain of modes corresponding to the right joined-wing for the case with no structural damage and freestream direction $(0°, 5°, 0°)$.

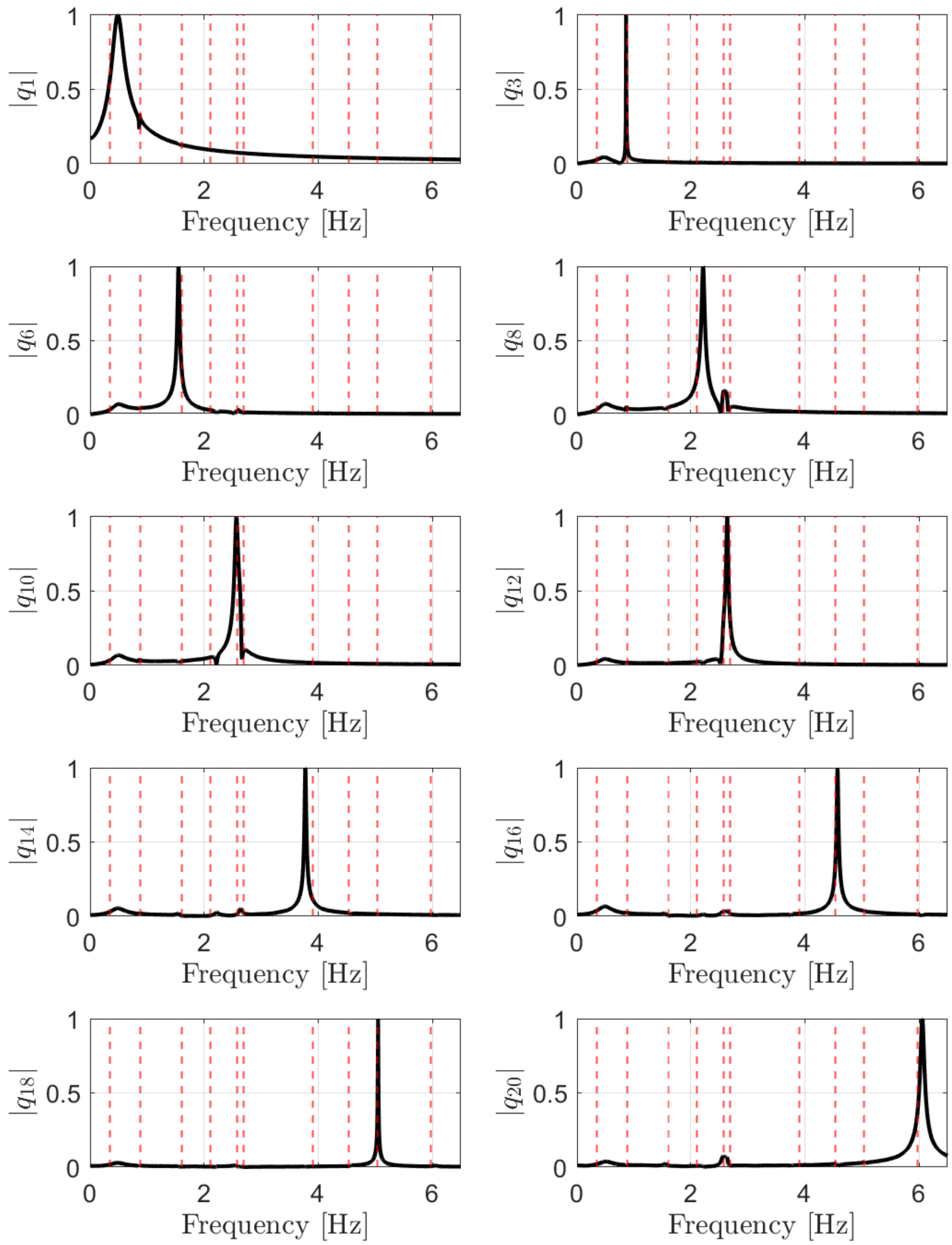

Figure 5.14: At subcritical speed $V_\infty = 120\,\mathrm{m/s}$, responses in the frequency domain of modes corresponding to the left joined-wing for the case with no structural damage and freestream direction $(0°, 5°, 0°)$.

response, all modes begin to present an oscillatory behavior of constant amplitude as time passes.

The projected responses in the phase planes of the right joined-wing and the left joined-wing are shown in Figures 5.17 and 5.18, respectively. In the responses of the second modes corresponding the right and left joined-wings, limit cycles can be seen.

In Figures 5.19 and 5.20, the normalized FFTs of the responses of the modes corresponding to the right joined-wing and the left joined-wing are presented, respectively. The free vibration frequencies are marked in the figures by dashed red lines. At least two dominant frequencies can be observed in the responses of the first, third, fourth, seventh, eighth, and tenth modes of each joined-wing.

The results shown in Figures 5.21 and 5.22 correspond to a case where the freestream speed is 160 m/s, which is over the critical flutter speed. The time responses of all modes corresponding to the right joined-wing are shown in Figures 5.21 and the time responses of all modes corresponding to the left joined-wing are shown in 5.22. In the two figures, it can be observed that after the transient response, all modes exhibit an oscillatory behavior, which initially increases in amplitude as time passes before reaching a steady state amplitude.

The projected responses in the phase planes of the right joined-wing and the left joined-wing are shown in Figures 5.23 and 5.24, respectively. In the responses of the about half of the modes corresponding the right and left joined-wings, limit cycles can be seen.

In Figures 5.25 and 5.26, the normalized FFTs of the responses of the modes

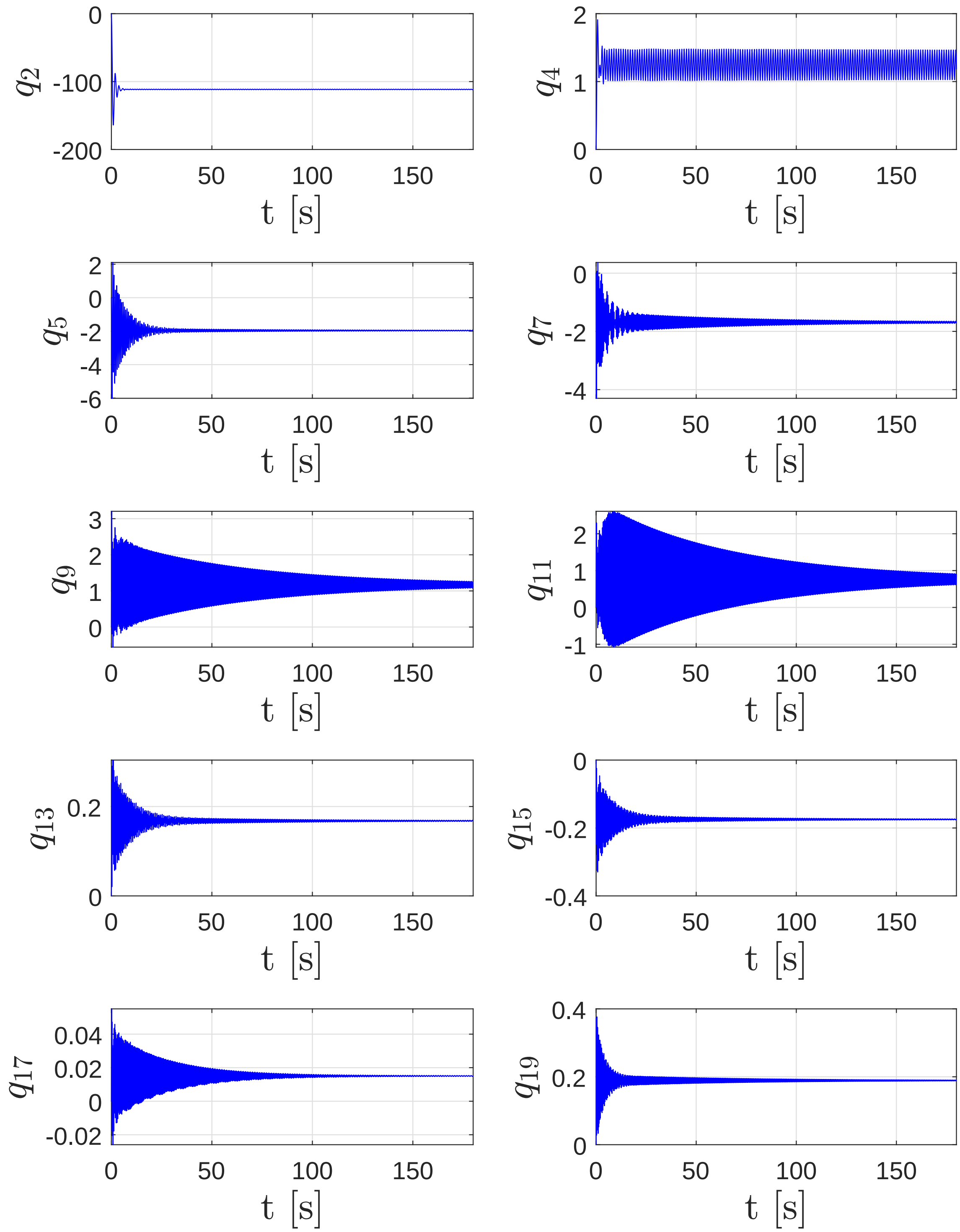

Figure 5.15: Time responses of modes corresponding to the right joined-wing for the case with no structural damage at critical speed $V_\infty = 156\,\mathrm{m/s}$ and freestream direction $(0°, 5°, 0°)$.

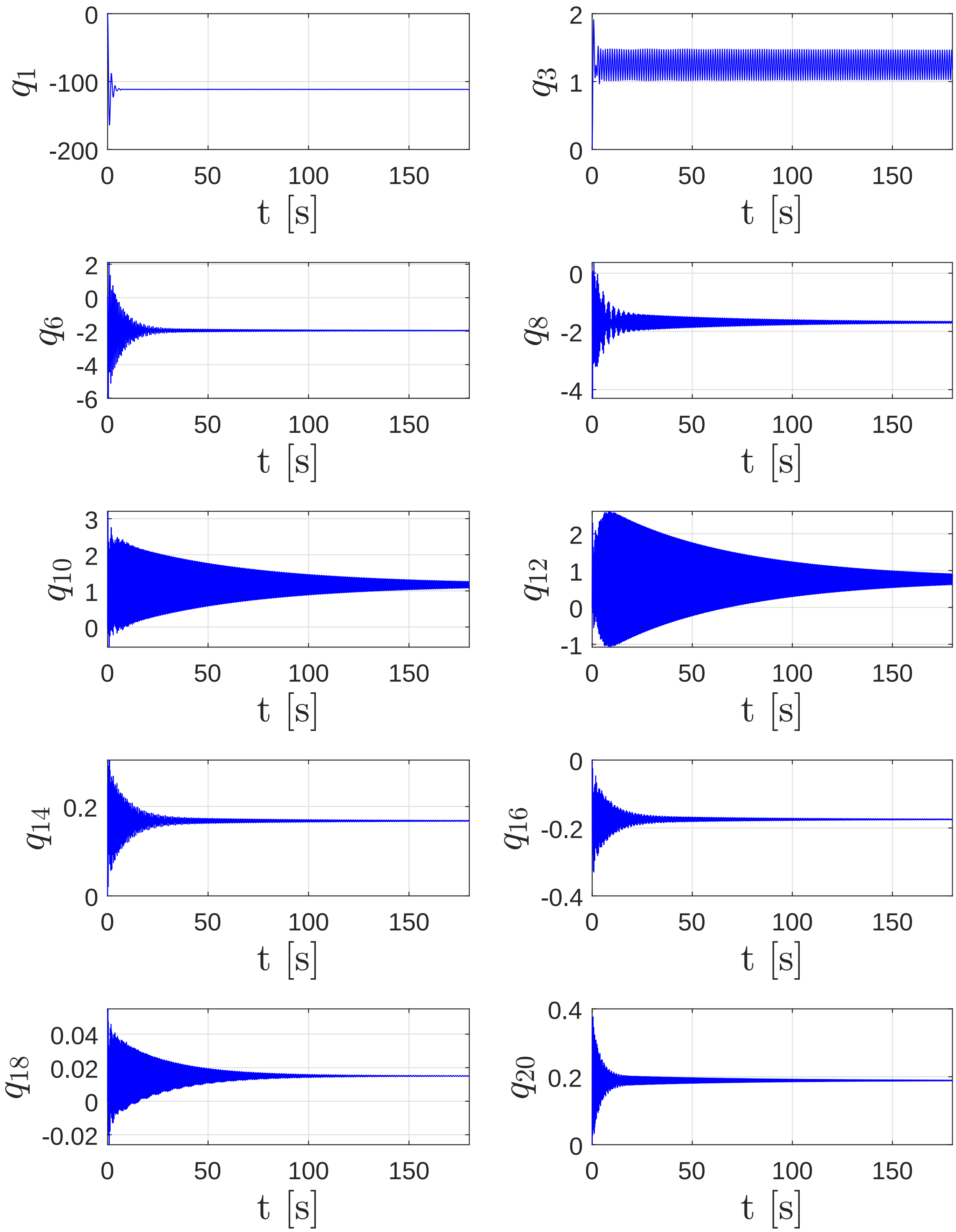

Figure 5.16: Time responses of modes corresponding to the left joined-wing for the case with no structural damage at critical speed $V_\infty = 156$ m/s and freestream direction $(0°, 5°, 0°)$.

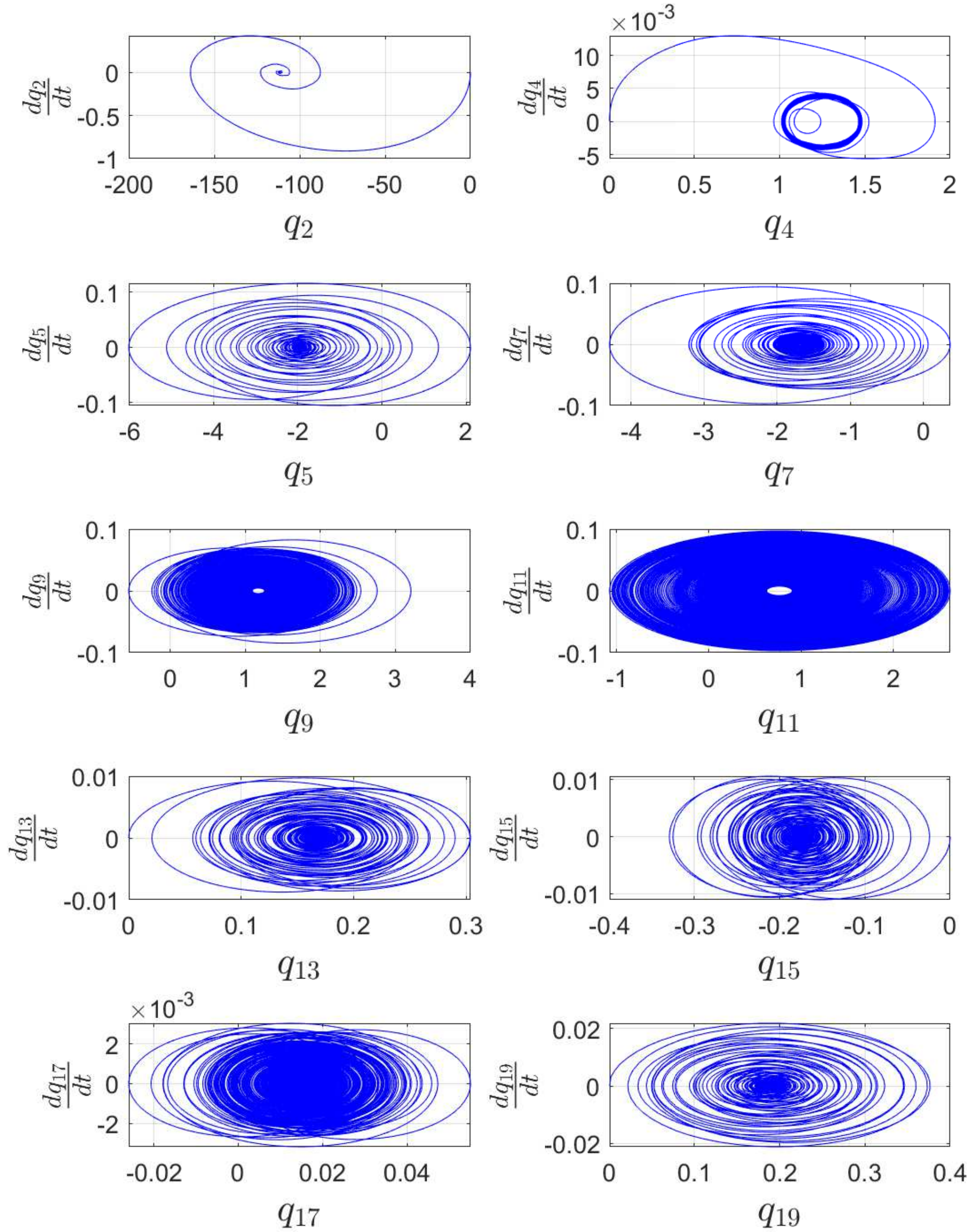

Figure 5.17: At critical speed $V_\infty = 156\,\mathrm{m/s}$, projections in phase planes of modes corresponding to the right joined-wing for the case with no structural damage and freestream direction $(0°, 5°, 0°)$.

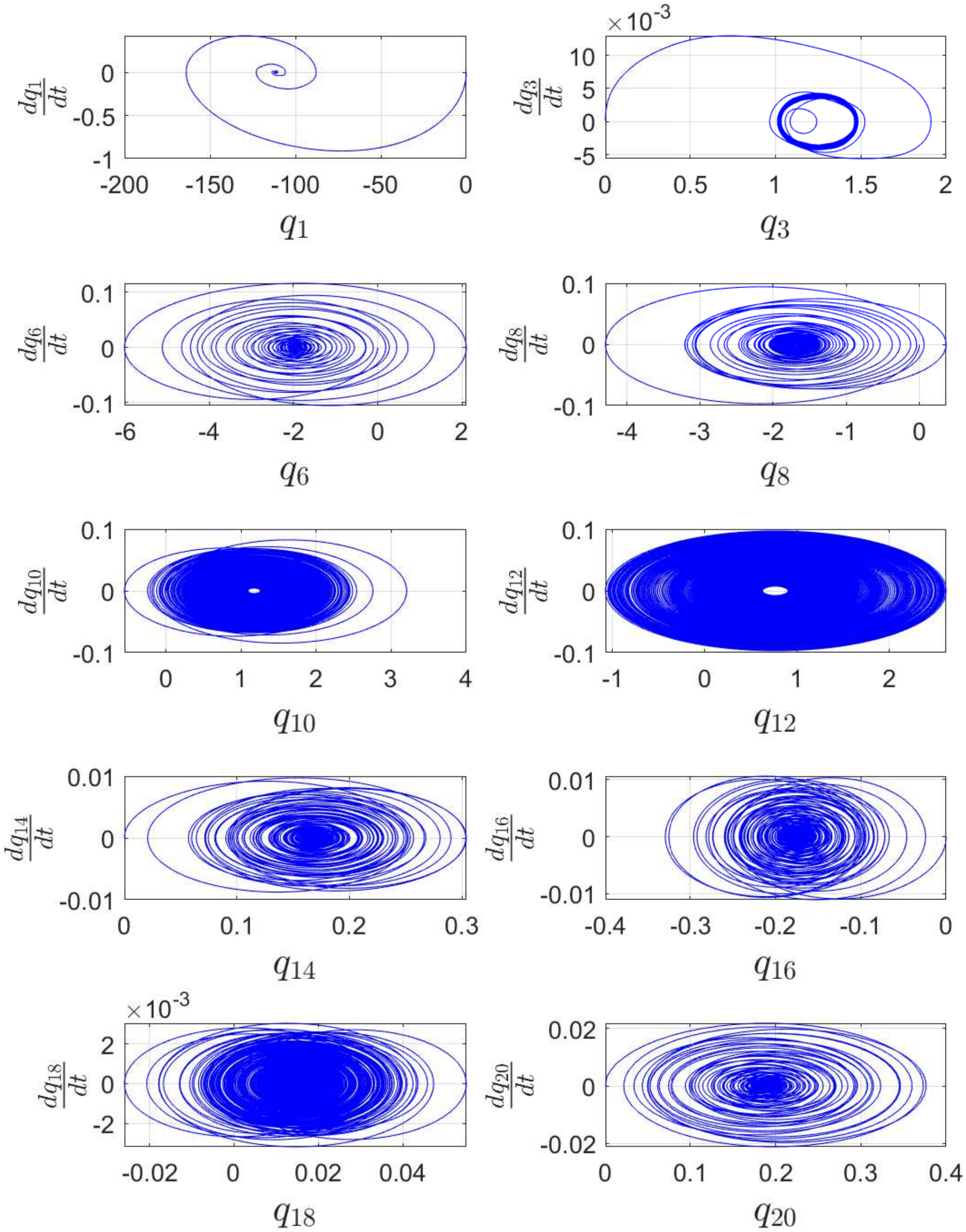

Figure 5.18: At critical speed $V_\infty = 156\,\mathrm{m/s}$, projections in phase planes of modes corresponding to the left joined-wing for the case with no structural damage and freestream direction $(0°, 5°, 0°)$.

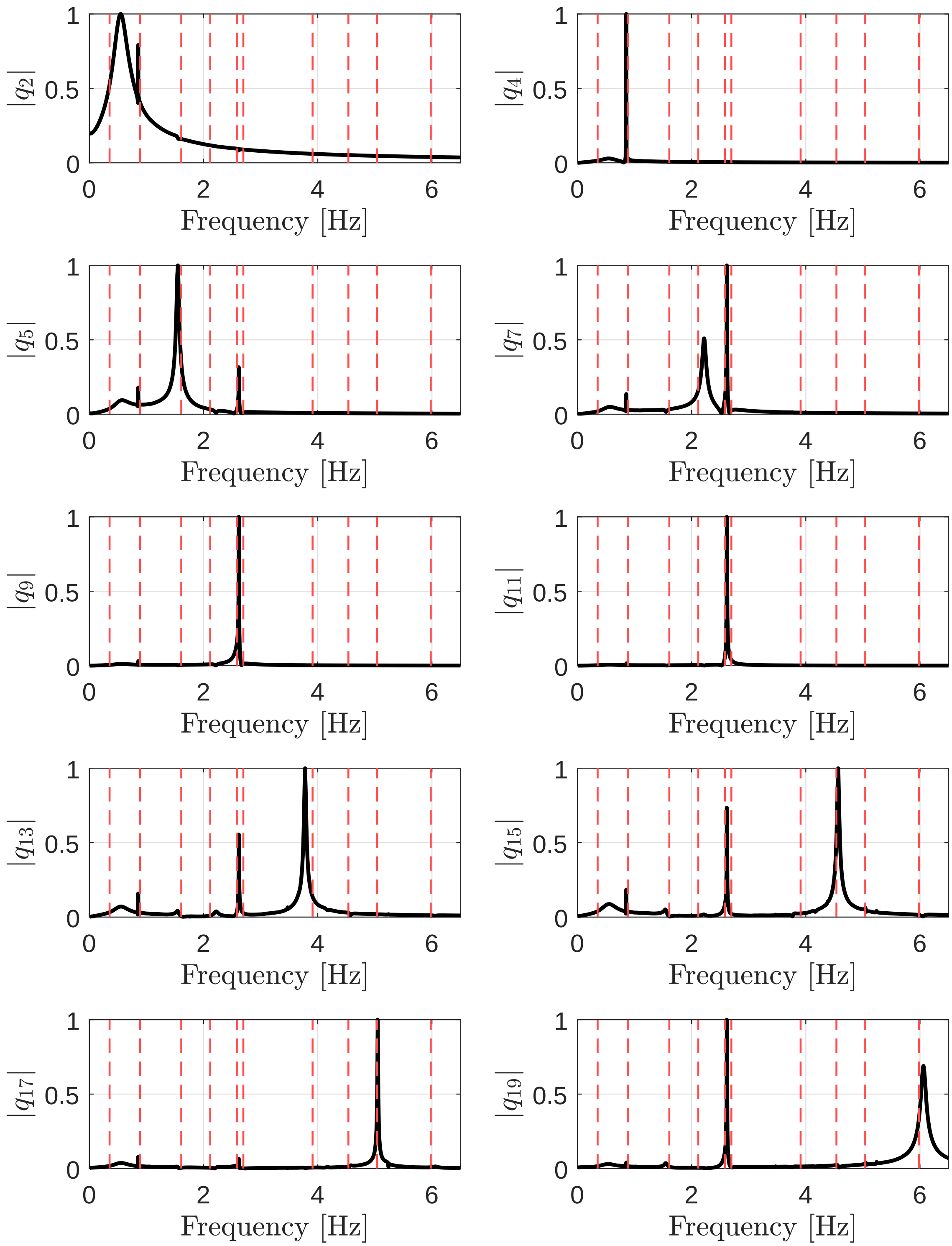

Figure 5.19: At critical speed $V_\infty = 156\,\mathrm{m/s}$, responses in the frequency domain of modes corresponding to the right joined-wing for the case with no structural damage and freestream direction $(0°, 5°, 0°)$.

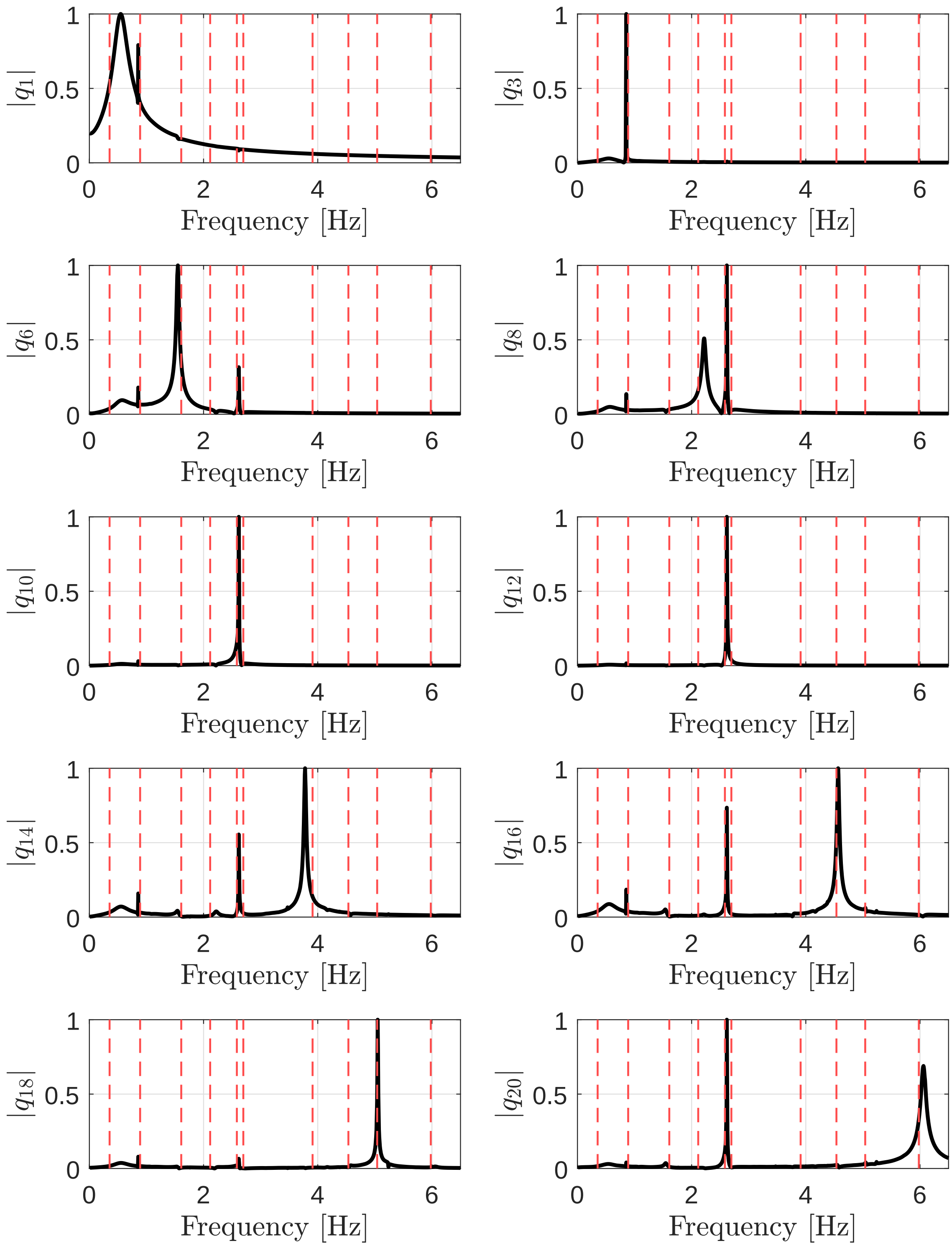

Figure 5.20: At critical speed $V_\infty = 156\,\mathrm{m/s}$, responses in the frequency domain of modes corresponding to the left joined-wing for the case with no structural damage and freestream direction $(0°, 5°, 0°)$.

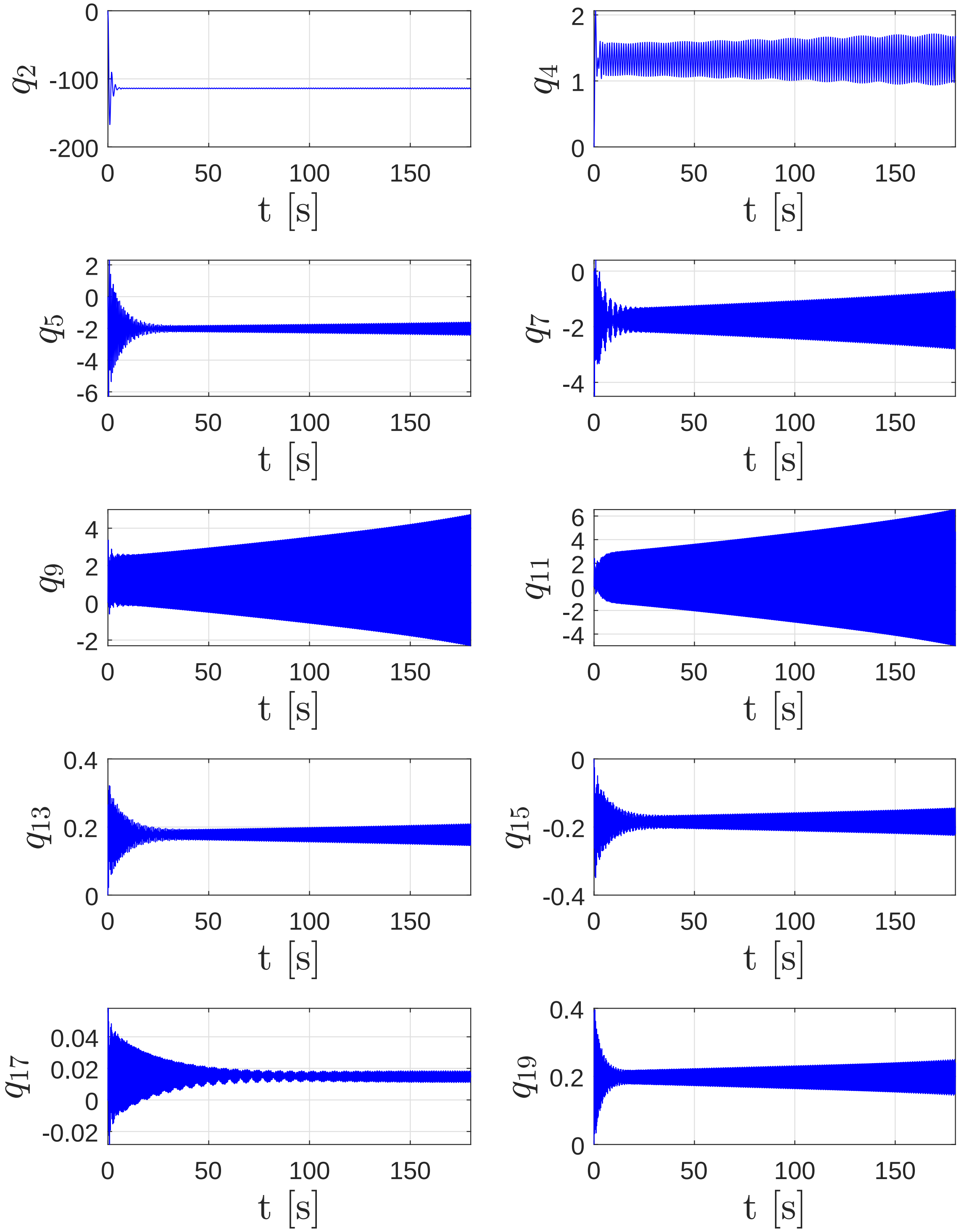

Figure 5.21: Time responses of modes corresponding to the right joined-wing for the case with no structural damage at supercritical speed $V_\infty = 160\,\mathrm{m/s}$ and freestream direction $(0°, 5°, 0°)$.

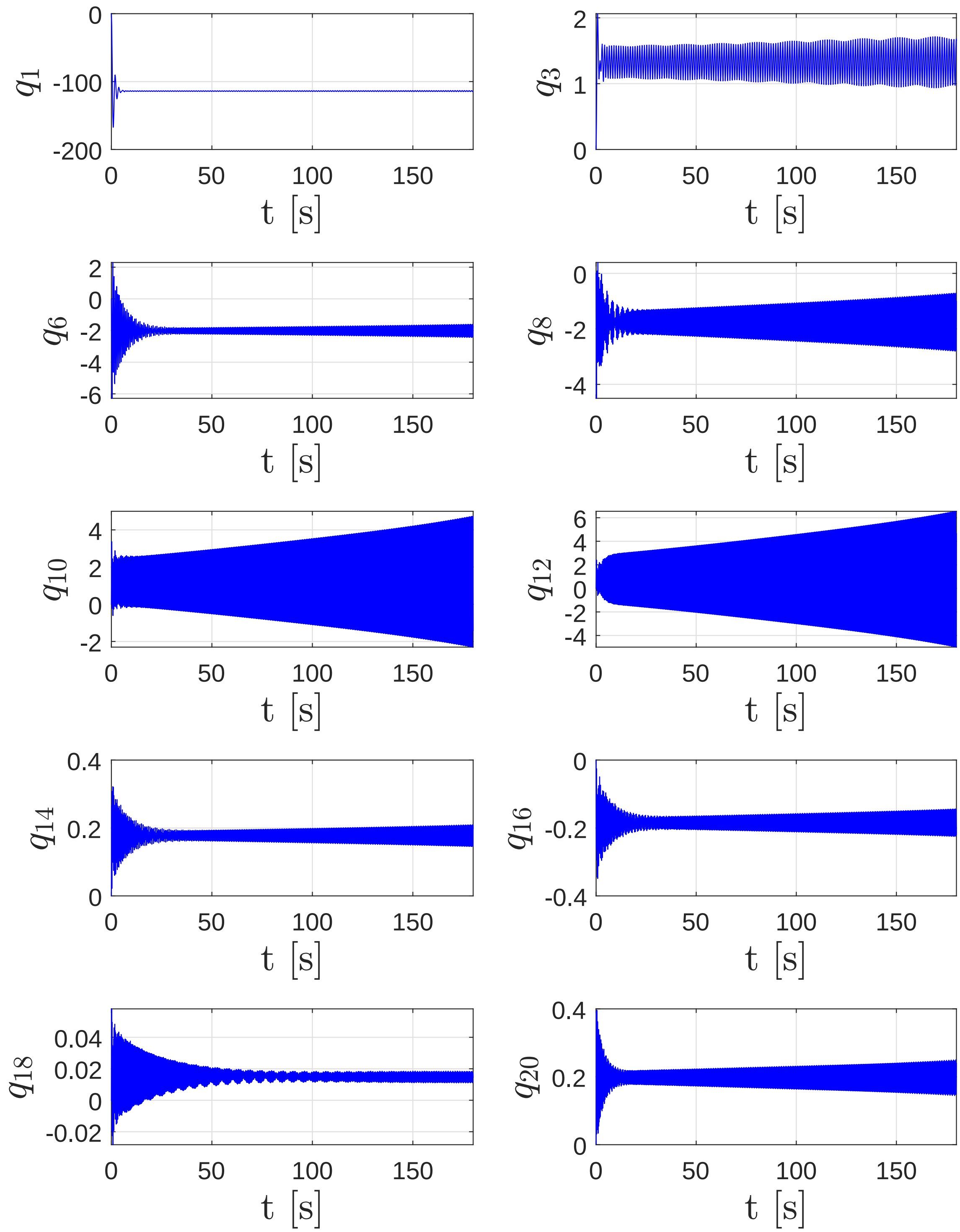

Figure 5.22: Time responses of modes corresponding to the left joined-wing for the case with no structural damage at supercritical speed $V_\infty = 160\,\mathrm{m/s}$ and freestream direction $(0°, 5°, 0°)$.

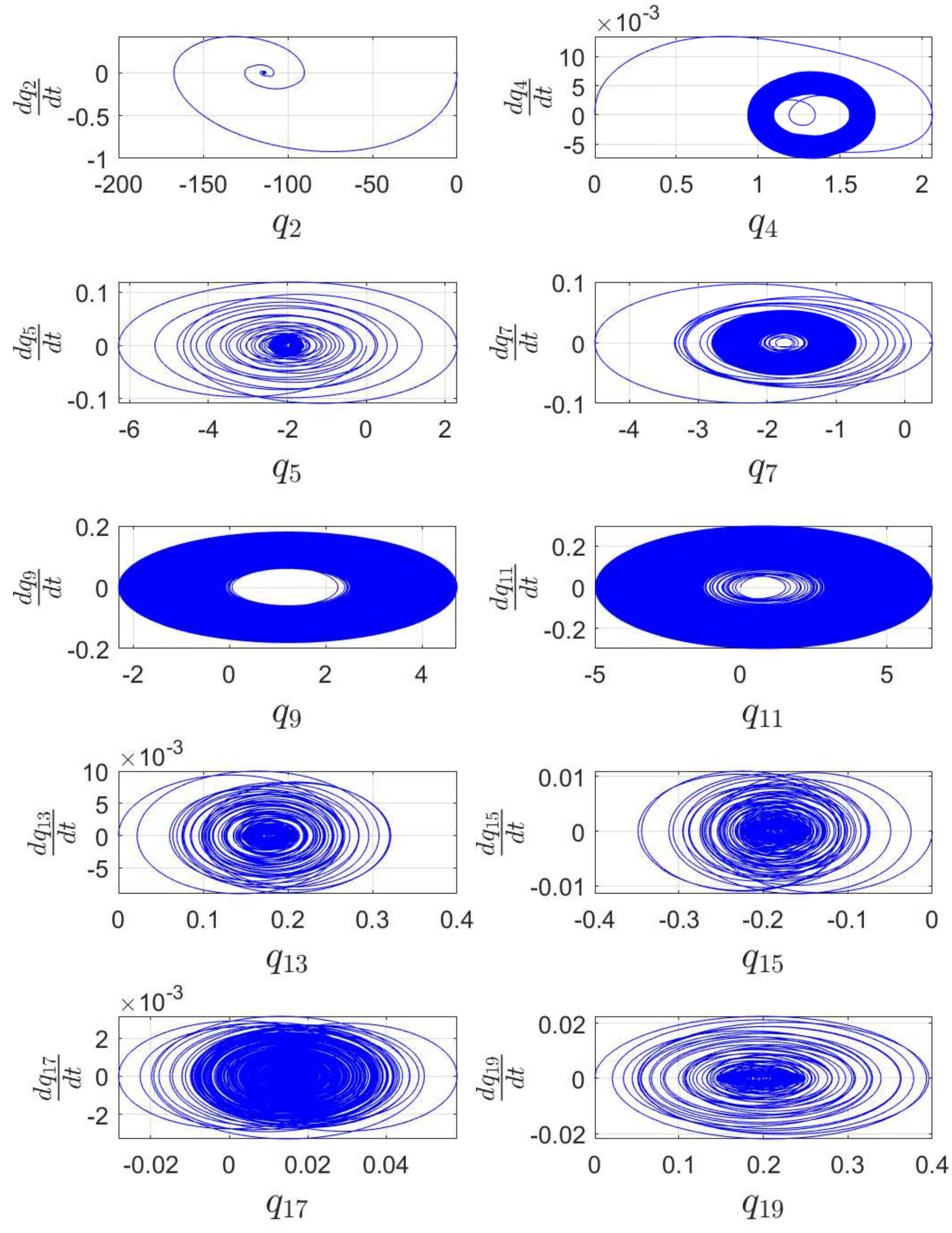

Figure 5.23: At supercritical speed $V_\infty = 160\,\mathrm{m/s}$, projections in phase planes of modes corresponding to the right joined-wing for the case with no structural damage and freestream direction $(0^\circ, 5^\circ, 0^\circ)$.

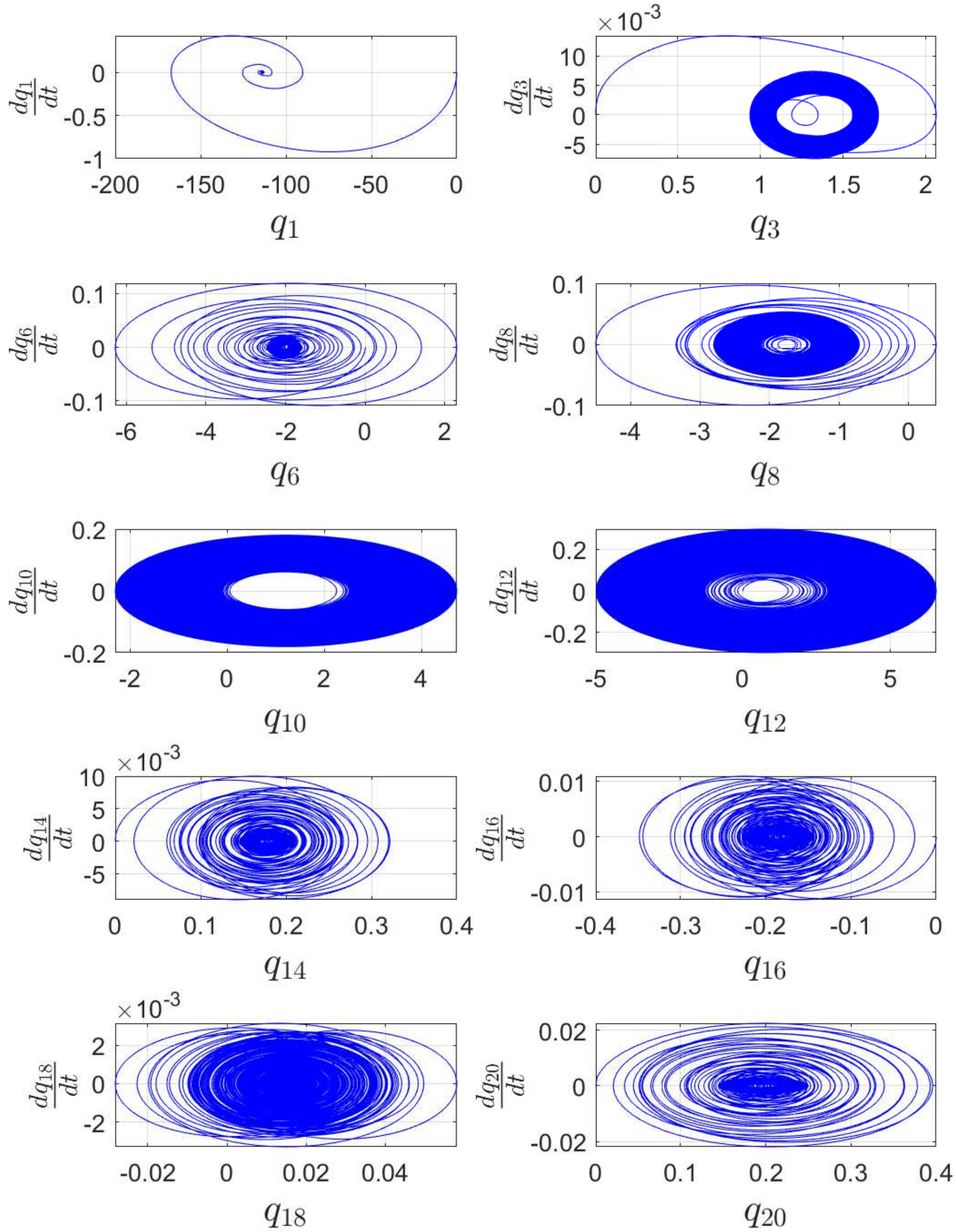

Figure 5.24: At supercritical speed $V_\infty = 160\,\mathrm{m/s}$, projections in phase planes of modes corresponding to the left joined-wing for the case with no structural damage and freestream direction $(0°, 5°, 0°)$.

corresponding to the right joined-wing and the left joined-wing, respectively, are presented. The free vibration frequencies are marked in the figures by dashed red lines. Except for the first, second, and ninth modes of each joined-wing, a predominant frequency of 2.615 Hz can be observed.

5.2.1.2 Freestream Direction: $(0°, 10°, 0°)$

In the second case of no damage to the structure, the freestream direction is given by a yaw angle of 0°, a pitch angle of 10°, and a roll angle of 0°. Over 20 different simulations were ran to determine the critical flutter speed. For this case, the critical flutter speed was predicted to be 153 m/s. This can be observed in the bifurcation diagrams of of the modes representing vibrations of the right joined-wing, shown in Figure 5.27, and the modes representing vibrations of the left joined-wing, shown in Figure 5.28. After the critical flutter speed (indicated by the red marker), the amplitudes of the limit cycles start to grow gradually with respect to the freestream speed. From the two cases studied, one can infer that the higher the pitch angle of the freestream direction, the lower the critical flutter speed would be. The predicted critical flutter speed with freestream direction $(0°, 10°, 0°)$ is 1.923% lower compared to the predicted critical flutter speed with freestream direction $(0°, 5°, 0°)$. The results for this case are presented in Appendix D.

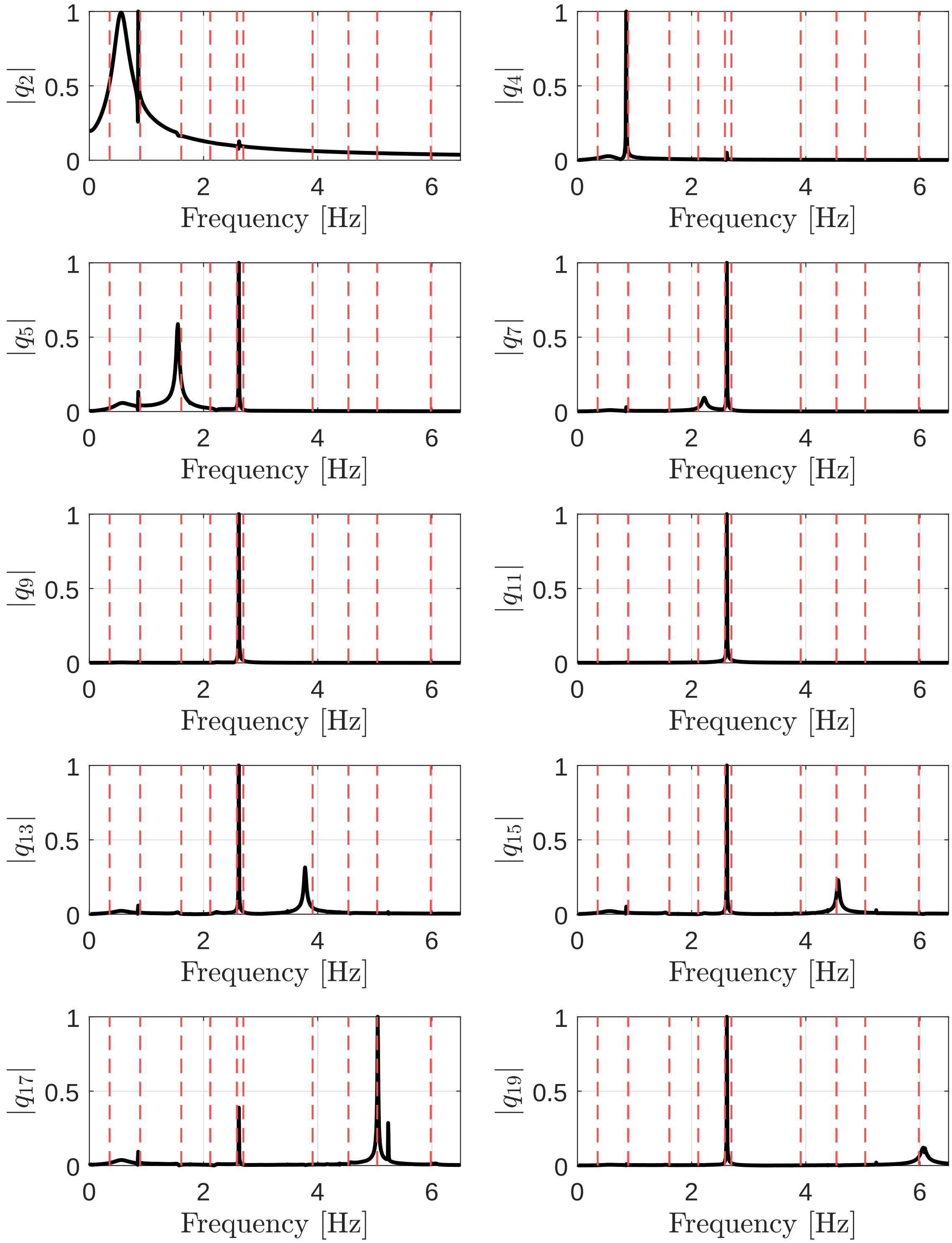

Figure 5.25: At supercritical speed $V_\infty = 160\mathrm{m/s}$, responses in the frequency domain of modes corresponding to the right joined-wing for the case with no structural damage and freestream direction $(0°, 5°, 0°)$.

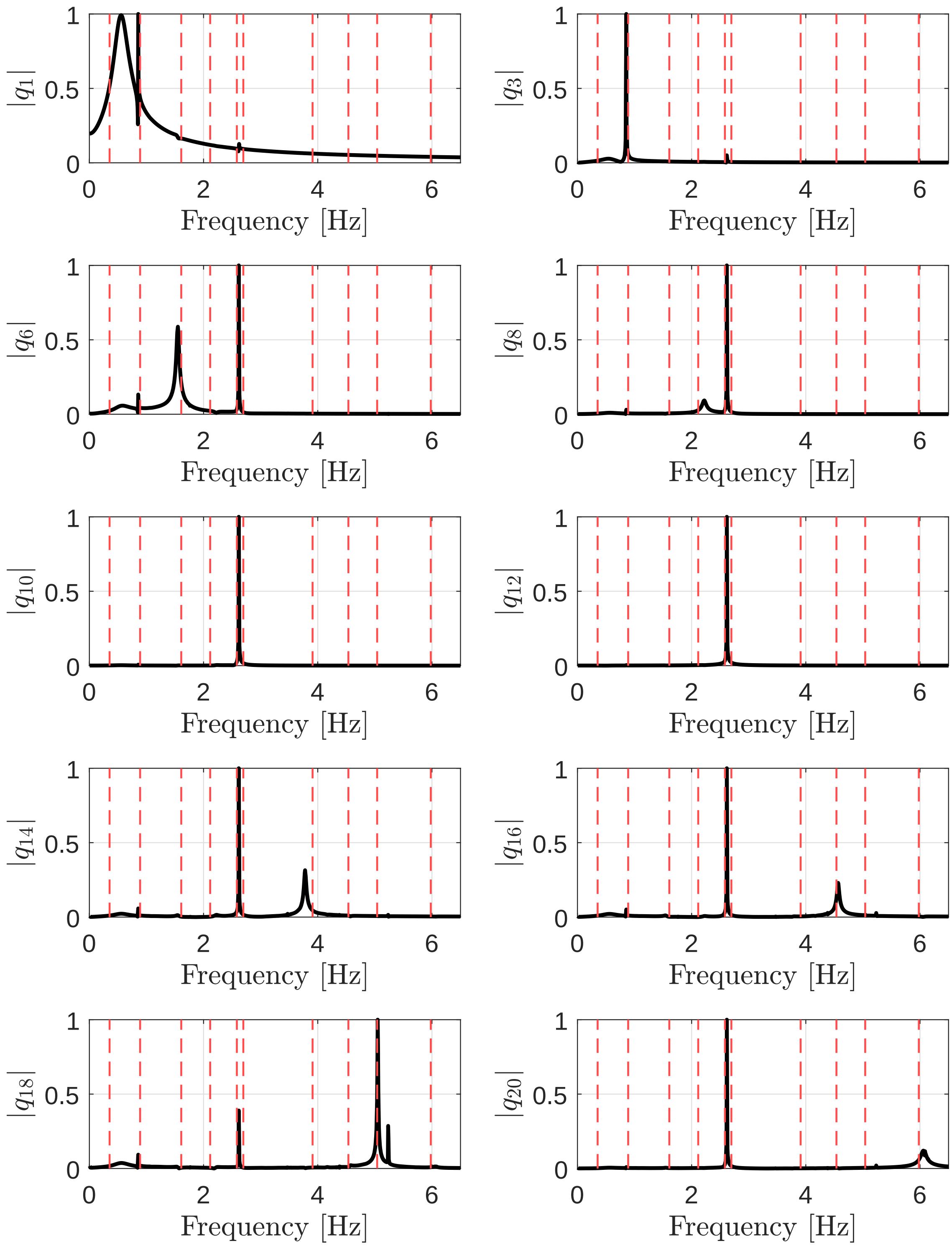

Figure 5.26: At supercritical speed $V_\infty = 160\text{m/s}$, responses in the frequency domain of modes corresponding to the left joined-wing for the case with no structural damage and freestream direction $(0°, 5°, 0°)$.

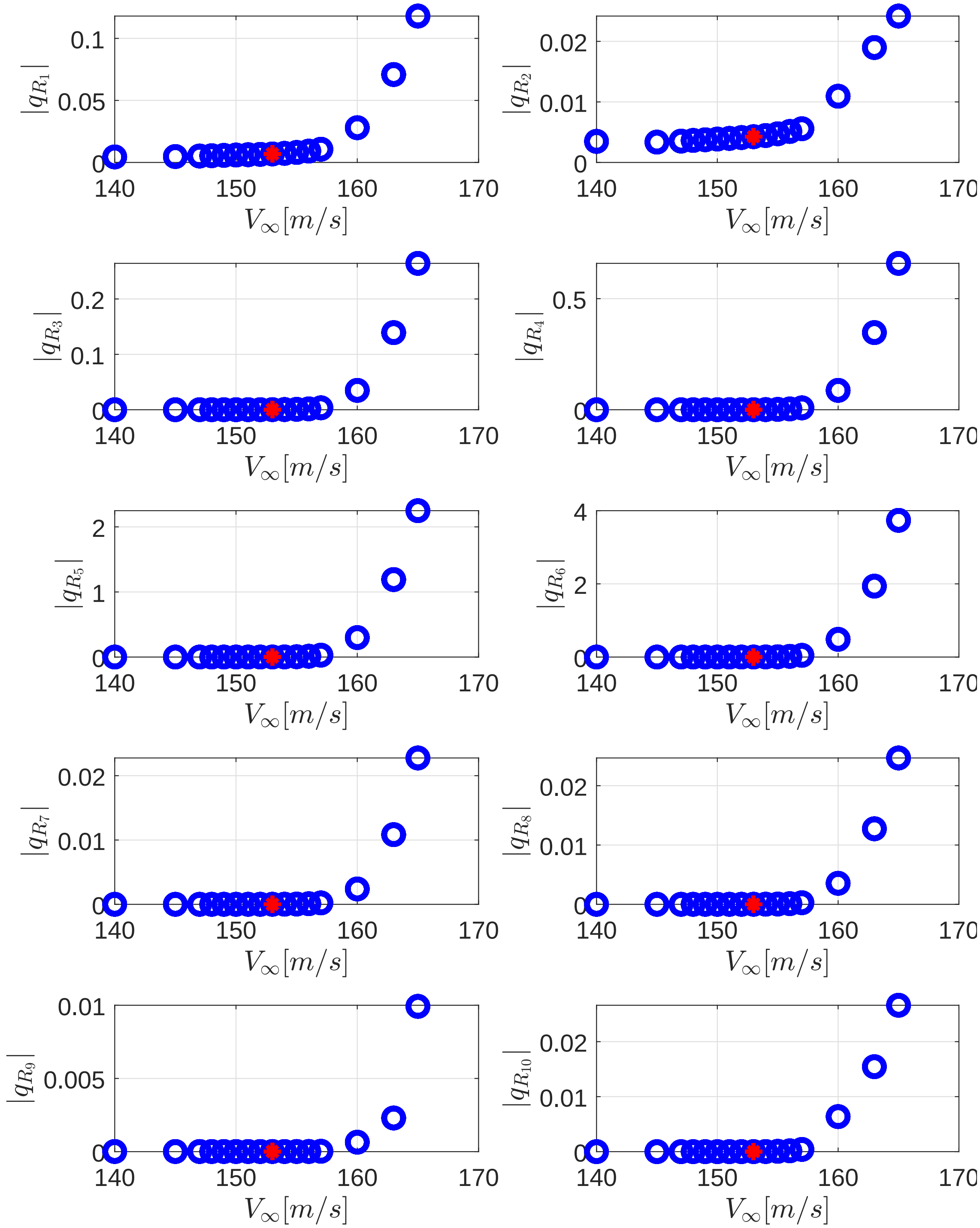

Figure 5.27: Bifurcation diagram constructed with $(0°, 10°, 0°)$ freestream direction and freestream speed as a control parameter. Responses of modes corresponding to the right joined-wing of the undamaged structure are shown.

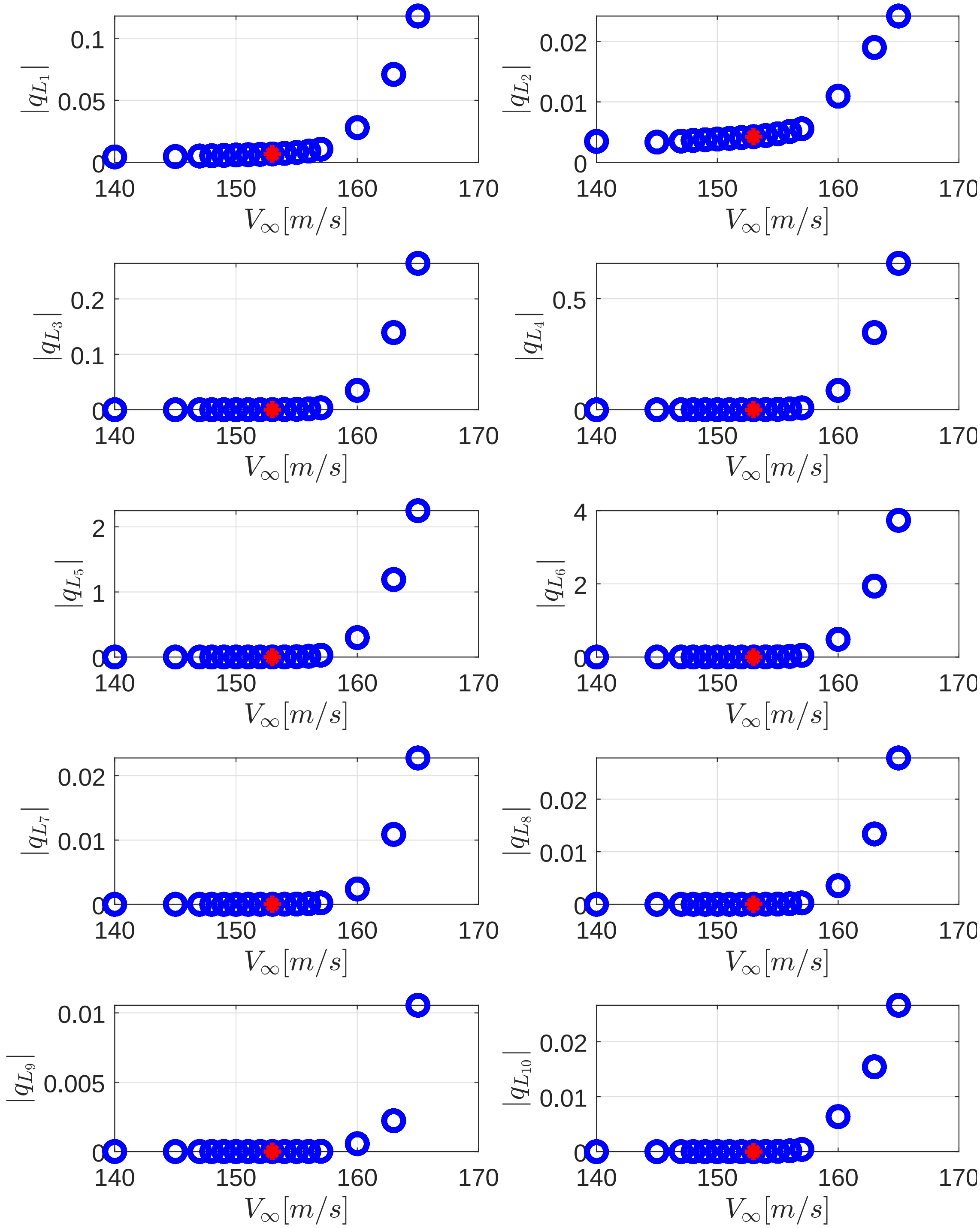

Figure 5.28: Bifurcation diagram constructed with $(0°, 10°, 0°)$ freestream direction and freestream speed as a control parameter. Responses of modes corresponding to the left joined-wing of the undamaged structure are shown.

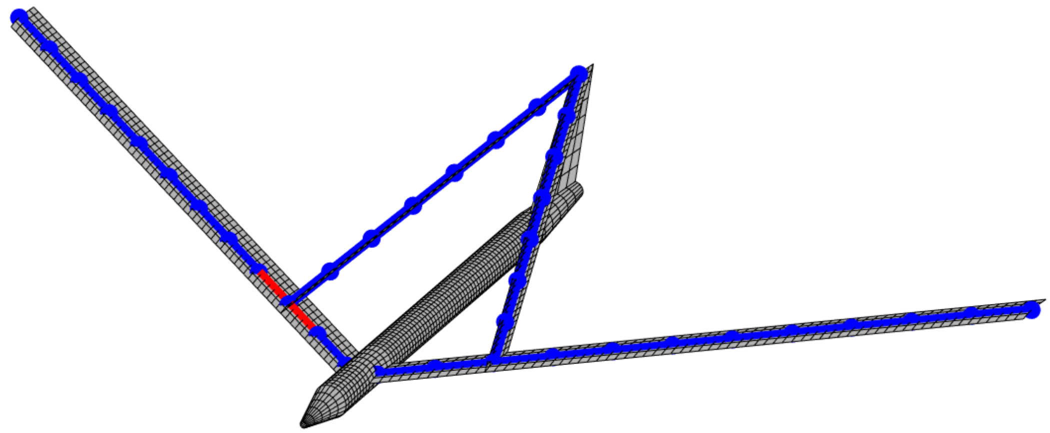

Figure 5.29: Structural beam model with damaged elements.

5.2.2 Cases with Damage

The critical flutter speeds of the joined-wing aircraft are predicted via the aeroelastic simulations for the two cases with damage in this section. For this work, two cases of damage are considered: 1) damage leading to reduction in bending stiffness (10% reduction in the polar moment of inertia, I_p); and 2) damage leading to reduction in torsion stiffness (10% reduction in the torsion constant, J_T). The damage is applied at the same location for both cases. As shown in Figure 5.29, the damaged elements of the structural beam are the right forward wing elements that share a nodal point with the right aft wing. In this case study, the geometric cross-sectional properties are alternated in the damaged region. The freestream direction is given by a yaw angle of 0°, a pitch angle of 5°, and a roll angle of 0°.

5.2.2.1 Damage Case with Loss of Bending Stiffness

In the first case, damage is considered in the two elements of the right forward wing that are connected to the right aft wing, as shown in Figure 5.29. The damage

Table 5.4: Cross-sectional properties of section of structural model with 10% bending damage

A [m^2]	I_y [m^4]	I_z [m^4]	I_p [m^4]	J_T [m^4]
1.744×10^{-2}	3.303×10^{-4}	7.576×10^{-3}	7.116×10^{-1}	1.055×10^{-3}

Table 5.5: First 20 natural frequencies of structural system with 10% bending damage

Mode i	Undamaged Frequency f_i [Hz]	Damaged Frequency f_i [Hz]	Percentage Difference
1	0.370	0.370	0.000
2	0.370	0.370	0.000
3	0.868	0.869	0.074
4	0.868	0.869	0.074
5	1.548	1.548	0.003
6	1.548	1.548	0.003
7	2.215	2.217	0.070
8	2.215	2.217	0.070
9	2.530	2.540	0.405
10	2.530	2.540	0.405
11	2.666	2.671	0.171
12	2.666	2.671	0.171
13	3.769	3.790	0.559
14	3.769	3.790	0.559
15	4.583	4.598	0.329
16	4.583	4.598	0.329
17	5.047	5.051	0.087
18	5.047	5.051	0.087
19	6.057	6.082	0.420
20	6.057	6.082	0.420

is represented by decreasing the polar moment of inertia I_p from Table 3.2 by 10%. This change can be seen in Table 5.4. The adjustment of I_p affected the mass matrix and caused the natural frequencies to slightly increase, which can be seen in Table 5.5. The modes appear unchanged from the no damage case which appear in Chapter 3 and Appendix B. This is to be expected as the magnitude of the damage is smaller than the wavelengths associated with the modes.

The freestream direction is given by a yaw angle of 0°, a pitch angle of 5°, and a roll angle of 0°. Over 20 different simulations were run to determine the critical flutter speed. For this case, the critical flutter speed was predicted to be 150 m/s. This can be observed in the bifurcation diagrams of of the modes representing vibrations of the right joined-wing, shown in Figure 5.30, and the modes representing vibrations of the left joined-wing, shown in Figure 5.31. After the critical flutter speed (indicated by the red marker), the amplitudes of the limit cycles start to grow gradually with increase in the freestream speed. From this case study, with the structural damage leading to a reduction in the polar moment of inertia, the critical flutter speed is found to decrease compared to the case with no damage for the chosen freestream direction $(0°, 5°, 0°)$. The critical flutter speed decreased by 3.846% compared to the corresponding value for the case with no structural damage. Additional results for this case are presented in Appendix D.

5.2.2.2 Damage Case with Loss of Torsional Stiffness

In the second case, damage is considered in the two elements of the right forward wing that are connected to the right aft wing, as shown in Figure 5.29. The considered damage results in a decrease of the torsion constant J_T from Table 3.2 by 10%. This change can be seen in Table 5.6. The adjustment of J_T affected the stiffness matrix and caused the natural frequencies to slightly decrease, which can be seen in Table 5.7. The modes appear unchanged from those obtained in the case with no damage; these are shown in Chapter 3 and Appendix B.

The freestream direction is given by a yaw angle of 0°, a pitch angle of 5°, and a

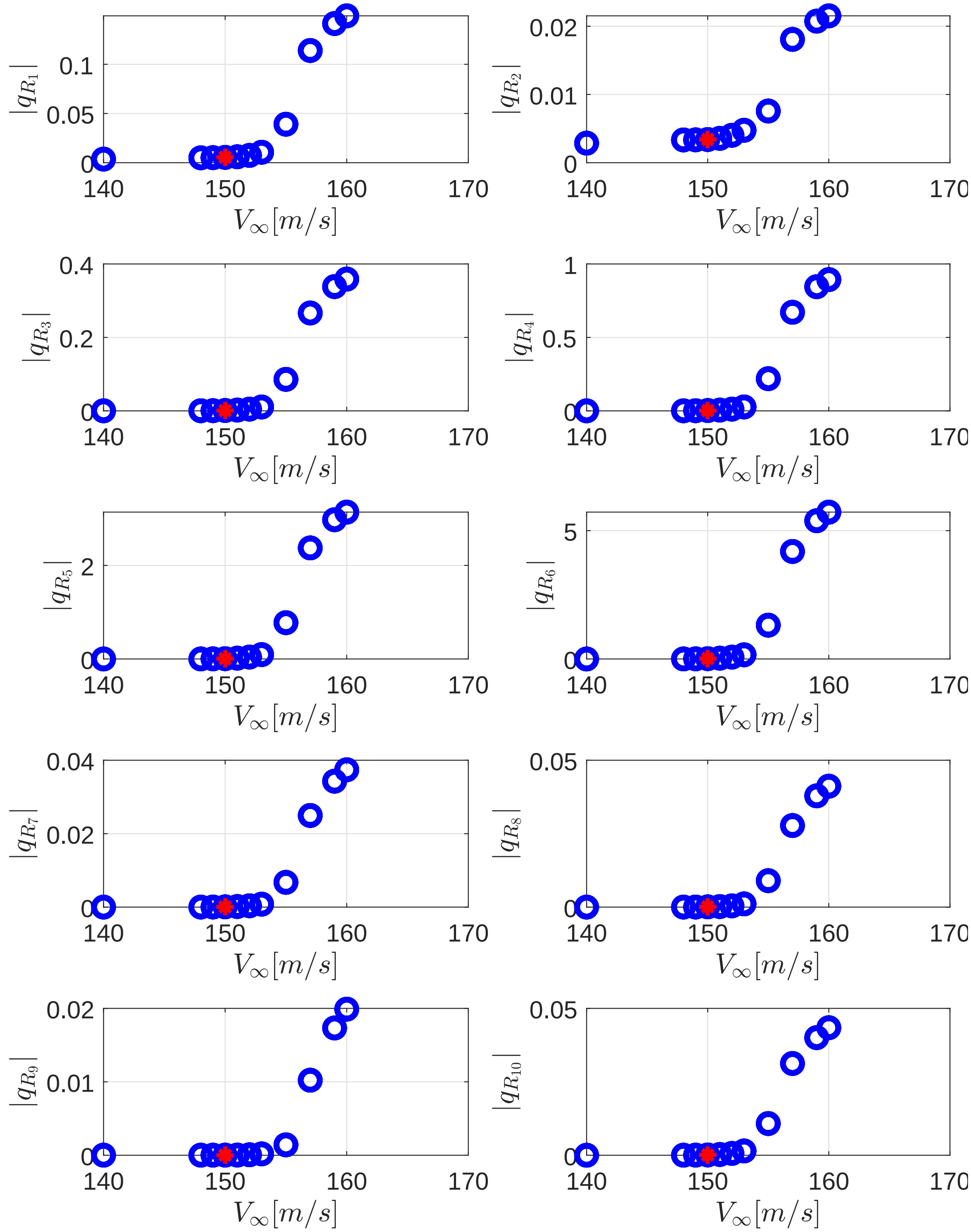

Figure 5.30: Bifurcation diagram constructed with $(0°, 5°, 0°)$ freestream direction and freestream speed as a control parameter. Responses of modes corresponding to the right joined-wing of the structure with 10% bending damage are shown.

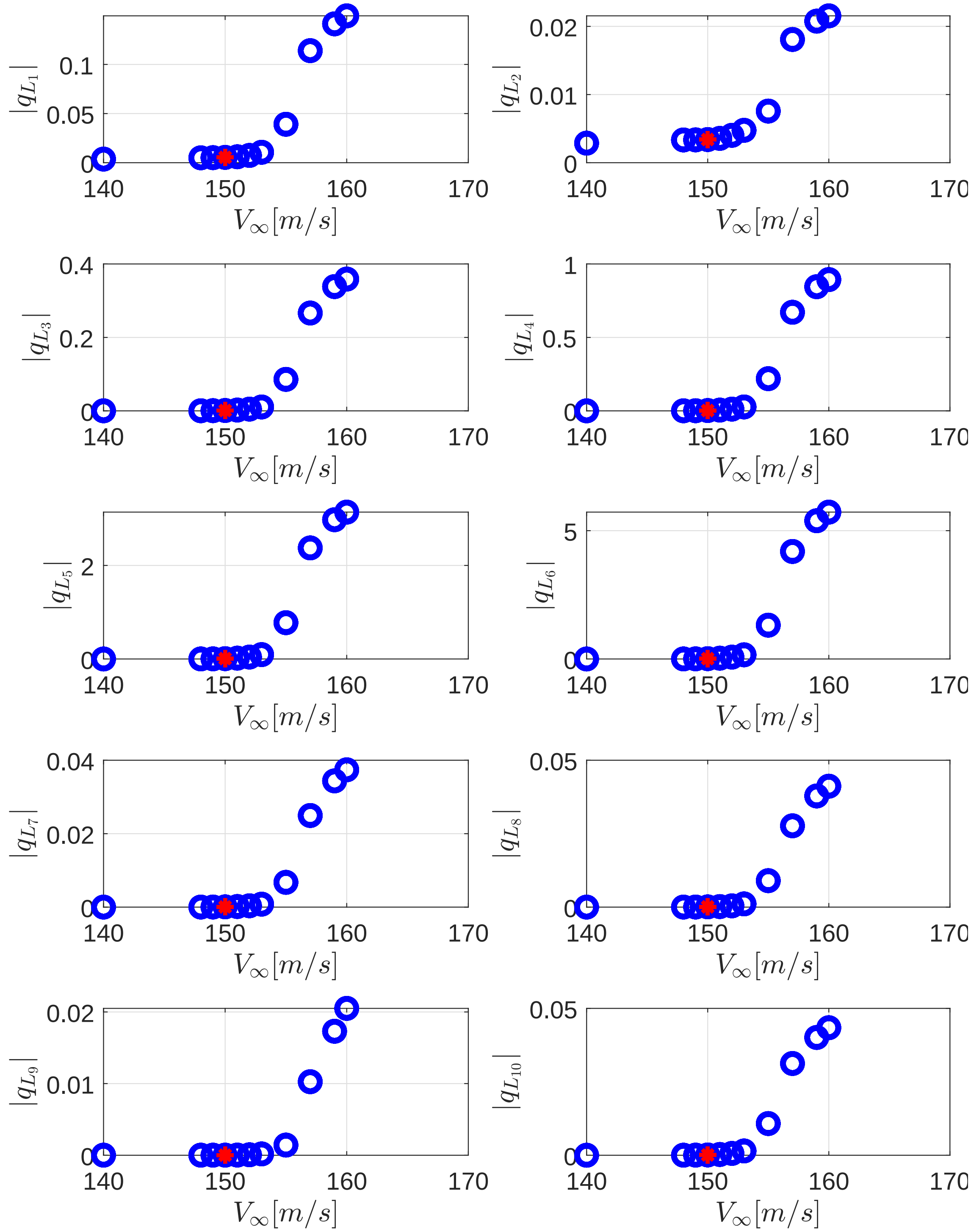

Figure 5.31: Bifurcation diagram constructed with $(0°, 5°, 0°)$ freestream direction and freestream speed as a control parameter. Responses of modes corresponding to the left joined-wing of the structure with 10% bending damage are shown.

Table 5.6: Cross-sectional properties of section of structural model with 10% torsional damage

A [m^2]	I_y [m^4]	I_z [m^4]	I_p [m^4]	J_T [m^4]
1.744×10^{-2}	3.303×10^{-4}	7.576×10^{-3}	7.907×10^{-1}	9.498×10^{-4}

Table 5.7: First 20 natural frequencies of structural system with 10% torsional damage

Mode i	Undamaged Frequency f_i [Hz]	Damaged Frequency f_i [Hz]	Percentage Difference
1	0.370	0.370	-0.023
2	0.370	0.370	-0.023
3	0.868	0.857	-1.309
4	0.868	0.857	-1.309
5	1.548	1.548	-0.007
6	1.548	1.548	-0.007
7	2.215	2.214	-0.069
8	2.215	2.214	-0.069
9	2.530	2.518	-0.457
10	2.530	2.518	-0.457
11	2.666	2.660	-0.248
12	2.666	2.660	-0.248
13	3.769	3.758	-0.308
14	3.769	3.758	-0.308
15	4.583	4.577	-0.120
16	4.583	4.577	-0.120
17	5.047	5.025	-0.435
18	5.047	5.025	-0.435
19	6.057	6.052	-0.076
20	6.057	6.052	-0.076

roll angle of 0°. Over 20 different simulations were run to determine the critical flutter speed. For this case, the critical flutter speed was predicted to be 156 m/s. This can be observed in the bifurcation diagrams of of the modes representing vibrations of the right joined-wing, shown in Figure 5.32, and the modes representing vibrations of the left joined-wing, shown in Figure 5.33. After the critical flutter speed (indicated by the red marker), the amplitudes of the limit cycles start to grow gradually with respect to the freestream speed. This is an interesting result given that in the case of no structural damage and freestream direction $(0°, 5°, 0°)$, the critical flutter speed was also predicted to be 156m/s. This could mean that in the case of damage with loss of torsional stiffness, the change in J_T may have to be greater than 10% or the damage has to occur in a different location, to see a difference from the case with no damage. Additional results for this case are shown in Appendix D.

5.3 Summary

In this chapter, the simulation results obtained with the accelerated computational aeroelastic model are presented. The capability of the computational aeroelastic model to predict the critical flutter speed was verified with a benchmark problem from the literature. The critical flutter speed of the joined-wing aircraft for cases of no structural damage and freestream directions $(0°, 5°, 0°)$ and $(0°, 10°, 0°)$ are obtained. In addition, the critical flutter speed for the cases of structural bending and torsional damage were also determined. The results for the no structural damage cases indicated that in the case of symmetric freestream flow, the higher the

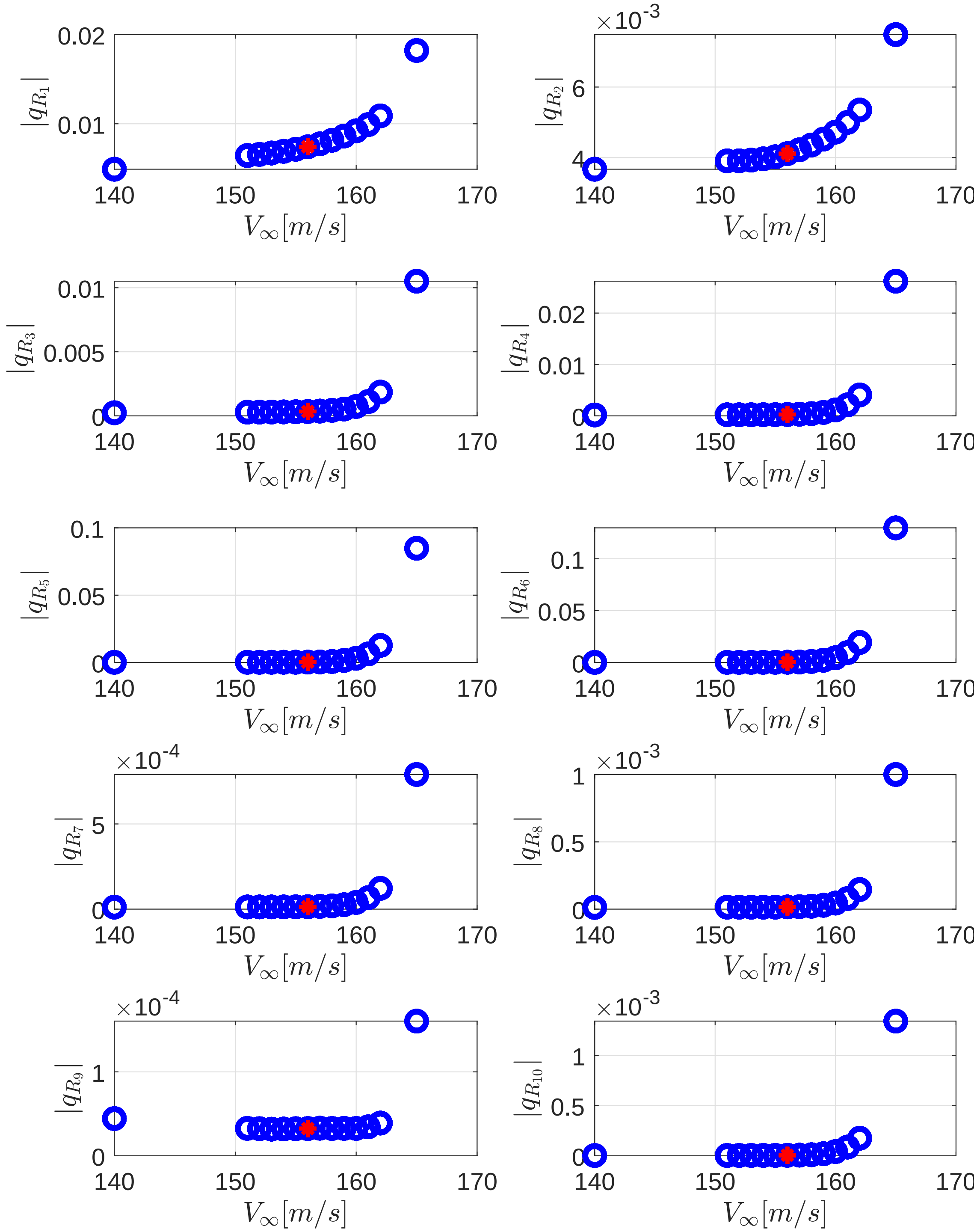

Figure 5.32: Bifurcation diagram constructed with $(0°, 5°, 0°)$ freestream direction and freestream speed as a control parameter. Responses of modes corresponding to the right joined-wing of the structure with 10% torsion damage are shown.

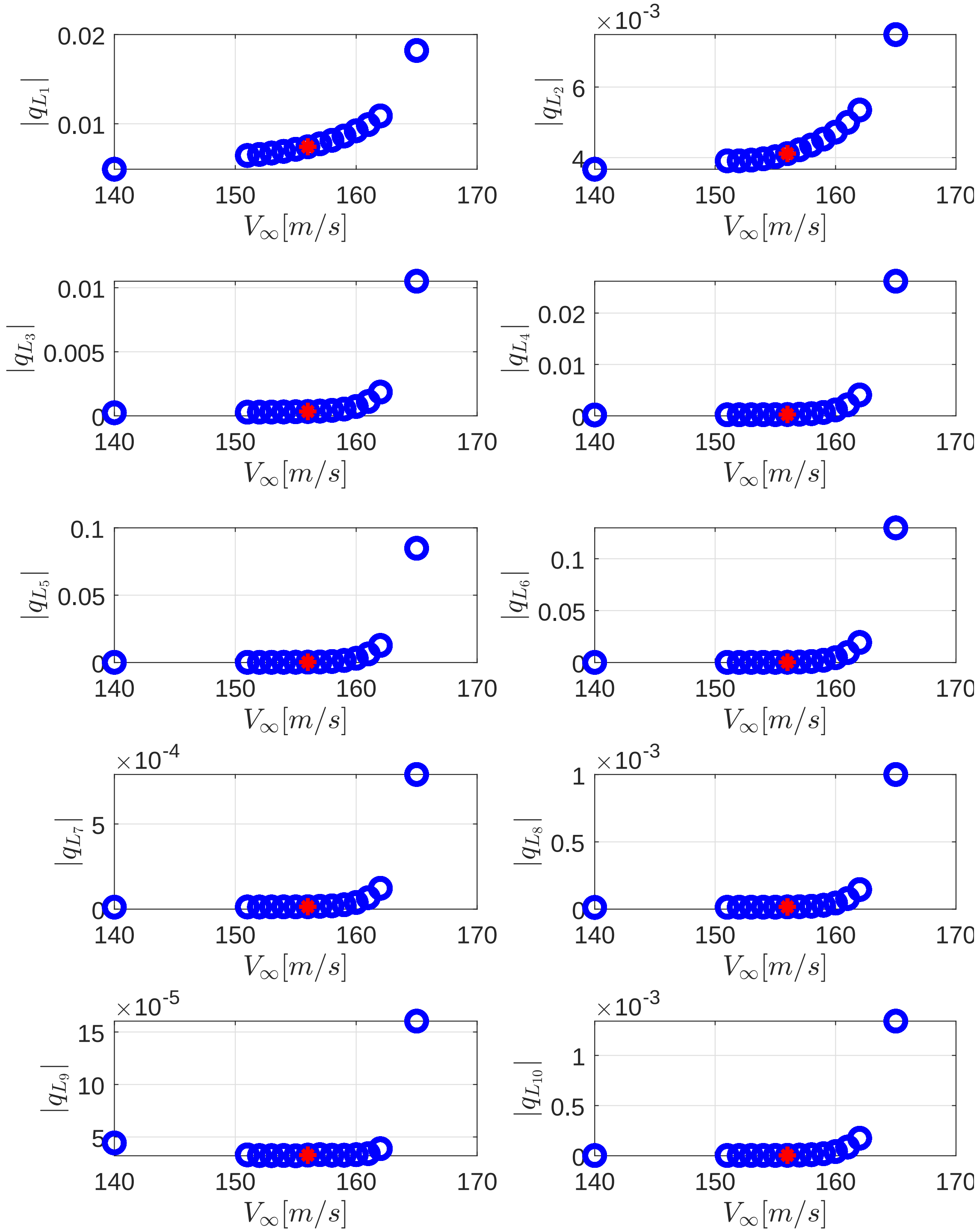

Figure 5.33: Bifurcation diagram constructed with $(0°, 5°, 0°)$ freestream direction and freestream speed as a control parameter. Responses of modes corresponding to the left joined-wing of the structure with 10% torsion damage are shown.

pitch angle, the lower the predicted critical flutter speed would be. With damage located on the elements of the right forward wing that intersect with the right aft wing, damage with loss of bending stiffness (reduction in I_p) affects the structure's response more than that of damage with loss of torsional stiffness (reduction in J_T).

In the next chapter, the conclusions drawn from this dissertation work and stated, along with recommendations for future work.

Chapter 6: Conclusions and Recommendations for Future Work

In this chapter, the concluding remarks of the dissertation are presented. In Section 6.1, a summary of the accelerated nonlinear aeroelastic model developed in this dissertation is provided and results are highlighted. The main contributions of this dissertation are provided in Section 6.2. Finally, some possible future directions for the dissertation work are discussed in Section 6.3.

6.1 Summary

In this dissertation work, the author estimated the flutter boundary of the joined-wing aircraft for different structural health conditions and freestream directions. This is made possible by the construction of an nonlinear aeroelastic computational model. The aeroelastic model is composed of the FE based structural dynamics and the FMM accelerated UVLM based aerodynamic model. The implementation of the FMM accelerated UVLM based aerodynamic model is one of the first efforts of its kind. This includes a numerical tradeoff study, through which the tuning parameters of the FMM algorithm used in this dissertation have been examined. The settings for the tuning parameters of the FMM algorithm that provided the fastest computational speed while keeping the accuracy of the results upto a certain standard were determined. Based on the results of the numerical trade-off study, the accelerated aerodynamic model is found to significantly reduce the computational time required for the evaluation of velocity fields. Parallelization of the code further sped up the aerodynamic model computations. Furthermore, the aerodynamic model can take into account non-symmetric freestream flows.

An FE based structural dynamics model is developed for the joined-wing aircraft. This model allows for inclusion of damage on the joined-wings. The location and magnitude of the damage can be specified depending on the type of damage that needs to be modeled. Rigid-body motions can be taken into account for structural model through the use of MFCs.

To integrate the FMM accelerated UVLM based aerodynamic model and the FE based structural dynamics model, a co-simulation framework is utilized. The aerodynamic mesh and structural grid are coupled via interpolation matrices that are used to transfer displacements and forces between the two models. The methodology used for solving the equations of motion of the system ensures that there is always a reasonable agreement between the aerodynamic mesh and the structural grid.

Based on the results obtained by using the accelerated nonlinear aeroelastic computational model, some preliminary statements can be made about how the flutter boundary of the joined-wing aircraft changes due to varying the freestream direction and consideration of structural damage. The results for the no structural damage cases indicate that the higher the pitch angle, the lower the predicted critical flutter speed. Fr the considered cases of structural damage, the joined-wing structure with damage due to loss of bending stiffness experiences flutter at a lower freestream speed compared to the joined-wing structure with damage due to loss of torsional stiffness. However, this needs further investigations.

The co-simulation framework utilized for this dissertation is broad and can be used with different aerodynamics and structural dynamics models. The most important component of the co-simulation approach is integration of the different models through the exchanging of the states of the models at predefined time instances. Thus, to implement the co-simulation framework for different models, a new methodology for transferring model information and integrating the equations of motion will need to be developed. It should be noted that the accelerated aeroelasticity approach developed for this dissertation can be applied to other problems with different aircraft. Thus, the type of flutter analysis presented in this dissertation is applicable to other UASs operating under subsonic flow conditions.

6.2 Dissertation Contributions

The contributions of this work are as follows:

- An accelerated computational aerodynamic model based on the implementation of the FMM with the UVLM based nonlinear, unsteady aerodynamic model has been developed. This is one of the first studies in which the integration of the FMM and UVLM based aerodynamic model has been explored. The speedup capabilities of the accelerated aerodynamic model was tested through a numerical tradeoff study. The computational model was also parallelized to take advantage of multi-threading capable technology. Research question **RQ1** is addressed with this work that is presented in Chapter 2.

- The construction of a joined-wing aircraft FE structural dynamics model that can take into account rigid-body motions and damage on the joined-wings has been carried out. To the best of the author's knowledge, the joined-wing aircraft computational structural models in the literature do not account for damage in the structure. This study allows for the investigation of how damage can affect the flight performance of the joined-wing aircraft. Research question **RQ2** is addressed with this work that is presented in Chapter 3.

- The construction of a nonlinear aeroelastic computational model for the joined-wing aircraft via the FMM accelerated UVLM based aerodynamic model and the FE structural model has been carried out for the first time. With the aforementioned aeroelastic model, a better understanding of the nonlinear aeroelastic behavior of the joined-wing aircraft can be attained. Studies in the literature focus more on the static nonlinear aeroelastic behavior of the joined-wing aircraft as opposed to what has been done in this work. Research questions **RQ3** and **RQ4** are addressed with this work that is presented in Chapters 4 and 5.

6.3 Directions for Future Work

The work presented in this dissertation can be considered a starting point for the larger objective of gaining a thorough understanding of the nonlinear aeroelastic behavior of the joined-wing aircraft. Given the current aeroelastic computational abilities, more simulations can be run to determine the critical flutter speed for various freestream directions. This will include cases wherein the freestream flow is not strictly symmetric (i.e., the yaw and/or roll angles of the freestream direction are not set to zero). Also, the effect of damage at different locations and of different magnitudes on the joined-wings can be investigated further. The flutter boundaries for different joined-wing aircraft configurations can also be determined. Different structural configurations of the joined-wing aircraft will affect the aeroelasticity of the system and through that the flutter boundaries can be affected. With this information, it will be possible to study how structural instability and nonlinear aeroelasticity can influence the design of the joined-wing aircraft configuration. To improve the current computational aeroelastic model, the computational structural dynamics model can be modified to include the geometric stiffness and determine the buckling loads in the structure.

For real-time decision support purposes, the accelerated nonlinear aeroelastic simulation developed in this dissertation is not fast enough. The computational aeroelastic model alone lacks information on current flight conditions needed to relate simulations results to the physical system. This could be addressed through the integration of simulation and sensor data via the DDDAS paradigm. The DDDAS paradigm can be used to produce data with accuracy comparable to the accelerated nonlinear aeroelastic simulation and instantaneous information available from sensor data. With this combination, online operation and control of the joined-wing UAS can be enabled.

Appendix A: Sample Parallelizable Code

While the code the produces the mode shapes and natural frequencies of the computational structural model is written in MATLAB, the program for the computational aeroelastic model is written in Fortran. This mainly includes the aerodynamic model procedures described in Chapter 2. In this appendix, portions of the program that benefited the most from parallelization are presented.

A.1 Aerodynamic Influence Matrix

Due to the inclusion of the full aerodynamic geometry, the aerodynamic influence matrix is quite large as shown in equation (2.21). Since the aerodynamic influence matrix has to be formed during each iteration of every timestep, this process is computationally expensive for very refined meshes. Given components n and m, the following code can be used to obtain the $\mathbf{A}_{mn}$ submatrix. It should be noted that this process needs to be performed 7^2 times per iteration in a timestep. Parallelizing this portion of the code helped reduced the computational workload.

```
!!!!!!!!!!!!!!!!!!!!!!!!!!!!!!!!!!!!!!!!!!!!!!!!!!!!!!!!!!!!!!!!!!!!
! Submatrix [A_mn] : component m on component n
!!!!!!!!!!!!!!!!!!!!!!!!!!!!!!!!!!!!!!!!!!!!!!!!!!!!!!!!!!!!!!!!!!!!
do j = 1, NP_m
        do i = 1, NP_n
                A_mn( i, j ) = coeff( XYZ_m, GA_m, XYZCP_m, NORMAL_m,     &
                                      VS_m, NV_m, LM_m, i, j, NP_n, NP_m, &
                                      NN_m, delta )
```

```
        enddo
enddo
```

A.2 Wake Vortex Shedding

Until the predefined truncation number, the length of the wake grows. At each timestep, the new vortex segments and circulations need to be calculated. In the code, this procedure is carried out. NWAKE continues to increase until the truncation number is reached and so parallelizing the loops is of major benefit to the program.

```
GAWK_R( 1:7, 1:NVWK ) = 0.00D+00
GAWK_L( 1:7, 1:NVWK ) = 0.0D+00

p = 0

!!Forward Wing Trailing Edge Wake: Vertical Vortex Segments
! Inward edge
do i = 1, NWAKE
        k = p + i
        j = (i-1)*NCRTEFW+1
        m = (i-1)*(NCRTEFW+1)+1
        n = m+(NCRTEFW+1)

        GAWK_R(1,k) = GRTEFW(j)
        GAWK_L(1,k) = -1.0D+00*GLTEFW(j)

        GAWK_R(2:4,k) = XYZRTEFW(1:3, m) - XYZRTEFW(1:3, n)
        GAWK_L(2:4,k) = XYZLTEFW(1:3, m) - XYZLTEFW(1:3, n)

        GAWK_R(5:7,k) = XYZRTEFW(1:3, n) + 0.5D+00*GAWK_R(2:4,k)
        GAWK_L(5:7,k) = XYZLTEFW(1:3, n) + 0.5D+00*GAWK_L(2:4,k)
enddo

p = NWAKE

! Internal vertical columns
do j = 1, NCRTEFW-1
        do i = 1, NWAKE
                k = p + (j-1)*NWAKE + i
                l = (i-1)*NCRTEFW+j
                m = (i-1)*(NCRTEFW+1)+(j+1)
                n = m+(NCRTEFW+1)

                GAWK_R(1,k) = GRTEFW(l+1) - GRTEFW(l)
                GAWK_L(1,k) = GLTEFW(l) - GLTEFW(l+1)

                GAWK_R(2:4,k) = XYZRTEFW(1:3, m) - XYZRTEFW(1:3, n)
                GAWK_L(2:4,k) = XYZLTEFW(1:3, m) - XYZLTEFW(1:3, n)

                GAWK_R(5:7,k) = XYZRTEFW(1:3, n) + 0.5D+00*GAWK_R(2:4,k)
```

```fortran
                GAWK_L(5:7,k) = XYZLTEFW(1:3, n) + 0.5D+00*GAWK_L(2:4,k)
        enddo
enddo

p = p + NWAKE*(NCRTEFW-1)

! Outward edge
do i = 1, NWAKE
        k = p + i
        l = i*NCRTEFW
        m = i*(NCRTEFW+1)
        n = m+(NCRTEFW+1)

        GAWK_R(1,k) = -1.0D+00*GRTEFW(l)
        GAWK_L(1,k) = GLTEFW(l)

        GAWK_R(2:4,k) = XYZRTEFW(1:3, m) - XYZRTEFW(1:3, n)
        GAWK_L(2:4,k) = XYZLTEFW(1:3, m) - XYZLTEFW(1:3, n)

        GAWK_R(5:7,k) = XYZRTEFW(1:3, n) + 0.5D+00*GAWK_R(2:4,k)
        GAWK_L(5:7,k) = XYZLTEFW(1:3, n) + 0.5D+00*GAWK_L(2:4,k)
enddo

p = p + NWAKE

!!Forward Wing Trailing Edge Wake: Horizontal Vortex Segments
! First row (Union of lifting surface and wake)
do i = 1, NCRTEFW
        k = p + i
        m = i
        n = m+1

        GAWK_R(1,k) = GRTEFW(i)
        GAWK_L(1,k) = GLTEFW(i)

        GAWK_R(2:4,k) = XYZRTEFW(1:3, n) - XYZRTEFW(1:3, m)
        GAWK_L(2:4,k) = XYZLTEFW(1:3, m) - XYZLTEFW(1:3, n)

        GAWK_R(5:7,k) = XYZRTEFW(1:3, m) + 0.5D+00*GAWK_R(2:4,k)
        GAWK_L(5:7,k) = XYZLTEFW(1:3, n) + 0.5D+00*GAWK_L(2:4,k)
enddo

p = p + NCRTEFW

! Internal rows
do j = 1, NWAKE-1
        do i = 1, NCRTEFW
                k = p + (j-1)*NCRTEFW + i
                l = (j-1)*NCRTEFW+i
                m = j*(NCRTEFW+1)+i
                n = m+1

                GAWK_R(1,k) = GRTEFW(l+NCRTEFW) - GRTEFW(l)
                GAWK_L(1,k) = GLTEFW(l+NCRTEFW) - GLTEFW(l)

                GAWK_R(2:4,k) = XYZRTEFW(1:3, n) - XYZRTEFW(1:3, m)
                GAWK_L(2:4,k) = XYZLTEFW(1:3, m) - XYZLTEFW(1:3, n)

                GAWK_R(5:7,k) = XYZRTEFW(1:3, m) + 0.5D+00*GAWK_R(2:4,k)
                GAWK_L(5:7,k) = XYZLTEFW(1:3, n) + 0.5D+00*GAWK_L(2:4,k)
        enddo
enddo

p = p + NCRTEFW*(NWAKE-1)

! Last row
do i = 1, NCRTEFW
        k = p + i
```

```fortran
        l = (NWAKE-1)*NCRTEFW+i
        m = NWAKE*(NCRTEFW+1)+i
        n = m+1

        GAWK_R(1,k) = -1.0D+00*GRTEFW(l)
        GAWK_L(1,k) = -1.0D+00*GLTEFW(l)

        GAWK_R(2:4,k) = XYZRTEFW(1:3, n) - XYZRTEFW(1:3, m)
        GAWK_L(2:4,k) = XYZLTEFW(1:3, m) - XYZLTEFW(1:3, n)

        GAWK_R(5:7,k) = XYZRTEFW(1:3, m) + 0.5D+00*GAWK_R(2:4,k)
        GAWK_L(5:7,k) = XYZLTEFW(1:3, n) + 0.5D+00*GAWK_L(2:4,k)
enddo

p = p + NCRTEFW

!!Forward Wing Wing-Tip Wake: Vertical Vortex Segments
! First column
do i = 1, NRRWTFW
        k = p + i
        m = i
        n = m+1

        GAWK_R(1,k) = GRWTFW(i)
        GAWK_L(1,k) = -1.0D+00*GLWTFW(i)

        GAWK_R(2:4,k) = XYZRWTFW(1:3, m) - XYZRWTFW(1:3, n)
        GAWK_L(2:4,k) = XYZLWTFW(1:3, m) - XYZLWTFW(1:3, n)

        GAWK_R(5:7,k) = XYZRWTFW(1:3, n) + 0.5D+00*GAWK_R(2:4,k)
        GAWK_L(5:7,k) = XYZLWTFW(1:3, n) + 0.5D+00*GAWK_L(2:4,k)
enddo

p = p + NRRWTFW

! Internal columns
do j = 1, NWAKE-1
        do i = 1, NRRWTFW
                k = p + (j-1)*NRRWTFW + i
                l = (j-1)*NRRWTFW+i
                m = j*(NRRWTFW+1)+i
                n = m+1

                GAWK_R(1,k) = GRWTFW(l+NRRWTFW) - GRWTFW(l)
                GAWK_L(1,k) = GLWTFW(l) - GLWTFW(l+NRRWTFW)

                GAWK_R(2:4,k) = XYZRWTFW(1:3, m) - XYZRWTFW(1:3, n)
                GAWK_L(2:4,k) = XYZLWTFW(1:3, m) - XYZLWTFW(1:3, n)

                GAWK_R(5:7,k) = XYZRWTFW(1:3, n) + 0.5D+00*GAWK_R(2:4,k)
                GAWK_L(5:7,k) = XYZLWTFW(1:3, n) + 0.5D+00*GAWK_L(2:4,k)
        enddo
enddo

p = p + NRRWTFW*(NWAKE-1)

! Last column
do i = 1, NRRWTFW
        k = p + i
        l = (NWAKE-1)*NRRWTFW+i
        m = NWAKE*(NRRWTFW+1)+i
        n = m+1

        GAWK_R(1,k) = -1.0D+00*GRWTFW(l)
        GAWK_L(1,k) = GLWTFW(l)

        GAWK_R(2:4,k) = XYZRWTFW(1:3, m) - XYZRWTFW(1:3, n)
        GAWK_L(2:4,k) = XYZLWTFW(1:3, m) - XYZLWTFW(1:3, n)
```

```fortran

        GAWK_R(5:7,k) = XYZRWTFW(1:3, n) + 0.5D+00*GAWK_R(2:4,k)
        GAWK_L(5:7,k) = XYZLWTFW(1:3, n) + 0.5D+00*GAWK_L(2:4,k)
enddo

p = p + NRRWTFW

!!Forward Wing Wing-Tip Wake: Horizontal Vortex Segments
! Top row
do i = 1, NWAKE
        k = p + i
        l = (i-1)*NRRWTFW+1
        m = (i-1)*(NRRWTFW+1)+1
        n = m+(NRRWTFW+1)

        GAWK_R(1,k) = GRWTFW(l)
        GAWK_L(1,k) = GLWTFW(l)

        GAWK_R(2:4,k) = XYZRWTFW(1:3, n) - XYZRWTFW(1:3, m)
        GAWK_L(2:4,k) = XYZLWTFW(1:3, m) - XYZLWTFW(1:3, n)

        GAWK_R(5:7,k) = XYZRWTFW(1:3, m) + 0.5D+00*GAWK_R(2:4,k)
        GAWK_L(5:7,k) = XYZLWTFW(1:3, n) + 0.5D+00*GAWK_L(2:4,k)
enddo

p = p + NWAKE

! Internal rows
do j = 1, NRRWTFW-1
        do i = 1, NWAKE
                k = p + (j-1)*NWAKE + i
                l = (i-1)*NRRWTFW+j
                m = (i-1)*(NRRWTFW+1)+(j+1)
                n = m+(NRRWTFW+1)

                GAWK_R(1,k) = GRWTFW(l+1) - GRWTFW(l)
                GAWK_L(1,k) = GLWTFW(l+1) - GLWTFW(l)

                GAWK_R(2:4,k) = XYZRWTFW(1:3, n) - XYZRWTFW(1:3, m)
                GAWK_L(2:4,k) = XYZLWTFW(1:3, m) - XYZLWTFW(1:3, n)

                GAWK_R(5:7,k) = XYZRWTFW(1:3, m) + 0.5D+00*GAWK_R(2:4,k)
                GAWK_L(5:7,k) = XYZLWTFW(1:3, n) + 0.5D+00*GAWK_L(2:4,k)
        enddo
enddo

p = p + NWAKE*(NRRWTFW-1)

! Last row
do i = 1, NWAKE
        k = p + i
        l = i*NRRWTFW
        m = i*(NRRWTFW+1)
        n = m+(NRRWTFW+1)

        GAWK_R(1,k) = -1.0D+00*GRWTFW(l)
        GAWK_L(1,k) = -1.0D+00*GLWTFW(l)

        GAWK_R(2:4,k) = XYZRWTFW(1:3, n) - XYZRWTFW(1:3, m)
        GAWK_L(2:4,k) = XYZLWTFW(1:3, m) - XYZLWTFW(1:3, n)

        GAWK_R(5:7,k) = XYZRWTFW(1:3, m) + 0.5D+00*GAWK_R(2:4,k)
        GAWK_L(5:7,k) = XYZLWTFW(1:3, n) + 0.5D+00*GAWK_L(2:4,k)
enddo

p = p + NWAKE

!!Forward Wing Corner Row Wake: Vertical Vortex Segment
```

```
! Union of FW and wake
k = p + 1
m = NRZ1*NCFW

GAWK_R(1,k) = GRCRFW(1)
GAWK_L(1,k) = -1.0D+00*GLCRFW(1)

GAWK_R(2:4,k) = XYZFW_R(1:3, LMFW_R(2, m)) - XYZFW_R(1:3, LMFW_R(3, m))
GAWK_L(2:4,k) = XYZFW_L(1:3, LMFW_L(1, m)) - XYZFW_L(1:3, LMFW_L(4, m))

GAWK_R(5:7,k) = XYZFW_R(1:3, LMFW_R(3, m)) + 0.5D+00*GAWK_R(2:4,k)
GAWK_L(5:7,k) = XYZFW_L(1:3, LMFW_L(4, m)) + 0.5D+00*GAWK_L(2:4,k)

p = k

! Union of FW trailing edge and corner row
do i = 1, NWAKE
        k = p + i
        m = i*(NCRTEFW+1)
        n = m+(NCRTEFW+1)

        GAWK_R(1,k) = GRCRFW(i)
        GAWK_L(1,k) = -1.0D+00*GLCRFW(i)

        GAWK_R(2:4,k) = XYZRTEFW(1:3, m) - XYZRTEFW(1:3, n)
        GAWK_L(2:4,k) = XYZLTEFW(1:3, m) - XYZLTEFW(1:3, n)

        GAWK_R(5:7,k) = XYZRTEFW(1:3, n) + 0.5D+00*GAWK_R(2:4,k)
        GAWK_L(5:7,k) = XYZLTEFW(1:3, n) + 0.5D+00*GAWK_L(2:4,k)
enddo

p = p + NWAKE

!!Forward Wing Corner Row Wake: Horizontal Vortex Segment
! Union of FW and wake
k = p + 1
m = NRZ1*NCFW

GAWK_R(1,k) = GRCRFW(1)
GAWK_L(1,k) = GLCRFW(1)

GAWK_R(2:4,k) = XYZFW_R(1:3, LMFW_R(3, m)) - XYZFW_R(1:3, LMFW_R(4, m))
GAWK_L(2:4,k) = XYZFW_L(1:3, LMFW_L(3, m)) - XYZFW_L(1:3, LMFW_L(4, m))

GAWK_R(5:7,k) = XYZFW_R(1:3, LMFW_R(4, m)) + 0.5D+00*GAWK_R(2:4,k)
GAWK_L(5:7,k) = XYZFW_L(1:3, LMFW_L(4, m)) + 0.5D+00*GAWK_L(2:4,k)

p = k

! Union of FW wing-tip and corner row
do i = 1, NWAKE
        k = p + i
        m = i*(NRRWTFW+1)
        n = m+(NRRWTFW+1)

        GAWK_R(1,k) = GRCRFW(i)
        GAWK_L(1,k) = GLCRFW(i)

        GAWK_R(2:4,k) = XYZRWTFW(1:3, n) - XYZRWTFW(1:3, m)
        GAWK_L(2:4,k) = XYZLWTFW(1:3, m) - XYZLWTFW(1:3, n)

        GAWK_R(5:7,k) = XYZRWTFW(1:3, m) + 0.5D+00*GAWK_R(2:4,k)
        GAWK_L(5:7,k) = XYZLWTFW(1:3, n) + 0.5D+00*GAWK_L(2:4,k)
enddo

p = p + NWAKE

!!Forward Wing Corner Row Wake: Diagonal Vortex Segment
```

```
! Internal rows
do i = 1, NWAKE-1
        k = p + i
        m = (i+1)*(NRRWTFW+1)
        n = (i+1)*(NCRTEFW+1)

        GAWK_R(1,k) = GRCRFW(i+1) - GRCRFW(i)
        GAWK_L(1,k) = GLCRFW(i+1) - GLCRFW(i)

        GAWK_R(2:4,k) = XYZRWTFW(1:3, m) - XYZRTEFW(1:3, n)
        GAWK_L(2:4,k) = XYZLTEFW(1:3, n) - XYZLWTFW(1:3, m)

        GAWK_R(5:7,k) = XYZRTEFW(1:3, n) + 0.5D+00*GAWK_R(2:4,k)
        GAWK_L(5:7,k) = XYZLWTFW(1:3, m) + 0.5D+00*GAWK_L(2:4,k)
enddo

p = p + (NWAKE-1)

! Last row
k = p + 1
m = (NWAKE+1)*(NRRWTFW+1)
n = (NWAKE+1)*(NCRTEFW+1)

GAWK_R(1,k) = -1.0D+00*GRCRFW(NWAKE)
GAWK_L(1,k) = -1.0D+00*GLCRFW(NWAKE)

GAWK_R(2:4,k) = XYZRWTFW(1:3, m) - XYZRTEFW(1:3, n)
GAWK_L(2:4,k) = XYZLTEFW(1:3, n) - XYZLWTFW(1:3, m)

GAWK_R(5:7,k) = XYZRTEFW(1:3, n) + 0.5D+00*GAWK_R(2:4,k)
GAWK_L(5:7,k) = XYZLWTFW(1:3, m) + 0.5D+00*GAWK_L(2:4,k)

p = k

!!Aft Wing Trailing Edge: Vertical Segments
! Inward edge
do i = 1, NWAKE
        k = p + i
        j = (i-1)*NCRTEAW+1
        m = (i-1)*(NCRTEAW+1)+1
        n = m+(NCRTEAW+1)

        GAWK_R(1,k) = GRTEAW(j)
        GAWK_L(1,k) = -1.0D+00*GLTEAW(j)

        GAWK_R(2:4,k) = XYZRTEAW(1:3, m) - XYZRTEAW(1:3, n)
        GAWK_L(2:4,k) = XYZLTEAW(1:3, m) - XYZLTEAW(1:3, n)

        GAWK_R(5:7,k) = XYZRTEAW(1:3, n) + 0.5D+00*GAWK_R(2:4,k)
        GAWK_L(5:7,k) = XYZLTEAW(1:3, n) + 0.5D+00*GAWK_L(2:4,k)
enddo

p = p + NWAKE

! Internal columns
do j = 1, NCRTEAW-1
        do i = 1, NWAKE
                k = p + (j-1)*NWAKE + i
                l = (i-1)*NCRTEAW+j
                m = (i-1)*(NCRTEAW+1)+(j+1)
                n = m+(NCRTEAW+1)

                GAWK_R(1,k) = GRTEAW(l+1) - GRTEAW(l)
                GAWK_L(1,k) = GLTEAW(l) - GLTEAW(l+1)

                GAWK_R(2:4,k) = XYZRTEAW(1:3, m) - XYZRTEAW(1:3, n)
                GAWK_L(2:4,k) = XYZLTEAW(1:3, m) - XYZLTEAW(1:3, n)

```

```
                GAWK_R(5:7,k) = XYZRTEAW(1:3, n) + 0.5D+00*GAWK_R(2:4,k)
                GAWK_L(5:7,k) = XYZLTEAW(1:3, n) + 0.5D+00*GAWK_L(2:4,k)
        enddo
enddo

p = p + NWAKE*(NCRTEAW-1)

! Outward edge
do i = 1, NWAKE
        k = p + i
        j = i*NCRTEAW
        m = i*(NCRTEAW+1)
        n = m+(NCRTEAW+1)

        GAWK_R(1,k) = -1.0D+00*GRTEAW(j)
        GAWK_L(1,k) = GLTEAW(j)

        GAWK_R(2:4,k) = XYZRTEAW(1:3, m) - XYZRTEAW(1:3, n)
        GAWK_L(2:4,k) = XYZLTEAW(1:3, m) - XYZLTEAW(1:3, n)

        GAWK_R(5:7,k) = XYZRTEAW(1:3, n) + 0.5D+00*GAWK_R(2:4,k)
        GAWK_L(5:7,k) = XYZLTEAW(1:3, n) + 0.5D+00*GAWK_L(2:4,k)
enddo

p = p + NWAKE

!!Aft Wing Trailing Edge: Horizontal Segments
! First row (Union of lifting surface and wake)
do i = 1, NCRTEAW
        k = p + i
        m = i
        n = m+1

        GAWK_R(1,k) = GRTEAW(i)
        GAWK_L(1,k) = GLTEAW(i)

        GAWK_R(2:4,k) = XYZRTEAW(1:3, n) - XYZRTEAW(1:3, m)
        GAWK_L(2:4,k) = XYZLTEAW(1:3, m) - XYZLTEAW(1:3, n)

        GAWK_R(5:7,k) = XYZRTEAW(1:3, m) + 0.5D+00*GAWK_R(2:4,k)
        GAWK_L(5:7,k) = XYZLTEAW(1:3, n) + 0.5D+00*GAWK_L(2:4,k)
enddo

p = p + NCRTEAW

! Internal rows
do j = 1, NWAKE-1
        do i = 1, NCRTEAW
                k = p + (j-1)*NCRTEAW + i
                l = (j-1)*NCRTEAW+i
                m = j*(NCRTEAW+1)+i
                n = m+1

                GAWK_R(1,k) = GRTEAW(l+NCRTEAW) - GRTEAW(l)
                GAWK_L(1,k) = GLTEAW(l+NCRTEAW) - GLTEAW(l)

                GAWK_R(2:4,k) = XYZRTEAW(1:3, n) - XYZRTEAW(1:3, m)
                GAWK_L(2:4,k) = XYZLTEAW(1:3, m) - XYZLTEAW(1:3, n)

                GAWK_R(5:7,k) = XYZRTEAW(1:3, m) + 0.5D+00*GAWK_R(2:4,k)
                GAWK_L(5:7,k) = XYZLTEAW(1:3, n) + 0.5D+00*GAWK_L(2:4,k)
        enddo
enddo

p = p + NCRTEAW*(NWAKE-1)

! Last row
do i = 1, NCRTEAW
```

```
        k = p + i
        l = (NWAKE-1)*NCRTEAW+i
        m = NWAKE*(NCRTEAW+1)+i
        n = m+1

        GAWK_R(1,k) = -1.0D+00*GRTEAW(l)
        GAWK_L(1,k) = -1.0D+00*GLTEAW(l)

        GAWK_R(2:4,k) = XYZRTEAW(1:3, n) - XYZRTEAW(1:3, m)
        GAWK_L(2:4,k) = XYZLTEAW(1:3, m) - XYZLTEAW(1:3, n)

        GAWK_R(5:7,k) = XYZRTEAW(1:3, m) + 0.5D+00*GAWK_R(2:4,k)
        GAWK_L(5:7,k) = XYZLTEAW(1:3, n) + 0.5D+00*GAWK_L(2:4,k)
enddo
```

A.3 Evaluation of Velocity

When the FMM is not active, the code below is used to evaluate the velocity fields. As the wake grows, both the number of field points NREC and the number vortex segments NV increase. Distributing the computational workload of the evaluation of the velocity fields among several threads significantly reduces the computational time required for a program run.

```
VEL( 1:3, 1:NREC ) = 0.0D+00

V  ( 1:3, 1:NREC, 1:NV ) = 0.0D+00

do j = 1, NREC

        do i = 1, NV

                GG = dipolestrengths( i )

                w( 1:3 ) = dipolemoments( 1:3, i )

                u( 1:3, 1 ) = sources( 1:3, i ) - 0.5D+00*w( 1:3 )
                u( 1:3, 2 ) = sources( 1:3, i ) + 0.5D+00*w( 1:3 )

                r( 1:3, 1 ) = receivers( 1:3, j ) - u( 1:3, 1 )
                r( 1:3, 2 ) = receivers( 1:3, j ) - u( 1:3, 2 )

                !%%%%%%%%%%%%%%%%%%%%%%%%%%%%%%%%%%%%%%%%%%%%%%%%%%%%%%%%%%%%%%%%%%%%%%%%%%%%%%%%%%%
                ! Implementation of Biot-Savart
                !%%%%%%%%%%%%%%%%%%%%%%%%%%%%%%%%%%%%%%%%%%%%%%%%%%%%%%%%%%%%%%%%%%%%%%%%%%%%%%%%%%%

                R1 = r( 1:3, 1 )
                R2 = r( 1:3, 2 )

                normR1 = dsqrt( dot_product( R1,R1 ) )
                normR2 = dsqrt( dot_product( R2,R2 ) )

```

```fortran
                dotR1R2 = dot_product( R1,R2 )

                lo = dot_product( w( 1:3 ), w( 1:3 ) )

                dum1 = normR1 * normR2 + dotR1R2

                !V( 1:3, j, i ) = 0.0D+00

                if (  dabs( dum1 ) .gt. ( lo * CUTOFF ) ) then

                        crossR1R2(1) = R1(2) * R2(3) - R1(3) * R2(2)
                        crossR1R2(2) = R1(3) * R2(1) - R1(1) * R2(3)
                        crossR1R2(3) = R1(1) * R2(2) - R1(2) * R2(1)

                        dum = ( 1/normR1 + 1/normR2 ) / dum1

                        V( 1:3, j, i ) = GG * dum * crossR1R2( 1:3 )

                endif

                !%%%%%%%%%%%%%%%%%%%%%%%%%%%%%%%%%%%%%%%%%%%%%%%%%%%%%%%%%%%%%%%%%%%%%%%%%%%%%%%%%

        enddo

enddo

VEL( 1:3, 1:NREC ) = sum( V, dim = 3 )
```

Appendix B: Modes from Computational Structural Dynamics Model

The last 16 of the 20 modes of the undamaged structure are shown in Figures B.1 through B.16. This structure had been earlier discussed in Chapter 3.

The fifth through eighth modes (Figures B.1-B.4) appear to be in purely bending motions of the forward wings. The ninth and tenth modes (Figures B.5 and B.6) appear to be in a mixture of bending and torsion motions of the forward wing and slight bending motion of the aft wing. The eleventh and twelfth modes (Figures B.7 and B.8) appear to be mainly in bending motion with a low torsion motion in the forward wing. The thirteenth and fourteenth modes (Figures B.9 and B.10) show similar behavior to the ninth and tenth modes but with some torsion of the aft wing included. The fifteenth and sixteenth modes (Figures B.11 and B.12) appear to be a mixture of bending and torsion motions of the forward wing with low bending of the aft wing. The seventeenth and eighteenth modes (Figures B.13 and B.14) appear to be in torsion motion of the forward and aft wings. The nineteenth and twentieth modes (Figures B.15 and B.16) appear to involve of bending and torsion motions of the forward wing.

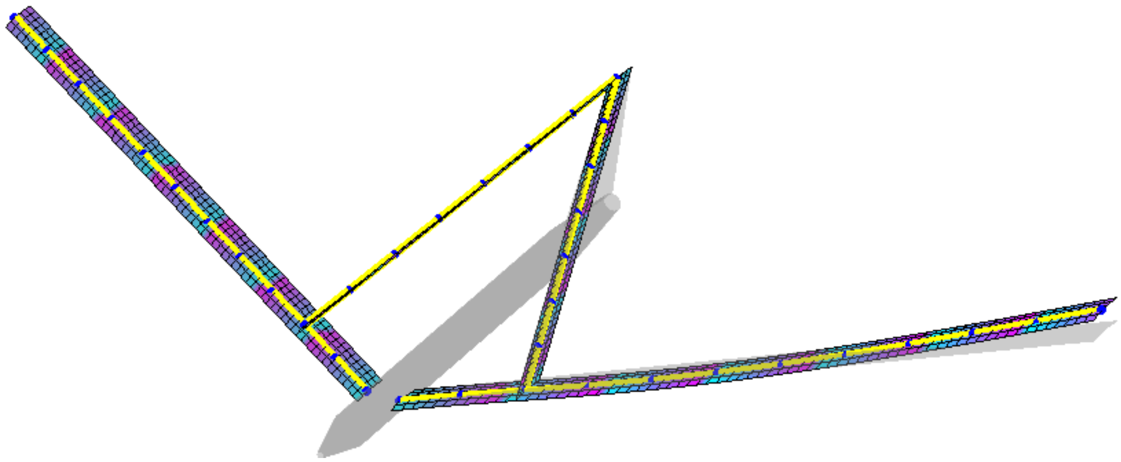

Figure B.1: Fifth mode corresponding to natural frequency $f_5 = 1.548\,\mathrm{Hz}$.

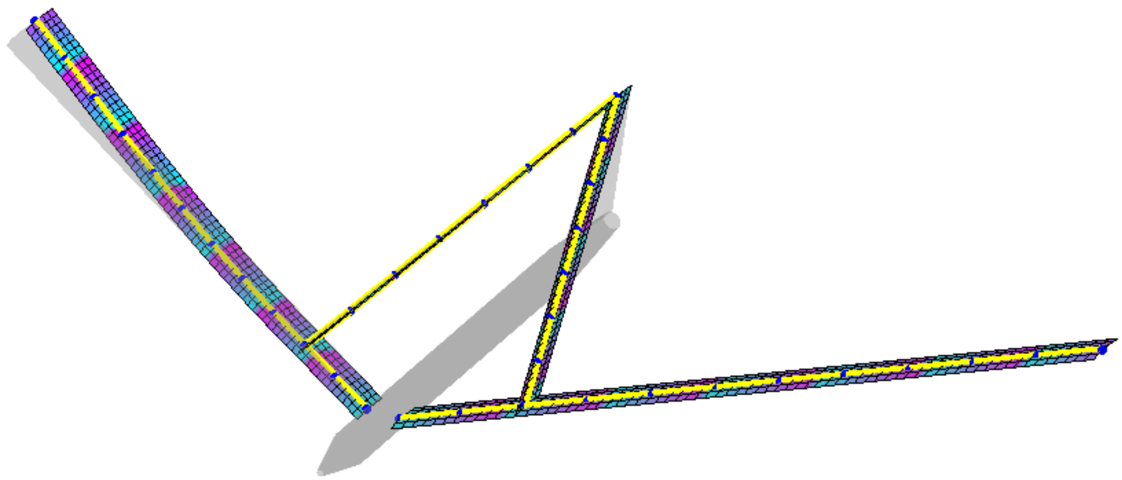

Figure B.2: Sixth mode corresponding to natural frequency $f_6 = 1.548\,\mathrm{Hz}$.

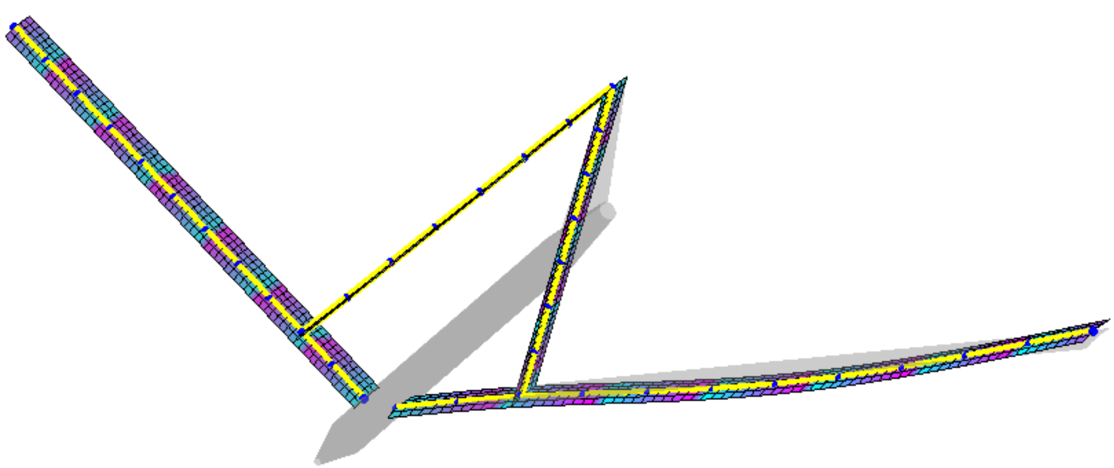

Figure B.3: Seventh mode corresponding to natural frequency $f_7 = 2.215\,\mathrm{Hz}$.

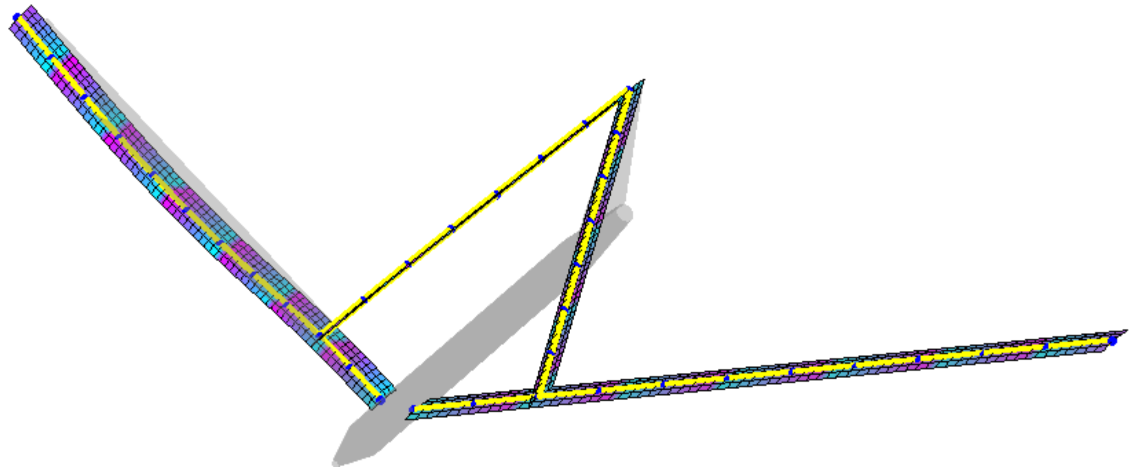

Figure B.4: Eighth mode corresponding to natural frequency $f_8 = 2.215\,\text{Hz}$.

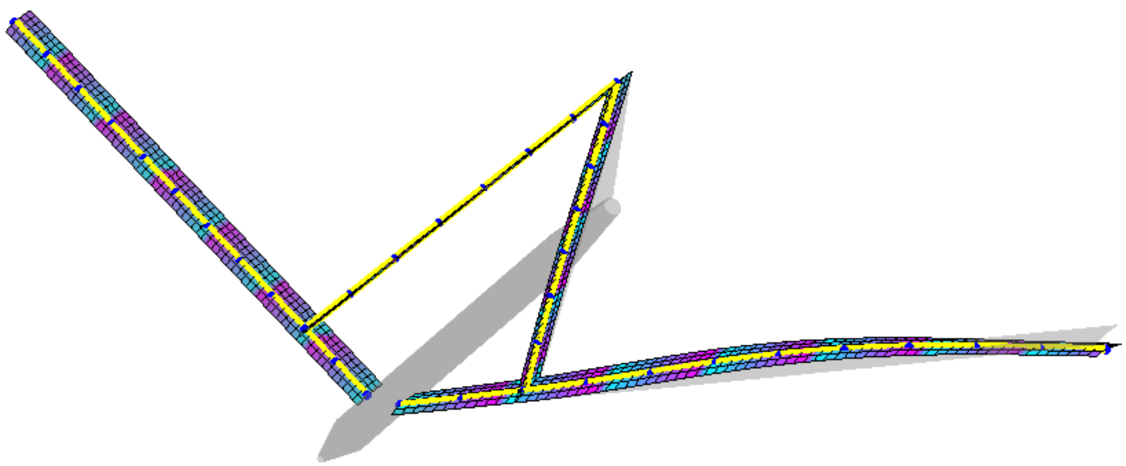

Figure B.5: Ninth mode corresponding to natural frequency $f_9 = 2.530\,\text{Hz}$.

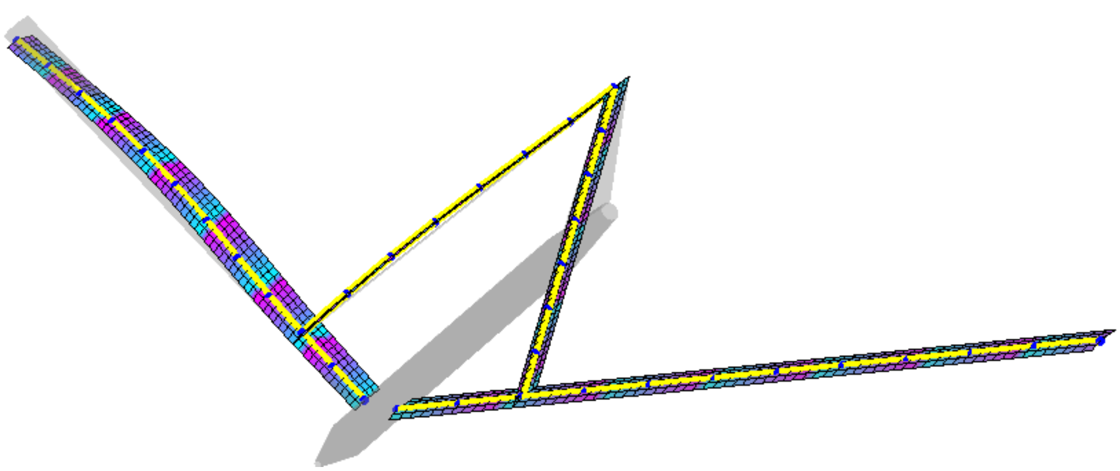

Figure B.6: Tenth mode corresponding to natural frequency $f_{10} = 2.530\,\text{Hz}$.

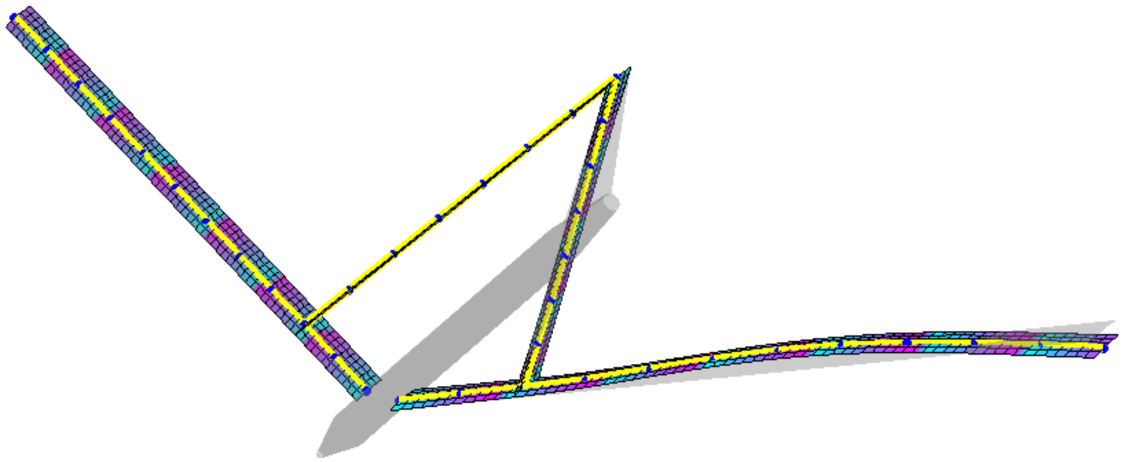

Figure B.7: Eleventh mode corresponding to natural frequency $f_{11} = 2.666\,\mathrm{Hz}$.

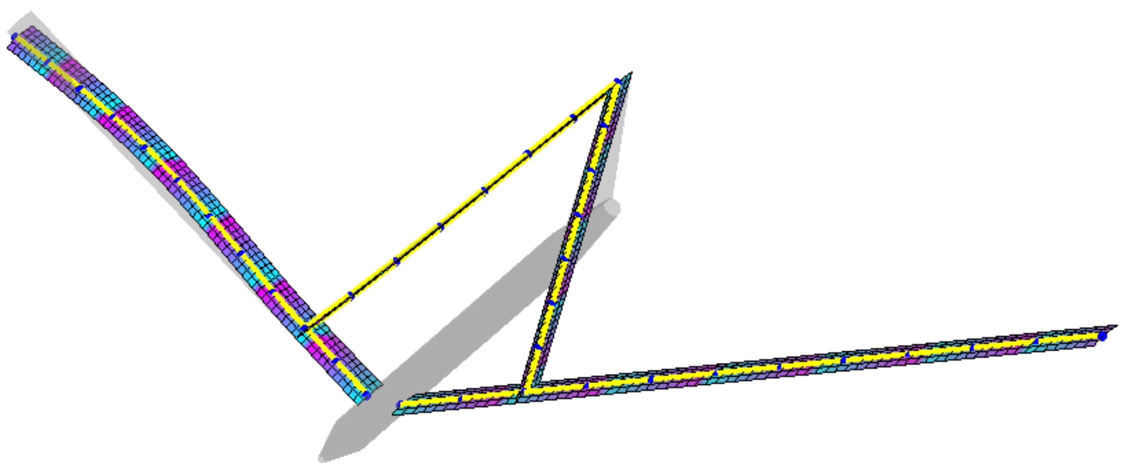

Figure B.8: Twelfth mode corresponding to natural frequency $f_{12} = 2.666\,\mathrm{Hz}$.

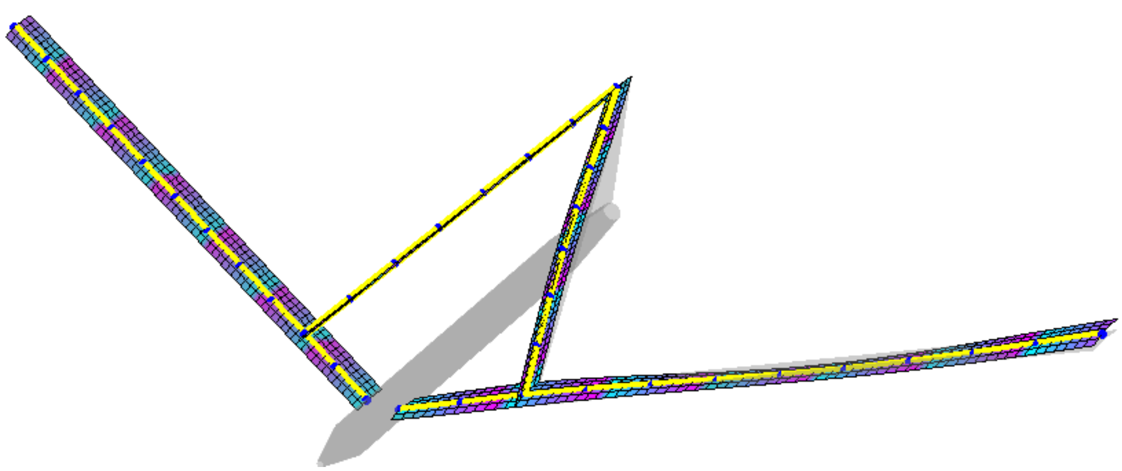

Figure B.9: Thirteenth mode corresponding to natural frequency $f_{13} = 3.769\,\mathrm{Hz}$.

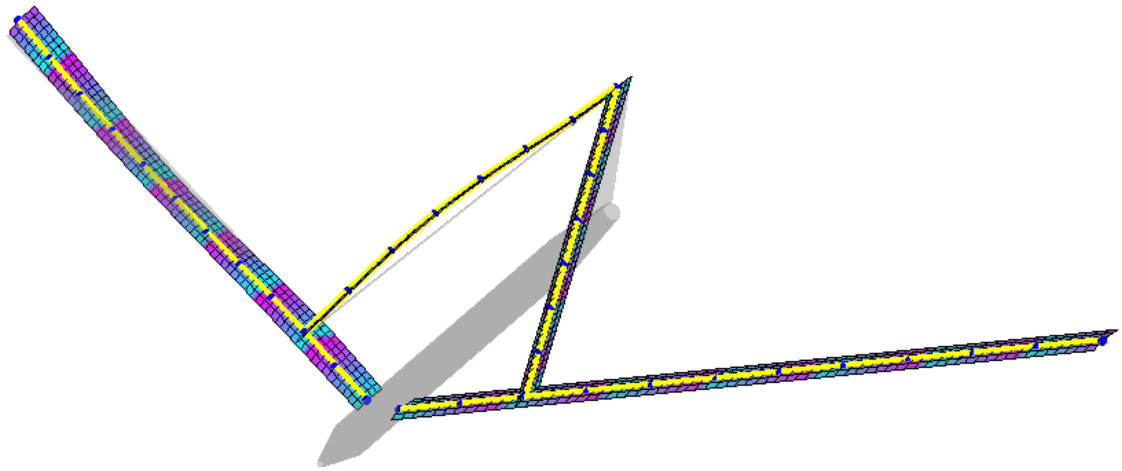

Figure B.10: Fourteenth mode corresponding to natural frequency $f_{14} = 3.769\,\mathrm{Hz}$.

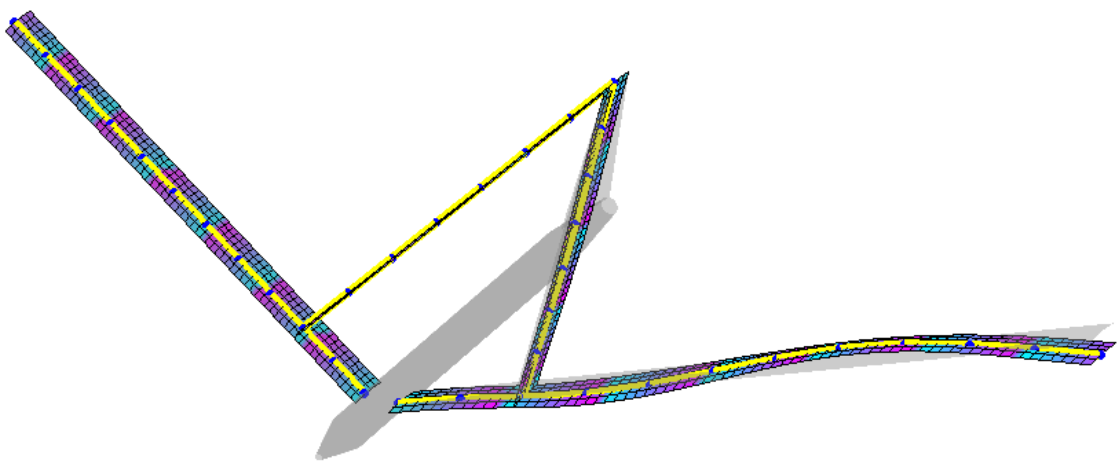

Figure B.11: Fifteenth mode corresponding to natural frequency $f_{15} = 4.583\,\mathrm{Hz}$.

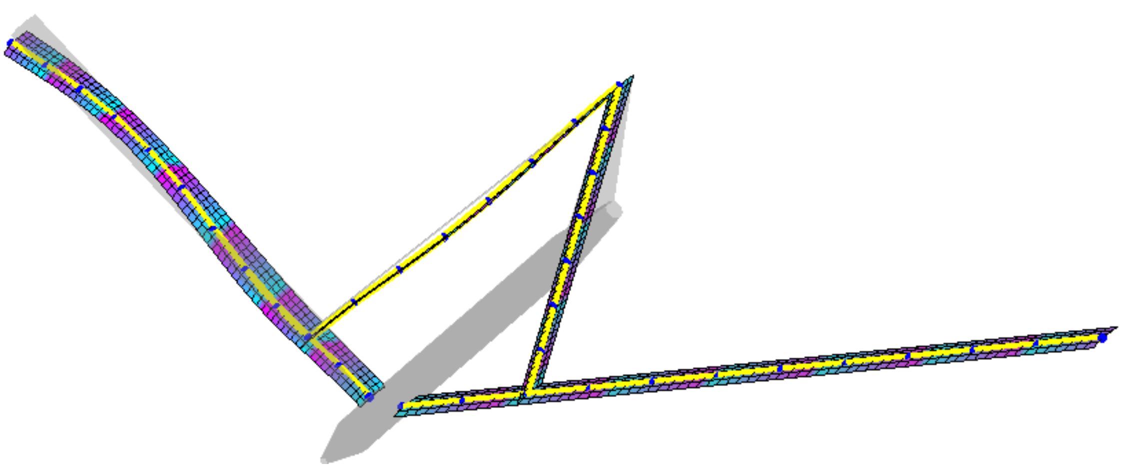

Figure B.12: Sixteenth mode corresponding to natural frequency $f_{16} = 4.583\,\mathrm{Hz}$.

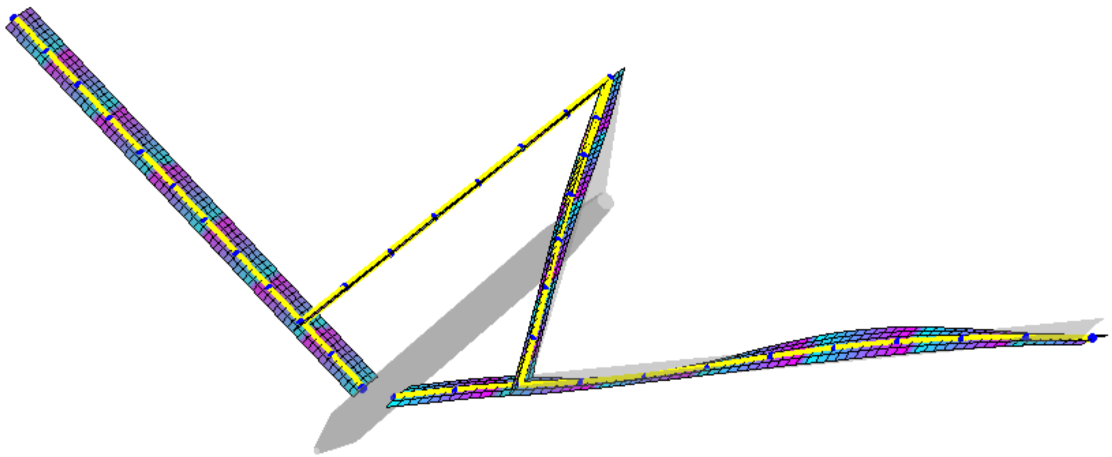

Figure B.13: Seventeenth mode corresponding to natural frequency $f_{17} = 5.047\,\text{Hz}$.

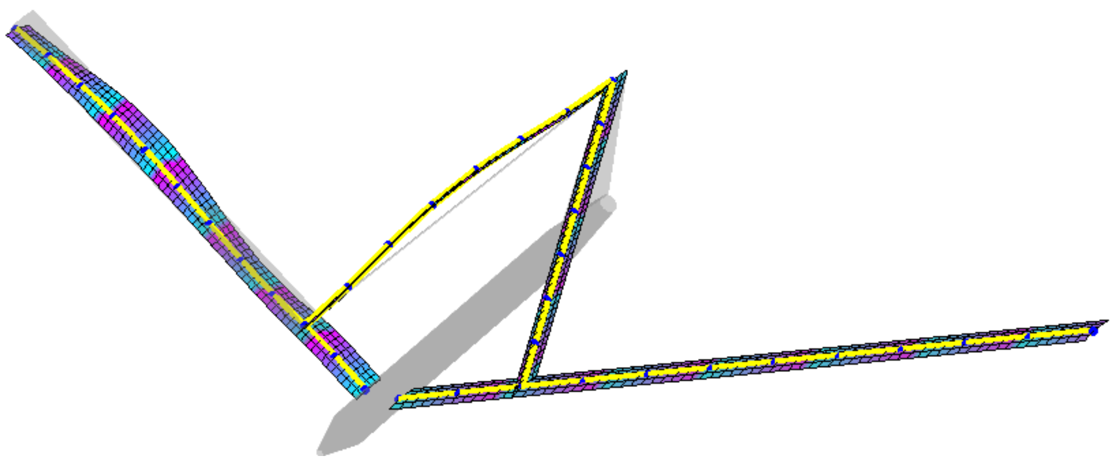

Figure B.14: Eighteenth mode corresponding to natural frequency $f_{18} = 5.047\,\text{Hz}$.

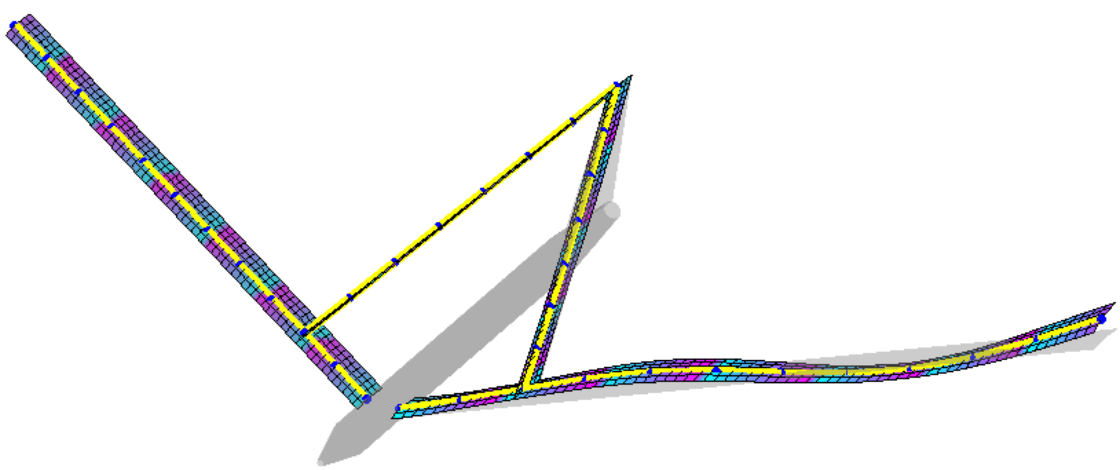

Figure B.15: Nineteenth mode corresponding to natural frequency $f_{19} = 6.057\,\text{Hz}$.

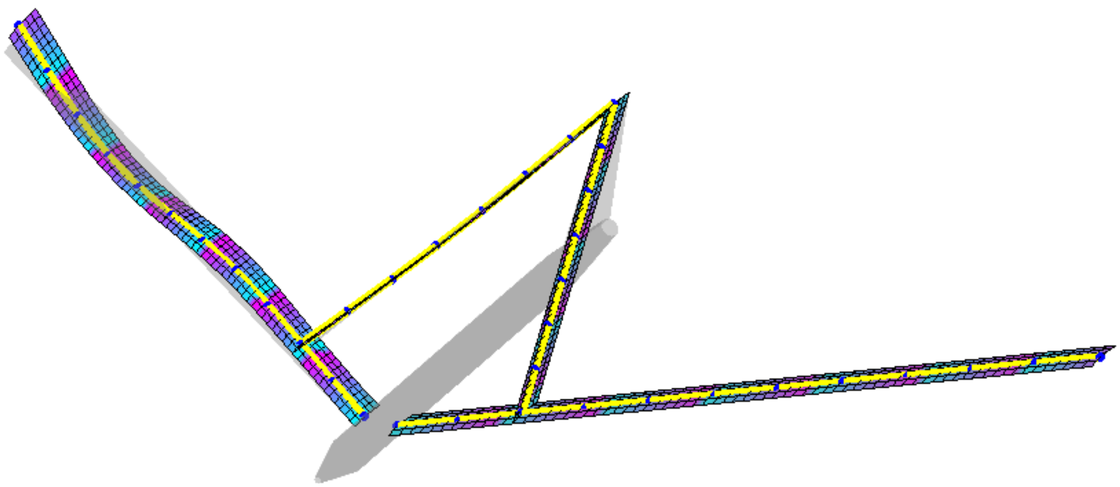

Figure B.16: Twentieth mode corresponding to natural frequency $f_{20} = 6.057\,\mathrm{Hz}$.

Appendix C: Additional Information on Joined-Wing Aircraft Simulations

In this appendix, more details are provided on why the settings used in joined-wing aircraft aeroelasticity simulations are adequate for determining the critical flutter speed of the joined-wing aircraft.

C.1 Sensitivity Analysis: Number of Elements in Structural Model

In this section, additional results for a joined-wing aircraft model with a higher number of elements are presented. The structural model used in this section has 146 elements constructed from 147 nodal points, which can be seen in Figure C.1. The left and right forward wing beams contain 45 elements made from 46 nodal points each. The left and right aft wing beams contain 28 elements made from 29 nodal points each. The structural model used in this section has four times the number of elements compared to the structural model used in the main body of the dissertation. This implies that the individual length of the elements used in the main body of the dissertation is four times the individual length of the elements used in this section. It is recalled that the structural model used in main body of the dissertation that 36 elements constructed from 37 nodal points, as can be seen in Figure 3.7. The

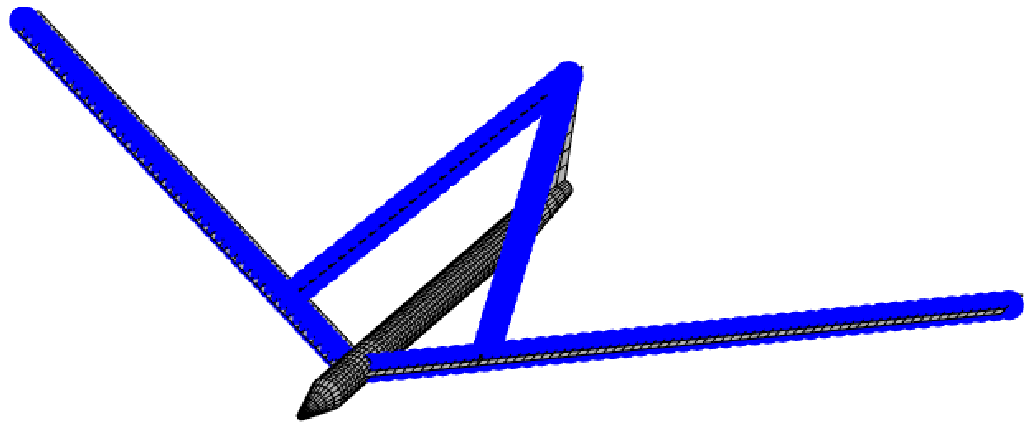

Figure C.1: Structural beam model with 146 elements.

results in this section are used to show that the aeroelasticity simulation results converge and do not change when smaller element sizes are considered. The joined-wing aircraft aeroelasticity simulation were run for 180 seconds in physical time. The freestream air density is $\rho = 0.1152\,\mathrm{kg/m^3}$. The initial conditions were chosen as

$$q_i(0) = 0 \qquad\qquad \dot{q}_i(0) = 0 \tag{C.1}$$

for $i = 1, 2, \cdots, 20$. The freestream speed is set to $156.00\,\mathrm{m/s}$ with freestream direction $(0^\circ, 5^\circ, 0^\circ)$. The wake in the aerodynamic model is truncated after six chord lengths or 30 timesteps.

The time responses of all modes corresponding to the right joined-wing are shown in Figure C.2 and the time responses of all modes corresponding to the left joined-wing are shown in Figure C.3. The responses in blue correspond to the structure with 36 elements and the responses in red correspond to the structure with 146 elements. The modal displacements corresponding to the right joined-wing of the two structures are nearly identical but with slight phase shifts in a few of modes, as can be discerned in modes 6, 9, and 10 of Figure C.2. The modal displacements corresponding to the left joined-wing of the two structures are nearly identical in magnitude but with opposite signs, as shown in modes 1 through 5 and modes 7 through 9 of Figure C.3. This sign change is acceptable, as the modal amplitudes are arbitrary to a scaling constant.

In Figures C.4 and C.5, the normalized FFTs of the modes corresponding to the right joined-wing and the left joined-wing, respectively, are presented. The free vibration frequencies are marked in the figures by dashed black lines. The phase shifts observed in displacement plots can be observed in the normalized FFTs plots.

It can be concluded that when the number of elements in the structural model is increased, the profiles of the responses do not significantly change. It would seem that with more structural elements, the simulations will need to run for a longer period of time to see oscillations in the response reduce to a similar level comparing to the responses of the structure with fewer elements. A slight phase shifts in the responses can also be observed from the normalized FFTs plots.

It should also be noted that the average length of an element in the structure used in the main body of the dissertation is 3.273 m. The smallest wavelength of each mode is 3.201 m. Since the smallest wavelength of each mode is smaller than the average length of an element, it can be concluded that the chosen element size used in the main body of the dissertation is adequate to capture the highest mode.

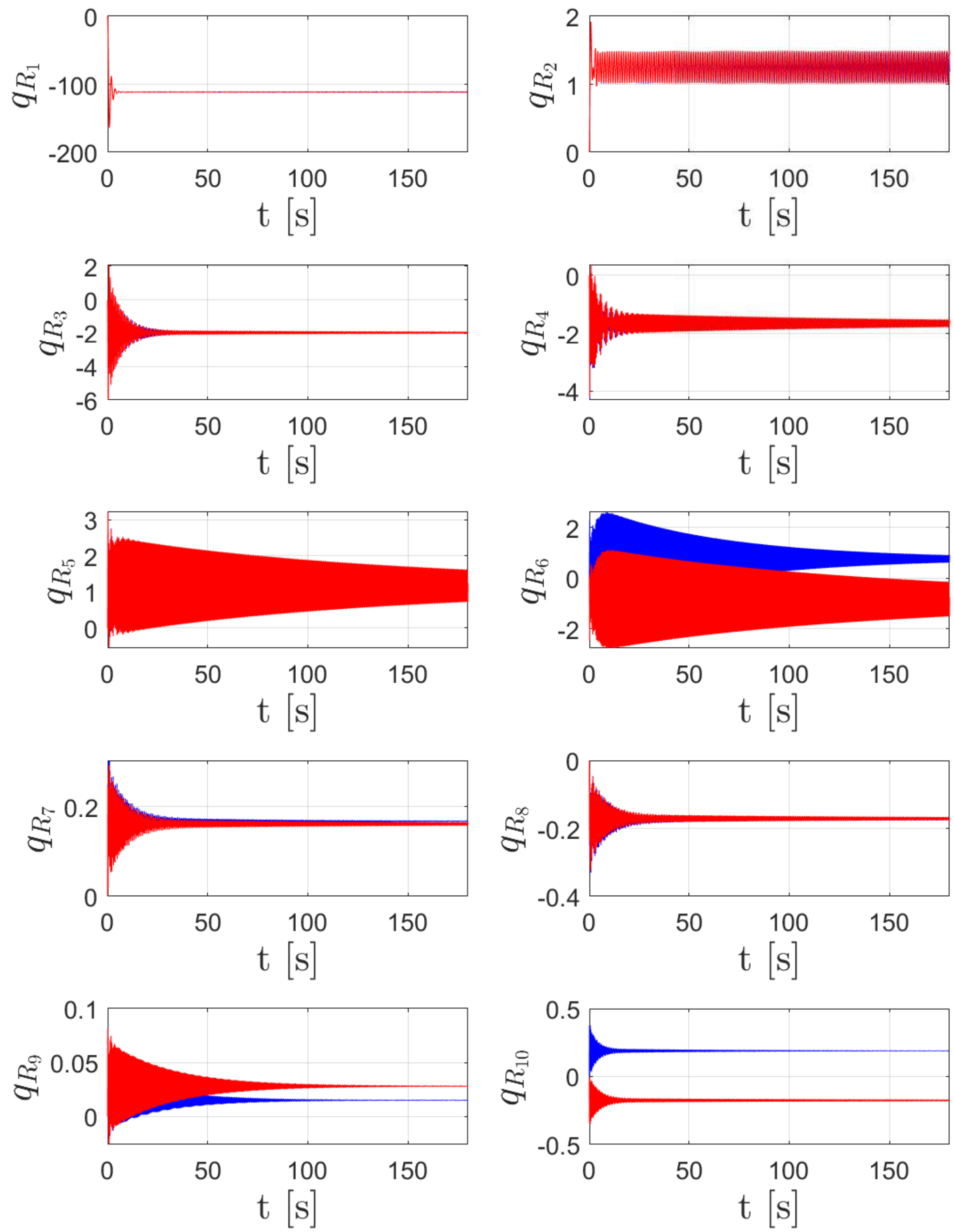

Figure C.2: Time responses of modes corresponding to the right joined-wing for the structure with 36 elements (in blue) and the structure with 146 elements (in red).

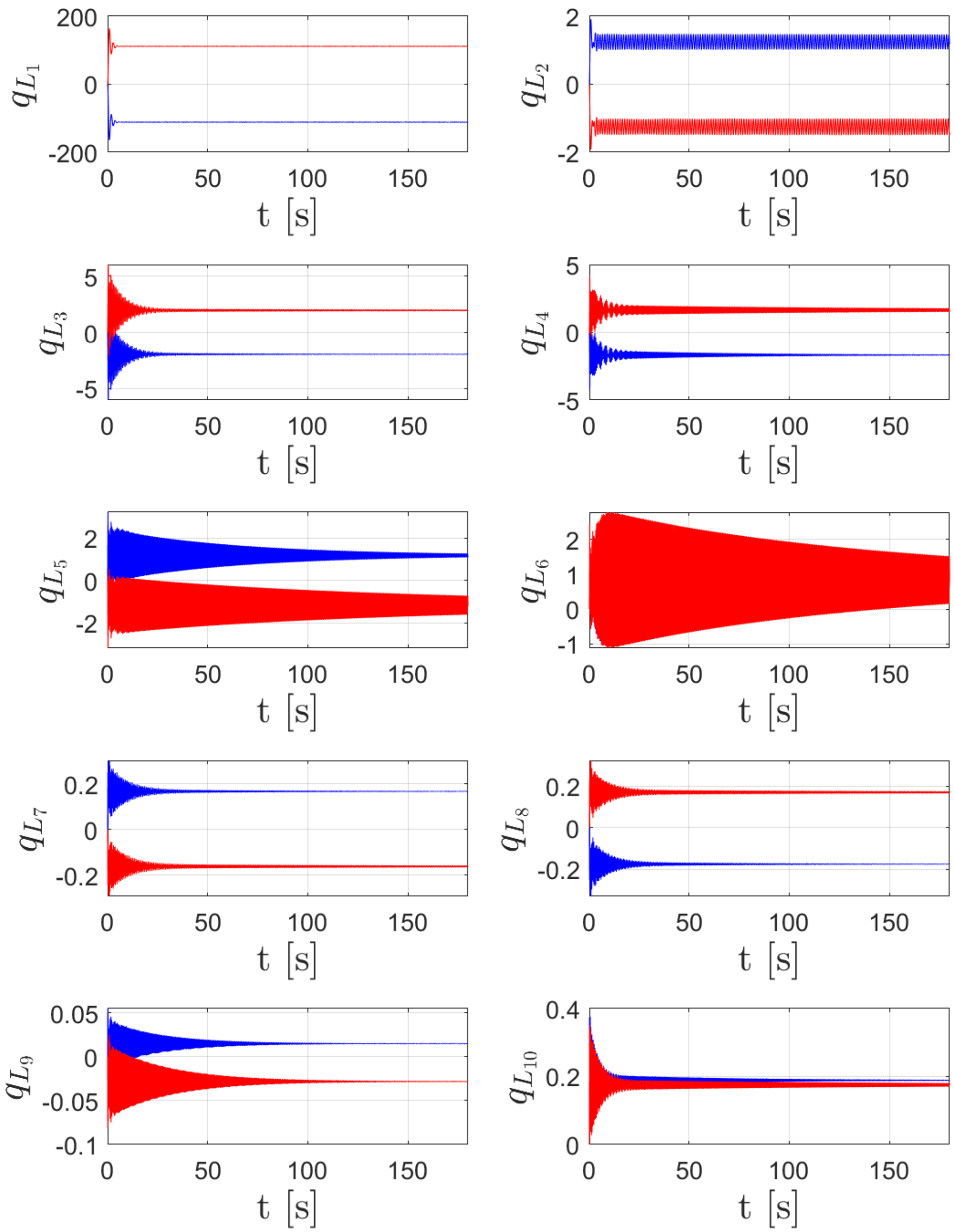

Figure C.3: Time responses of modes corresponding to the left joined-wing for the structure with 36 elements (in blue) and the structure with 146 elements (in red).

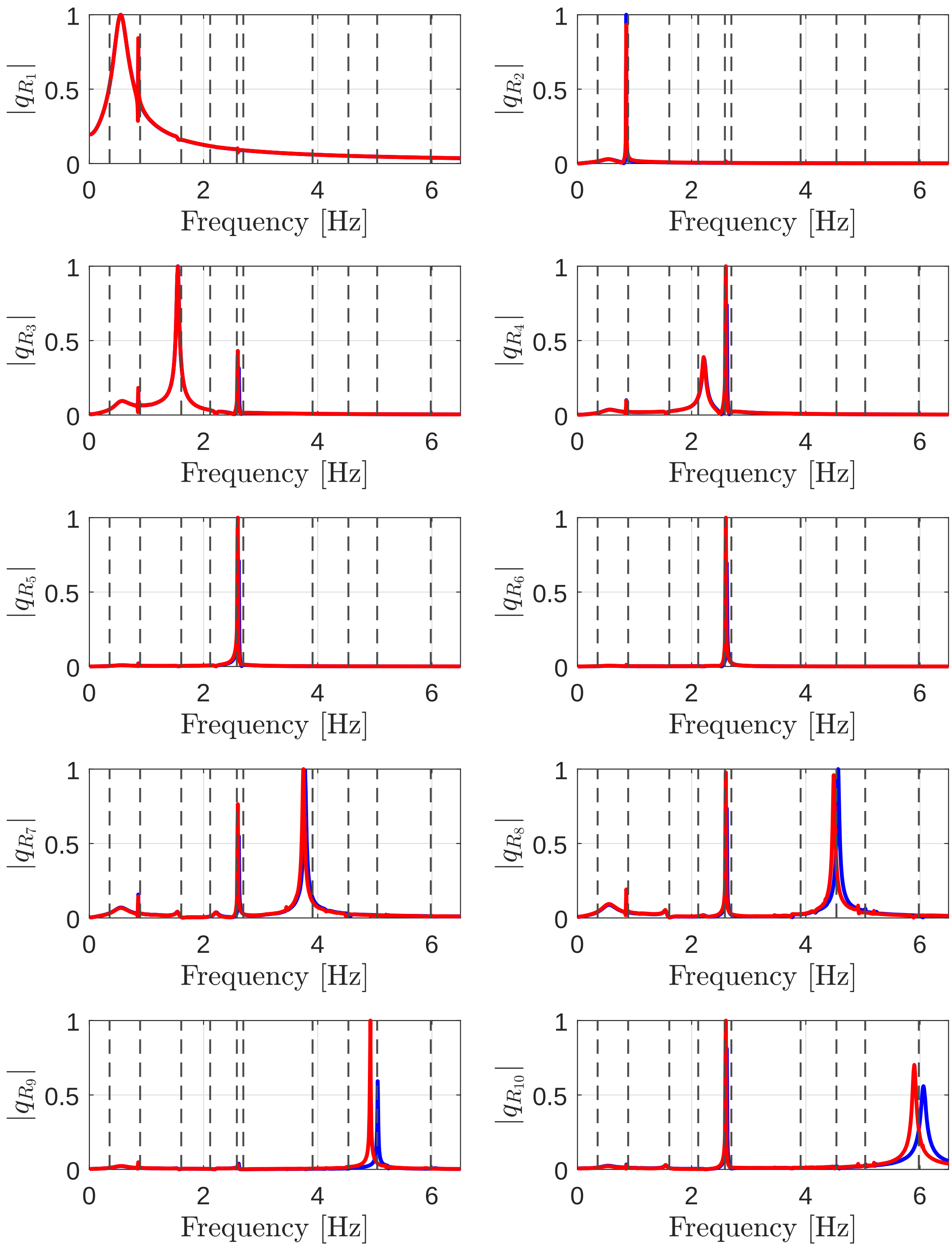

Figure C.4: Responses in the frequency domain of modes corresponding to the right joined-wing for the structure with 36 elements (in blue) and the structure with 146 elements (in red).

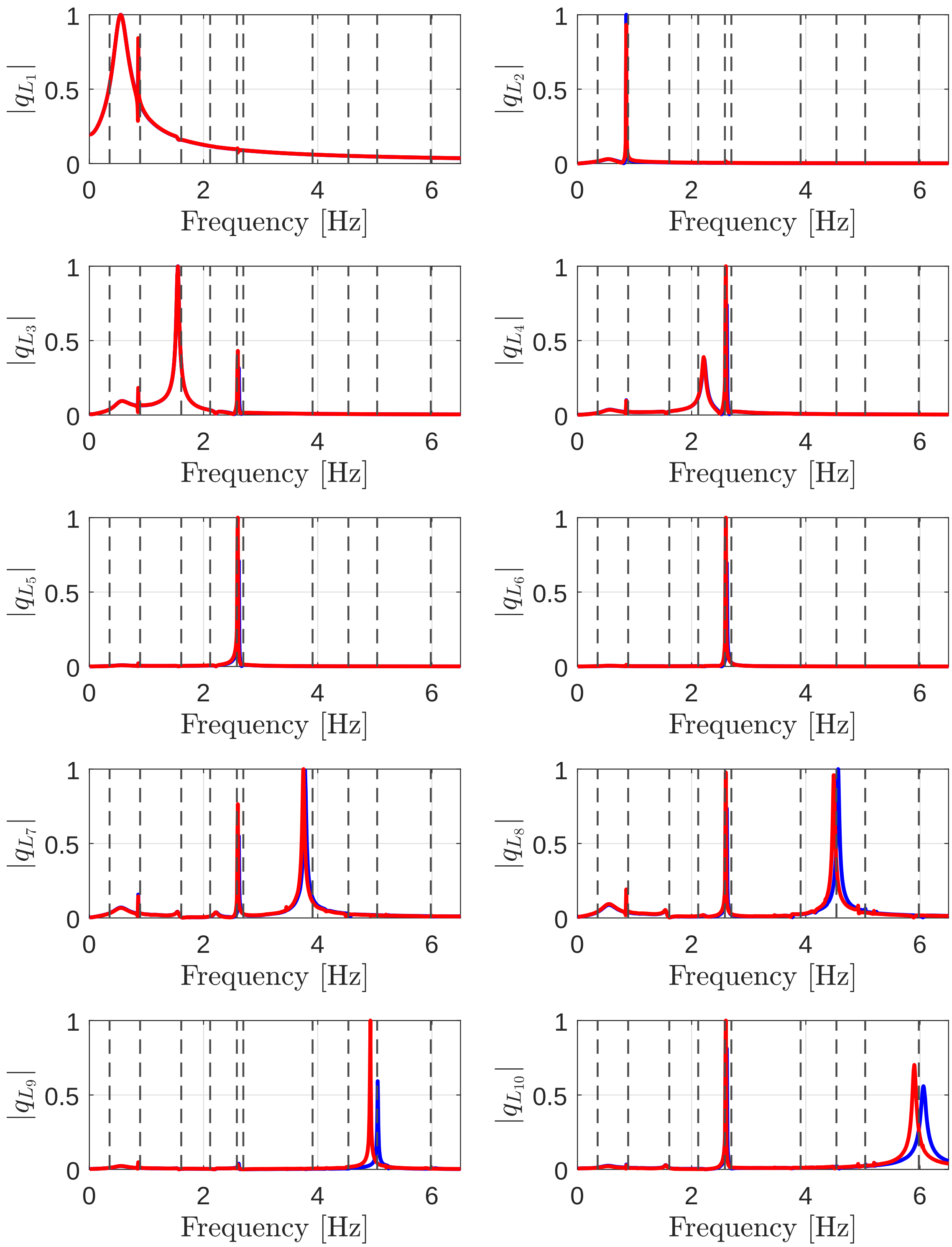

Figure C.5: Responses in the frequency domain of modes corresponding to the left joined-wing for the structure with 36 elements (in blue) and the structure with 146 elements (in red).

Table C.1: Freestream air density with corresponding altitude.

	Freestream air density $[\frac{\text{kg}}{\text{m}^3}]$	Altitude above sea level [ft]
ρ_1	0.4135000	10,000
ρ_2	0.1152000	15,000-20,000
ρ_3	0.0184100	30,000
ρ_4	0.0003097	60,000

C.2 Effects of Freestream Air Density

In this section, additional results for a joined-wing aircraft model with different freestream air densities are presented. The structural model used in this section has 36 elements constructed from 37 nodal points, which can be seen in Figure 3.7. The results in this section are used to show how the air density of the freestream affects the aeroelasticity simulation results. The joined-wing aircraft aeroelasticity simulation were run for 180 seconds in physical time. The initial conditions were chosen as

$$q_i(0) = 0 \qquad \dot{q}_i(0) = 0 \tag{C.2}$$

for $i = 1, 2, \cdots, 20$. The freestream speed is set to 156.00 m/s with freestream direction $(0°, 5°, 0°)$. The wake in the aerodynamic model is truncated after six chord lengths or 30 timesteps. The varying freestream air densities along with the corresponding altitudes used for these simulation runs are shown in Table C.1. The freestream air densities ρ_3 and ρ_4 correspond to cases of the joined-wing aircraft flying at a higher cruising altitude. ρ_1 corresponds to the case of the joined-wing aircraft in the landing or take-off stage of flight.

The modal displacements for simulation runs with the three lowest freestream air densities corresponding to the right and left joined-wing are shown in Figures C.6 and C.7, respectively. The responses in black correspond to freestream air density ρ_2, the responses in blue correspond to freestream air density ρ_3, and the responses in red correspond to freestream air density ρ_4. It can be observed that responses corresponding to higher freestream air densities have large oscillations at the transient stage. In the case with freestream air density ρ_1, the simulation comes to a halt before 10,000 timesteps (or a little over 32 seconds in physical time) as the solution fails converge past this point. This is an indication that the responses of the joined-wing aircraft at higher freestream air densities become unstable. In Figures C.8 and C.9, the responses corresponding to freestream air density ρ_1 (in green) can be observed to dwarf the responses observed at the lowest freestream air density. It can be concluded that the joined-wing aircraft aeroelastic model developed for this dissertation is more suited for determining the response of the aircraft during the cruising stage of flight.

C.3 Nontrivial Initial Conditions

In this section, additional results for a joined-wing aircraft model with different initial conditions are presented. In this dissertation, a trivial response has been used as an initial condition as this is the equilibrium point in the pre-flutter case. After the flutter instability, the system response is attracted to a limit cycle. The numerical results suggest supercritical flutter [69, 70] and one does not expect the

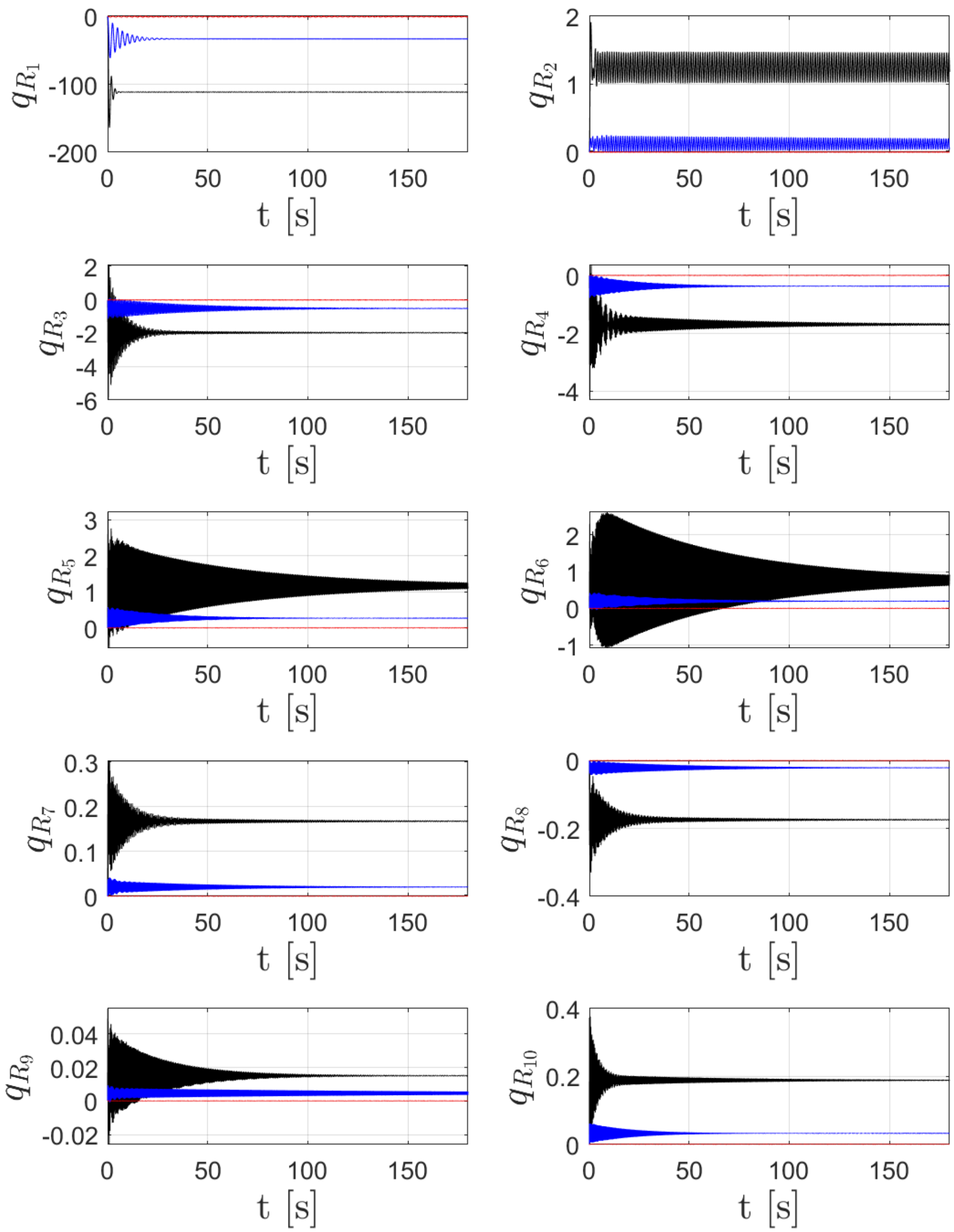

Figure C.6: Time responses of modes corresponding to the right joined-wing for freestream air densities: ρ_2 (in black), ρ_3 (in blue), and ρ_4 (in red).

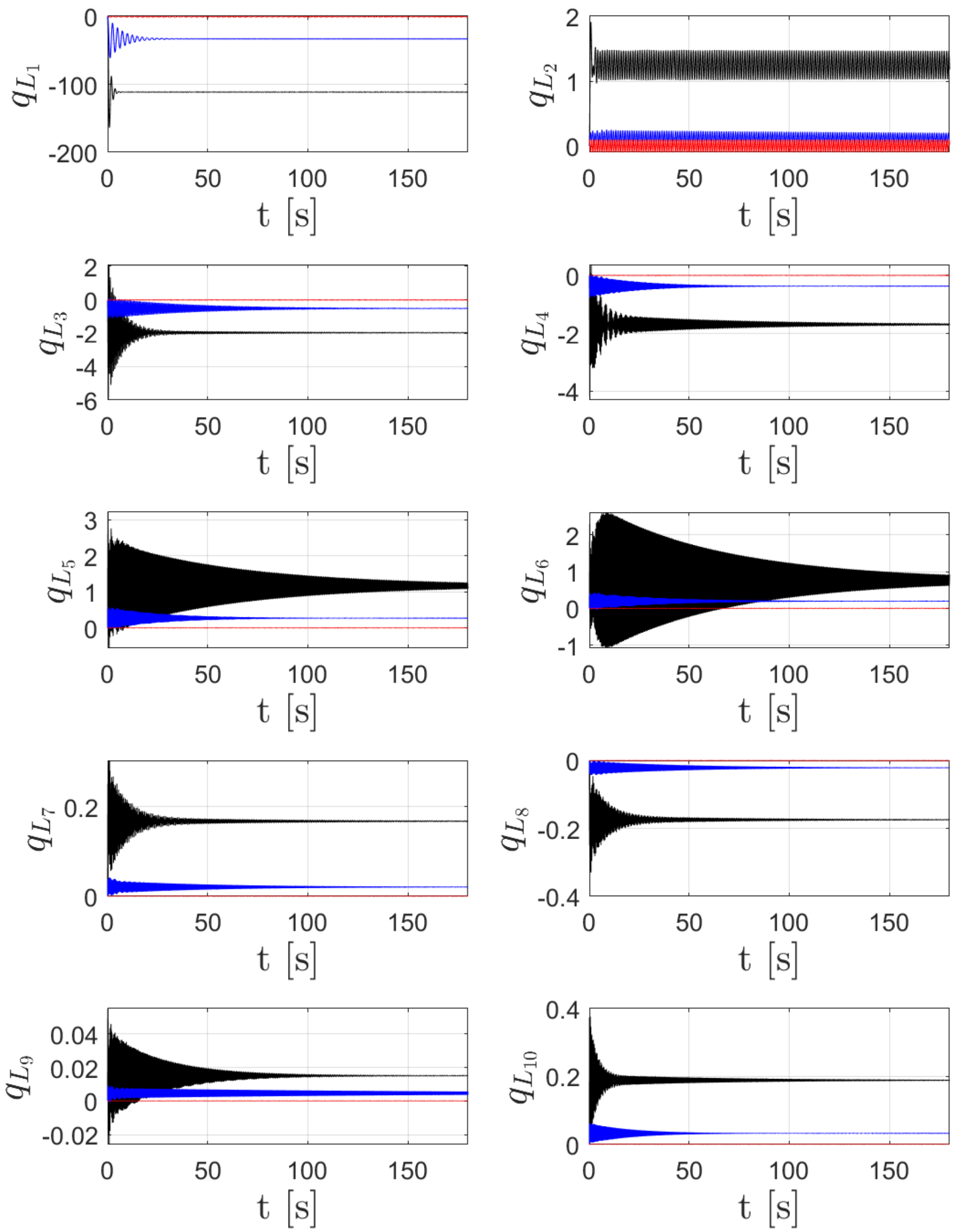

Figure C.7: Time responses of modes corresponding to the left joined-wing for freestream air densities: ρ_2 (in black), ρ_3 (in blue), and ρ_4 (in red).

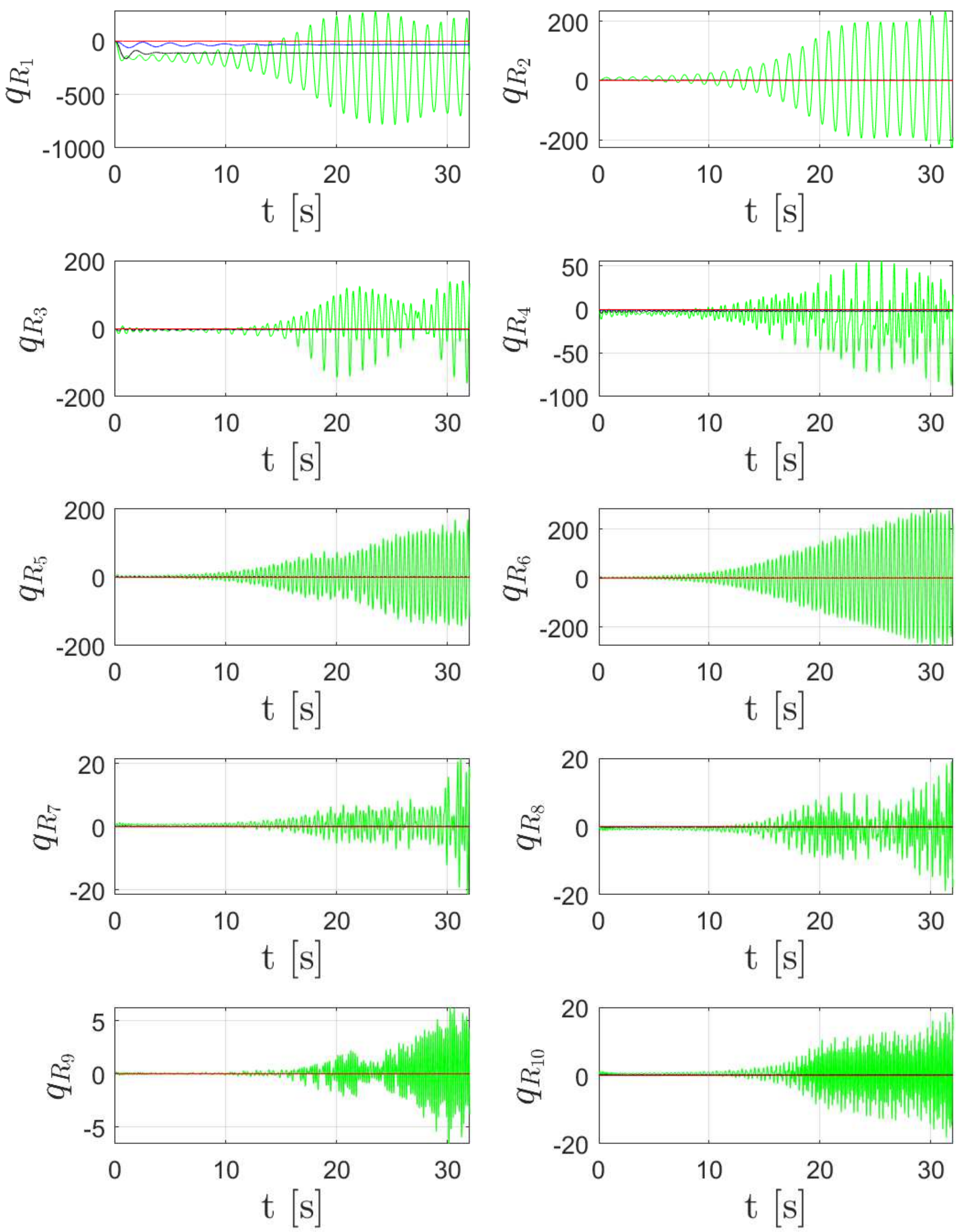

Figure C.8: Time responses of modes corresponding to the right joined-wing for freestream air densities: ρ_1 (in green), ρ_2 (in black), ρ_3 (in blue), and ρ_4 (in red).

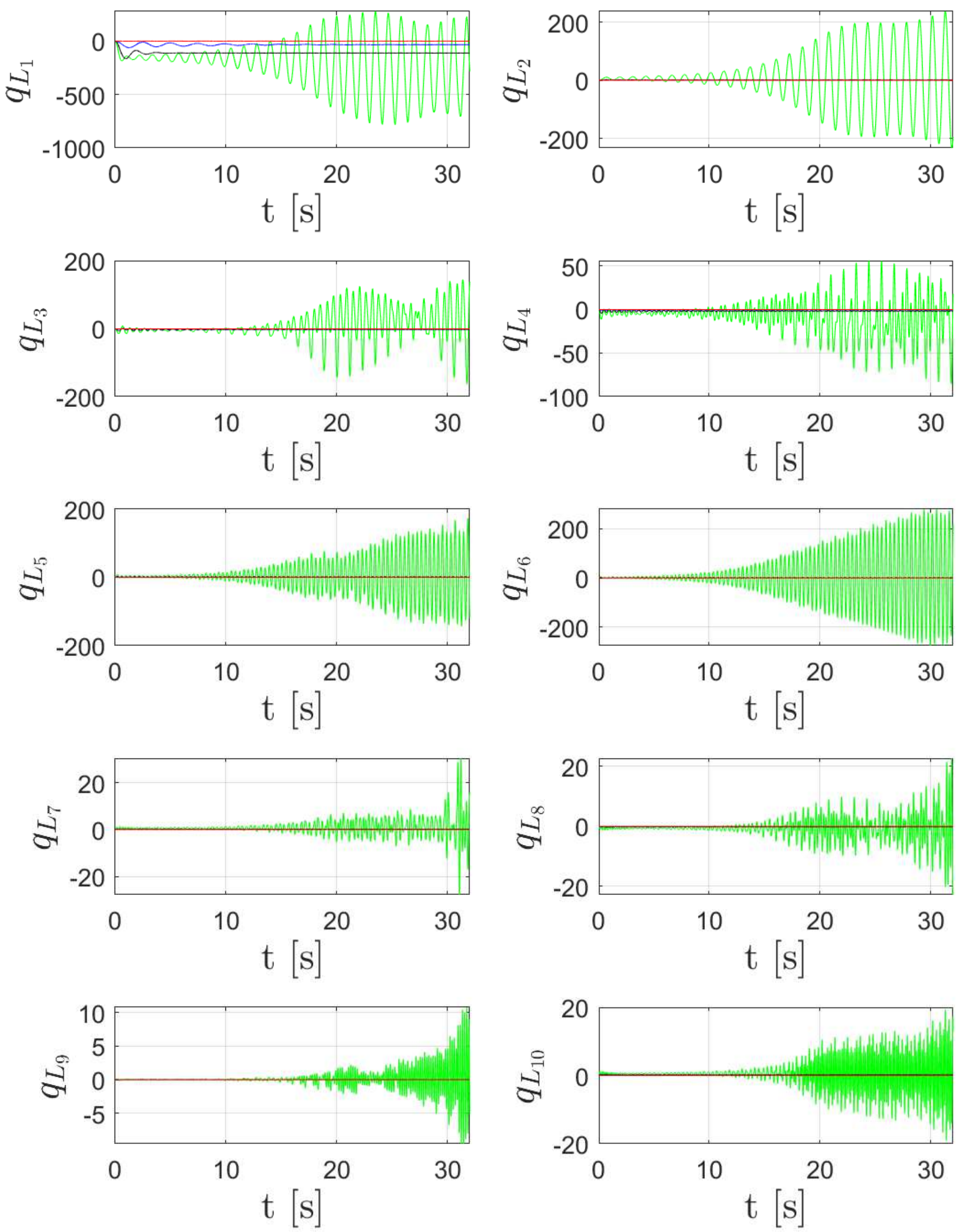

Figure C.9: Time responses of modes corresponding to the left joined-wing for freestream air densities: ρ_1 (in green), ρ_2 (in black), ρ_3 (in blue), and ρ_4 (in red).

response initiated from other initial conditions to go to a different response.

The structural model used in this section has 36 elements constructed from 37 nodal points, which can be seen in Figure 3.7. The results in this section are used to show how the air density of the freestream affect the aeroelasticity simulation results. The joined-wing aircraft aeroelasticity simulation were run for 180 seconds in physical time. The freestream speed is set to 156.00 m/s with freestream direction $(0°, 5°, 0°)$. The freestream air density is $\rho = 0.1152\,\mathrm{kg/m^3}$. The wake in the aerodynamic model is truncated after six chord lengths or 30 timesteps. The nontrivial initial conditions for the right joined-wing were chosen as

$$q_1(0) = 1.0 \times 10^{10} \qquad\qquad q_8(0) = 1. \tag{C.3}$$

and the nontrivial initial conditions for the left joined-wing were chosen as

$$q_3(0) = 1.0 \times 10^{-1} \qquad\qquad q_{11}(0) = 3. \tag{C.4}$$

The projected responses (of the last 5 seconds of physical time) in the phase planes of the right joined-wing and the left joined-wing are shown in Figures C.10 and C.11, respectively. The limit cycles of the different cases have nearly identical shapes for all modes corresponding the right and left joined-wings. In the case of the modes corresponding to the left joined-wing, the sizes of the limit cycle oscillations (LCOs) of the nontrivial initial conditions are smaller compared to those obtained for the trivial initial conditions. Further numerical work needs to be carried out to resolve this.

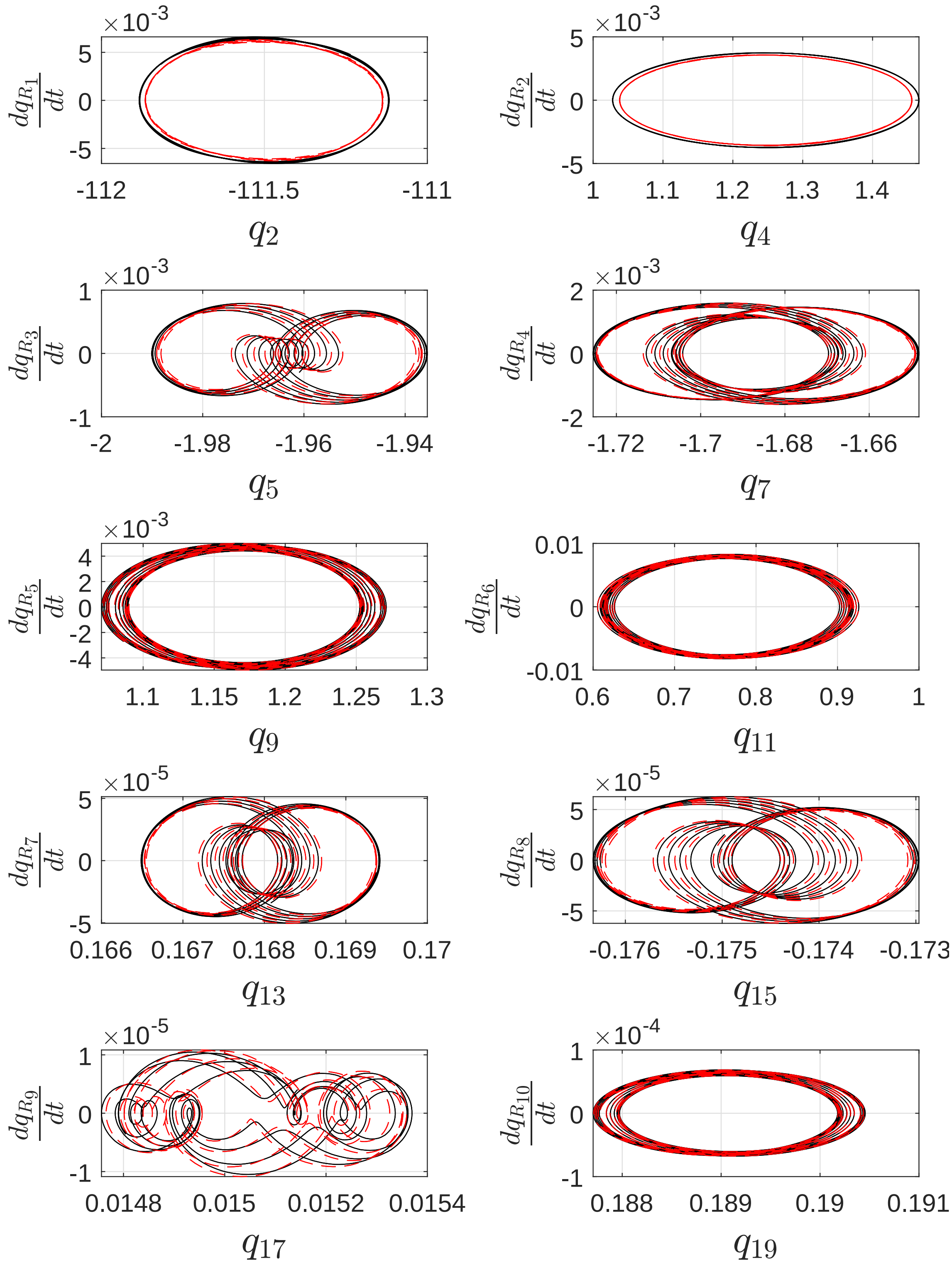

Figure C.10: Projections in phase planes of modes corresponding to the left joined-wing with trivial initial conditions (in black) and nontrivial initial conditions (in red).

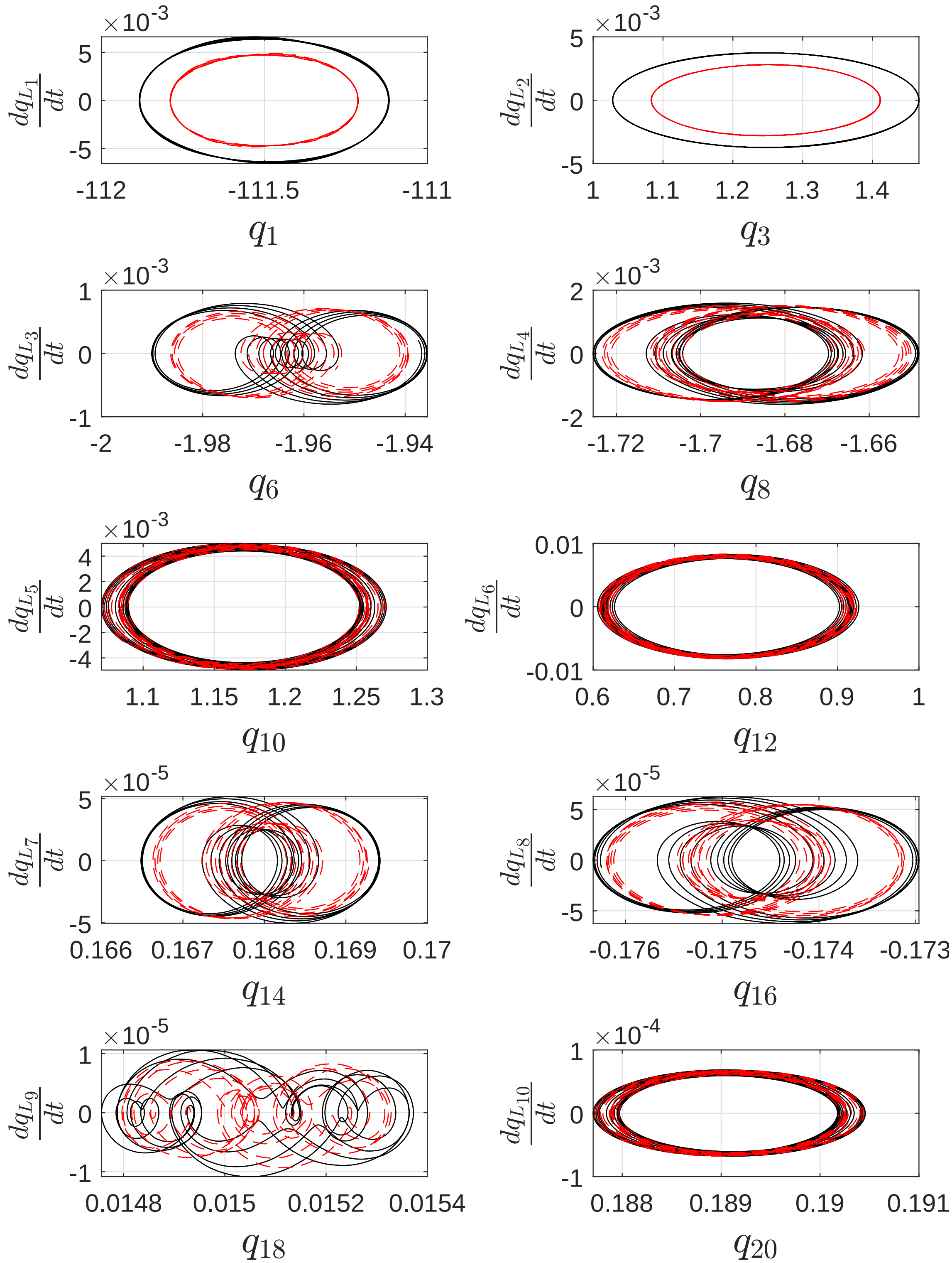

Figure C.11: Projections in phase planes of modes corresponding to the right joined-wing with trivial initial conditions (in black) and nontrivial initial conditions (in red).

Appendix D: Additional Results on Joined-Wing Aircraft Aeroelastic Responses

The aeroelastic responses of the joined-wing aircraft for last three cases discussed in Chapter 5 are presented in this Appendix. This includes the results of the no structural damage case for freestream direction $(0°, 10°, 0°)$ and the cases with structural bending and torsional damage for freestream direction $(0°, 5°, 0°)$.

D.1 Case with No Damage: Freestream Direction $(0°, 10°, 0°)$

The results shown in Figures D.1 and D.2 correspond to a case where the freestream speed is 135 m/s, which is below the critical flutter speed. The time responses of all modes corresponding to the right joined-wing are shown in Figures D.1 and the time responses of all modes corresponding to the left joined-wing are shown in D.2. In the two figures, it can be observed that after a brief transient, all modes exhibit an oscillatory behavior that decreases in amplitude as time passes. This is caused by the presence of just aerodynamic damping.

The projected responses in the phase planes of the right joined-wing and the left joined-wing are shown in Figures D.3 and D.4, respectively. Stable focus type of characteristics can be observed in all modes as the spirals converge to an equilibrium

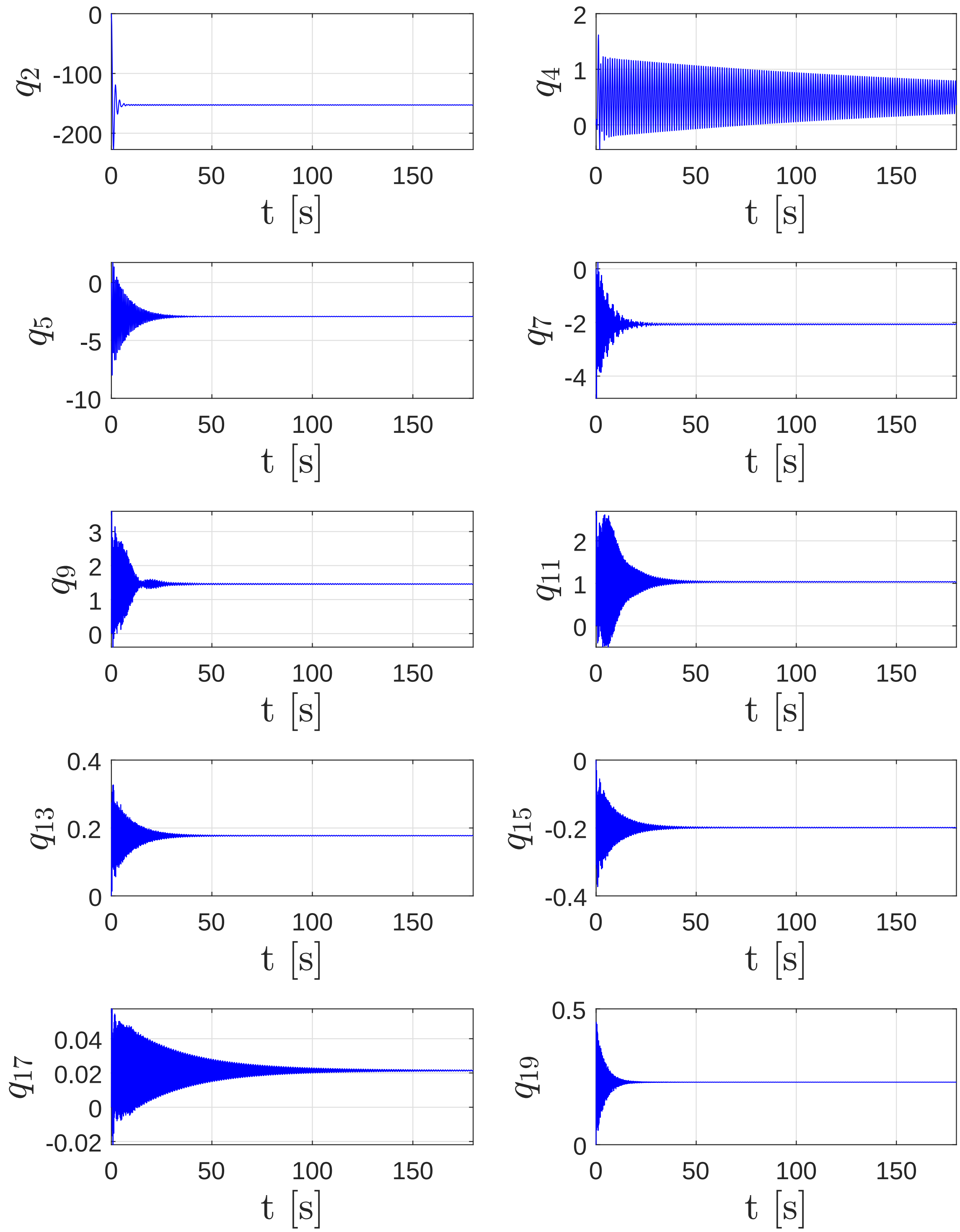

Figure D.1: Time responses of modes corresponding to the right joined-wing for the case with no structural damage at subcritical speed $V_\infty = 135$ m/s and freestream direction $(0°, 10°, 0°)$.

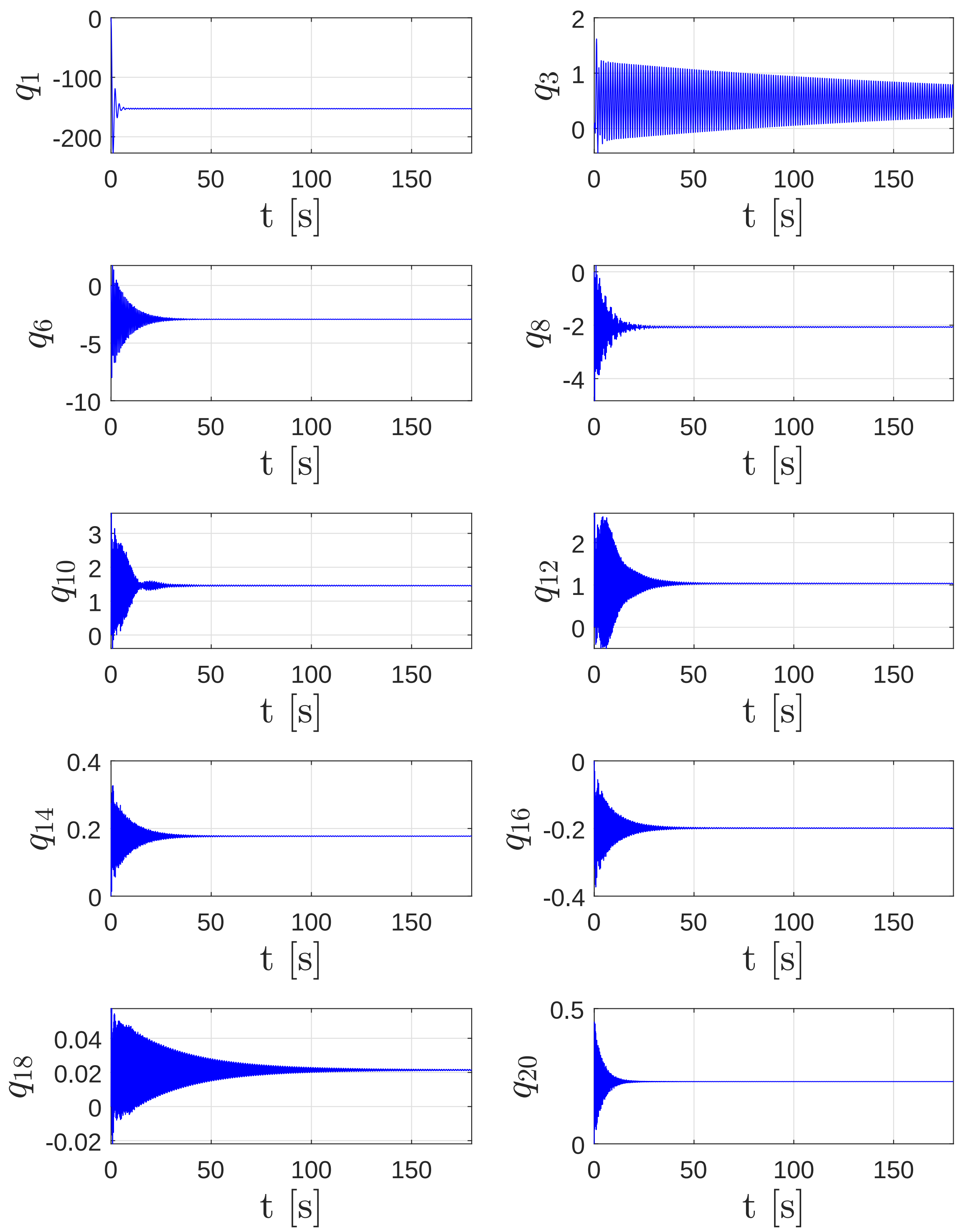

Figure D.2: Time responses of modes corresponding to the left joined-wing for the case with no structural damage at subcritical speed $V_\infty = 135\,\mathrm{m/s}$ and freestream direction $(0°, 10°, 0°)$.

point.

In Figures D.5 and D.6, the normalized FFTs of the modes corresponding to the right joined-wing and the left joined-wing, respectively, are presented. The free vibration frequencies are marked in the figures by dashed red lines. In all cases, a dominant frequency can be observed from a composition of two or more frequency signals of different frequencies.

The results shown in Figures D.7 and D.8 correspond to a case where the freestream speed is 153 m/s, which is close to the critical flutter speed. The time responses of all modes corresponding to the right joined-wing are shown in Figures D.7 and the time responses of all modes corresponding to the left joined-wing are shown in D.8. In the two figures, it can be observed that after the transient response, all modes begin to exhibit an oscillatory behavior of constant amplitude as time passes.

The projected responses in the phase planes of the right joined-wing and the left joined-wing are shown in Figures D.9 and D.10, respectively. In the responses of the second modes corresponding the right and left joined-wings, limit cycles can be seen.

In Figures D.11 and D.12, the normalized FFTs of the modes corresponding to the right joined-wing and the left joined-wing, respectively, are presented. The free vibration frequencies are marked in the figures by dashed red lines. At least two dominant frequencies can be observed from the first, third, fourth, seventh, eighth, and tenth modes of each joined-wing.

The results shown in Figures D.13 and D.14 correspond to a case where the freestream speed is 160 m/s, which is over the critical flutter speed. The time

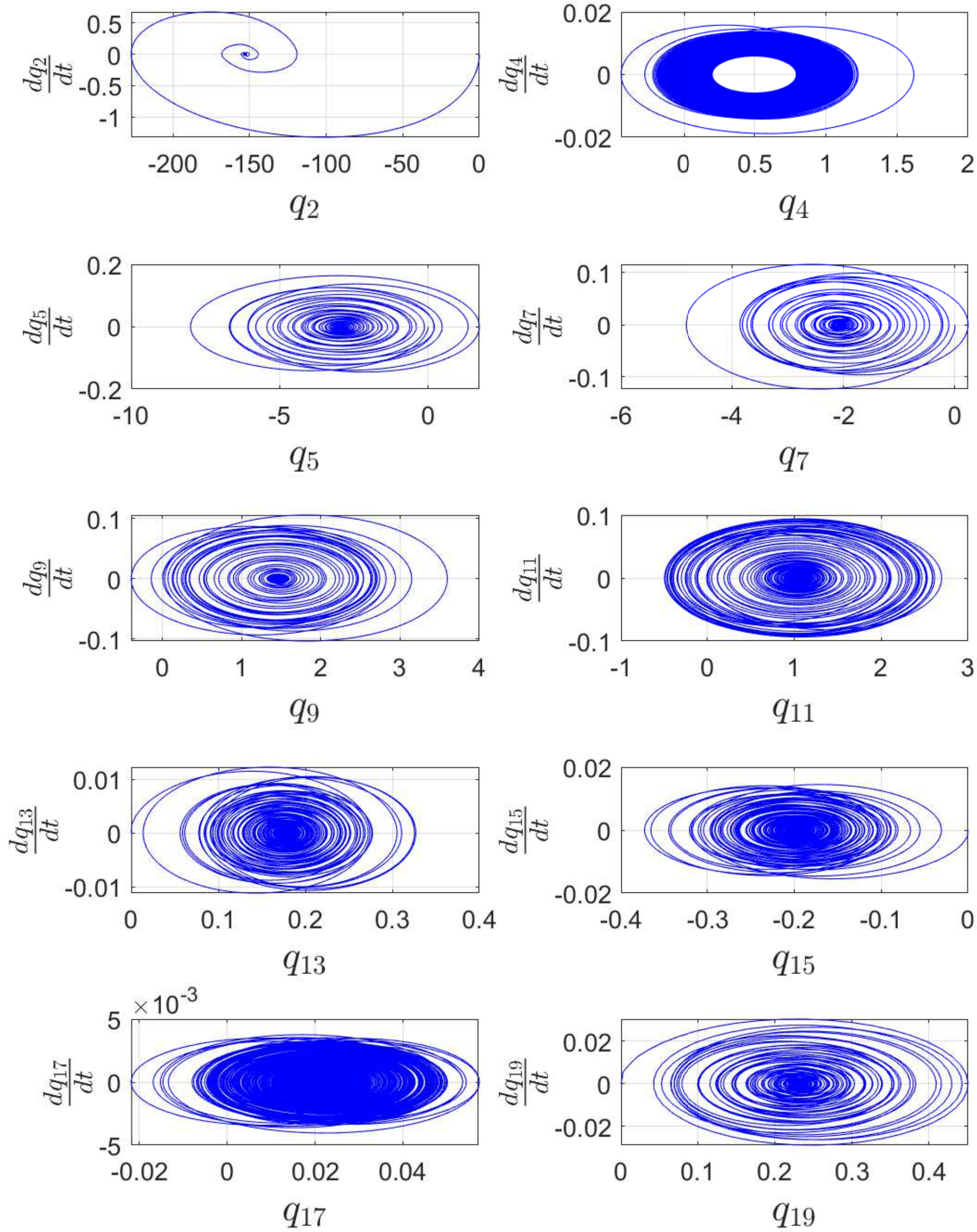

Figure D.3: At subcritical speed $V_\infty = 135\text{m/s}$, projections in phase planes of modes corresponding to the right joined-wing for the case with no structural damage and freestream direction $(0^\circ, 10^\circ, 0^\circ)$.

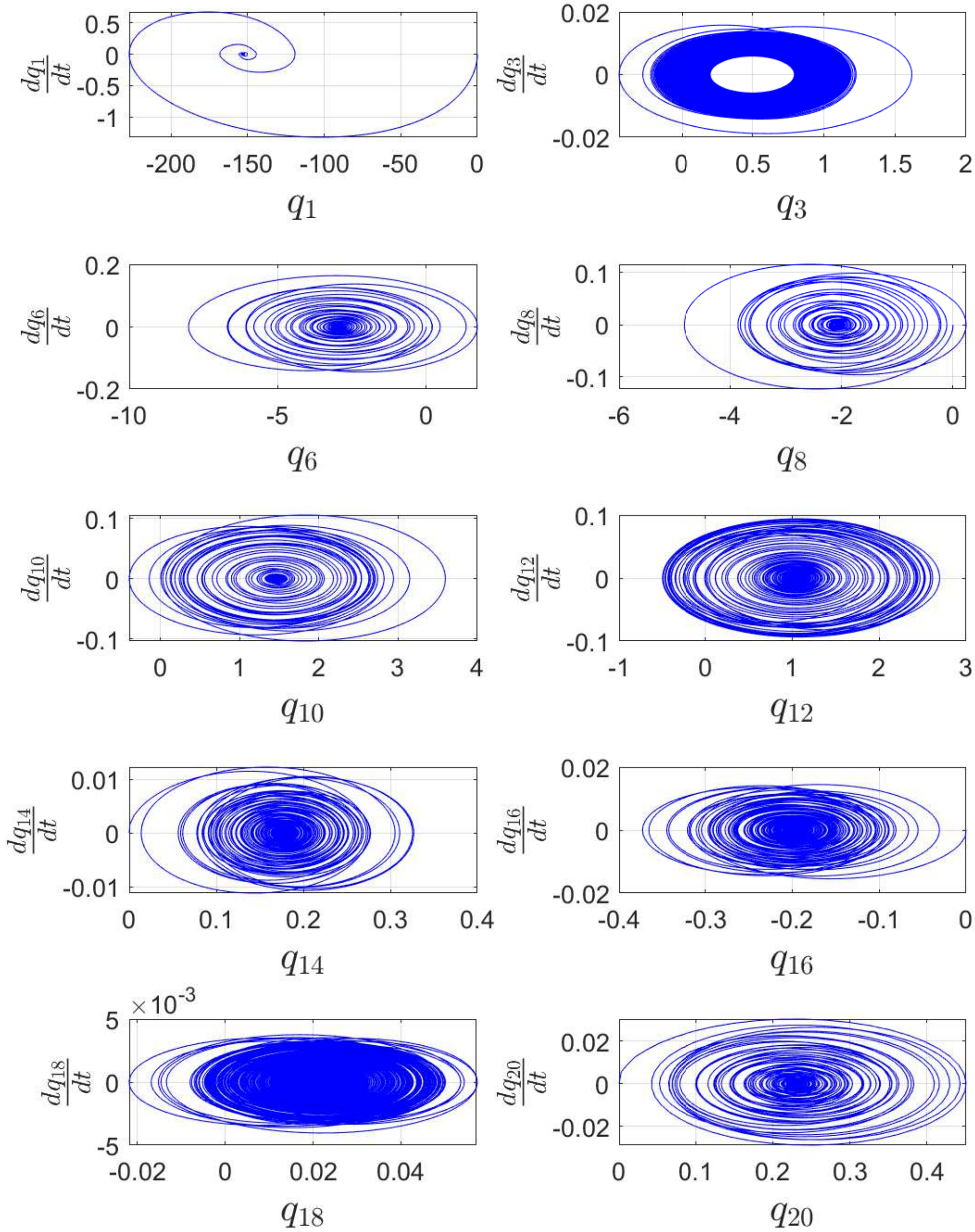

Figure D.4: At subcritical speed $V_\infty = 135\mathrm{m/s}$, projections in phase planes of modes corresponding to the left joined-wing for the case with no structural damage and freestream direction $(0^\circ, 10^\circ, 0^\circ)$.

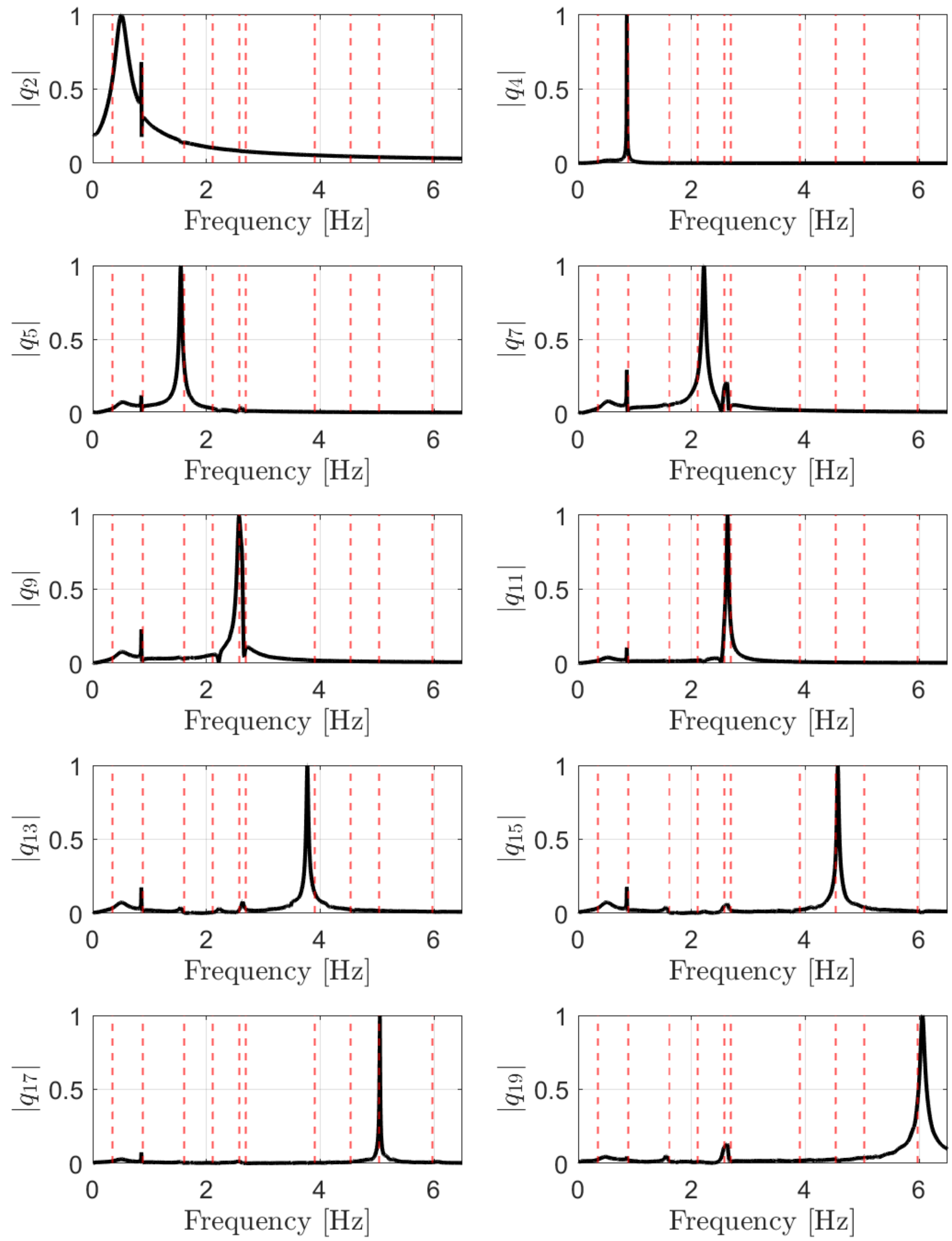

Figure D.5: At subcritical speed $V_\infty = 135\,\mathrm{m/s}$, responses in the frequency domain of modes corresponding to the right joined-wing for the case with no structural damage and freestream direction $(0°, 10°, 0°)$.

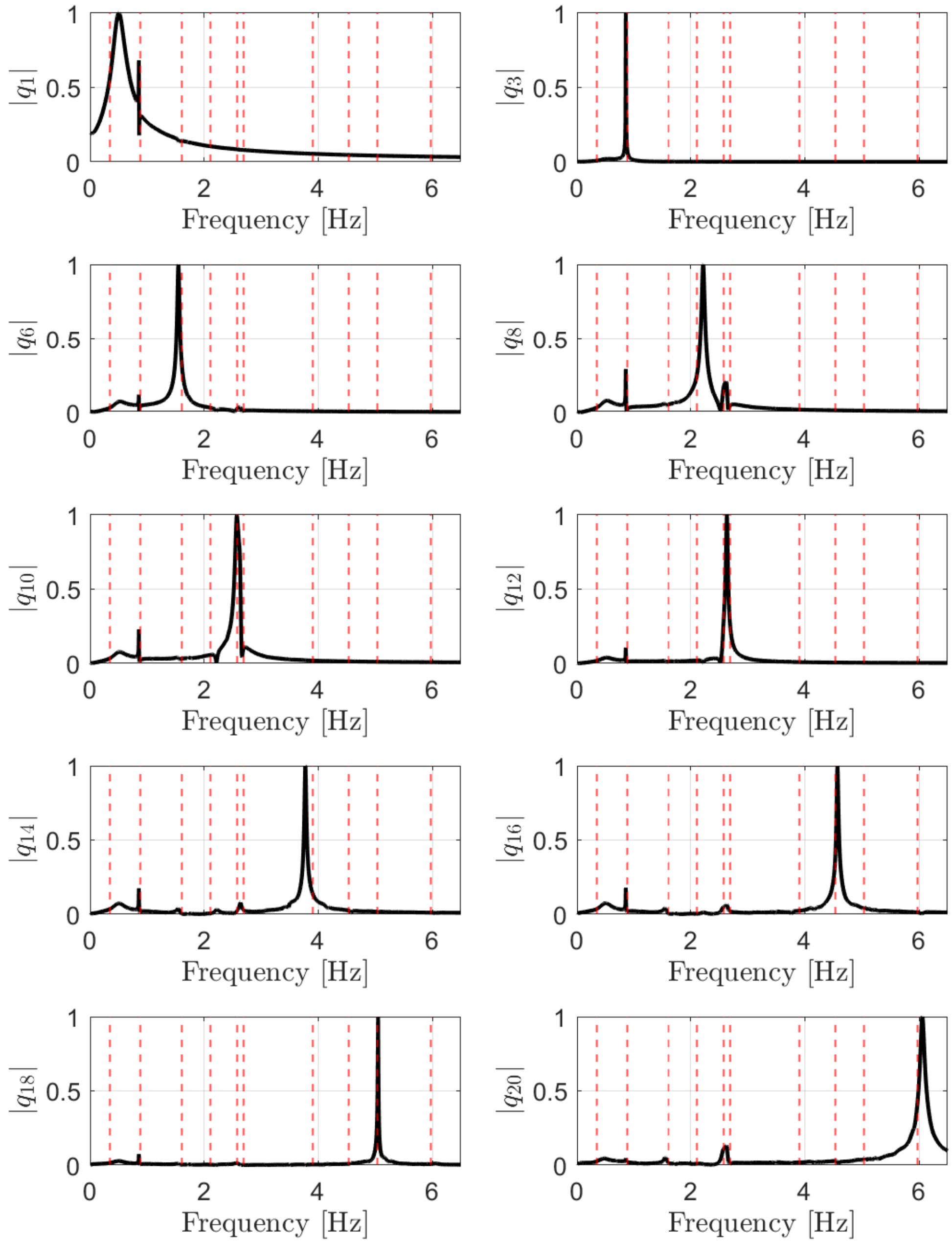

Figure D.6: At subcritical speed $V_\infty = 135$m/s, responses in the frequency domain of modes corresponding to the left joined-wing for the case with no structural damage and freestream direction $(0°, 10°, 0°)$.

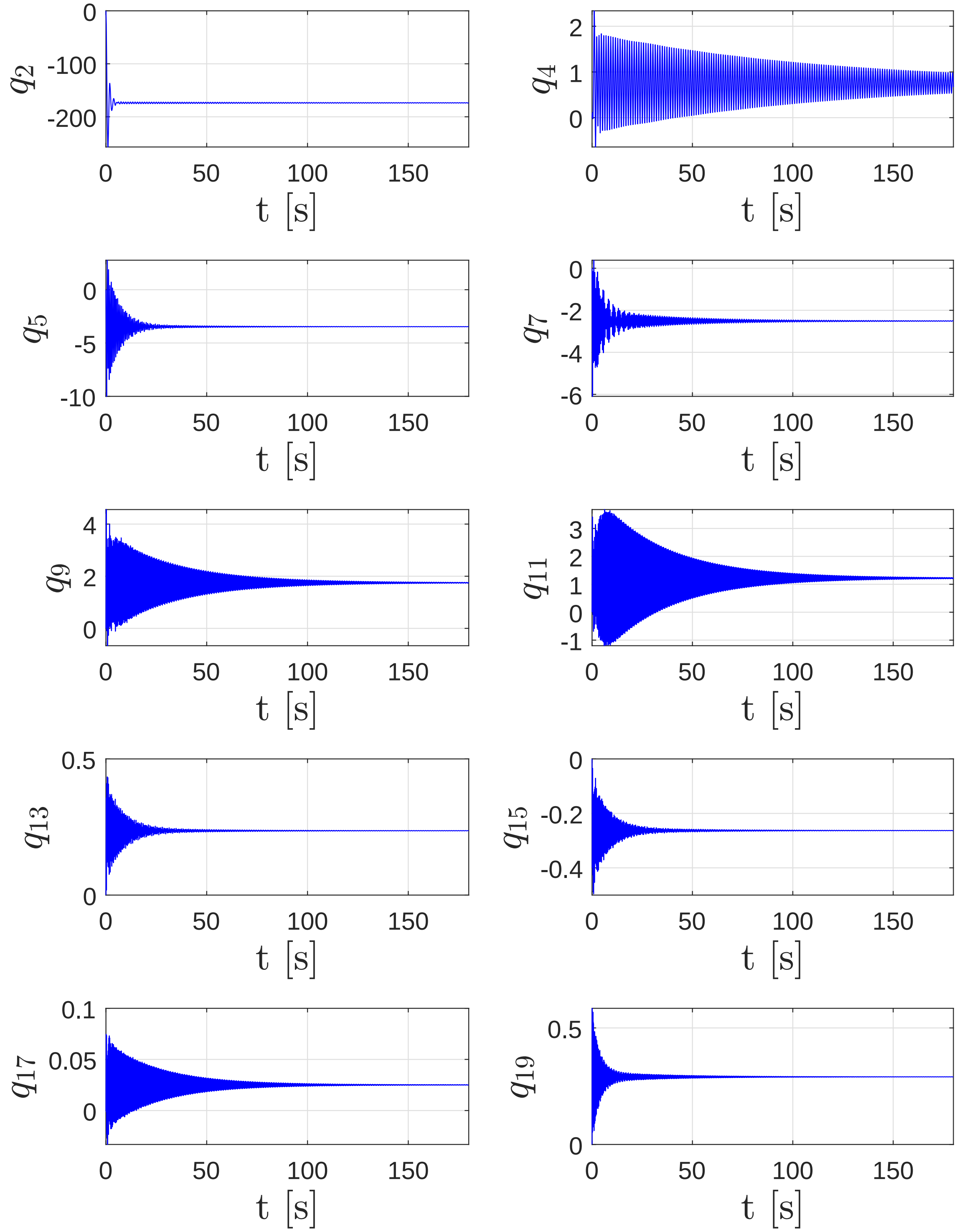

Figure D.7: Time responses of modes corresponding to the right joined-wing for the case with no structural damage at critical speed $V_\infty = 153\,\mathrm{m/s}$ and freestream direction $(0^\circ, 10^\circ, 0^\circ)$.

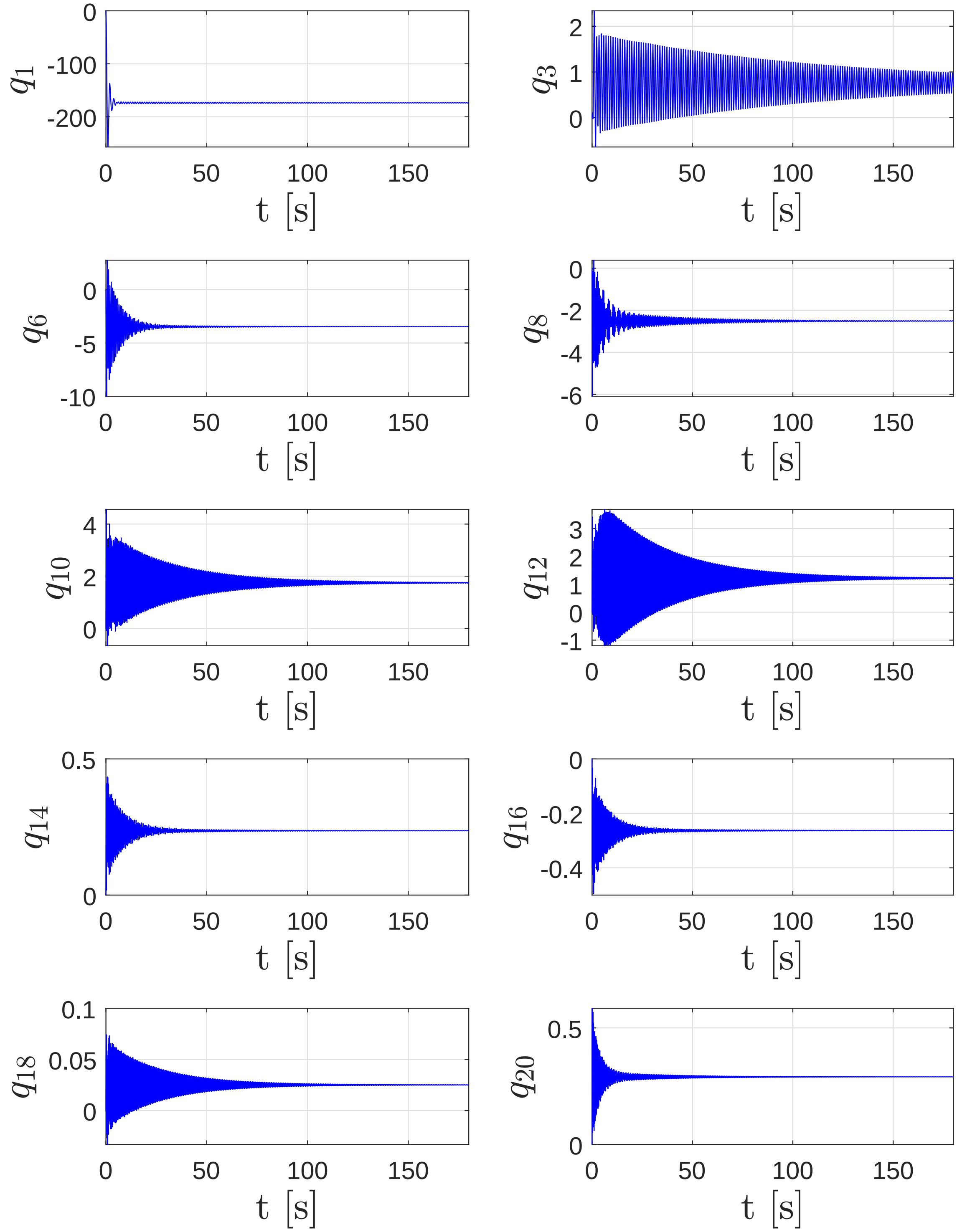

Figure D.8: Time responses of modes corresponding to the left joined-wing for the case with no structural damage at critical speed $V_\infty = 153$ m/s and freestream direction $(0°, 10°, 0°)$.

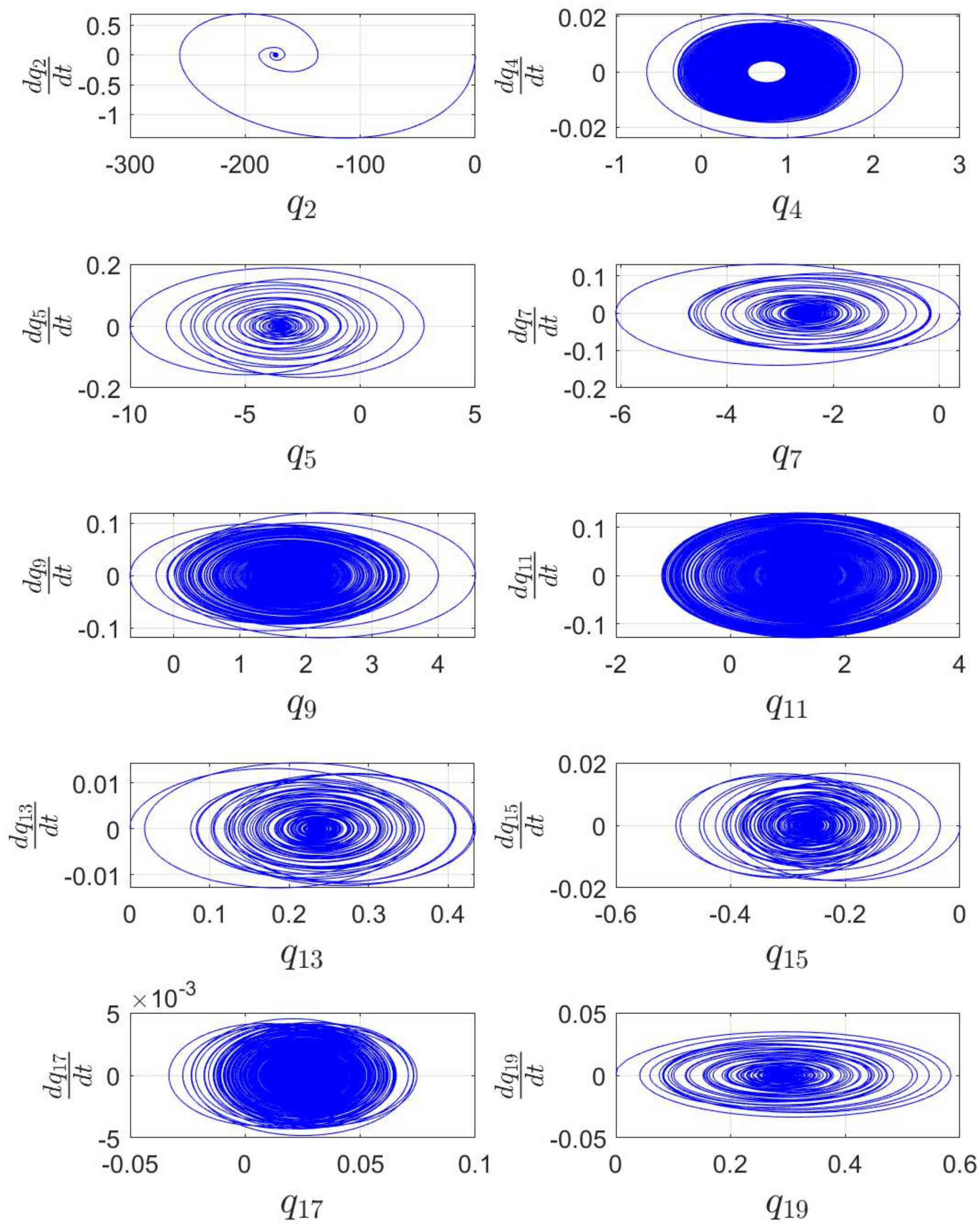

Figure D.9: At critical speed $V_\infty = 153\,\mathrm{m/s}$, projections in phase planes of modes corresponding to the right joined-wing for the case with no structural damage and freestream direction $(0°, 10°, 0°)$.

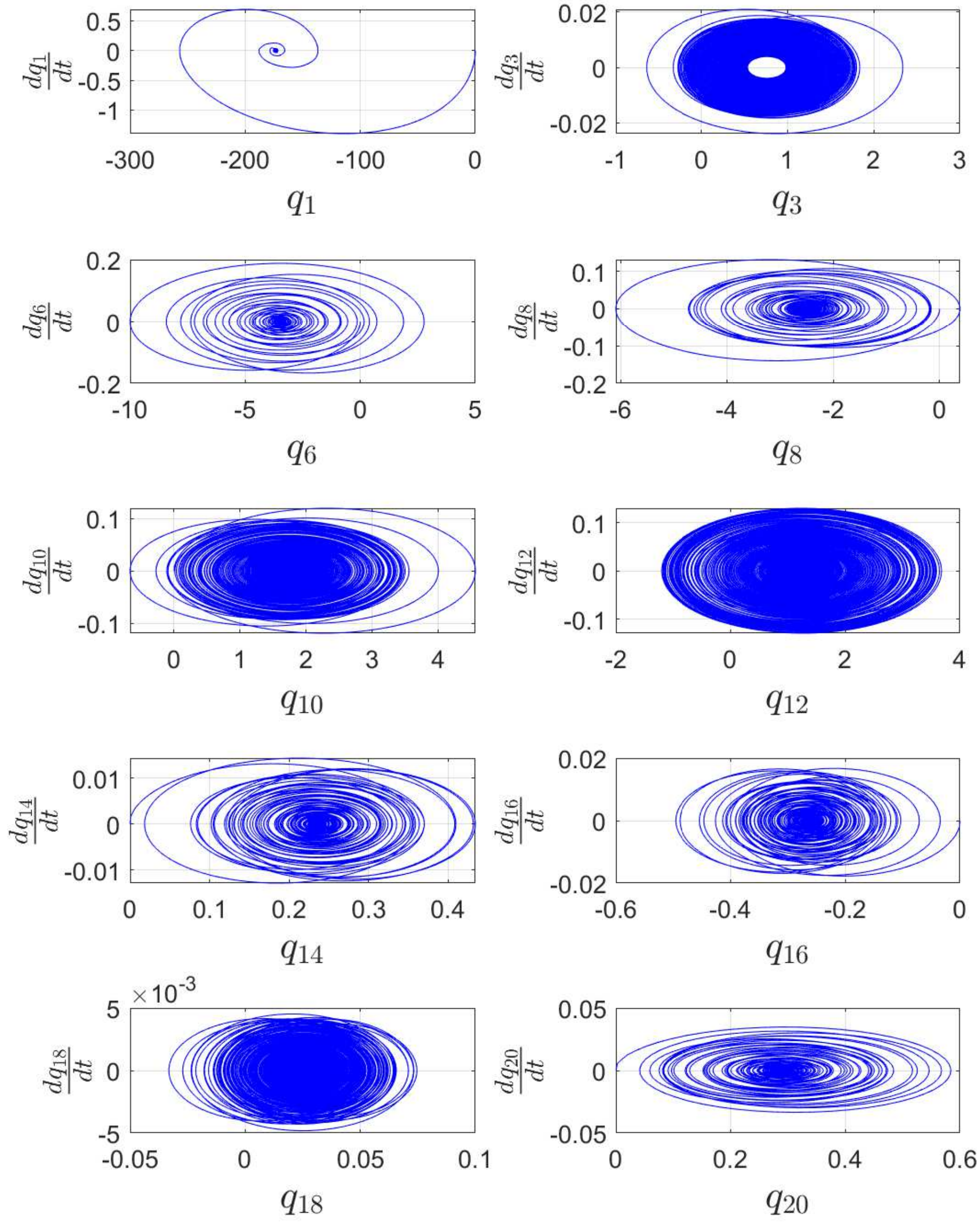

Figure D.10: At critical speed $V_\infty = 153\,\mathrm{m/s}$, projections in phase planes of modes corresponding to the left joined-wing for the case with no structural damage and freestream direction $(0^\circ, 10^\circ, 0^\circ)$.

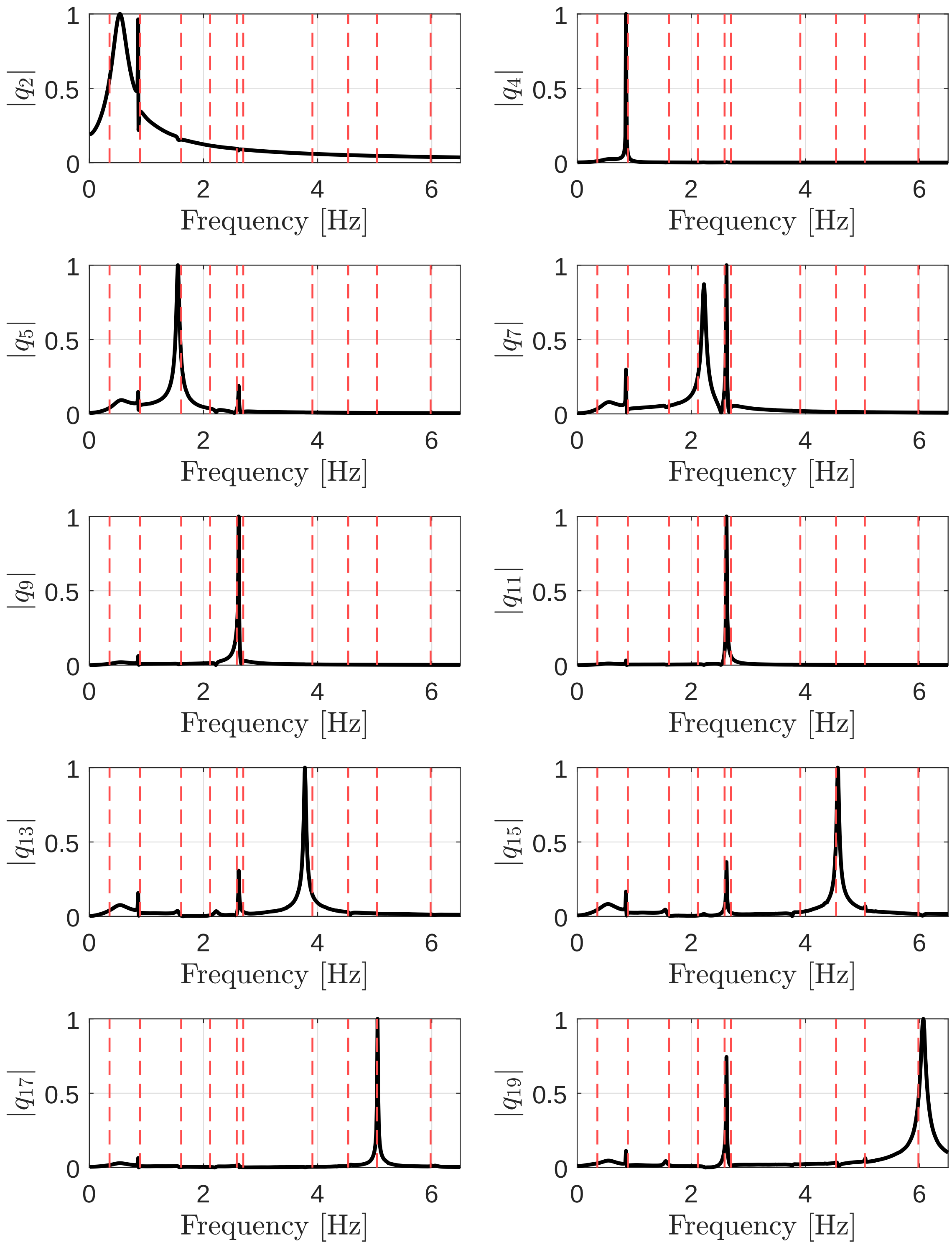

Figure D.11: At critical speed $V_\infty = 153\,\mathrm{m/s}$, responses in the frequency domain of modes corresponding to the right joined-wing for the case with no structural damage and freestream direction $(0°, 10°, 0°)$.

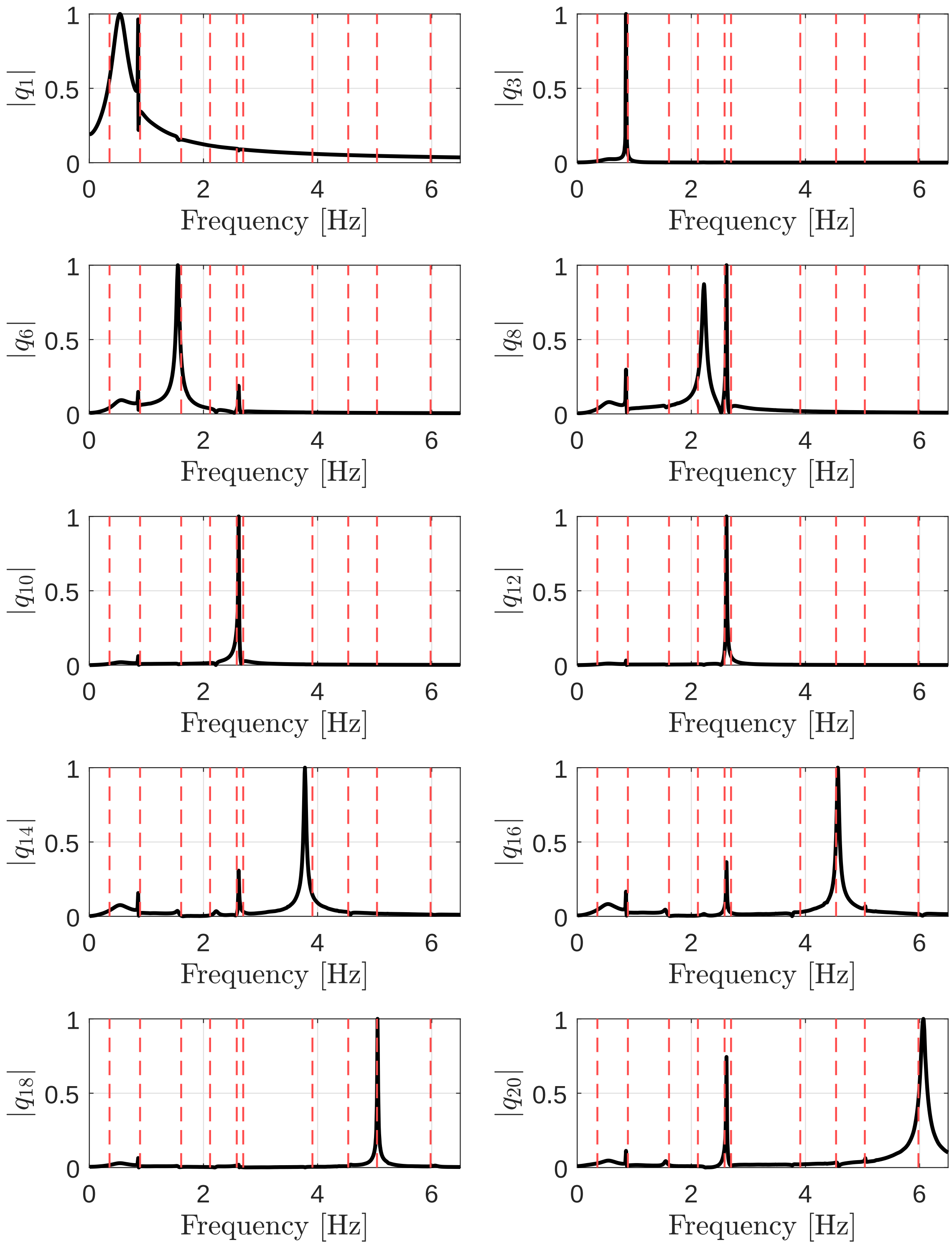

Figure D.12: At critical speed $V_\infty = 153\,\mathrm{m/s}$, responses in the frequency domain of modes corresponding to the left joined-wing for the case with no structural damage and freestream direction $(0°, 10°, 0°)$.

responses of all modes corresponding to the right joined-wing are shown in Figures D.13 and the time responses of all modes corresponding to the left joined-wing are shown in D.14. In the two figures, it can be observed that after the transient response, all modes exhibit an oscillatory behavior that increases in amplitude as time passes.

The projected responses in the phase planes of the right joined-wing and the left joined-wing are shown in Figures D.15 and D.16, respectively. In the responses of the about half of the modes corresponding the right and left joined-wings, limit cycles can be seen.

In Figures D.17 and D.18, the normalized FFTs of the modes corresponding to the right joined-wing and the left joined-wing, respectively, are presented. The free vibration frequencies are marked in the figures by dashed red lines. Except for the first, second, and ninth modes of each joined-wing, a predominant frequency of 2.617 Hz can be observed.

D.2 Case with Bending Damage: Freestream Direction $(0°, 5°, 0°)$

The results shown in Figures D.19 and D.20 correspond to a case where the freestream speed is 140 m/s, which is below the critical flutter speed. The time responses of all modes corresponding to the right joined-wing are shown in Figures D.19 and the time responses of all modes corresponding to the left joined-wing are shown in D.20. In the two figures, it can be observed that after a brief transient, all modes exhibit an oscillatory behavior that decreases in amplitude as time passes.

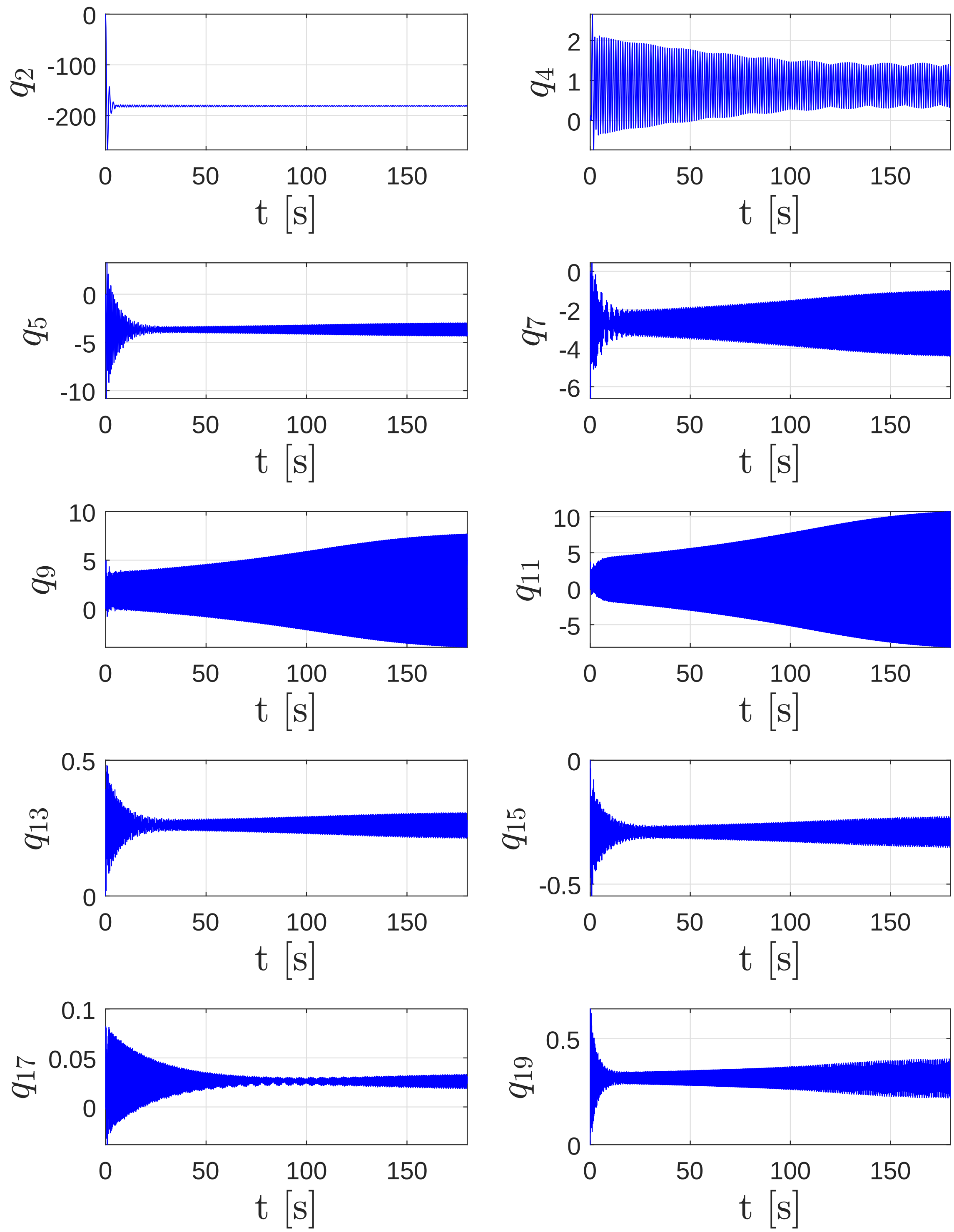

Figure D.13: Time responses of modes corresponding to the right joined-wing for the case with no structural damage at supercritical speed $V_\infty = 160\,\mathrm{m/s}$ and freestream direction $(0^\circ, 10^\circ, 0^\circ)$.

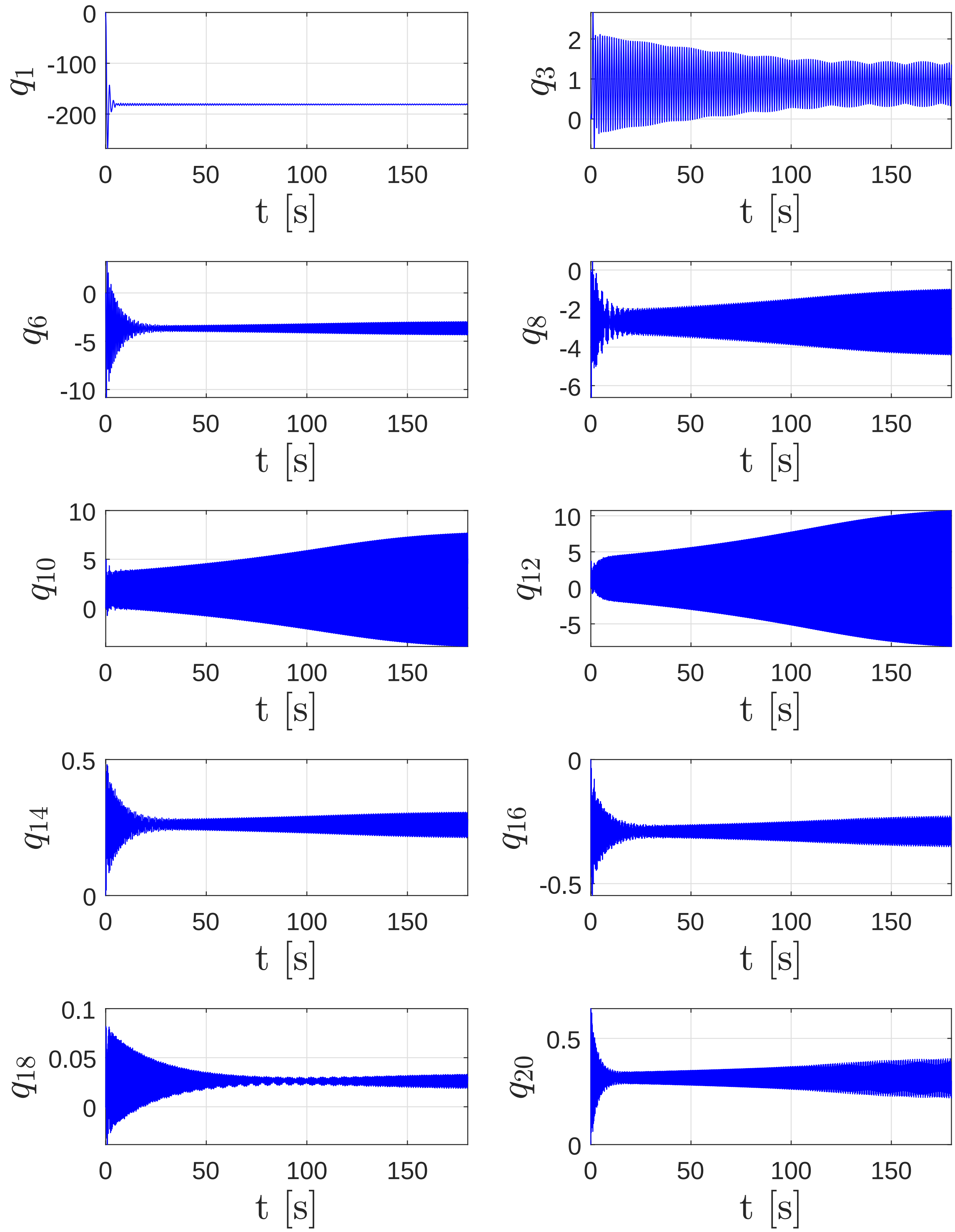

Figure D.14: Time responses of modes corresponding to the left joined-wing for the case with no structural damage at supercritical speed $V_\infty = 160\,\mathrm{m/s}$ and freestream direction $(0°, 10°, 0°)$.

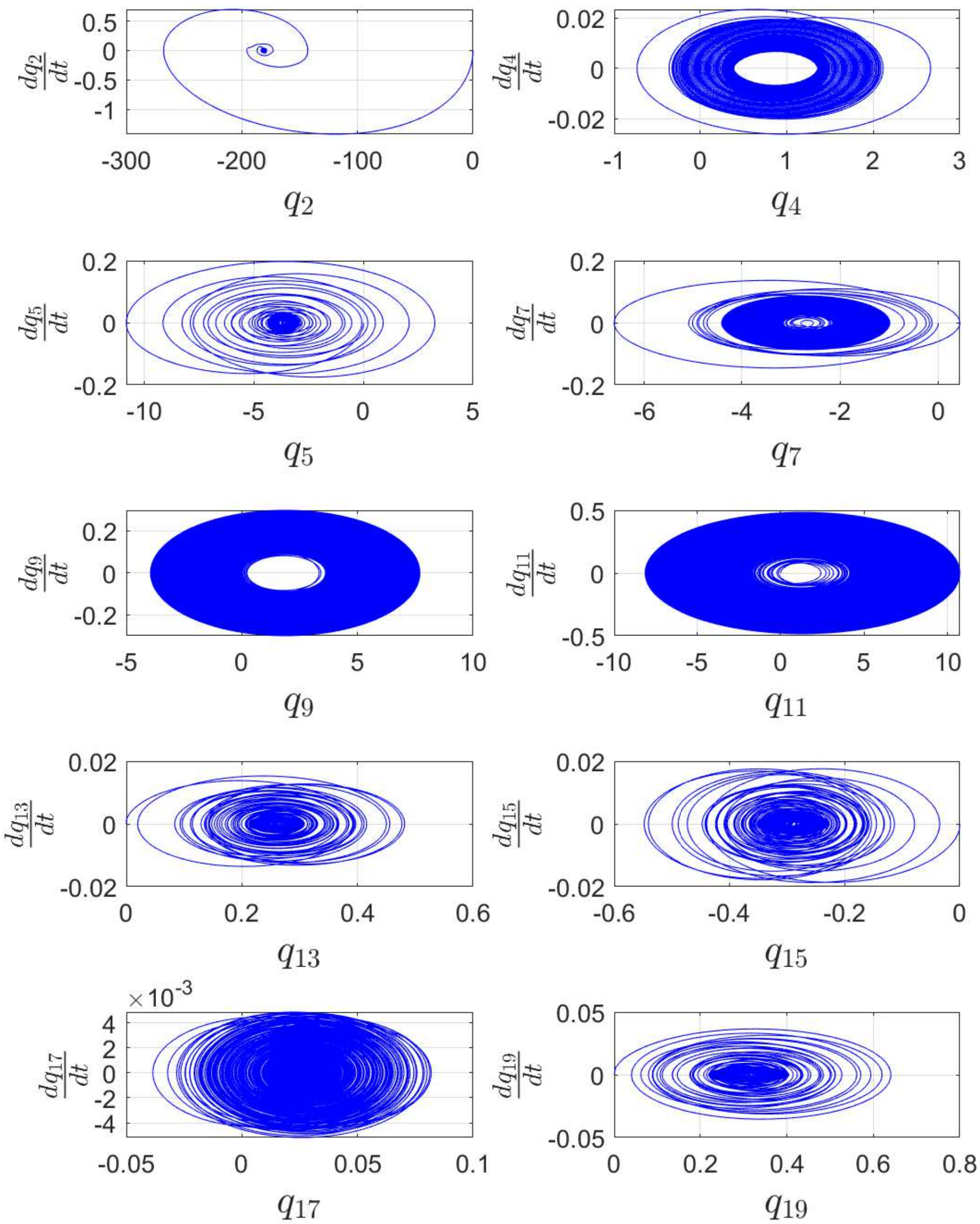

Figure D.15: At supercritical speed $V_\infty = 160\,\mathrm{m/s}$, projections in phase planes of modes corresponding to the right joined-wing for the case with no structural damage and freestream direction $(0^\circ, 10^\circ, 0^\circ)$.

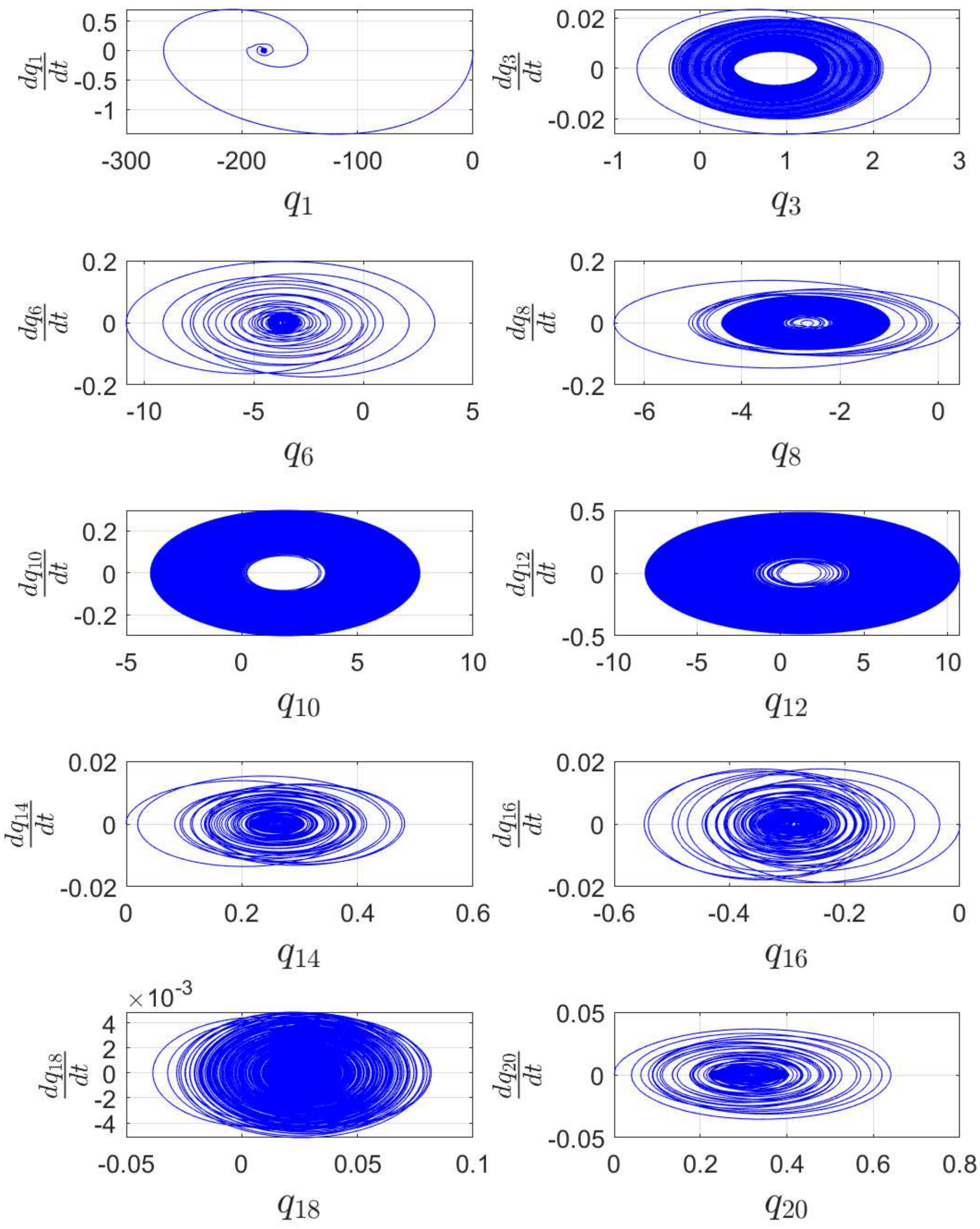

Figure D.16: At supercritical speed $V_\infty = 160\,\mathrm{m/s}$, projections in phase planes of modes corresponding to the left joined-wing for the case with no structural damage and freestream direction $(0°, 10°, 0°)$.

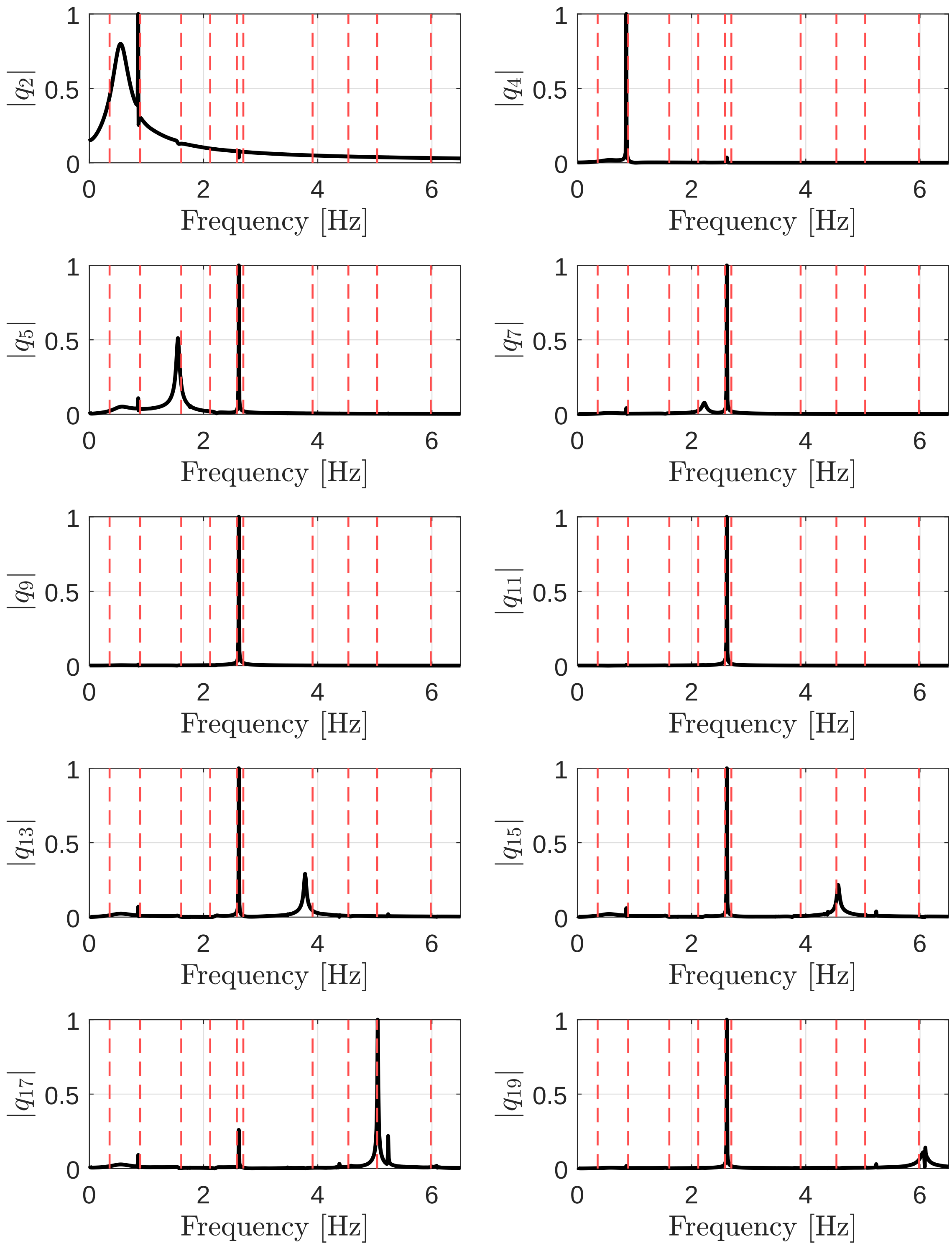

Figure D.17: At supercritical speed $V_\infty = 160$ m/s, responses in the frequency domain of modes corresponding to the right joined-wing for the case with no structural damage and freestream direction $(0°, 10°, 0°)$.

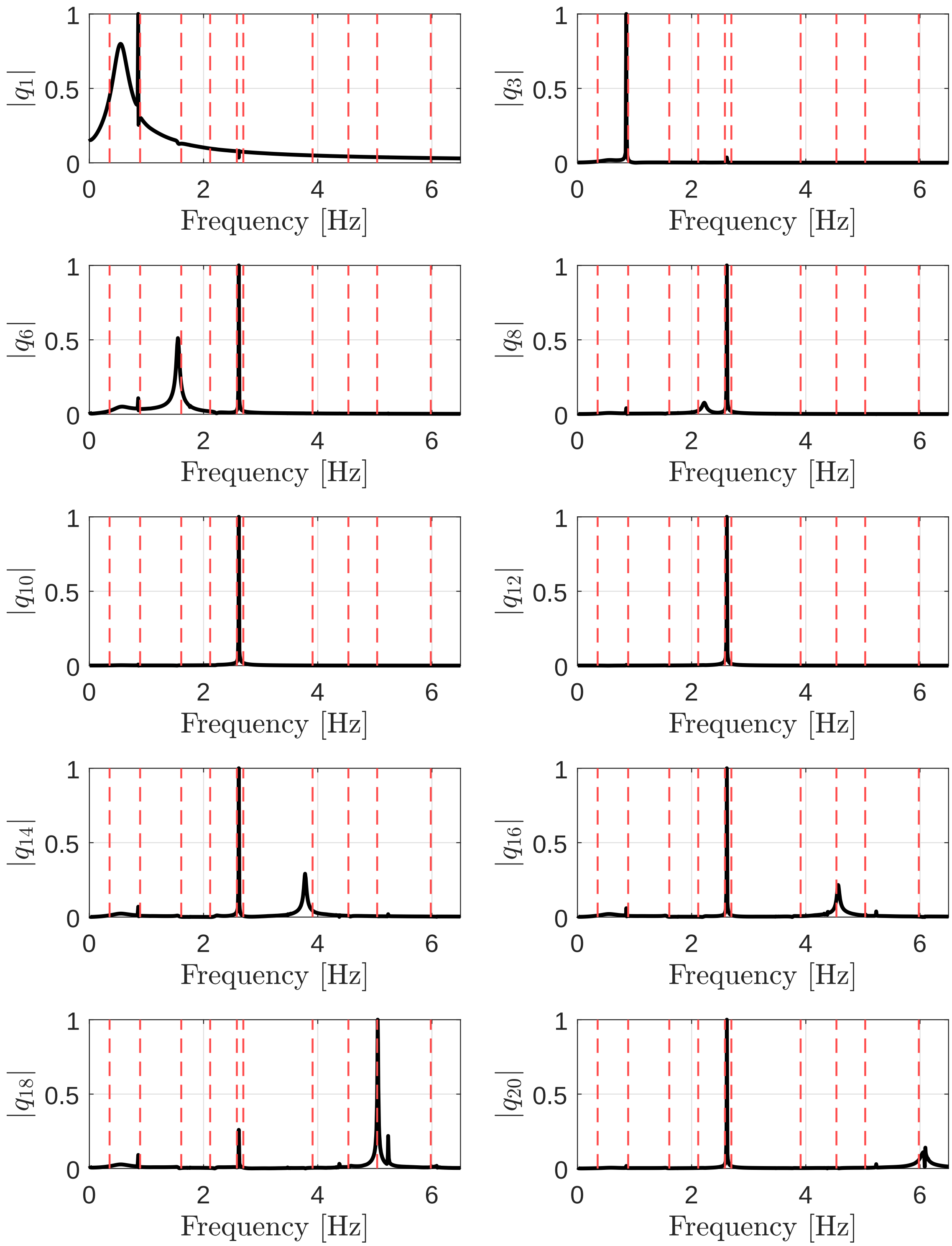

Figure D.18: At supercritical speed $V_\infty = 160$ m/s, responses in the frequency domain of modes corresponding to the left joined-wing for the case with no structural damage and freestream direction $(0°, 10°, 0°)$.

This is caused by the presence of just aerodynamic damping.

The projected responses in the phase planes of the right joined-wing and the left joined-wing are shown in Figures D.21 and D.22, respectively. Stable focus type of characteristics can be observed in all modes as the spirals converge to an equilibrium point.

In Figures D.23 and D.24, the normalized FFTs of the modes corresponding to the right joined-wing and the left joined-wing, respectively, are presented. The free vibration frequencies are marked in the figures by dashed red lines. In all cases, a dominant frequency can be observed from a composition of two or more signals of different frequencies.

The results shown in Figures D.25 and D.26 correspond to a case where the freestream speed is 150 m/s, which is close to the critical flutter speed. The time responses of all modes corresponding to the right joined-wing are shown in Figures D.25 and the time responses of all modes corresponding to the left joined-wing are shown in D.26. In the two figures, it can be observed that after the transient response, all modes begin to exhibit an oscillatory behavior of constant amplitude as time passes.

The projected responses in the phase planes of the right joined-wing and the left joined-wing are shown in Figures D.27 and D.28, respectively. In the responses of the second modes corresponding the right and left joined-wings, limit cycles can be seen.

In Figures D.29 and D.30, the normalized FFTs of the modes corresponding to the right joined-wing and the left joined-wing, respectively, are presented. The

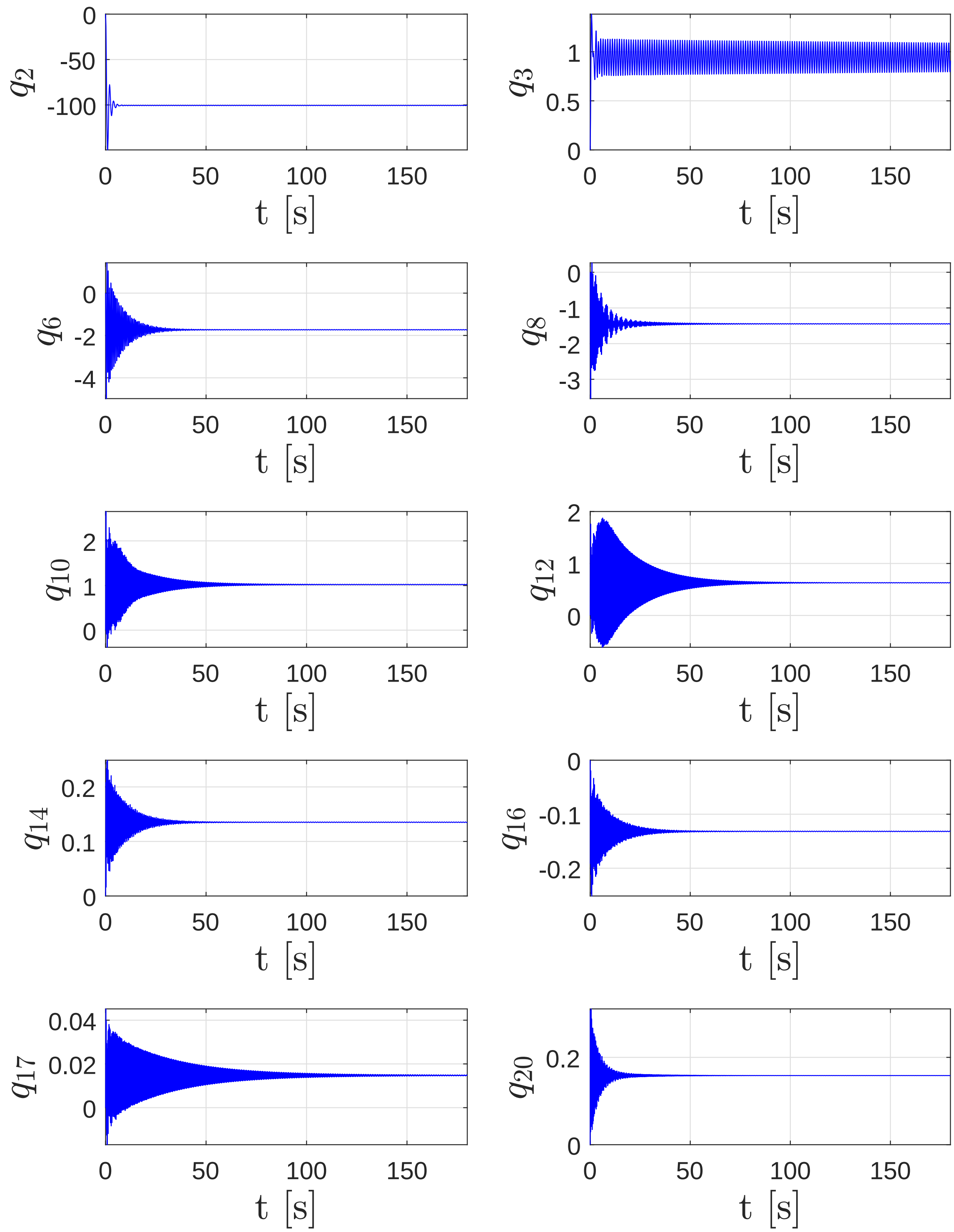

Figure D.19: Time responses of modes corresponding to the right joined-wing for the case with structural bending damage at subcritical speed $V_\infty = 140$ m/s and freestream direction $(0°, 5°, 0°)$.

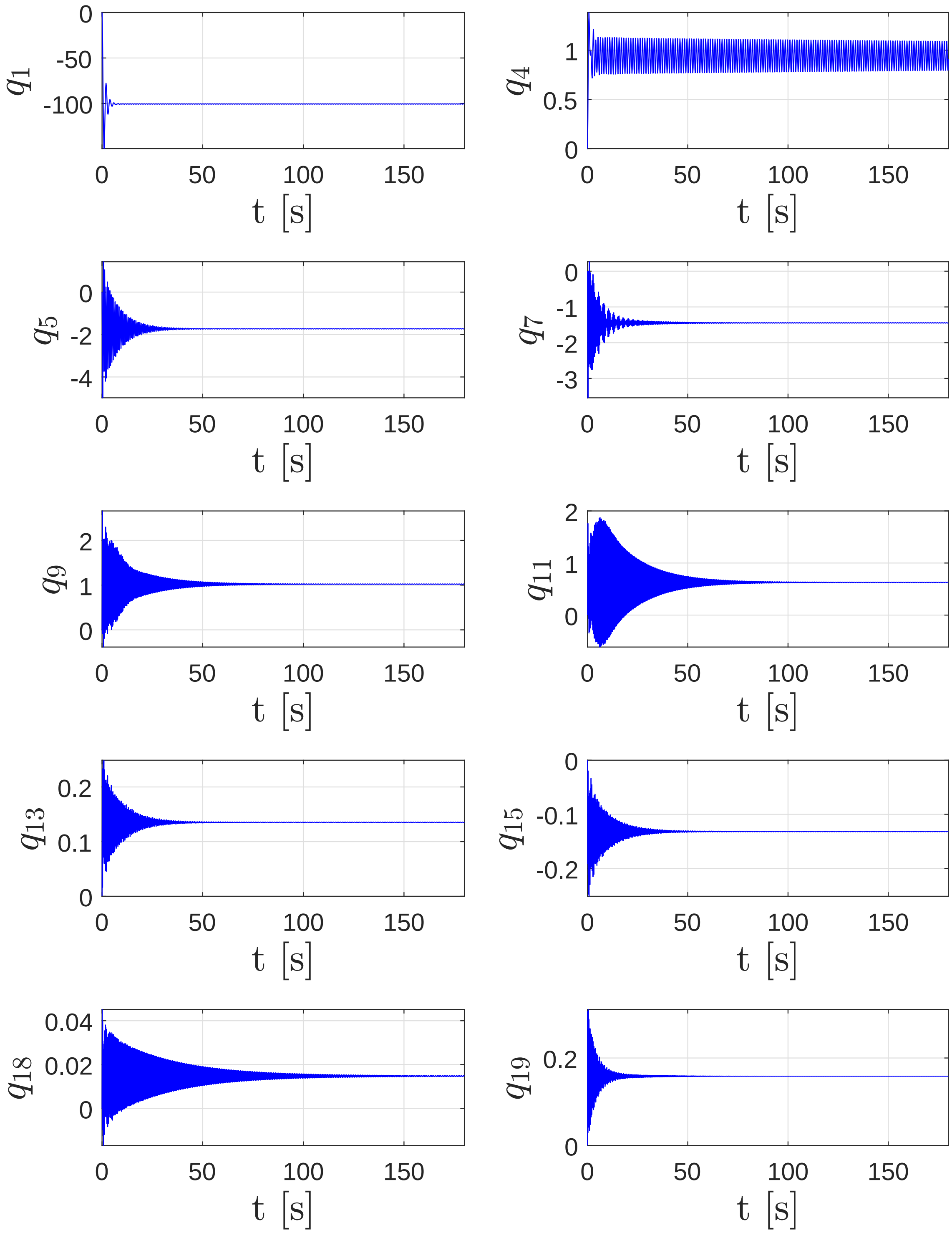

Figure D.20: Time responses of modes corresponding to the left joined-wing for the case with structural bending damage at subcritical speed $V_\infty = 140$ m/s and freestream direction $(0°, 5°, 0°)$.

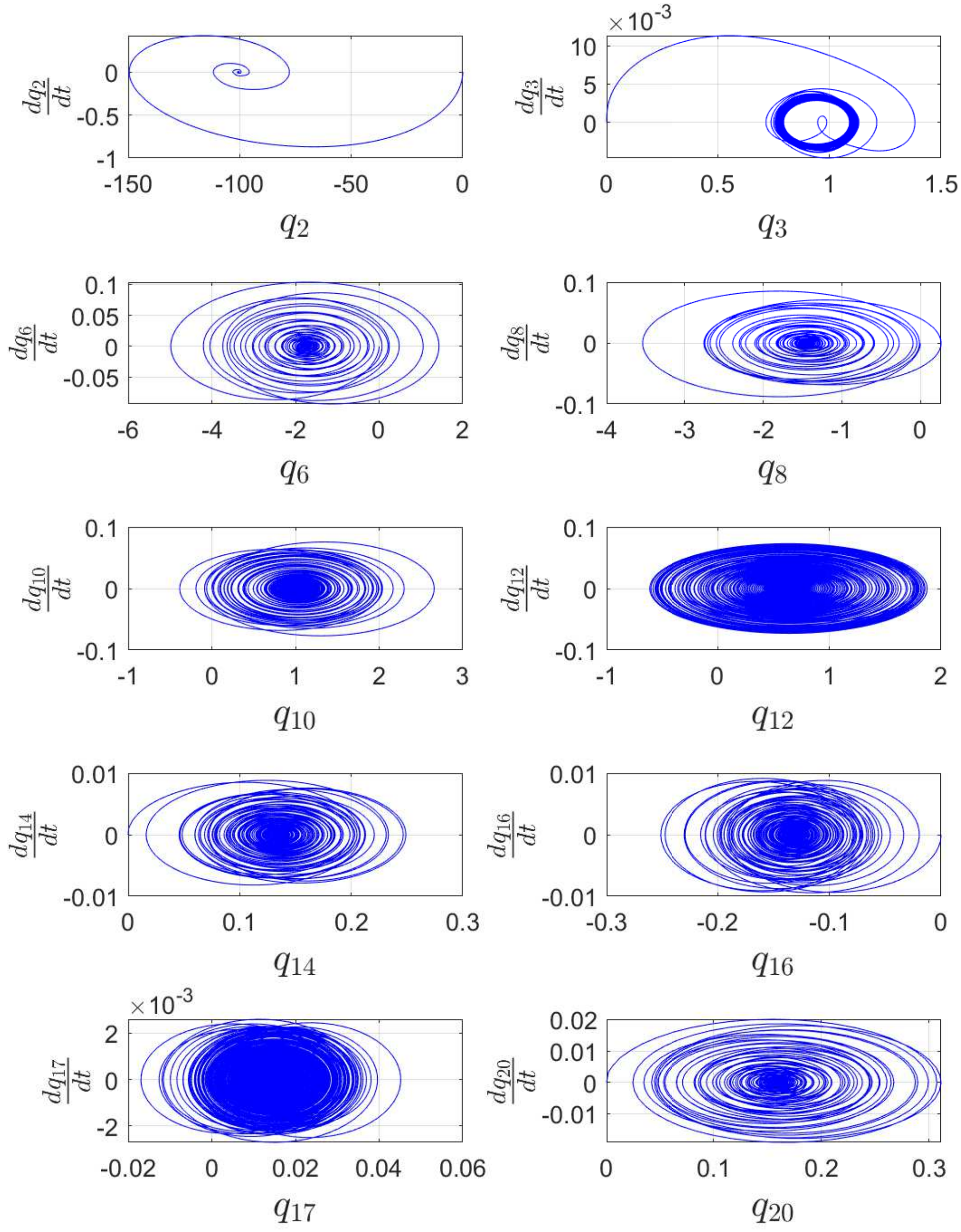

Figure D.21: At subcritical speed $V_\infty = 140$ m/s, projections in phase planes of modes corresponding to the right joined-wing for the case with structural bending damage and freestream direction $(0°, 5°, 0°)$.

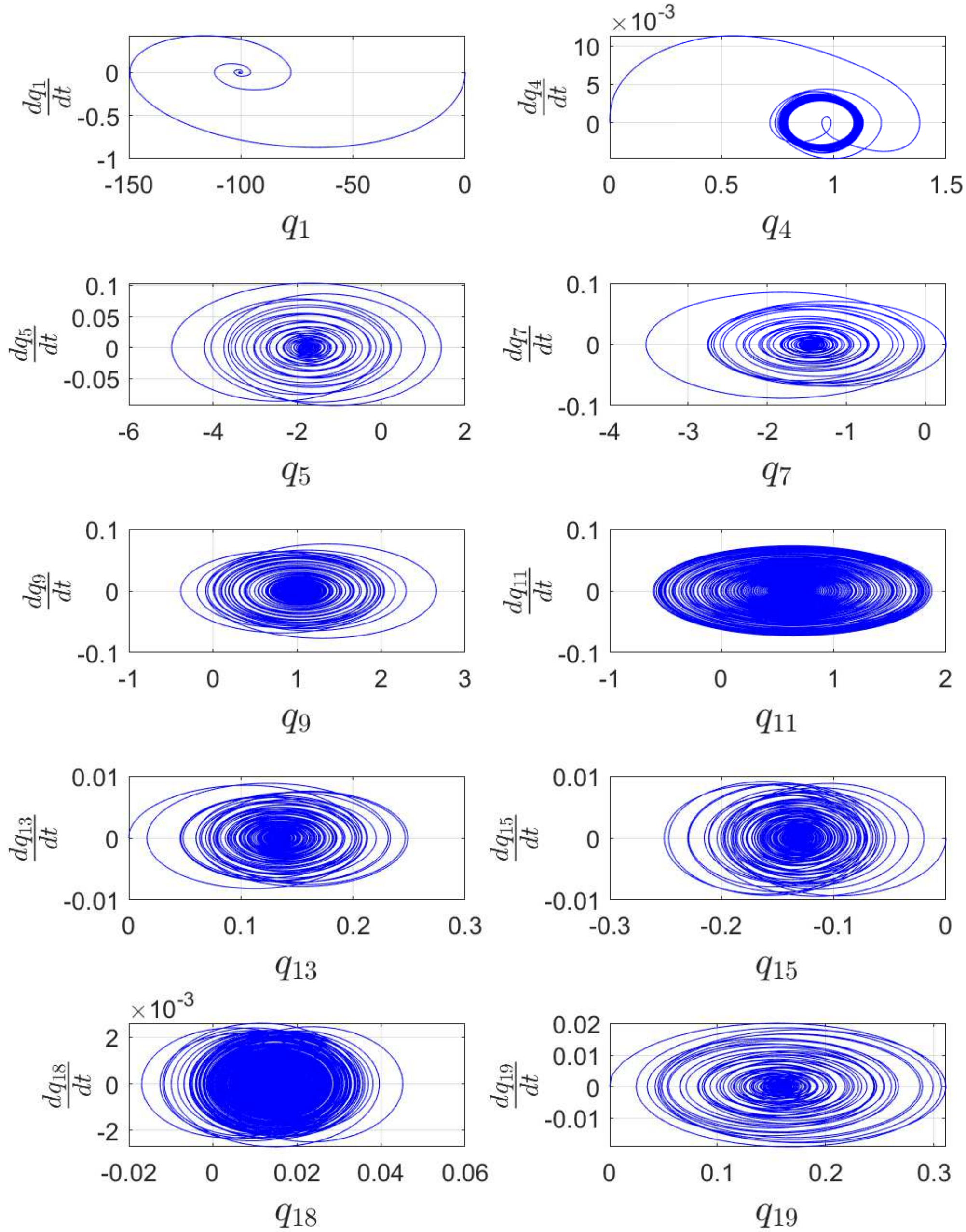

Figure D.22: At subcritical speed $V_\infty = 140$ m/s, projections in phase planes of modes corresponding to the left joined-wing for the case with structural bending damage and freestream direction $(0°, 5°, 0°)$.

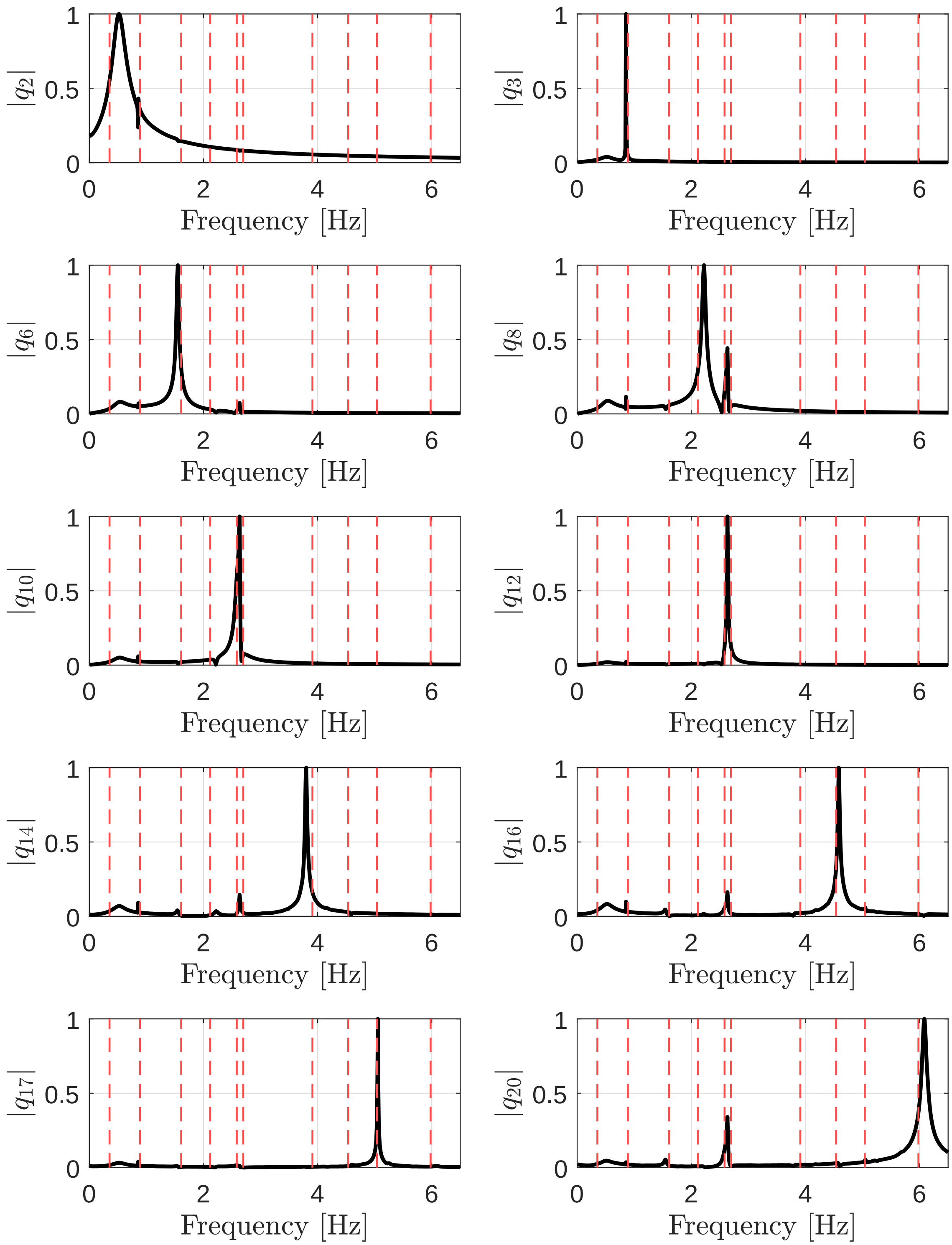

Figure D.23: At subcritical speed $V_\infty = 140\,\mathrm{m/s}$, responses in the frequency domain of modes corresponding to the right joined-wing for the case with structural bending damage and freestream direction $(0°, 5°, 0°)$.

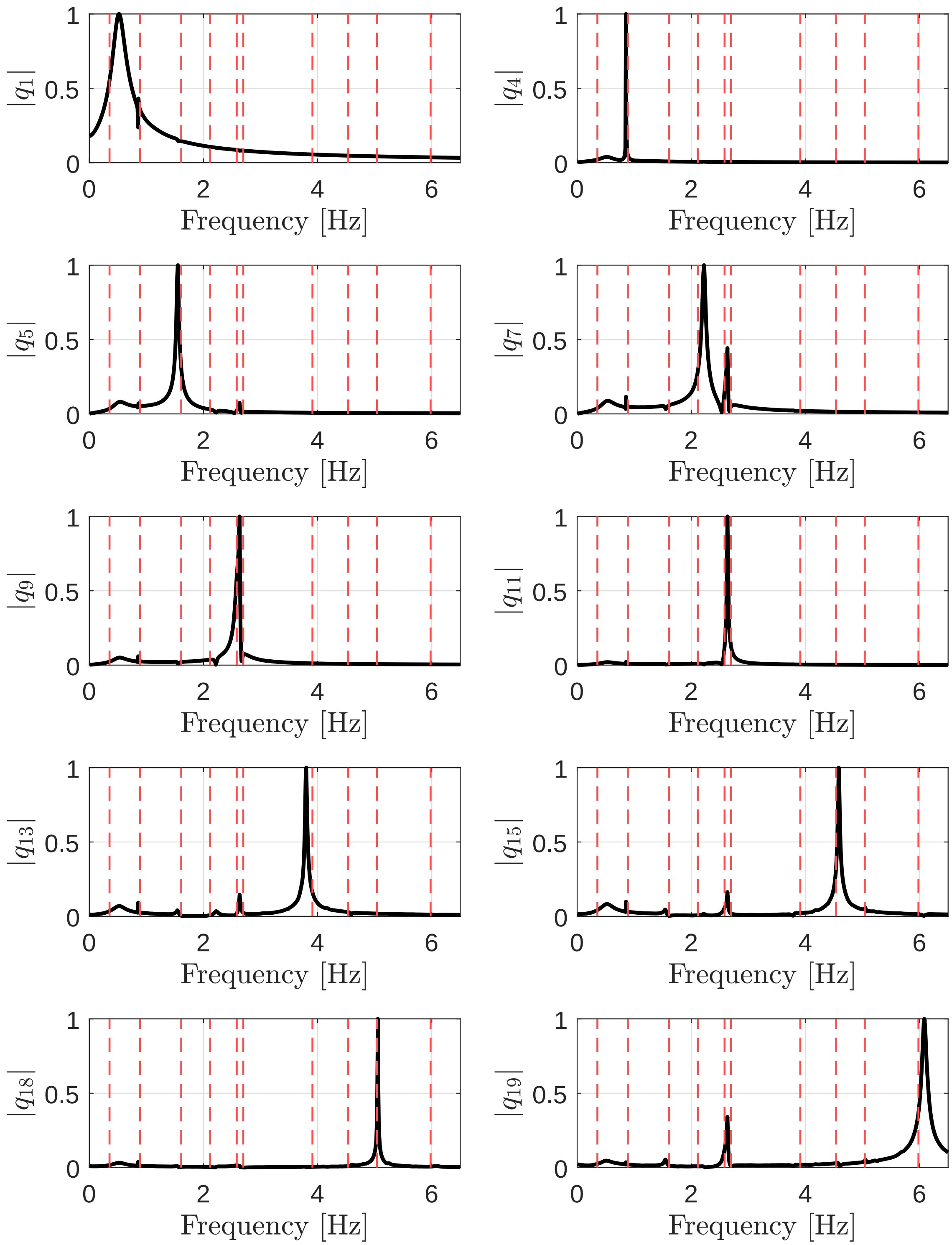

Figure D.24: At subcritical speed $V_\infty = 140\,\mathrm{m/s}$, responses in the frequency domain of modes corresponding to the left joined-wing for the case with structural bending damage and freestream direction $(0°, 5°, 0°)$.

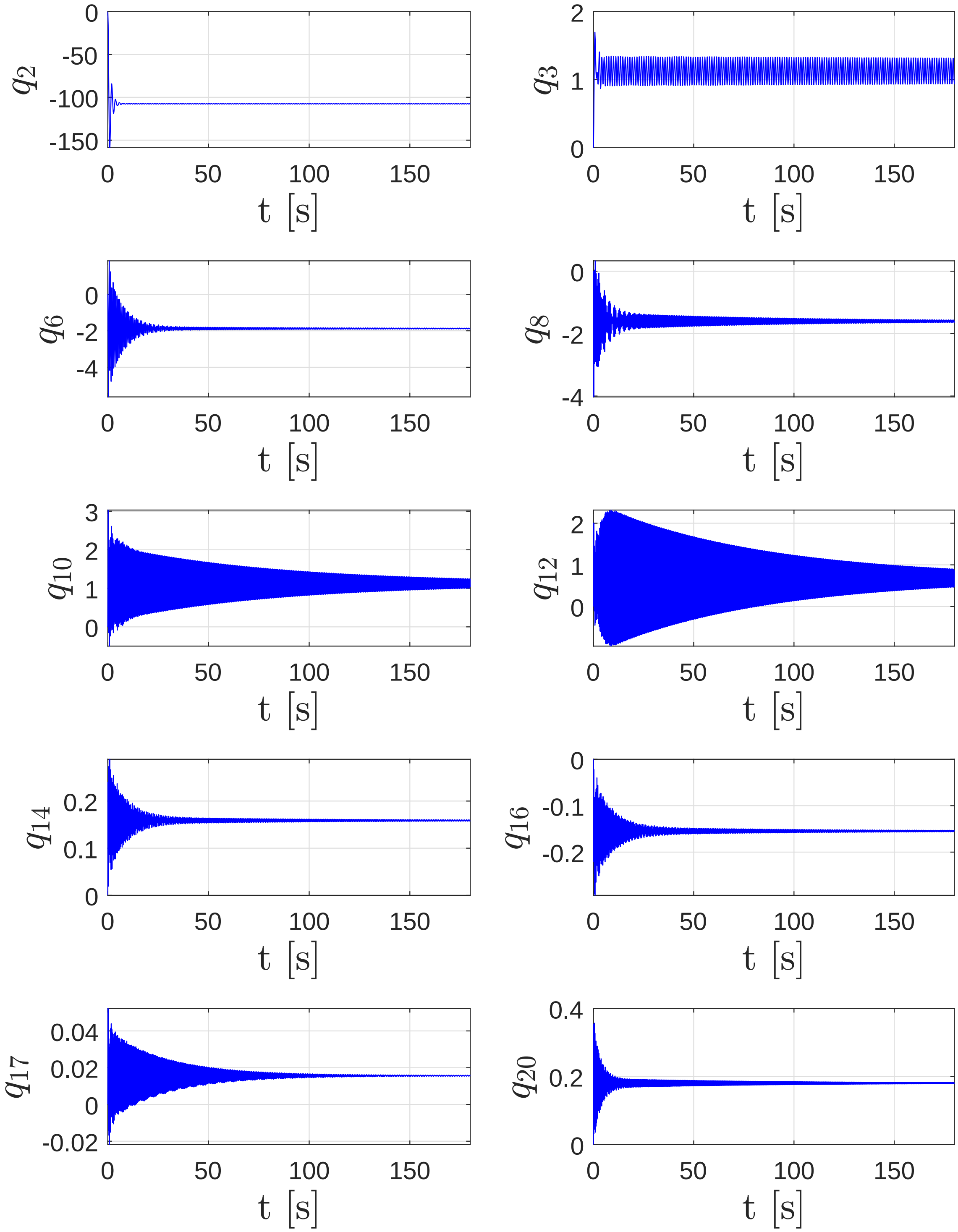

Figure D.25: Time responses of modes corresponding to the right joined-wing for the case with structural bending damage at critical speed $V_\infty = 150\,\mathrm{m/s}$ and freestream direction $(0°, 5°, 0°)$.

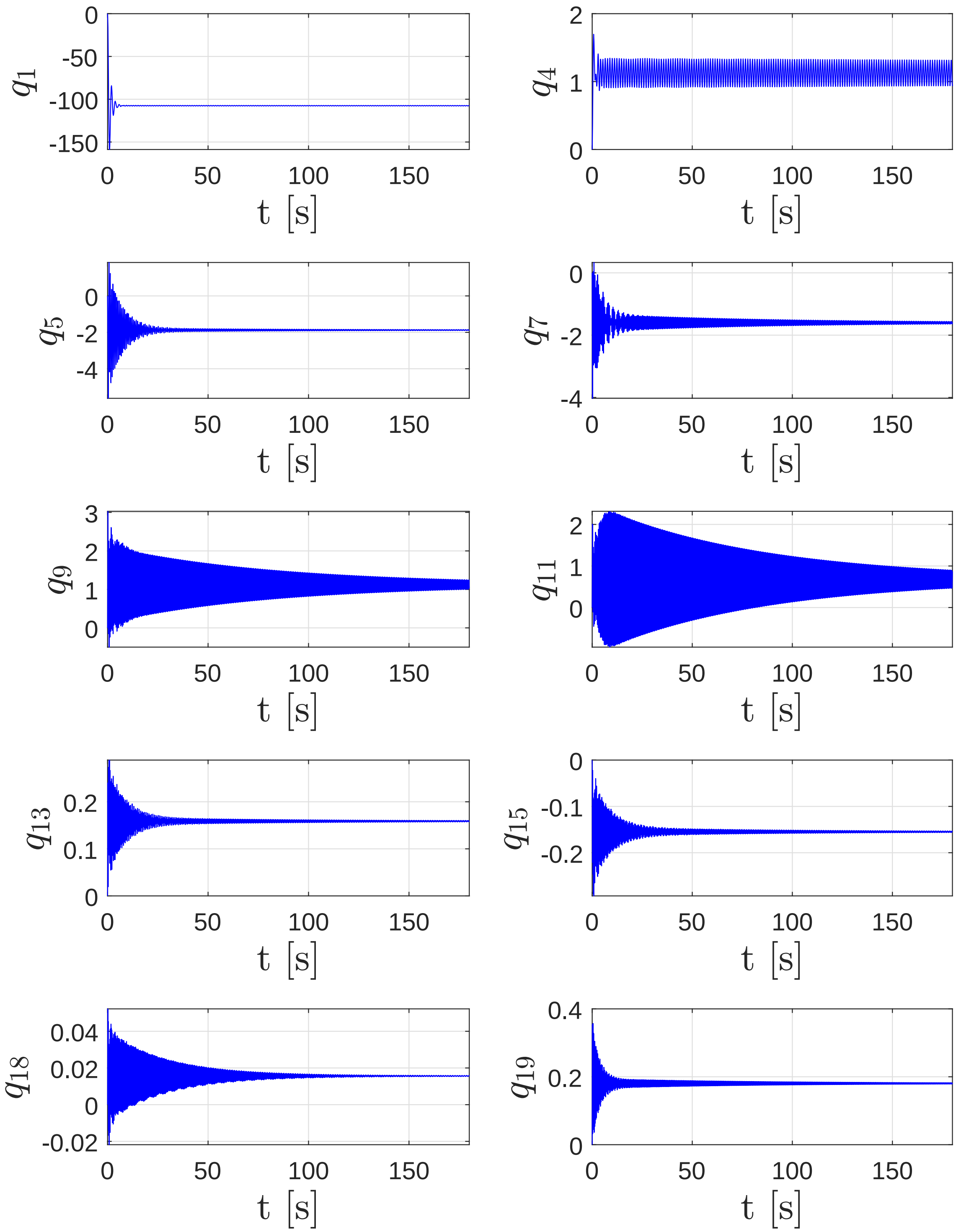

Figure D.26: Time responses of modes corresponding to the left joined-wing for the case with structural bending damage at critical speed $V_\infty = 150\,\mathrm{m/s}$ and freestream direction $(0°, 5°, 0°)$.

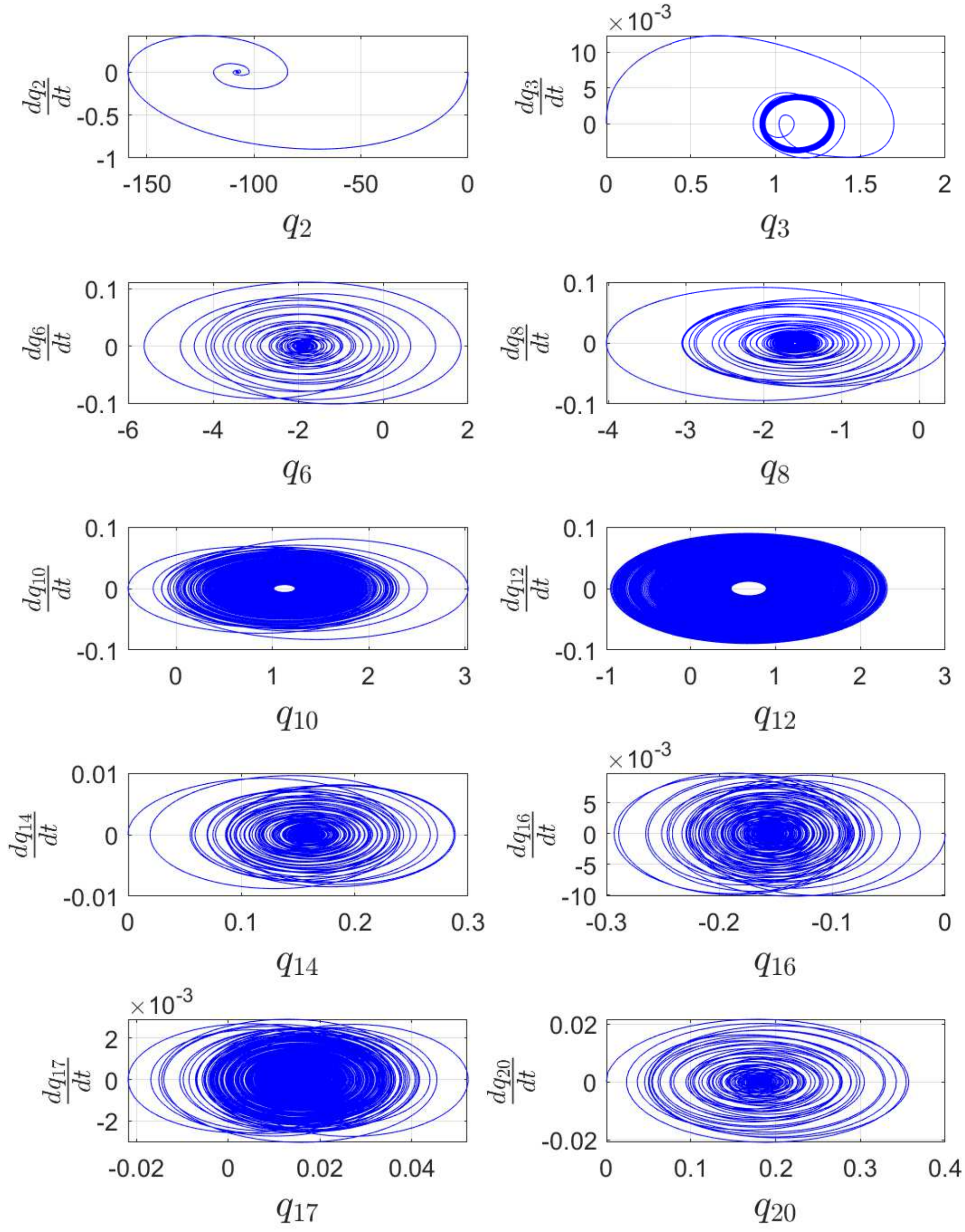

Figure D.27: At critical speed $V_\infty = 150\,\mathrm{m/s}$, projections in phase planes of modes corresponding to the right joined-wing for the case with structural bending damage and freestream direction $(0°, 5°, 0°)$.

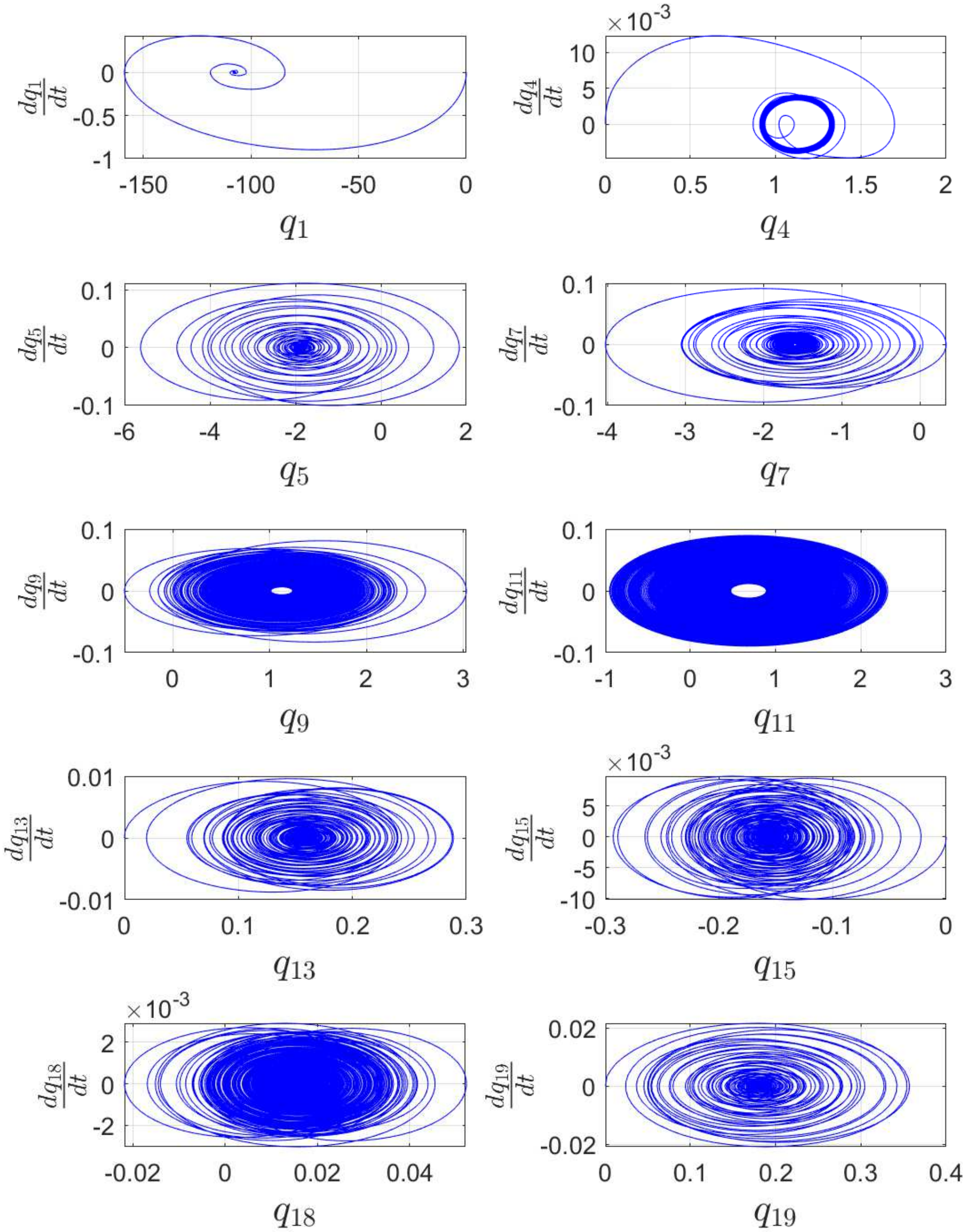

Figure D.28: At critical speed $V_\infty = 150\,\mathrm{m/s}$, projections in phase planes of modes corresponding to the left joined-wing for the case with structural bending damage and freestream direction $(0^\circ, 5^\circ, 0^\circ)$.

free vibration frequencies are marked in the figures by dashed red lines. At least two dominant frequencies can be observed from the first, third, fourth, seventh, eighth, and tenth modes of each joined-wing.

The results shown in Figures D.31 and D.32 correspond to a case where the freestream speed is 160 m/s, which is over the critical flutter speed. The time responses of all modes corresponding to the right joined-wing are shown in Figures D.31 and the time responses of all modes corresponding to the left joined-wing are shown in D.32. In the two figures, it can be observed that after the transient response, all modes exhibit an oscillatory behavior that increases in amplitude as time passes.

The projected responses in the phase planes of the right joined-wing and the left joined-wing are shown in Figures D.33 and D.34, respectively. In the responses of the about half of the modes corresponding the right and left joined-wings, limit cycles can be seen.

In Figures D.35 and D.36, the normalized FFTs of the modes corresponding to the right joined-wing and the left joined-wing, respectively, are presented. The free vibration frequencies are marked in the figures by dashed red lines. For all the modes of each joined-wing, a predominant frequency of 2.628 Hz can be observed.

D.3 Case with Torsional Damage: Freestream Direction $(0°, 5°, 0°)$

The results shown in Figures D.37 and D.38 correspond to a case where the freestream speed is 130 m/s, which is below the critical flutter speed. The time

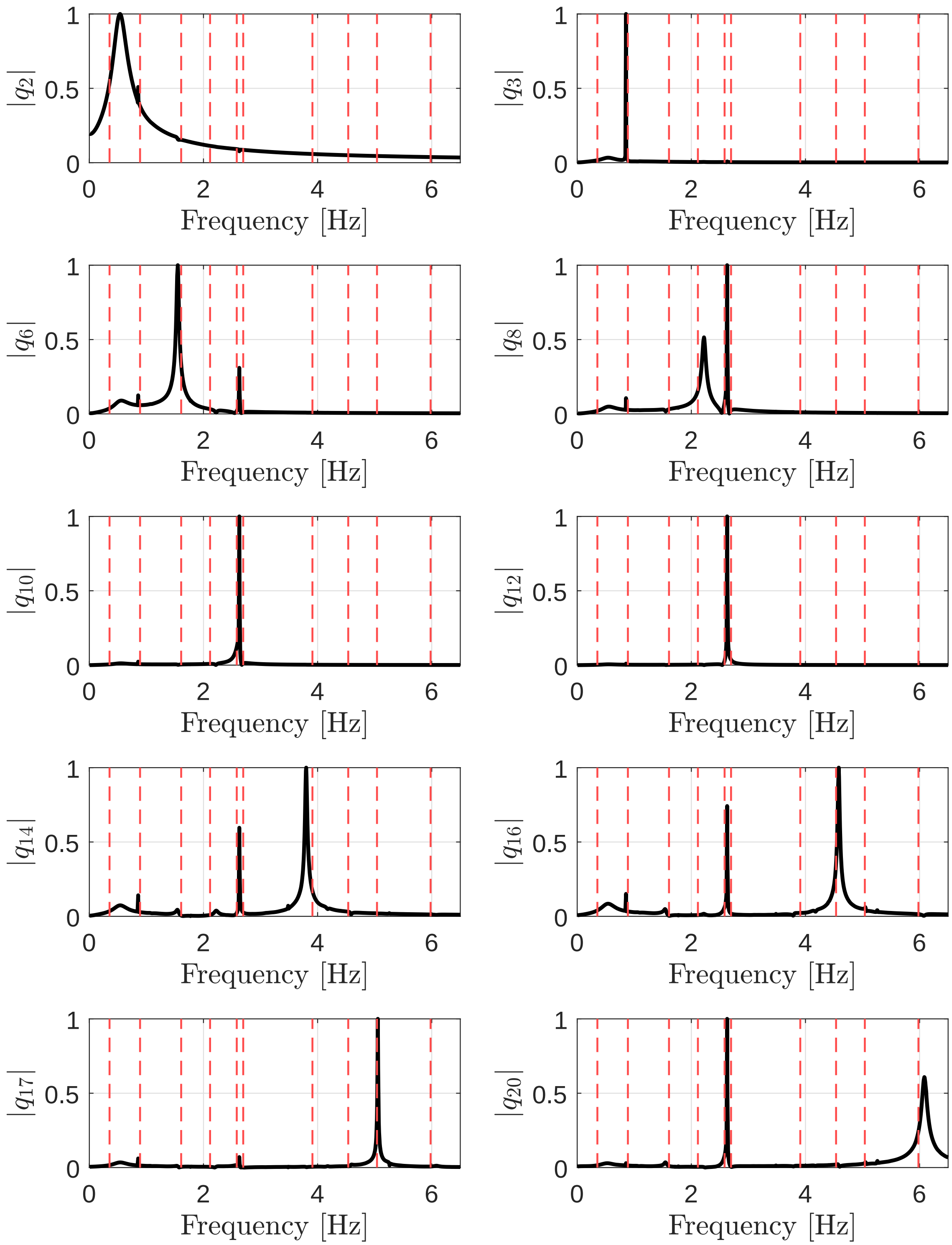

Figure D.29: At critical speed $V_\infty = 150\,\mathrm{m/s}$, responses in the frequency domain of modes corresponding to the right joined-wing for the case with structural bending damage and freestream direction $(0°, 5°, 0°)$.

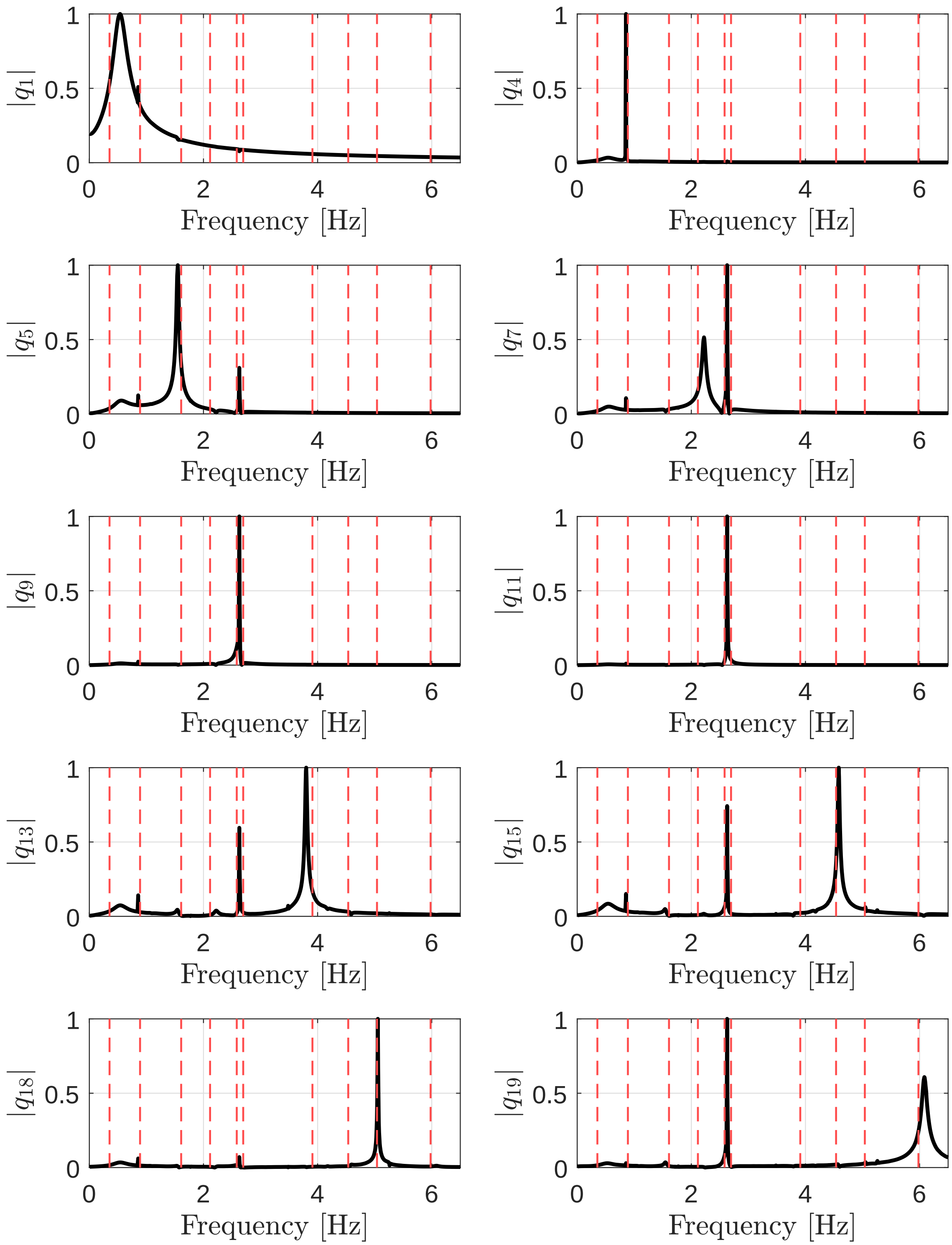

Figure D.30: At critical speed $V_\infty = 150$ m/s, responses in the frequency domain of modes corresponding to the left joined-wing for the case with structural bending damage and freestream direction $(0°, 5°, 0°)$.

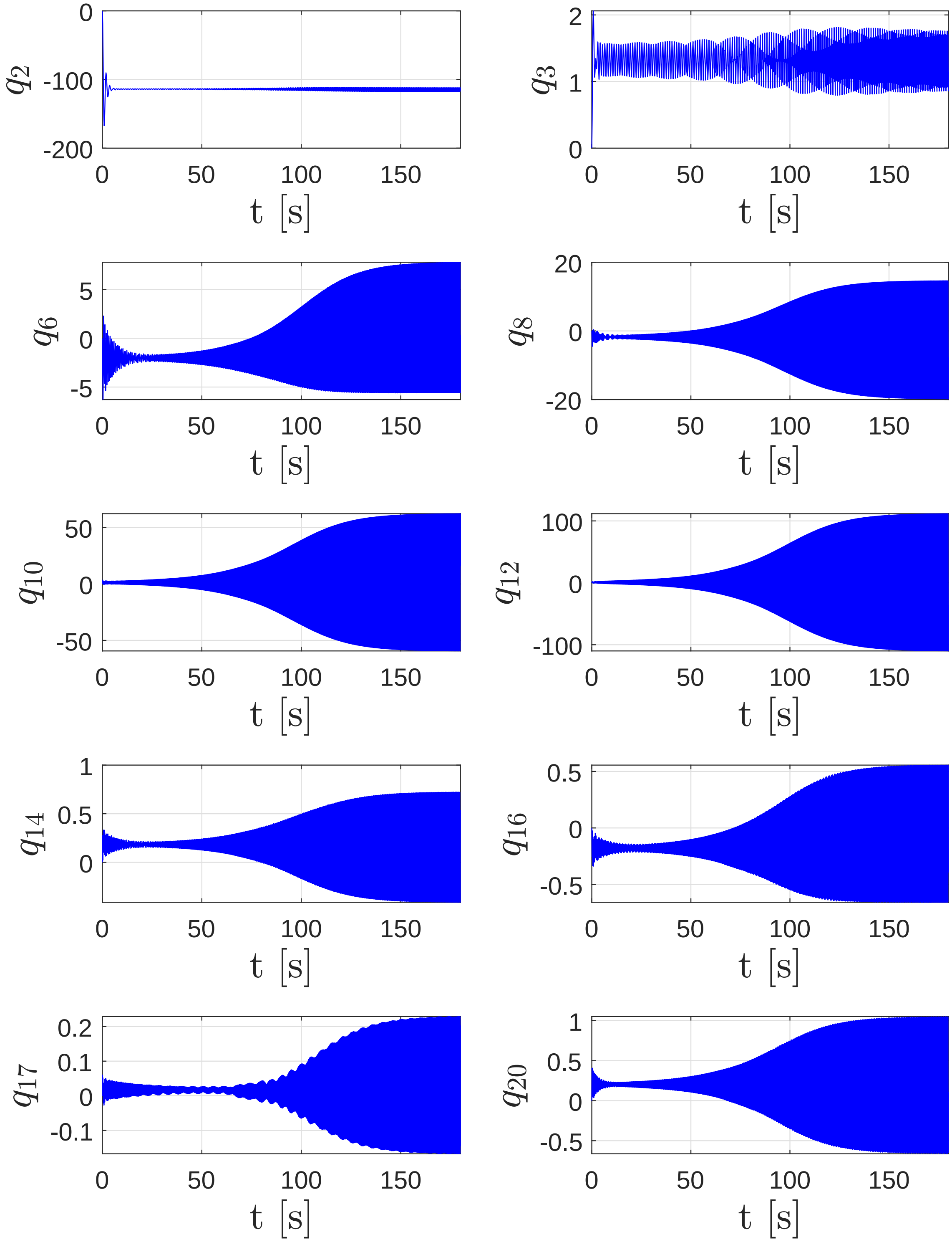

Figure D.31: Time responses of modes corresponding to the right joined-wing for the case with structural bending damage at supercritical speed $V_\infty = 160\,\mathrm{m/s}$ and freestream direction $(0°, 5°, 0°)$.

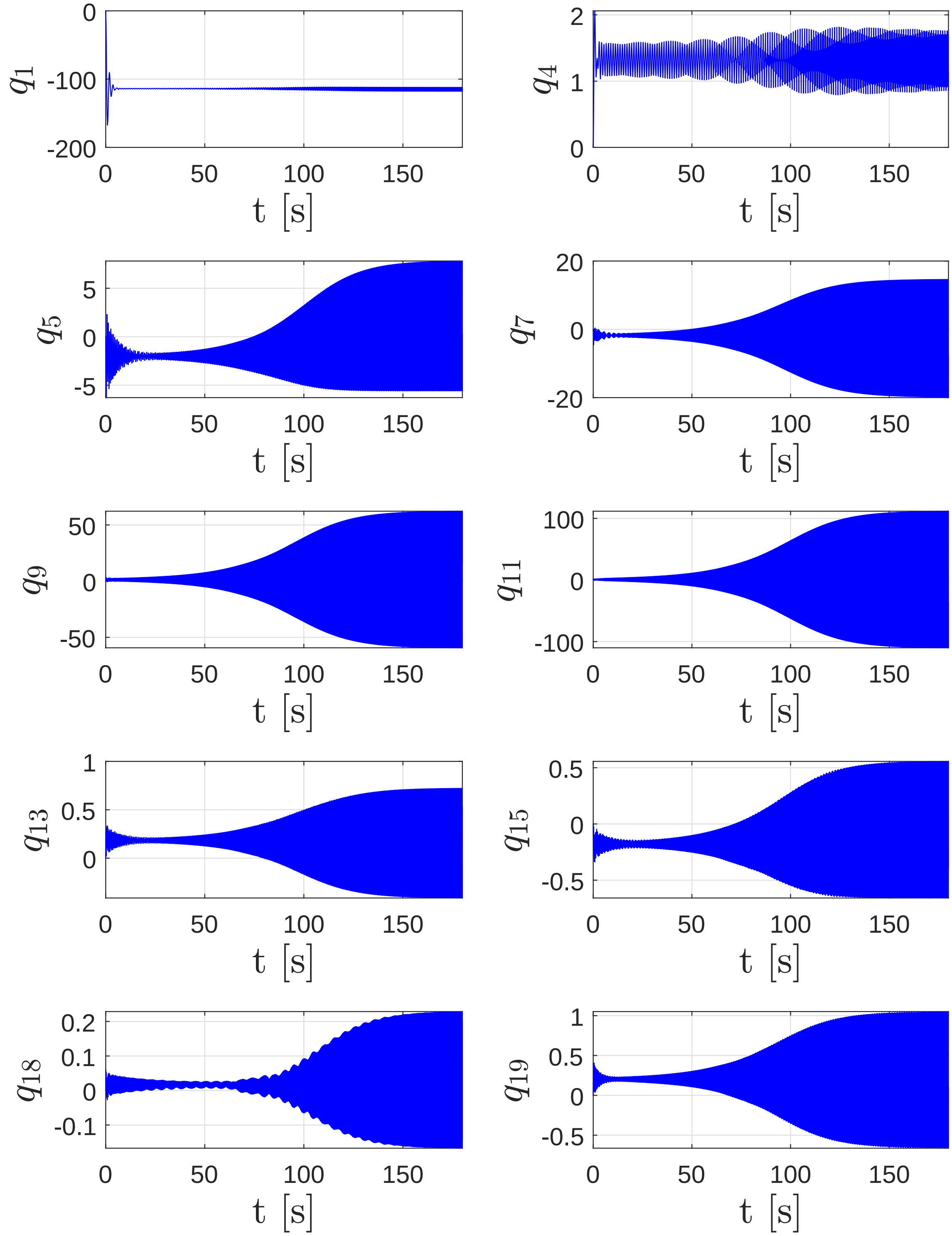

Figure D.32: Time responses of modes corresponding to the left joined-wing for the case with structural bending damage at supercritical speed $V_\infty = 160\,\mathrm{m/s}$ and freestream direction $(0°, 5°, 0°)$.

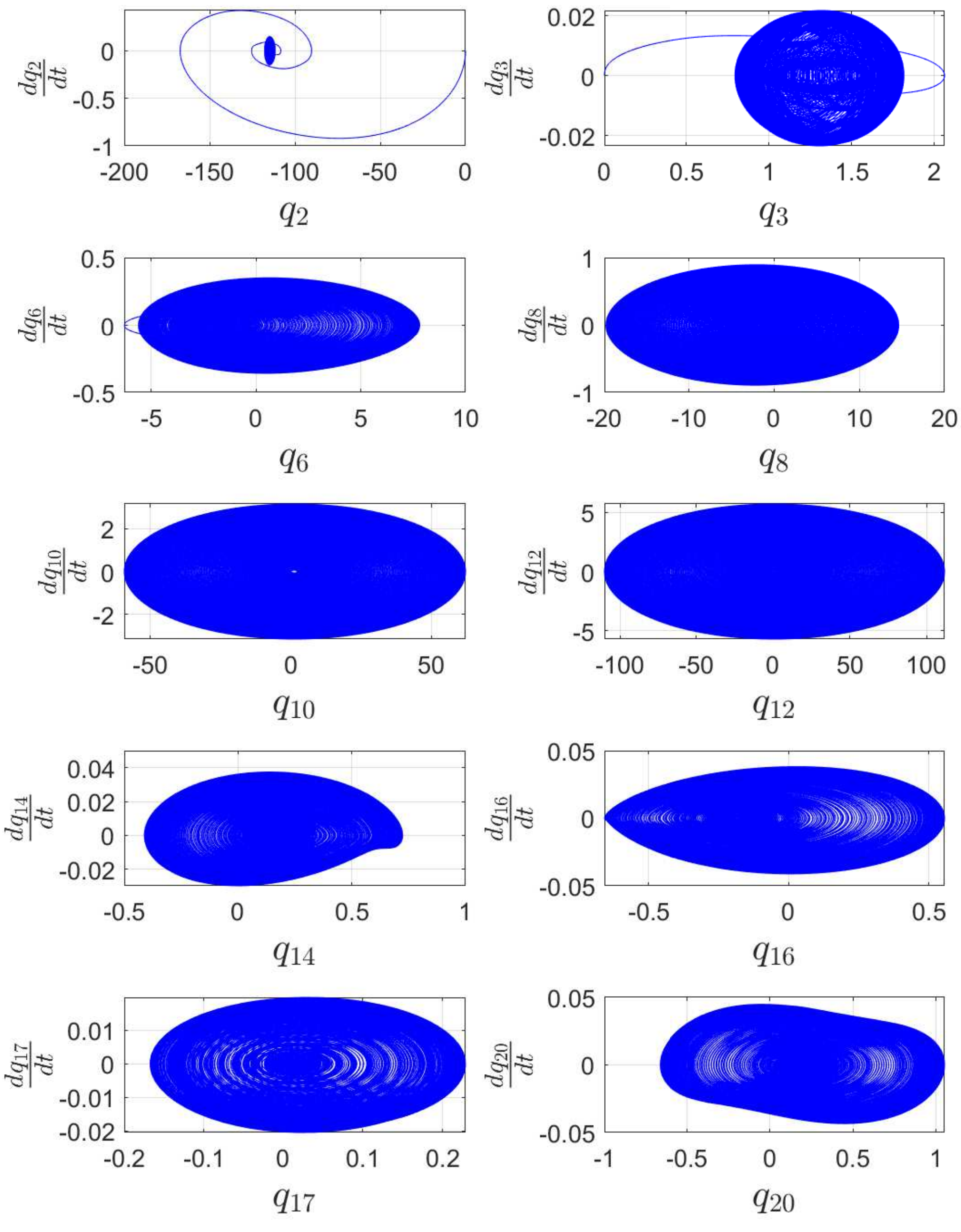

Figure D.33: At supercritical speed $V_\infty = 160\,\mathrm{m/s}$, projections in phase planes of modes corresponding to the right joined-wing for the case with structural bending damage and freestream direction $(0^\circ, 5^\circ, 0^\circ)$.

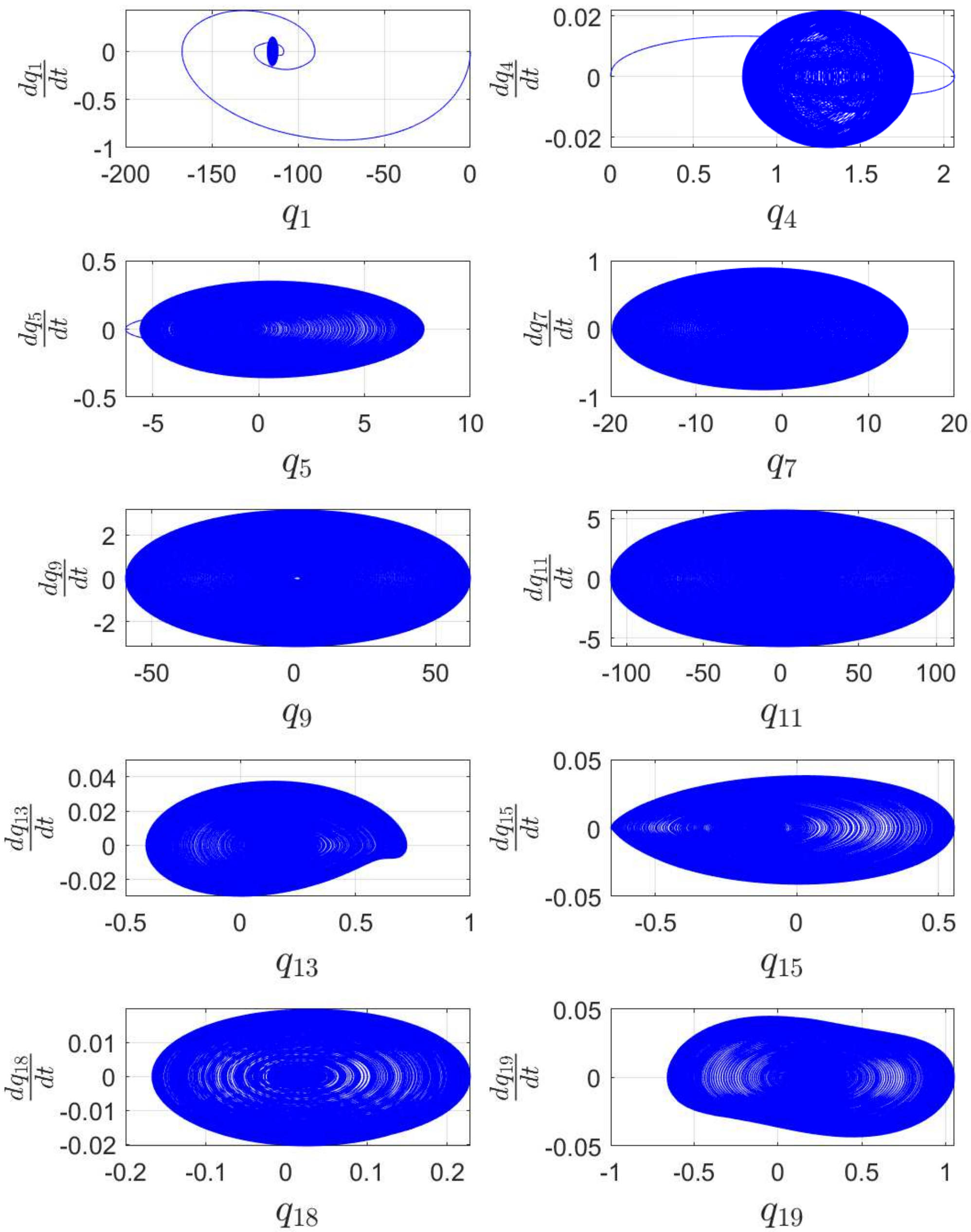

Figure D.34: At supercritical speed $V_\infty = 160\,\mathrm{m/s}$, projections in phase planes of modes corresponding to the left joined-wing for the case with structural bending damage and freestream direction $(0^\circ, 5^\circ, 0^\circ)$.

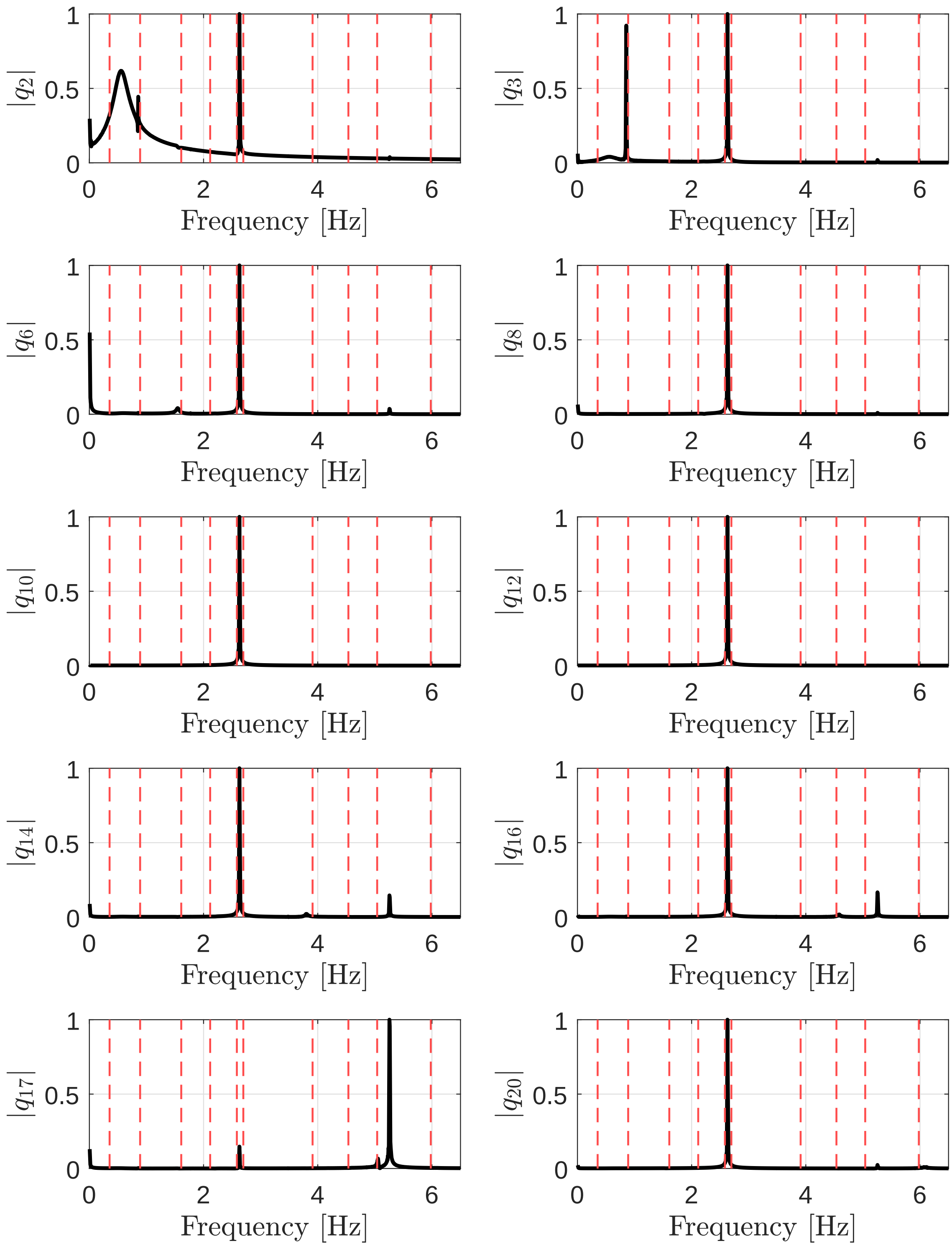

Figure D.35: At supercritical speed $V_\infty = 160$ m/s, responses in the frequency domain of modes corresponding to the right joined-wing for the case with structural bending damage and freestream direction $(0°, 5°, 0°)$.

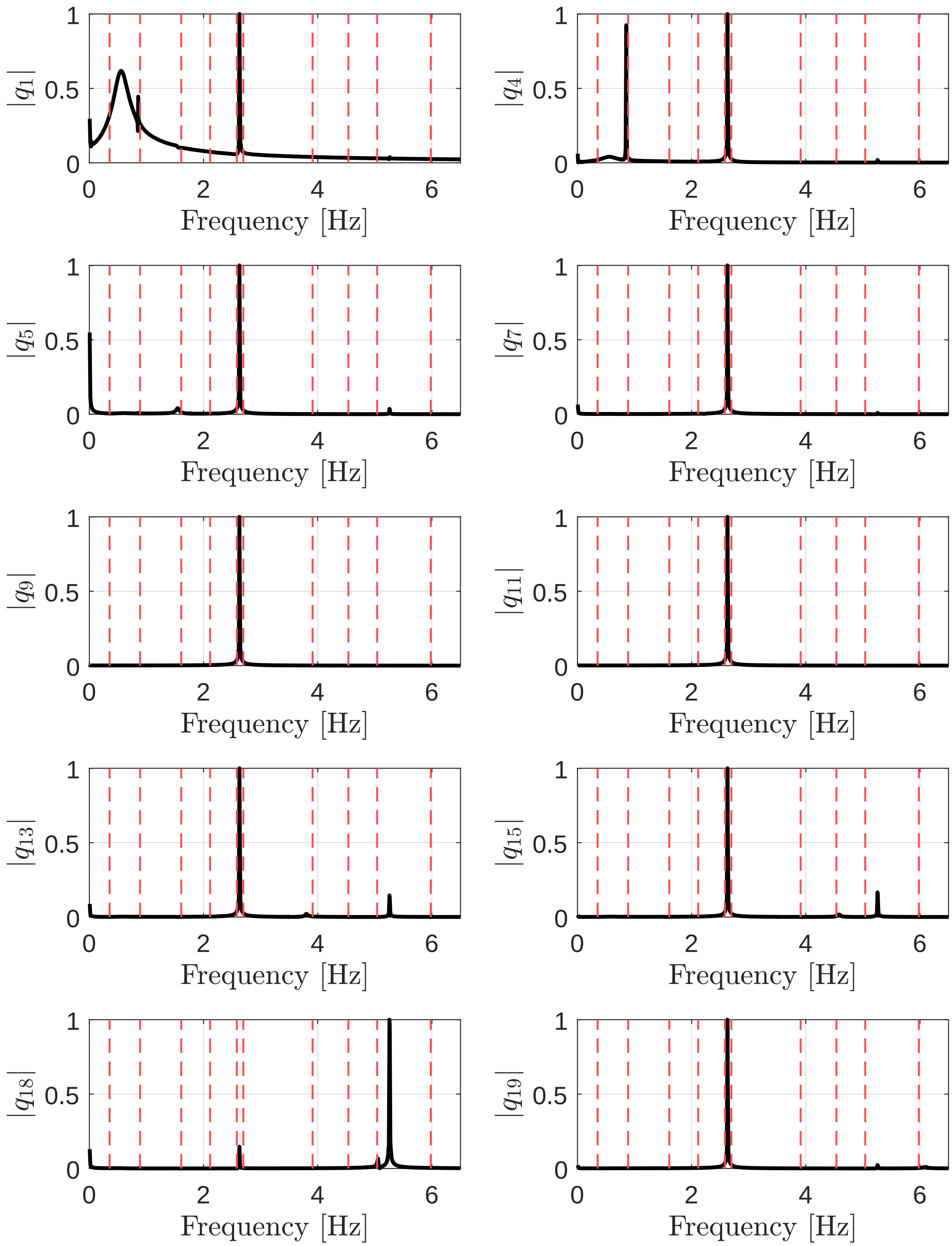

Figure D.36: At supercritical speed $V_\infty = 160$ m/s, responses in the frequency domain of modes corresponding to the left joined-wing for the case with structural bending damage and freestream direction $(0°, 5°, 0°)$.

responses of all modes corresponding to the right joined-wing are shown in Figures D.37 and the time responses of all modes corresponding to the left joined-wing are shown in D.38. In the two figures, it can be observed that after a brief transient, all modes exhibit an oscillatory behavior that decreases in amplitude as time passes. This is caused by the presence of just aerodynamic damping.

The projected responses in the phase planes of the right joined-wing and the left joined-wing are shown in Figures D.39 and D.40, respectively. Stable focus type of characteristics can be observed in all modes as the spirals converge to an equilibrium point.

In Figures D.41 and D.42, the normalized FFTs of the modes corresponding to the right joined-wing and the left joined-wing, respectively, are presented. The free vibration frequencies are marked in the figures by dashed red lines. In all cases, a dominant frequency can be observed from a composition of two or more signals of different frequencies.

The results shown in Figures D.43 and D.44 correspond to a case where the freestream speed is 156 m/s, which is close to the critical flutter speed. The time responses of all modes corresponding to the right joined-wing are shown in Figures D.43 and the time responses of all modes corresponding to the left joined-wing are shown in D.44. In the two figures, it can be observed that after the transient response, all modes begin to exhibit an oscillatory behavior of constant amplitude as time passes.

The projected responses in the phase planes of the right joined-wing and the left joined-wing are shown in Figures D.45 and D.46, respectively. In the responses

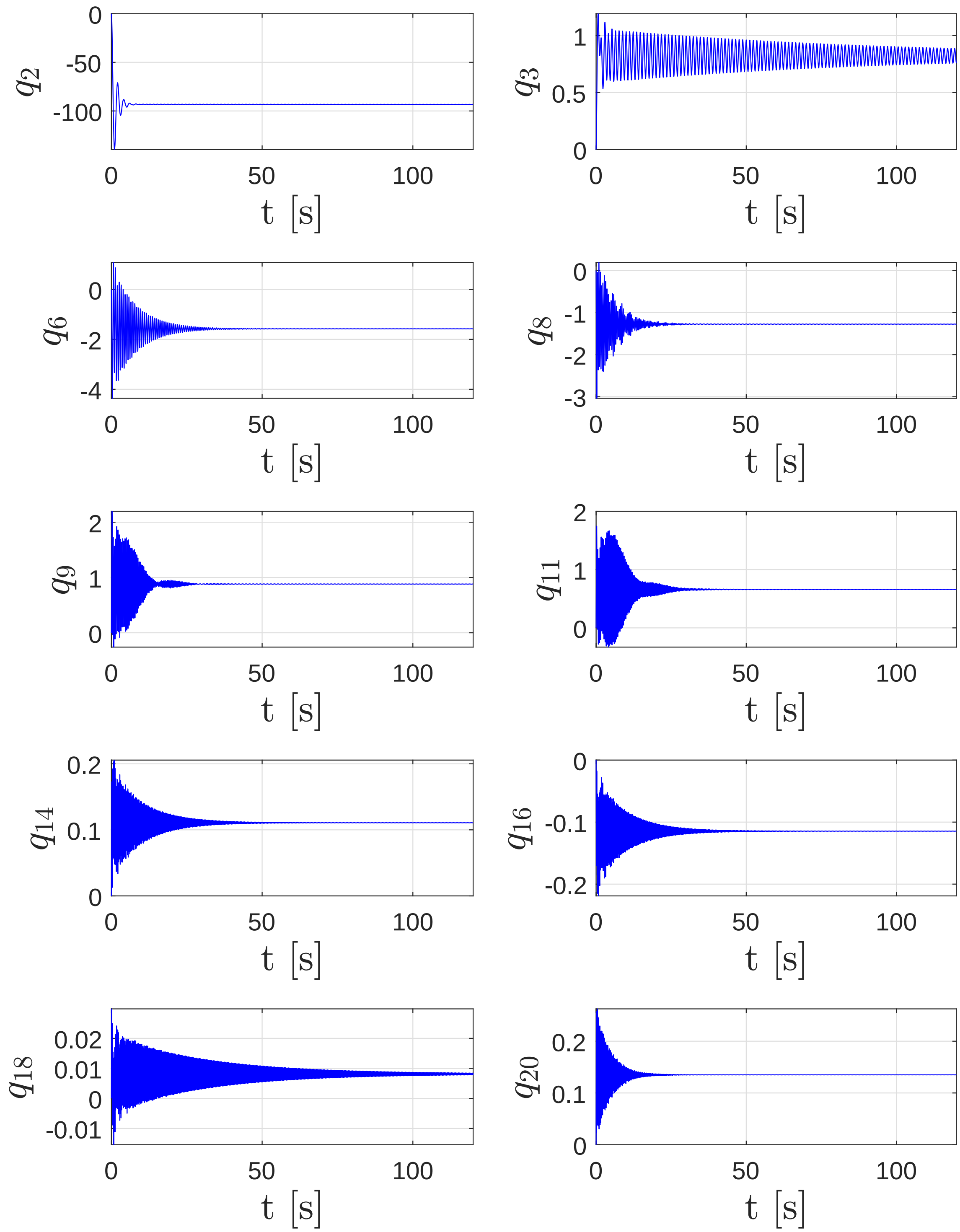

Figure D.37: Time responses of modes corresponding to the right joined-wing for the case with structural torsional damage at subcritical speed $V_\infty = 130\,\mathrm{m/s}$ and freestream direction $(0°, 5°, 0°)$.

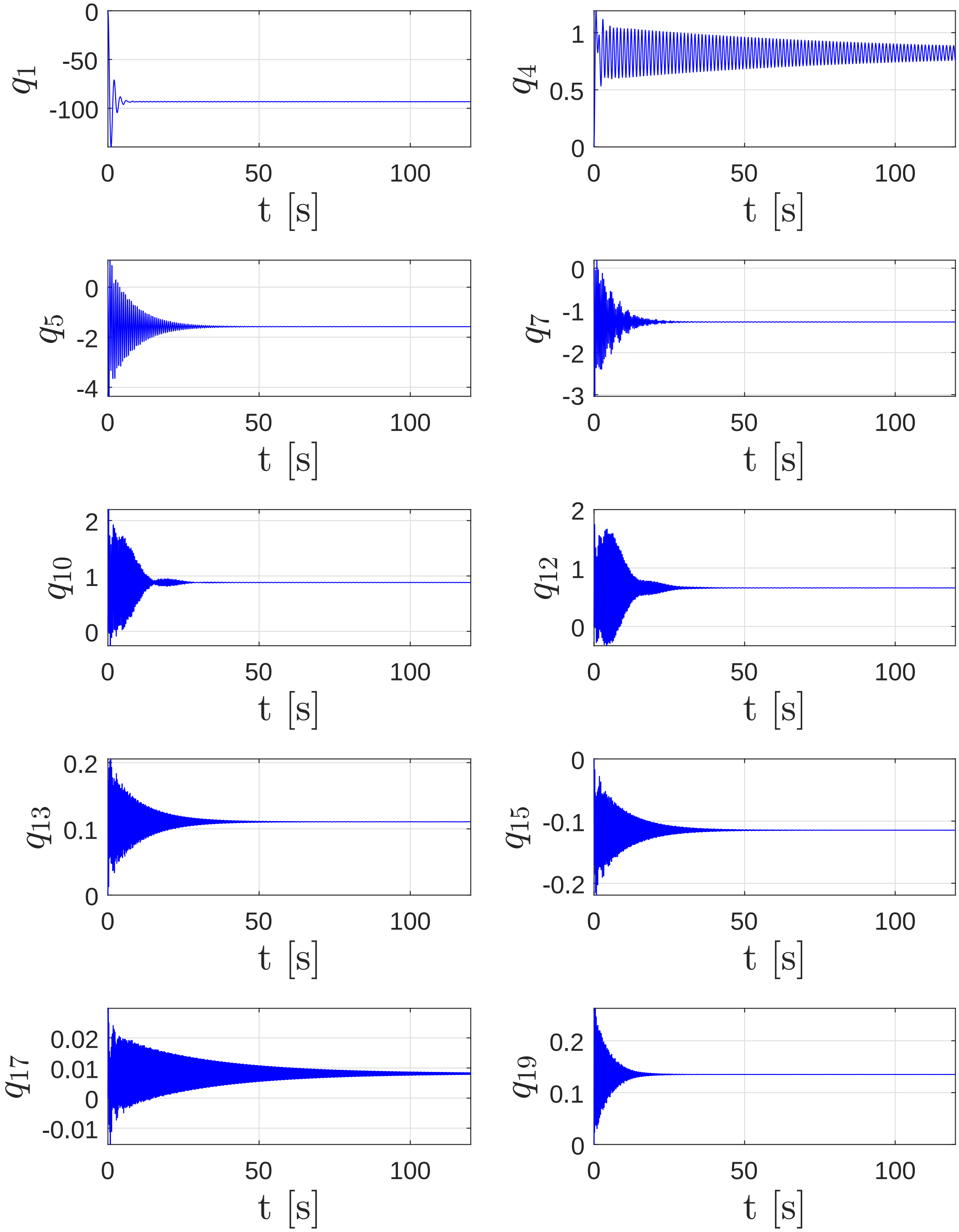

Figure D.38: Time responses of modes corresponding to the left joined-wing for the case with structural torsional damage at subcritical speed $V_\infty = 130\,\mathrm{m/s}$ and freestream direction $(0°, 5°, 0°)$.

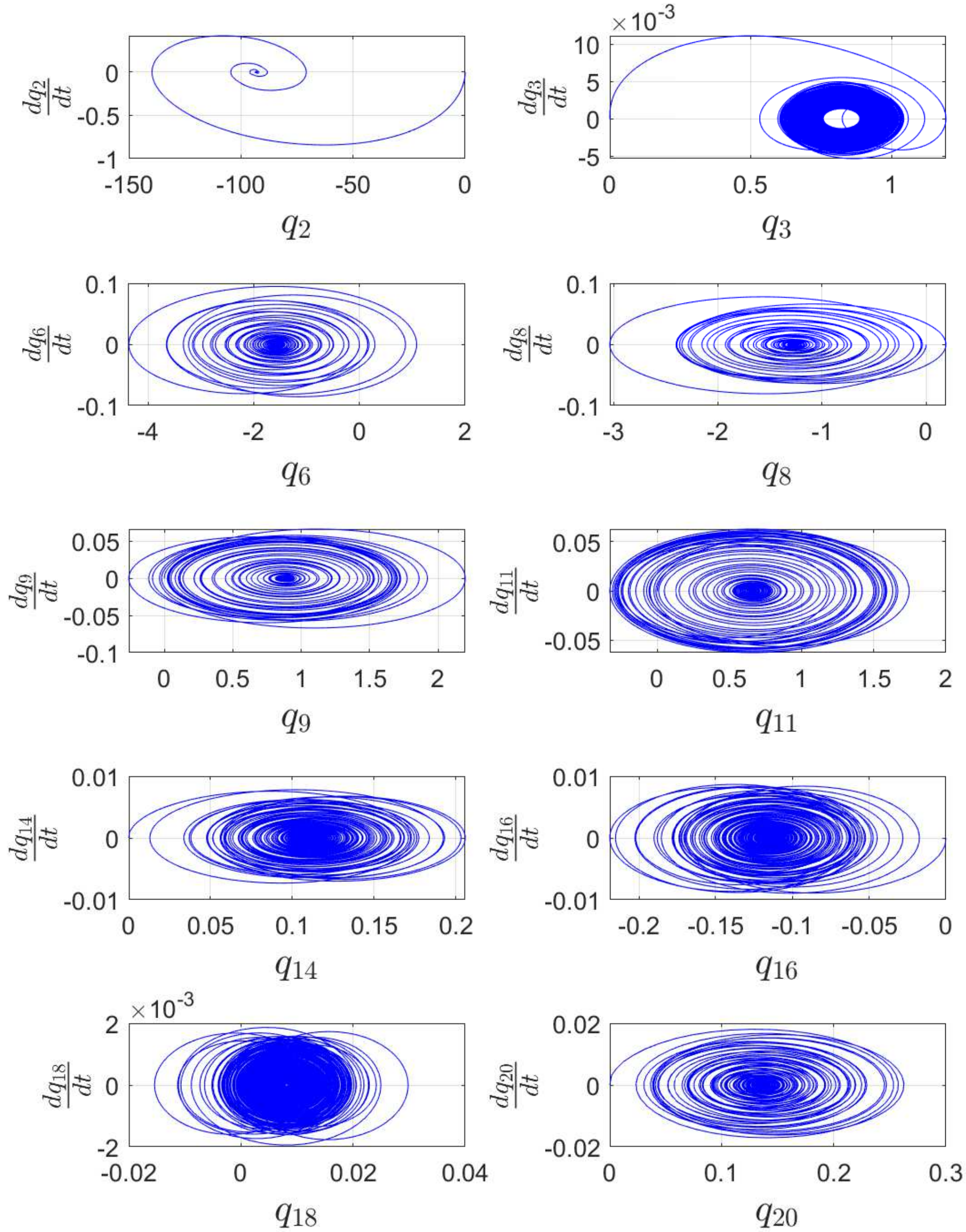

Figure D.39: At subcritical speed $V_\infty = 130$ m/s, projections in phase planes of modes corresponding to the right joined-wing for the case with structural torsional damage and freestream direction $(0°, 5°, 0°)$.

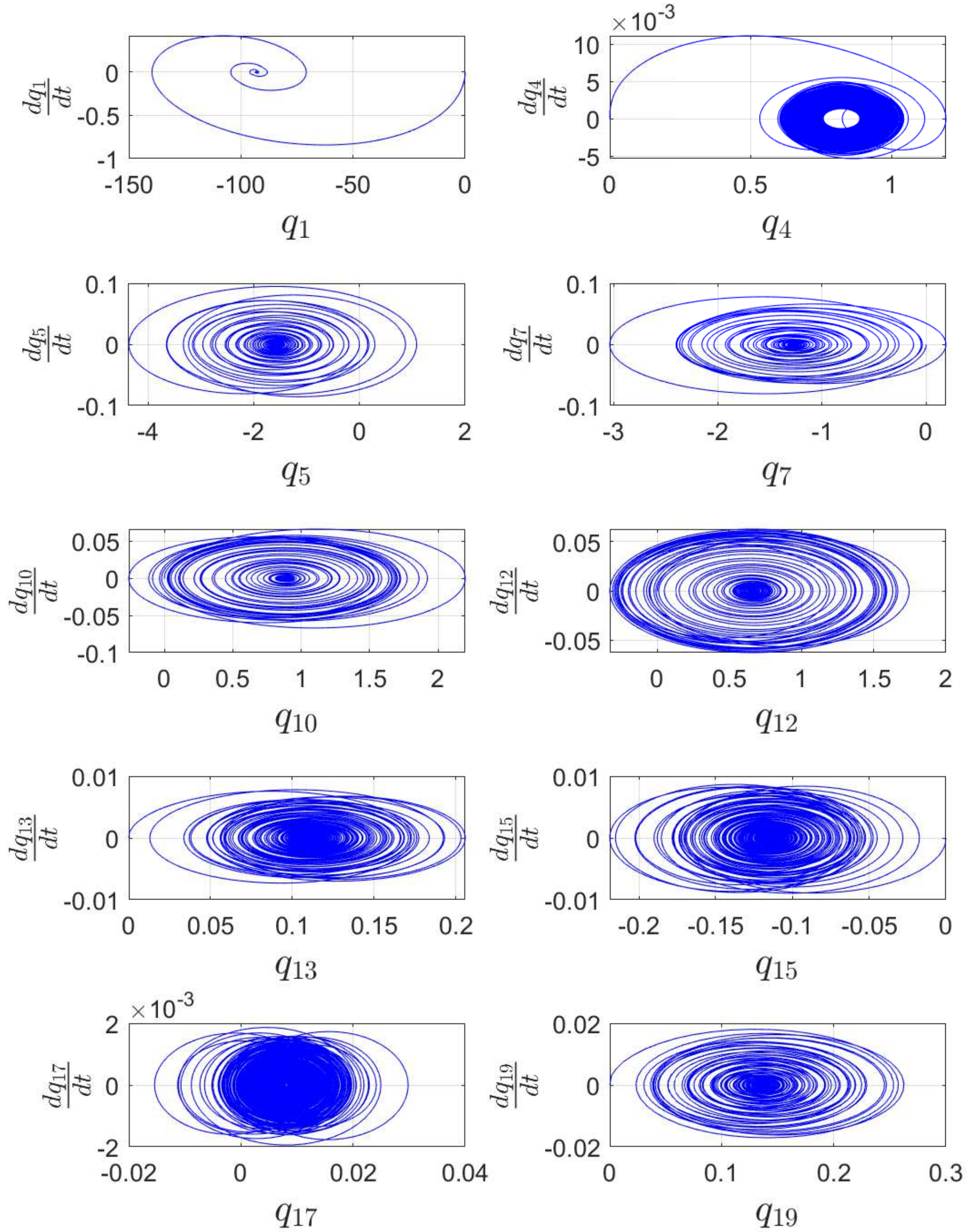

Figure D.40: At subcritical speed $V_\infty = 130$ m/s, projections in phase planes of modes corresponding to the left joined-wing for the case with structural torsional damage and freestream direction $(0°, 5°, 0°)$.

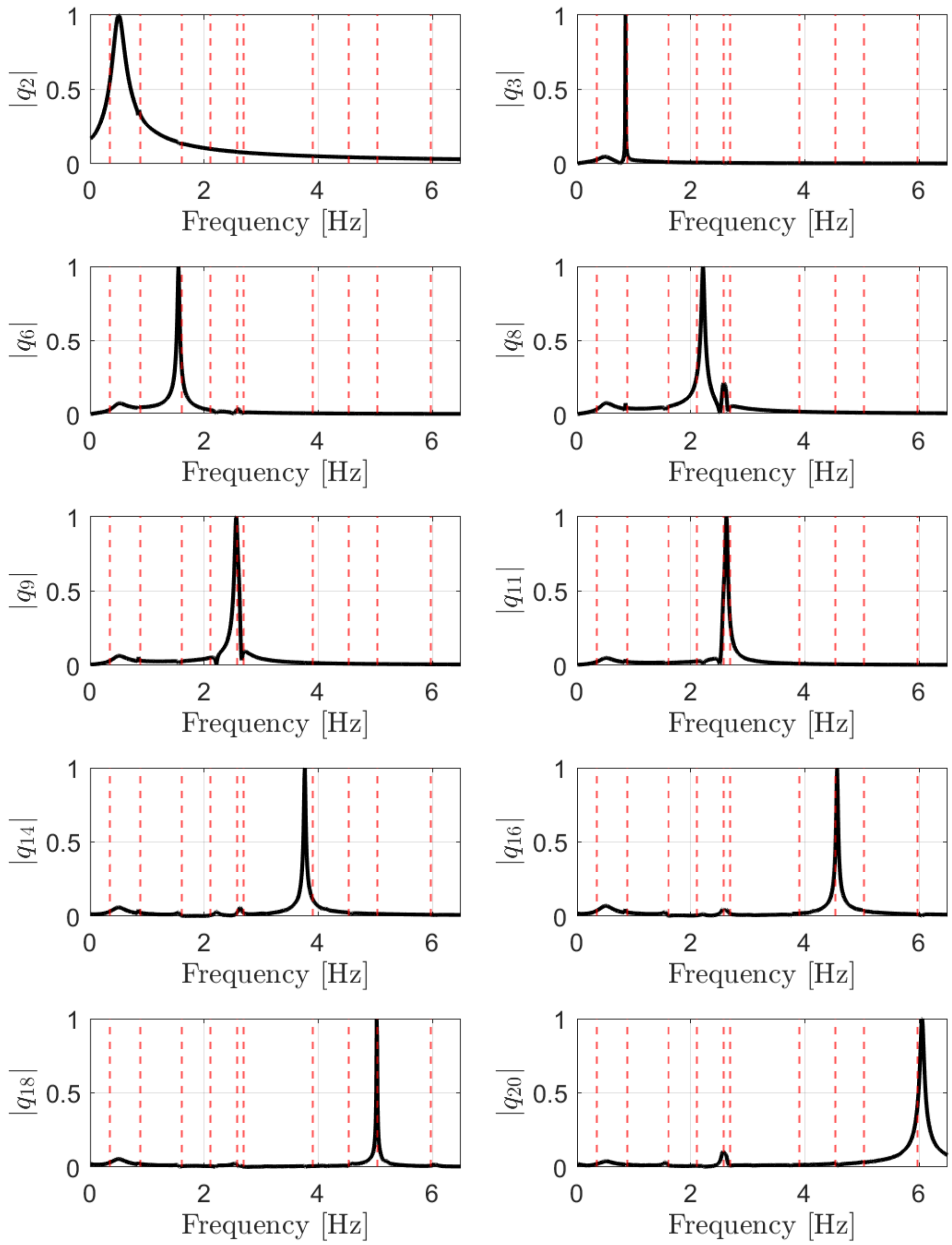

Figure D.41: At subcritical speed $V_\infty = 130\,\mathrm{m/s}$, responses in the frequency domain of modes corresponding to the right joined-wing for the case with structural torsional damage and freestream direction $(0°, 5°, 0°)$.

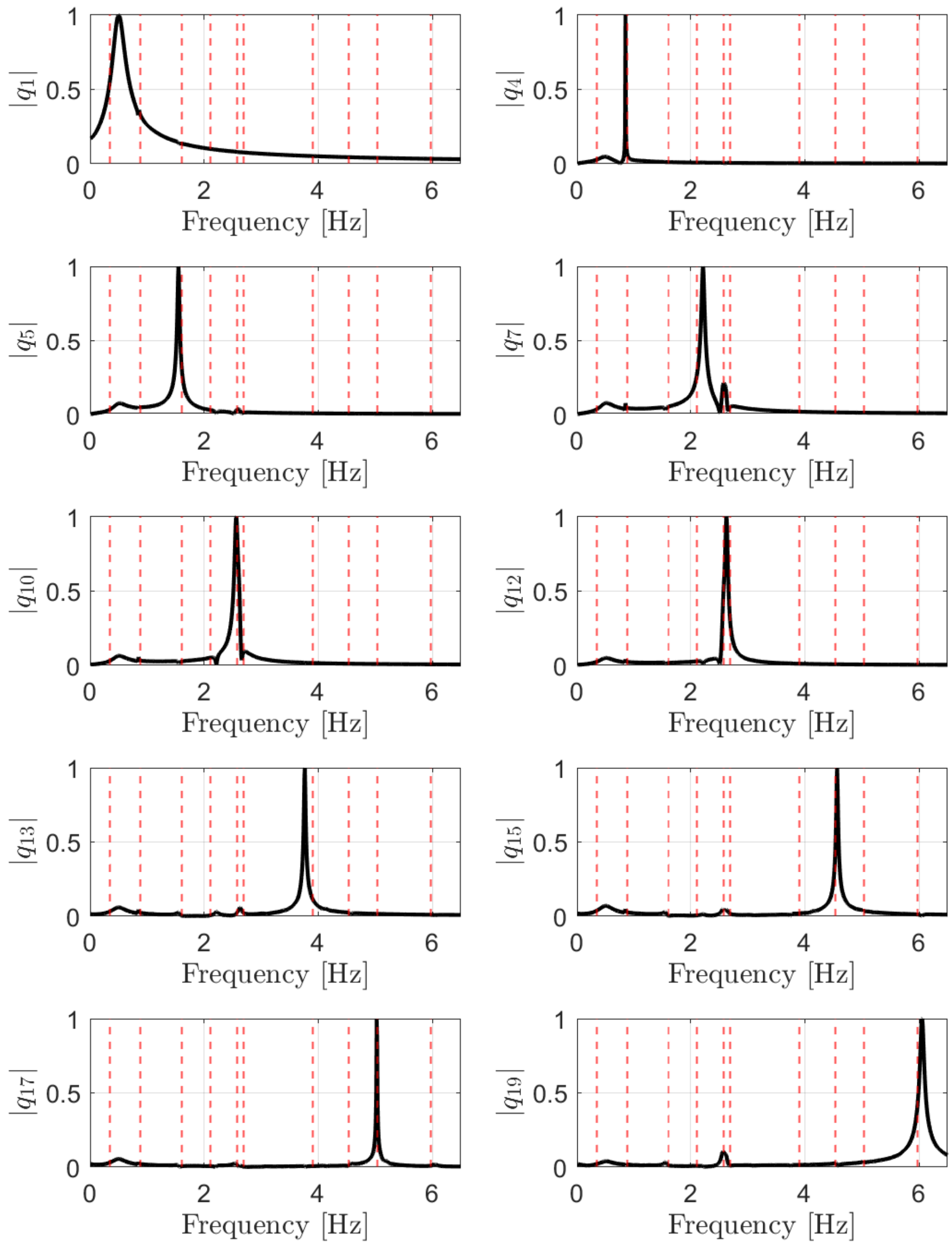

Figure D.42: At subcritical speed $V_\infty = 130\,\mathrm{m/s}$, responses in the frequency domain of modes corresponding to the left joined-wing for the case with structural torsional damage and freestream direction $(0°, 5°, 0°)$.

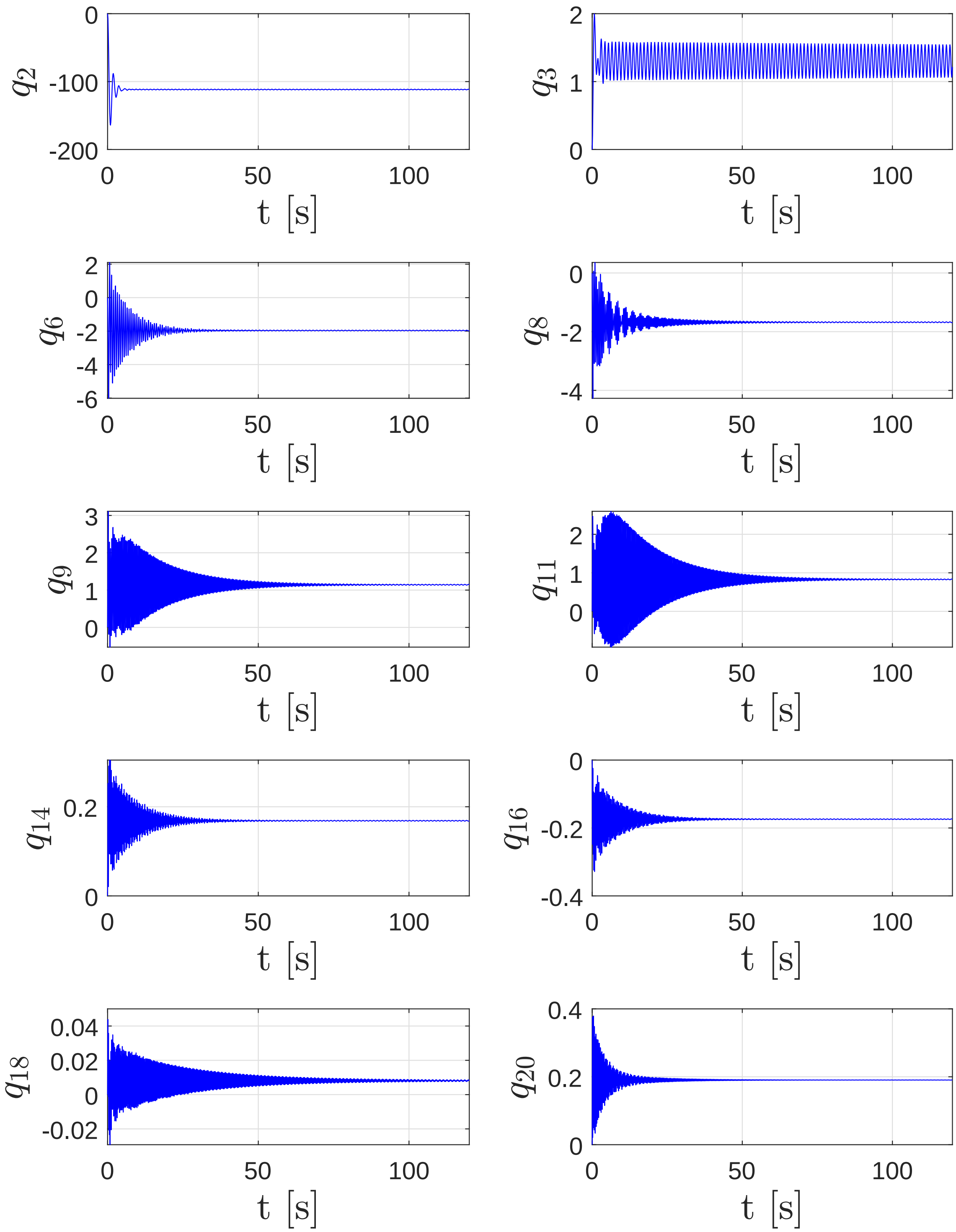

Figure D.43: Time responses of modes corresponding to the right joined-wing for the case with structural torsional damage at critical speed $V_\infty = 156\,\mathrm{m/s}$ and freestream direction $(0°, 5°, 0°)$.

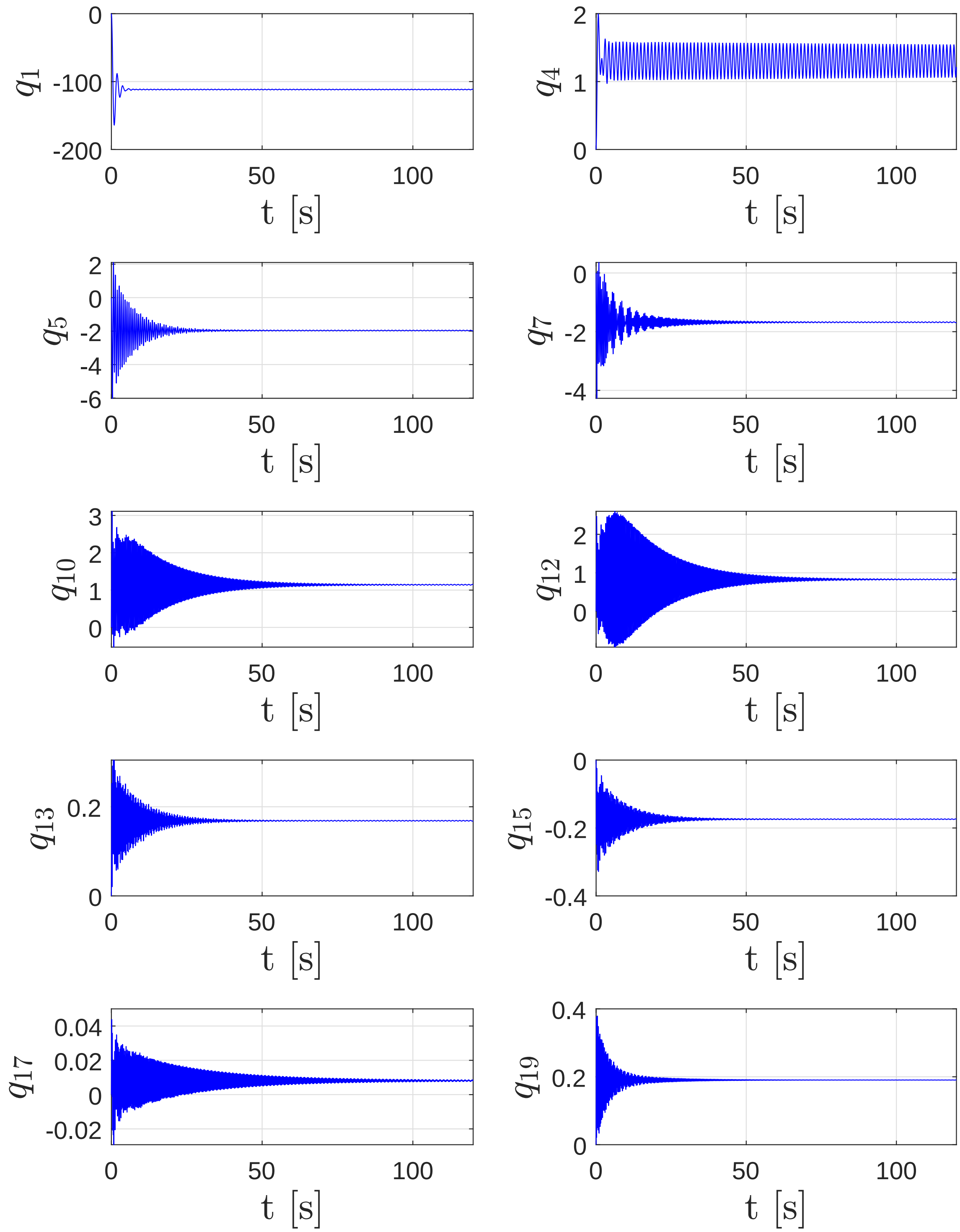

Figure D.44: Time responses of modes corresponding to the left joined-wing for the case with structural torsional damage at critical speed, $V_\infty = 156$m/s and freestream direction $(0°, 5°, 0°)$.

of the second modes corresponding the right and left joined-wings, limit cycles can be seen.

In Figures D.47 and D.48, the normalized FFTs of the modes corresponding to the right joined-wing and the left joined-wing, respectively, are presented. The free vibration frequencies are marked in the figures by dashed red lines. At least two dominant frequencies can be observed from the first, third, fourth, seventh, eighth, and tenth modes of each joined-wing.

The results shown in Figures D.49 and D.50 correspond to a case where the freestream speed is 165 m/s, which is over the critical flutter speed. The time responses of all modes corresponding to the right joined-wing are shown in Figures D.49 and the time responses of all modes corresponding to the left joined-wing are shown in D.50. In the two figures, it can be observed that after the transient response, all modes exhibit an oscillatory behavior that increases in amplitude as time passes.

The projected responses in the phase planes of the right joined-wing and the left joined-wing are shown in Figures D.51 and D.52, respectively. In the responses of the about half of the modes corresponding the right and left joined-wings, limit cycles can be seen.

In Figures D.53 and D.54, the normalized FFTs of the modes corresponding to the right joined-wing and the left joined-wing, respectively, are presented. The free vibration frequencies are marked in the figures by dashed red lines. Except for the first and second modes of each joined-wing, a predominant frequency of 2.600 Hz can be observed.

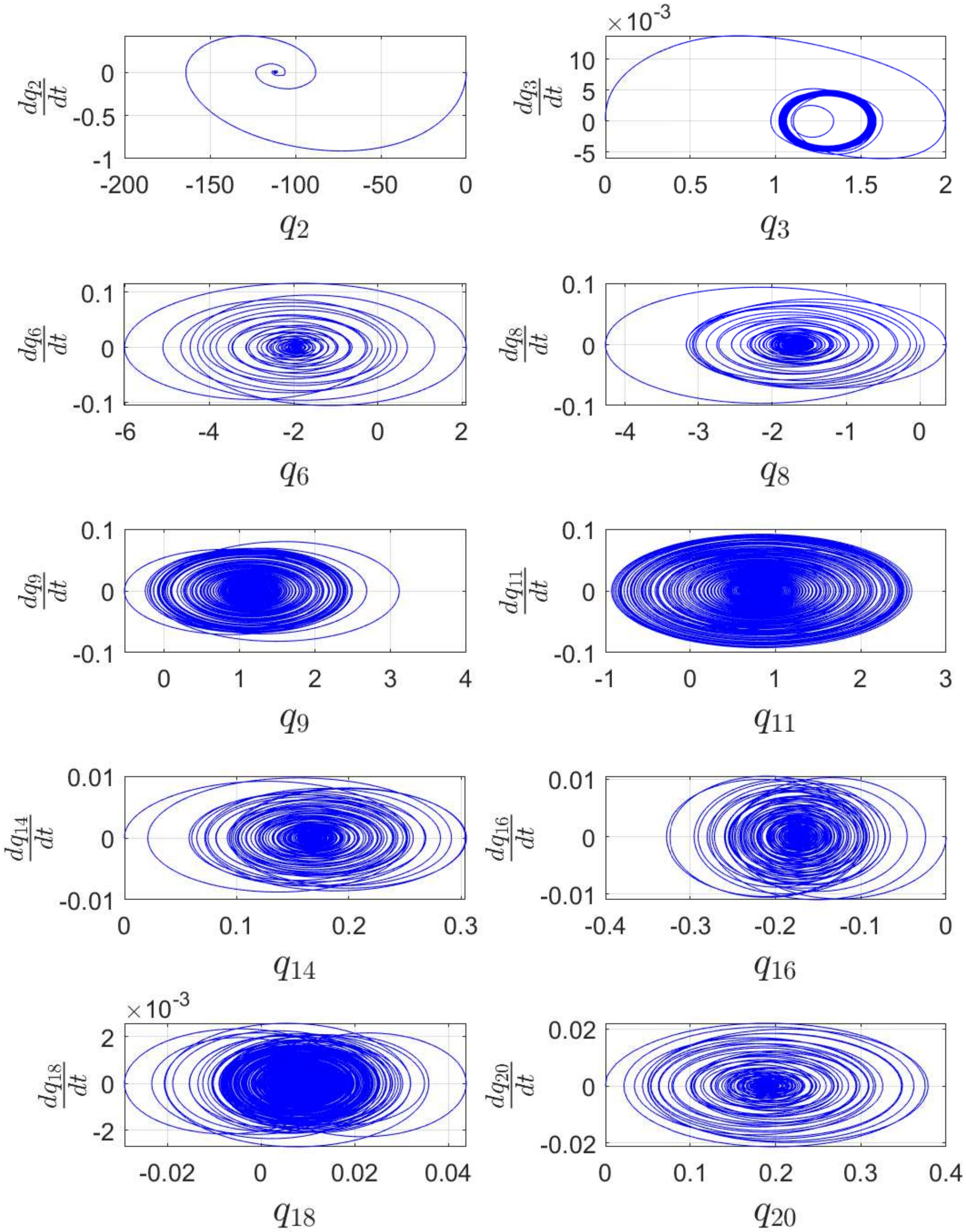

Figure D.45: At critical speed $V_\infty = 156\,\mathrm{m/s}$, projections in phase planes of modes corresponding to the right joined-wing for the case with structural torsional damage and freestream direction $(0^\circ, 5^\circ, 0^\circ)$.

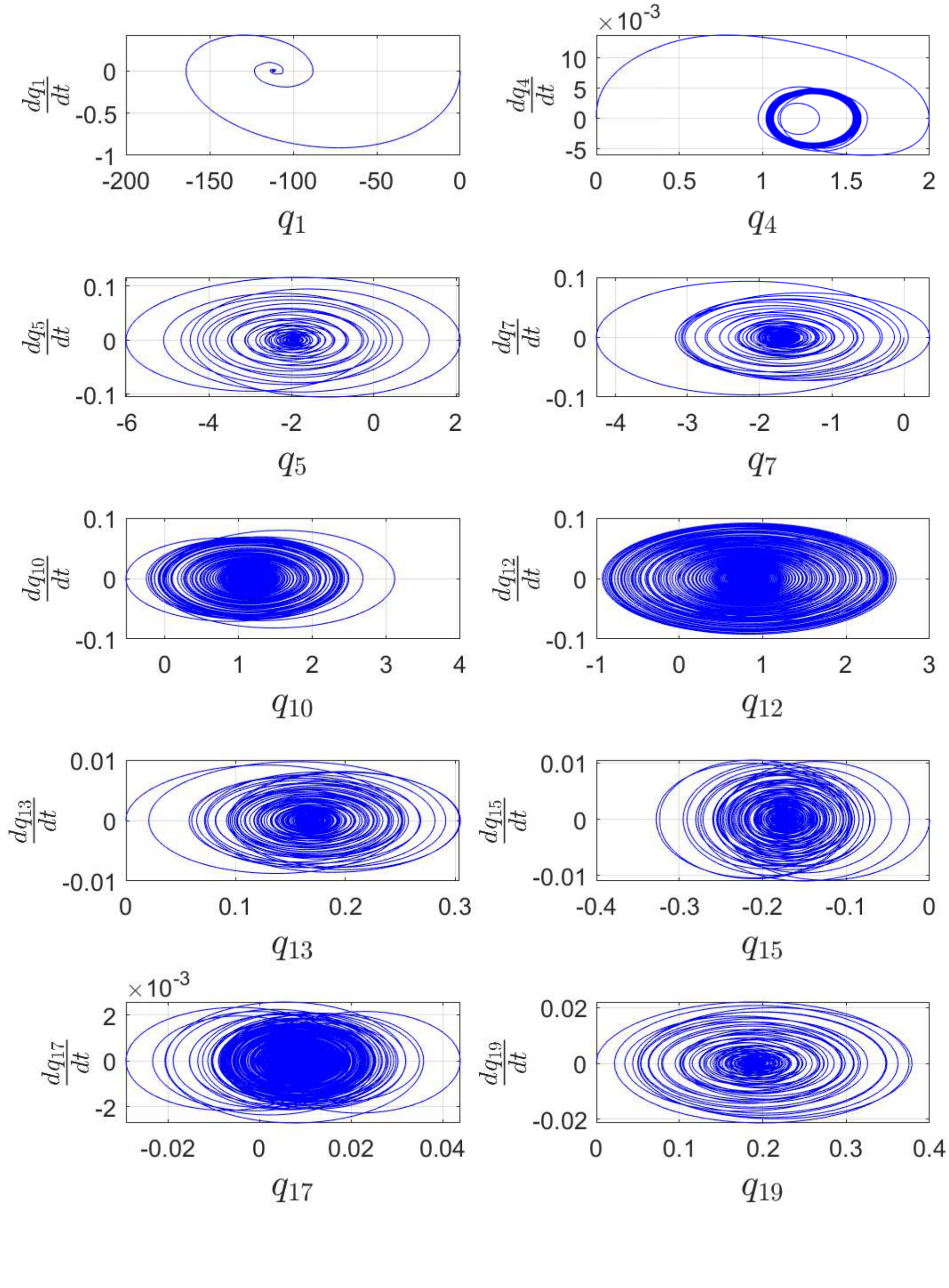

Figure D.46: At critical speed $V_\infty = 156\,\mathrm{m/s}$, projections in phase planes of modes corresponding to the left joined-wing for the case with structural torsional damage and freestream direction $(0°, 5°, 0°)$.

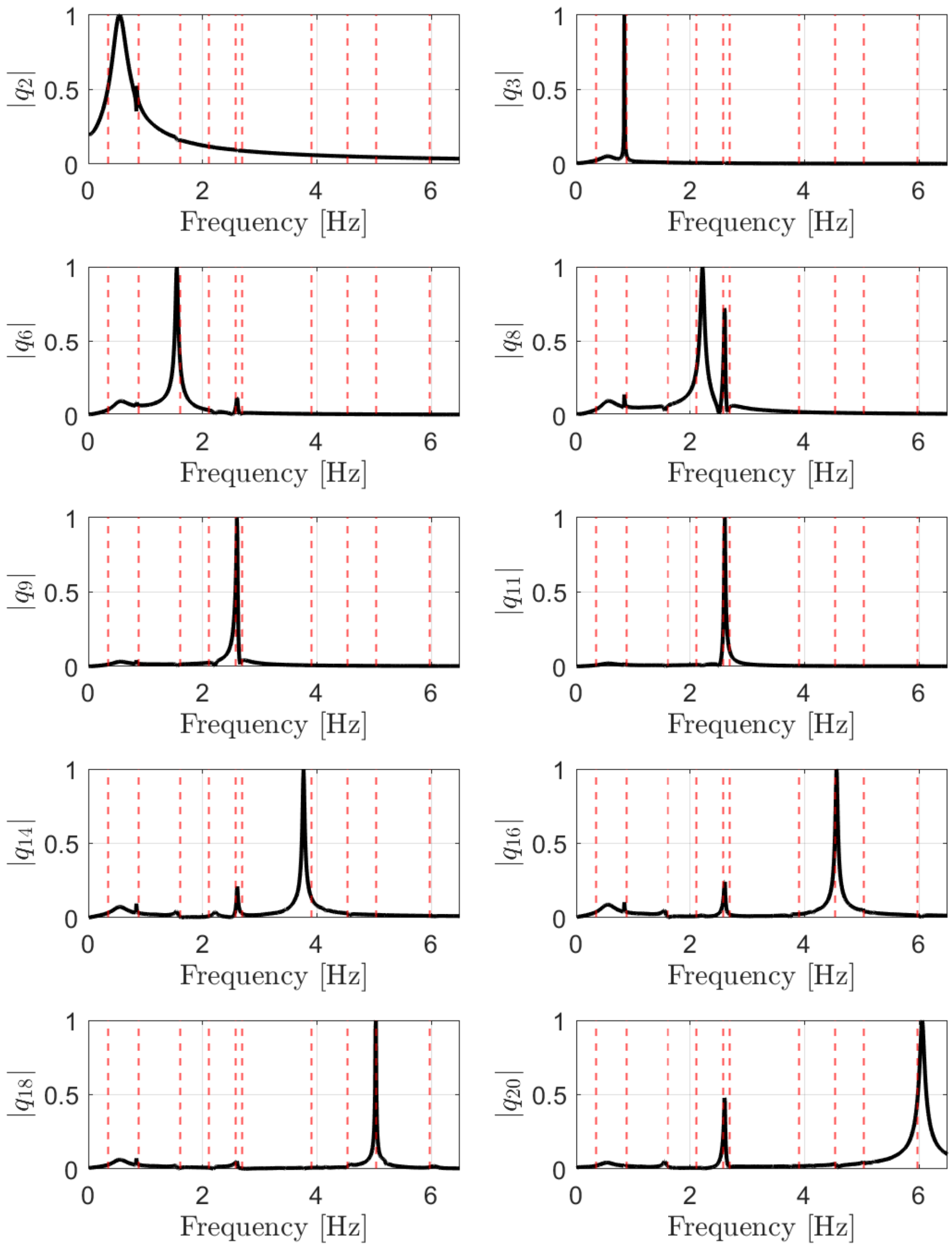

Figure D.47: At critical speed $V_\infty = 156\,\mathrm{m/s}$, responses in the frequency domain of modes corresponding to the right joined-wing for the case with structural torsional damage and freestream direction $(0°, 5°, 0°)$.

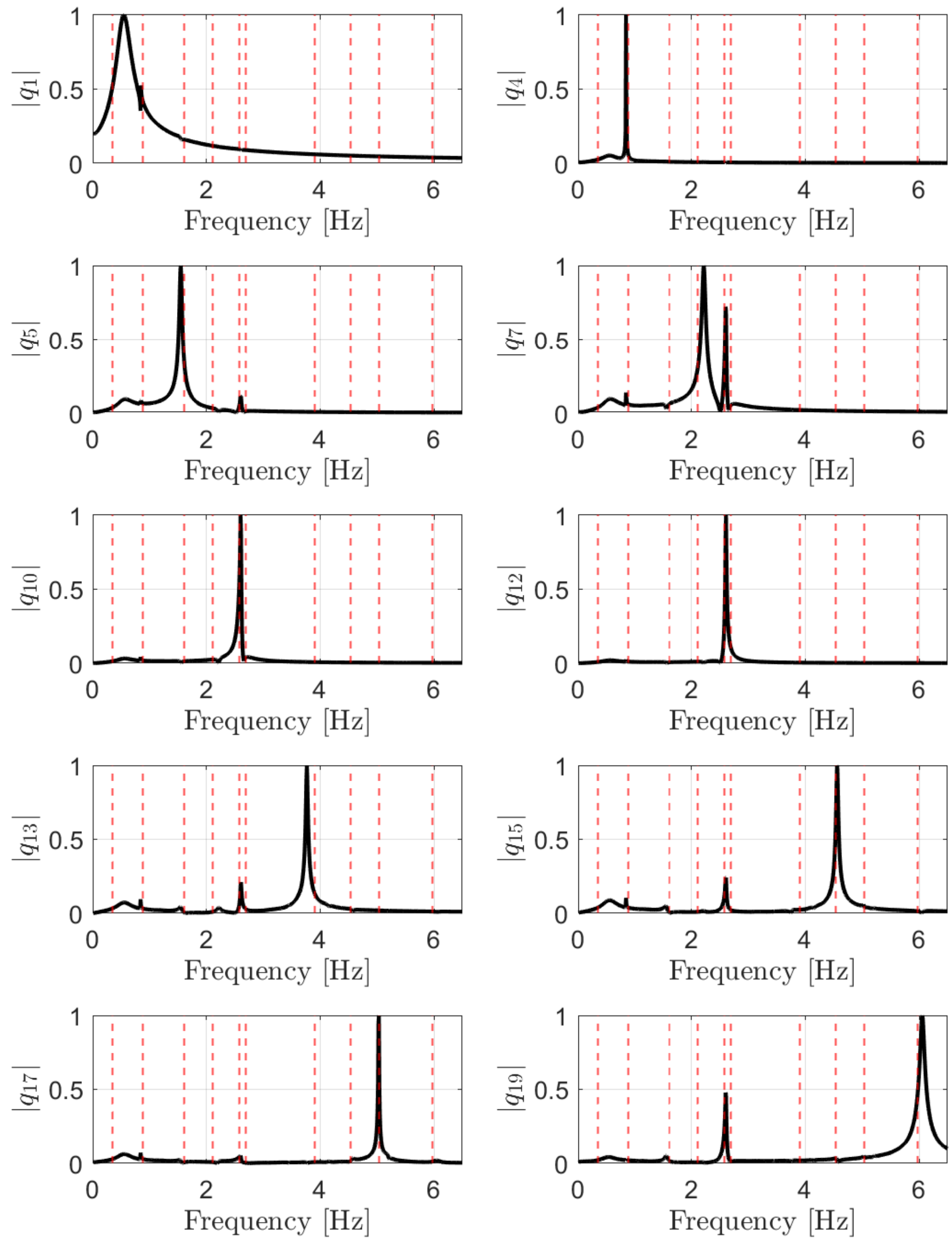

Figure D.48: At critical speed $V_\infty = 156\,\mathrm{m/s}$, responses in the frequency domain of modes corresponding to the left joined-wing for the case with structural torsional damage and freestream direction $(0°, 5°, 0°)$.

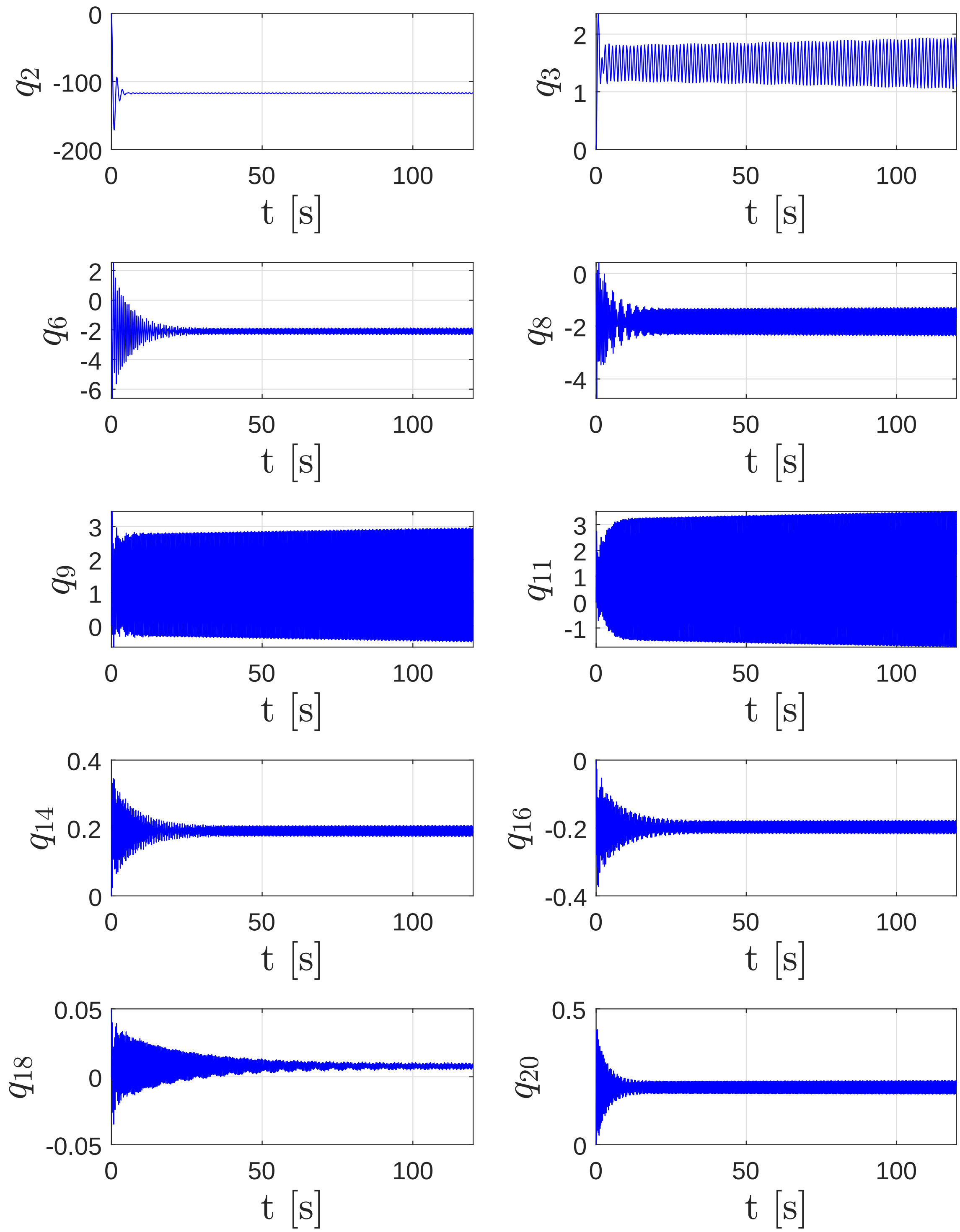

Figure D.49: Time responses of modes corresponding to the right joined-wing for the case with structural torsional damage at supercritical speed $V_\infty = 165\,\mathrm{m/s}$ oand freestream direction $(0°, 5°, 0°)$.

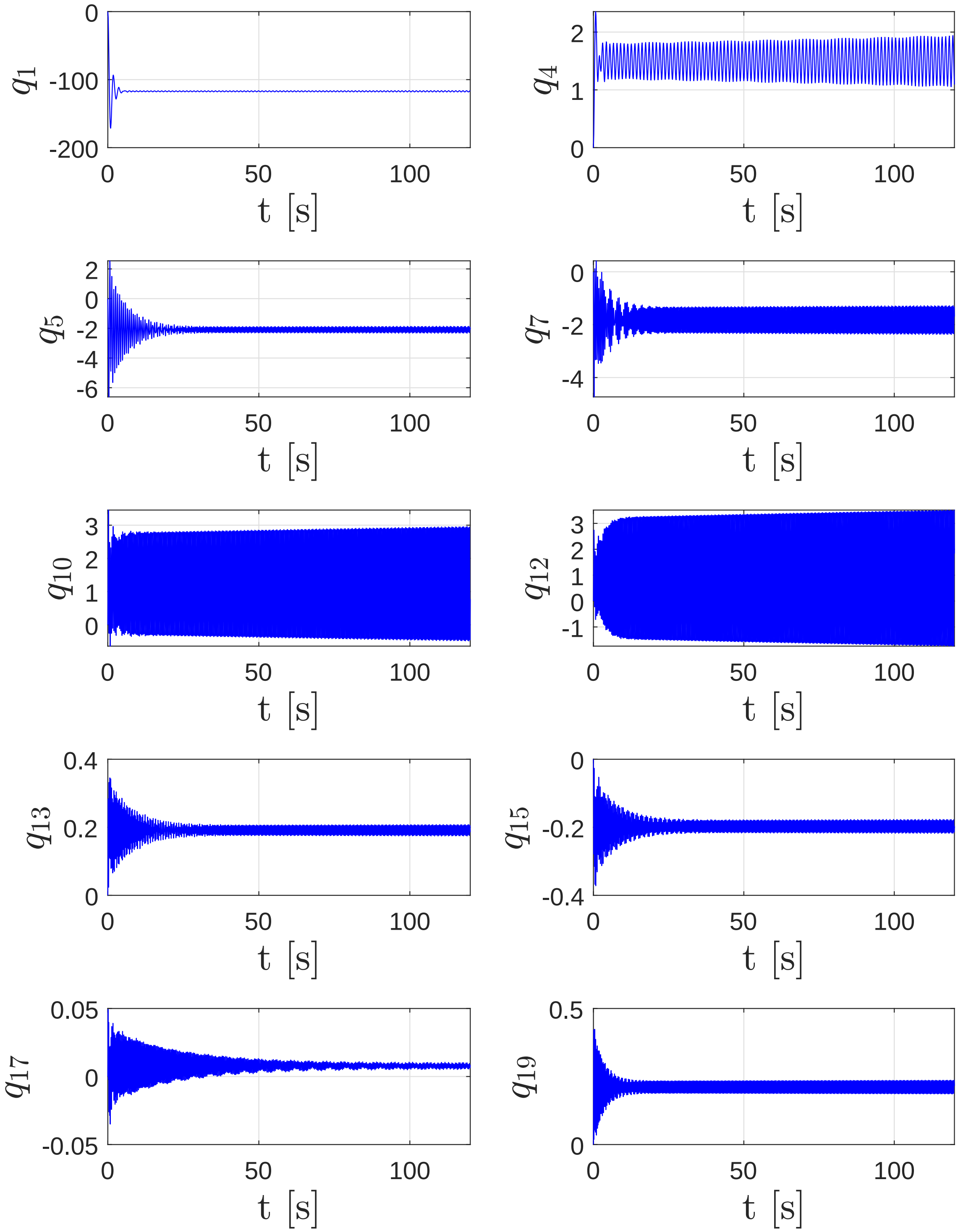

Figure D.50: Time responses of modes corresponding to the left joined-wing for the case with structural torsional damage at supercritical speed $V_\infty = 165\,\mathrm{m/s}$ and freestream direction $(0°, 5°, 0°)$.

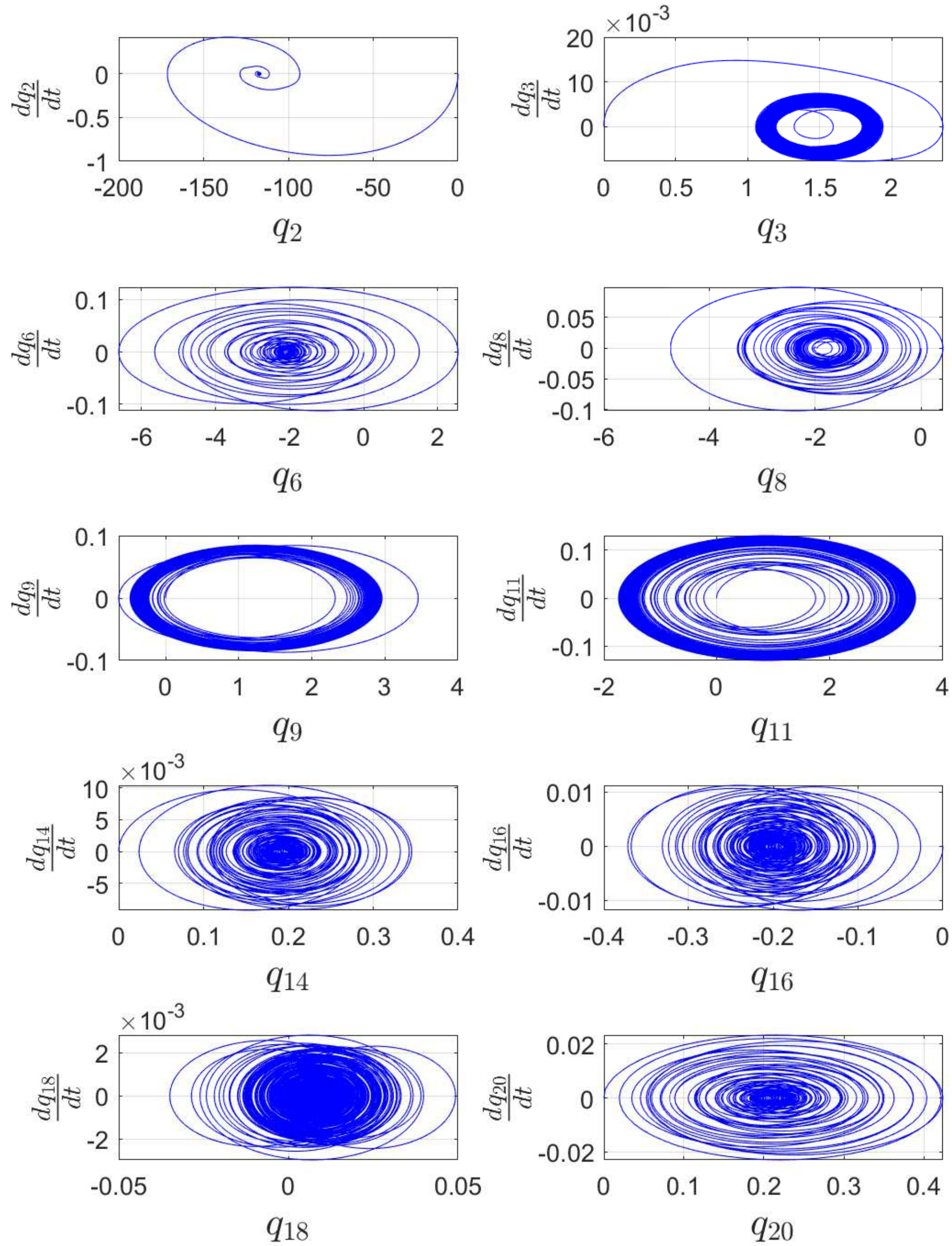

Figure D.51: At supercritical speed $V_\infty = 165\,\mathrm{m/s}$, projections in phase planes of modes corresponding to the right joined-wing for the case with structural torsional damage and freestream direction $(0^\circ, 5^\circ, 0^\circ)$.

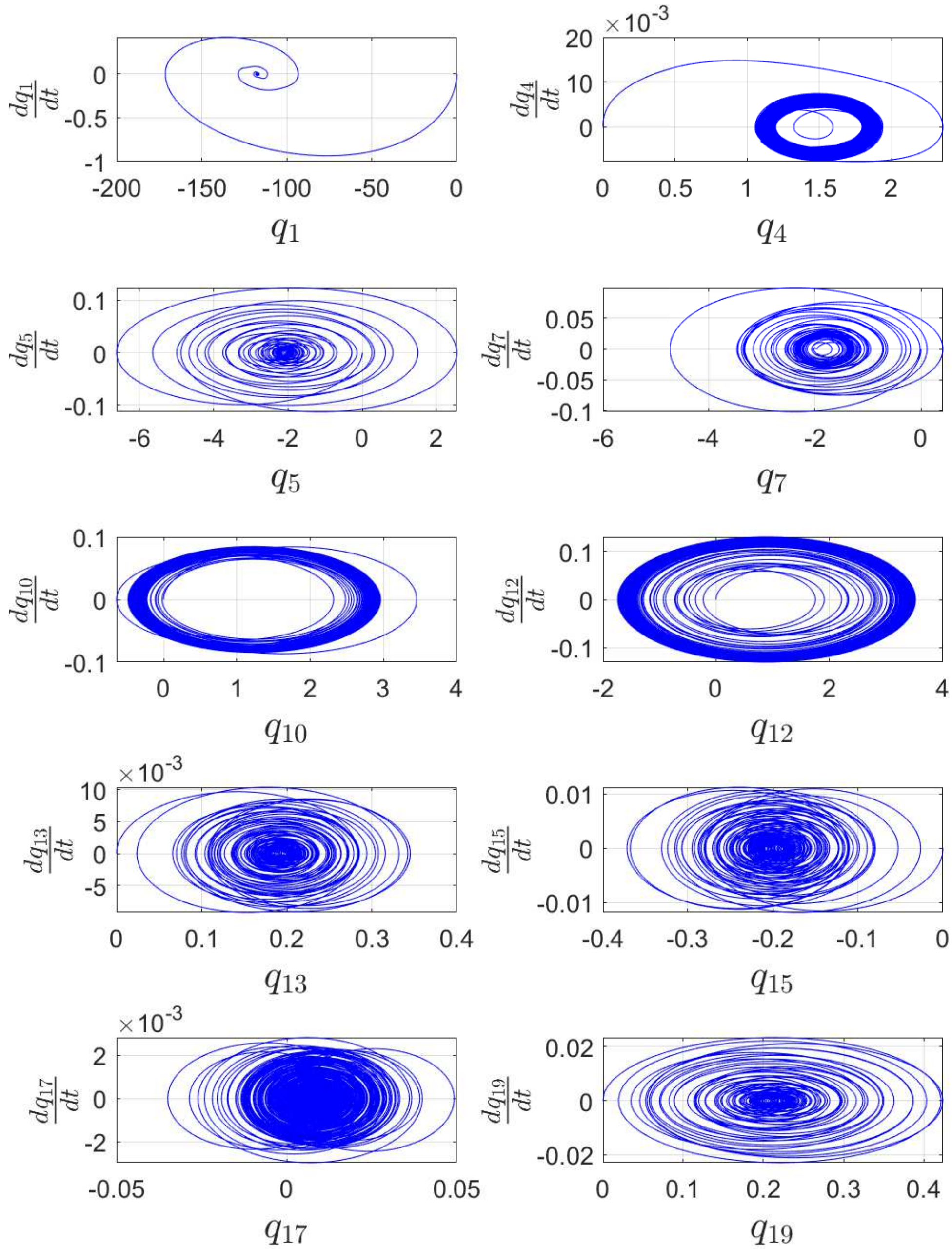

Figure D.52: At supercritical speed $V_\infty = 165\,\mathrm{m/s}$, projections in phase planes of modes corresponding to the right joined-wing for the case with structural torsional damage and freestream direction $(0°, 5°, 0°)$.

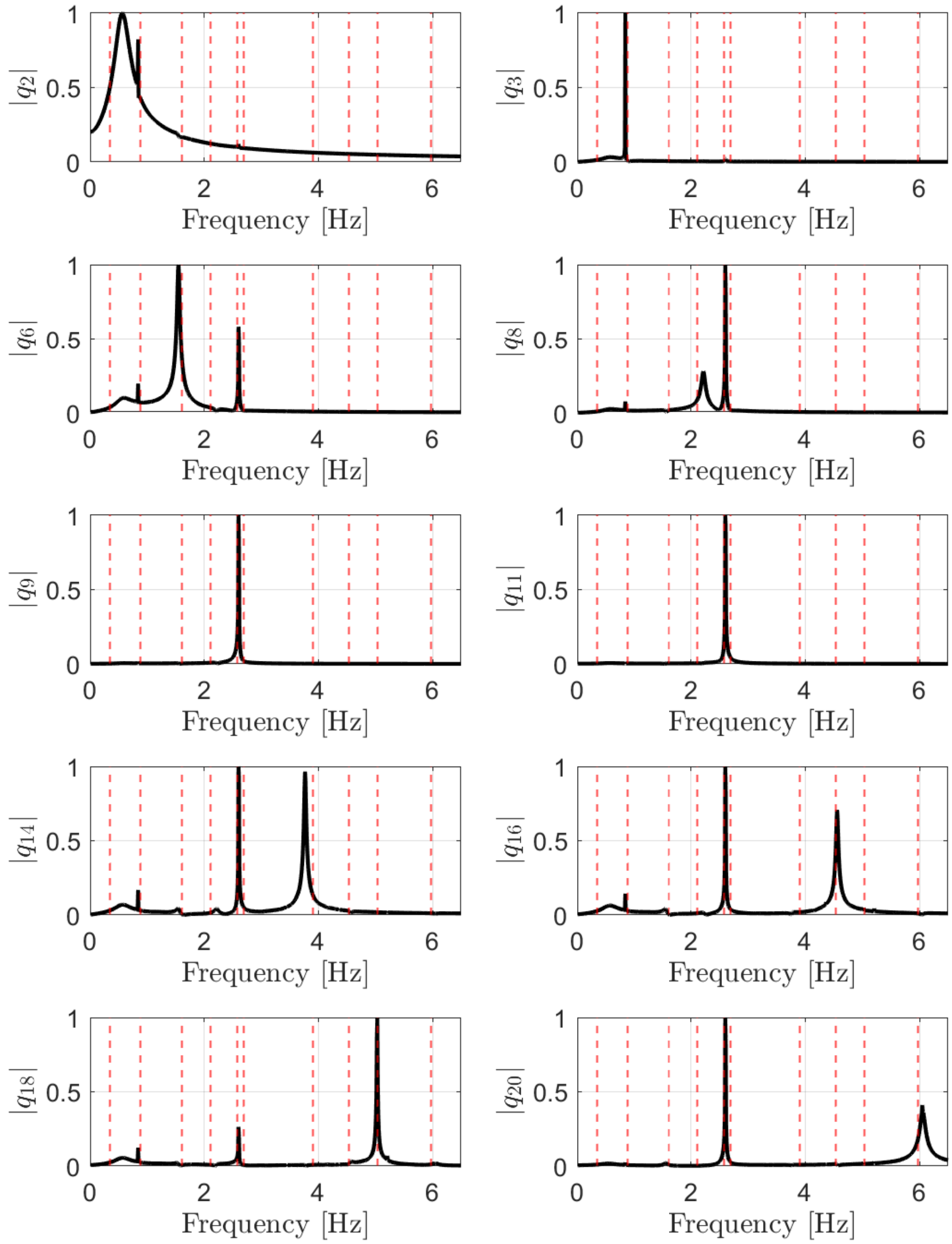

Figure D.53: At supercritical speed $V_\infty = 165$ m/s, responses in the frequency domain of modes corresponding to the right joined-wing for the case with structural torsional damage and freestream direction $(0°, 5°, 0°)$.

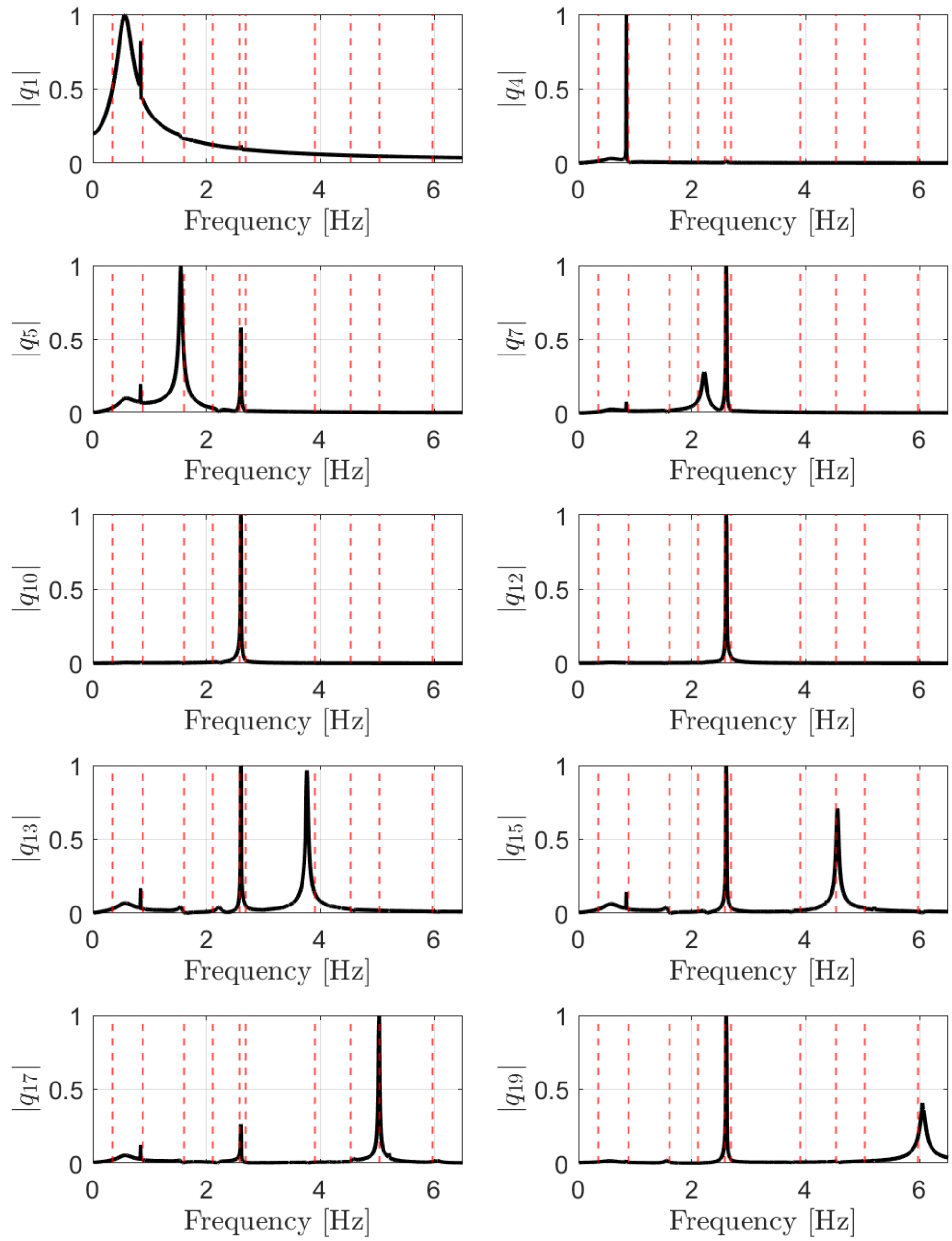

Figure D.54: At supercritical speed $V_\infty = 165$ m/s, responses in the frequency domain of modes corresponding to the left joined-wing for the case with structural torsional damage and freestream direction $(0°, 5°, 0°)$.

Bibliography

[1] N. S. Green, "Structural optimization of joined-wing beam model with bend-twist coupling using equivalent static loads," Master's thesis, Air Force Institute of Technology, Wright-Patterson AFB, Ohio, 2009.

[2] C. P. Tilmann, "Emerging aerodynamic technologies for high-altitude long-endurance sensorcraft uavs," Tech. Rep. ADA428754, Air Vehicles Directorate, U.S. Air Force Research Lab, Wright-Patterson AFB, Ohio, November 2002.

[3] R. K. Nangia, M. E. Palmer, and C. P. Tilmann, "Unconventional high aspect ratio joined-wing aircraft with aft and forward swept wing tips," in *41st Aerospace Sciences Meeting and Exhibit*, p. 605, 2003.

[4] T.-S. S. Hsu, T. Fitzgerald, V. P. Nguyen, T. Patel, and B. Balachandran, "Motion visualization and estimation for flapping wing systems," *Acta Mechanica Sinica*, vol. 33, no. 2, pp. 327–340, 2017.

[5] S. Preidikman, *Numerical Simulations of Interactions among Aerodynamics, Structural Dynamics, and Control Systems.* PhD thesis, Virginia Polytechnic Institute and State University, Blacksburg, Virginia, 1998.

[6] T. Kalmar-Nagy and I. Stanciulescu, "Can complex systems really be simulated?," *Applied Mathematics and Computation*, vol. 227, pp. 199–211, 2014.

[7] C. Gomes, C. Thule, D. Broman, P. G. Larsen, and H. Vangheluwe, "Co-simulation: State of the art," *arXiv preprint arXiv:1702.00686*, 2017.

[8] C. Gomes, C. Thule, D. Broman, P. G. Larsen, and H. Vangheluwe, "Co-simulation: A survey," *ACM Computing Surveys (CSUR)*, vol. 51, no. 3, p. 49, 2018.

[9] T. Fitzgerald, M. Valdez, M. Vanella, E. Balaras, and B. Balachandran, "Flexible flapping systems: Computational investigations into fluid-structure interactions," *The Aeronautical Journal*, vol. 115, no. 1172, pp. 593–604, 2011.

[10] B. A. Roccia, S. Preidikman, and B. Balachandran, "Computational dynamics of flapping wings in hover flight: a co-simulation strategy," *AIAA Journal*, vol. 55, no. 6, pp. 1806–1822, 2017.

[11] S. Preidikman, B. A. Roccia, M. L. Verstraete, M. F. Valdez, D. T. Mook, and B. Balachandran, "Computational aeroelasticity of flying robots with flexible wings," in *Aerial Robots: Aerodynamics, Control and Applications* (O. D. L. Mejia and J. A. E. G. Gomez, eds.), ch. 1, pp. 3–30, InTech, 2017.

[12] A. Varello, E. Carrera, and L. Demasi, “Vortex lattice method coupled with advanced one-dimensional structural models,” *Journal of Aeroelasticity and Structural Dynamics*, vol. 2, no. 2, pp. 53–78, 2011.

[13] J. Murua, R. Palacios, and J. M. R. Graham, “Applications of the unsteady vortex-lattice method in aircraft aeroelasticity and flight dynamics,” *Progress in Aerospace Sciences*, vol. 55, pp. 46–72, 2012.

[14] C. Riso, G. Riccardi, and F. Mastroddi, “Nonlinear aeroelastic modeling via conformal mapping and vortex method for a flat-plate airfoil in arbitrary motion,” *Journal of Fluids and Structures*, vol. 62, pp. 230–251, 2016.

[15] J. Wolkovitch, “The joined wing: An overview,” *Journal of Aircraft*, vol. 23, no. 3, pp. 161–178, 1986.

[16] E. Livne, “Aeroelasticity of joined-wing airplane configurations: Past work and future challenges - a survey,” in *42nd AIAA/ASME/ASCE/AHS/ASC Structures, Structural Dynamics, and Materials Conference*, p. 1370, 2001.

[17] C. C. Rasmussen, R. A. Canfield, and M. Blair, “Joined-wing sensor-craft configuration design,” *Journal of Aircraft*, vol. 43, no. 5, pp. 1471–1478, 2006.

[18] C. E. S. Cesnik and W. Su, “Nonlinear aeroelastic modeling and analysis of fully flexible aircraft,” in *46th AIAA/ASME/ASCE/AHS/ASC Structures, Structural Dynamics & Materials Conference*, p. 2169, 2005.

[19] R. D. Snyder, J. Hur, D. D. Strong, and P. S. Beran, “Aeroelastic analysis of a high-altitude long-endurance joined-wing aircraft,” in *46th*

AIAA/ASME/ASCE/AHS/ASC Structures, Structural Dynamics and Materials Conference, p. 1948, 2005.

[20] W. Su, Y. Huang, and J. R. Hammerton, "Nonlinear aeroelasticity of highly flexible joined-wing aircraft using unsteady vortex-lattice method," in *58th AIAA/ASCE/AHS/ASC Structures, Strucutral Dynamics, and Materials Conference*, p. 1353, 2017.

[21] D. A. Peters, S. Karunamoorthy, and W.-M. Cao, "Finite state induced flow models. i-two-dimensional thin airfoil," *Journal of Aircraft*, vol. 32, no. 2, pp. 161–178, 1995.

[22] J. Katz and A. Plotkin, *Low-speed aerodynamics*, vol. 13. Cambridge university press, 2001.

[23] C. Chabalko, T. Fitzgerald, and B. Balachandran, "Gpgpu implementation and benchmarking of the unsteady vortex lattice method," in *51st AIAA Aerospace Sciences Meeting Including the New Horizons Forum and Aerospace Exposition*, p. 288, 2013.

[24] C. Chabalko and B. Balachandran, "Gpu based simulations of physical systems characterized by mobile discrete interactions," *BHV Topping and P. Ivanyi (Editor),Developements in Parallel, Distributed, Grid and Cloud Computing for Engineering, Saxe-Cobrug Publications, Stirlingshire, UK*, pp. 95–124, 2013.

[25] C. C. Chabalko and B. Balachandran, "Implementation and benchmarking of two-dimensional vortex interactions on a graphics processing unit," *Journal of Aerospace Information Systems*, vol. 11, no. 6, pp. 372–385, 2014.

[26] D. Fleischmann, S. Weber, and M. M. Lone, "Fast computational aeroelastic analysis of helicopter rotor blades," in *2018 AIAA Aerospace Sciences Meeting*, p. 1044, 2018.

[27] J. Dongarra and F. Sullivan, "Guest editors introduction: The top 10 algorithms," *Computing in Science & Engineering*, vol. 2, no. 1, p. 22, 2000.

[28] L. Greengard and V. Rokhlin, "A fast algorithm for particle simulations," *Journal of computational physics*, vol. 73, no. 2, pp. 325–348, 1987.

[29] J. Carrier, L. Greengard, and V. Rokhlin, "A fast adaptive multipole algorithm for particle simulations," *SIAM journal on scientific and statistical computing*, vol. 9, no. 4, pp. 669–686, 1988.

[30] L. Greengard and V. Rokhlin, "A new version of the fast multipole method for the laplace equation in three dimensions," *Acta numerica*, vol. 6, pp. 229–269, 1997.

[31] H. Cheng, L. Greengard, and V. Rokhlin, "A fast adaptive multipole algorithm in three dimensions," *Journal of computational physics*, vol. 155, no. 2, pp. 468–498, 1999.

[32] N. A. Gumerov, R. Duraiswami, and E. A. Borovikov, "Data structures, optimal choice of parameters, and complexity results for generalized multilevel

fast multipole methods in d dimensions," tech. rep., University of Maryland Institute for Advanced Computer Studies, 2003.

[33] N. A. Gumerov and R. Duraiswami, *Fast multipole methods for the Helmholtz equation in three dimensions.* Elsevier, 2005.

[34] N. A. Gumerov and R. Duraiswami, "Efficient fmm accelerated vortex methods in three dimensions via the lamb–helmholtz decomposition," *Journal of Computational Physics*, vol. 240, pp. 310–328, 2013.

[35] P. Collins, P. Bernard, and B. MacCall, "Modeling thermally driven flow problems with a grid-free vortex filament scheme: Part 1," tech. rep., US Army Research Labatory, Adelphi, MD, 2018.

[36] T. R. Ricciardi, W. R. Wolf, and A. M. Bimbato, "Fast multipole method applied to lagrangian simulations of vortical flows," *Communications in Nonlinear Science and Numerical Simulation*, vol. 51, pp. 180–197, 2017.

[37] R. C. Cheung, C. Wales, D. Rezgui, J. E. Cooper, and T. Wilson, "Modelling of folding wing-tip devices for gust loads alleviation," in *2018 AIAA/ASCE/AHS/ASC Structures, Structural Dynamics, and Materials Conference*, p. 0462, 2018.

[38] N. A. Gumerov and R. Duraiswami, "Fast multipole methods on graphics processors," *Journal of Computational Physics*, vol. 227, no. 18, pp. 8290–8313, 2008.

[39] R. Yokota, T. Narumi, R. Sakamaki, S. Kameoka, S. Obi, and K. Yasuoka, "Fast multipole methods on a cluster of gpus for the meshless simulation of turbulence," *Computer Physics Communications*, vol. 180, no. 11, pp. 2066–2078, 2009.

[40] Q. Hu, N. A. Gumerov, and R. Duraiswami, "Gpu accelerated fast multipole methods for vortex particle simulation," *Computers & Fluids*, vol. 88, pp. 857–865, 2013.

[41] S. Deng, C. Jiang, Y. Wang, and H. Wang, "Acceleration of unsteady vortex lattic method via dipole panel fast multipole method," *Chinese Journal of Aeronautics*, pp. 1–16, 2020.

[42] B. Jones, P. Dunning, and A. Maheri, "The double-tree method: An $o(n)$ unsteady aerodynamic lifting surface method," *International Journal of Numerical Methods in Fluids*, pp. 1–21, 2020.

[43] F. Darema, "Dynamic data driven applications systems: A new paradigm for application simulations and measurements," in *International Conference on Computational Science*, pp. 662–669, Springer, 2004.

[44] C. Farhat and D. Amsallem, "Recent advances in reduced-order modeling and application to nonlinear computational aeroelasticity," in *46th AIAA Aerospace Sciences Meeting and Exhibit*, p. 562, 2008.

[45] D. Allaire, K. David, M. Lecerf, L. Mainini, and K. Wilcox, "Multifidelity dddas methods with application to a self-aware aerospace vehicle," *Procedia Computer Science*, vol. 29, pp. 1182–1192, 2014.

[46] X. Zhao, R. Kania, A. B. Kebbie-Anthony, S. Azarm, and B. Balachandran, "Dynamic data-driven aeroelastic response prediction with discrete sensor observations," in *2018 AIAA Non-Deterministic Approaches Conference*, p. 2173, 2018.

[47] X. Zhao, S. Azarm, and B. Balachandran, "Dynamic data-driven spatiotemporal system behavior prediction with simulations and sensor measurement data," in *ASME 2018 International Design Engineering Technical Conferences and Computers and Information in Engineering Conference*, pp. V02BT03A060–V02BT03A060, 2018.

[48] R. Kania, A. B. Kebbie-Anthony, X. Zhao, S. Azarm, and B. Balachandran, "Dynamic data-driven approach for unmanned aircraft systems and aeroelastic response analysis," in *Handbook of Dynamic Data Driven Applications Systems* (E. Blasch, S. Ravela, and A. Aved, eds.), pp. 193–211, Springer, Cham, 2018.

[49] X. Zhao, A. B. Kebbie-Anthony, S. Azarm, and B. Balachandran, "Dynamic data-driven multi-step-ahead prediction with simulation data and sensor measurements," *AIAA Journal*, vol. 57, no. 6, pp. 2270–2279, 2019.

[50] X. Zhao, S. Azarm, and B. Balachandran, "Online data-driven prediction of spatio-temporal system behavior using high-fidelity simulations and sparse sen-

sor measurements," *Journal of Mechanical Design*, vol. 143, no. 2, p. 021701, 2021.

[51] V. Stojanović, P. Ribeiro, and S. Stoykov, "Non-linear vibration of timoshenko damaged beams by a new p-version finite element method," *Computers & Structures*, vol. 120, pp. 107–119, 2013.

[52] C. Wei and X. Shang, "Analysis on nonlinear vibration of breathing cracked beam," *Journal of Sound and Vibration*, vol. 461, p. 114901, 2019.

[53] H. S. Hoseini, *A Joined 3D/1D Finite Element Method for Aeroservoelastic Analysis of Damage HALE Aircraft Wings*. PhD thesis, Georgia Institute of Technology, Atlanta, Goergia, USA, 2018.

[54] H. S. Hoseini and D. H. Hodges, "Nonlinear flutter and limit-cycle oscillations of damaged highly flexible composite wings," *Nonlinear Dynamics*, vol. 97, no. 1, pp. 247–268, 2019.

[55] H. S. Hoseini and D. H. Hodges, "Aeroelastic stability analysis of damaged high-aspect-ratio composite wings," *Journal of Aircraft*, vol. 56, no. 5, pp. 1794–1808, 2019.

[56] H. S. Hoseini and D. H. Hodges, "Flutter suppression for damaged high-aspect-ratio wings: Implementations in abaqus," *AIAA Journal*, vol. 57, no. 10, pp. 4355–4367, 2019.

[57] R. Tenenbaum, L. Stutz, and K. Fernandes, "Comparison of vibration and wave propagation approaches applied to assess damage influence on the behavior of

euler-bernoulli beams," *Computers & structures*, vol. 89, no. 19-20, pp. 1820–1828, 2011.

[58] A. Tomaszewska, "Influence of statistical errors on damage detection based on structural flexibility and mode shape curvature," *Computers & structures*, vol. 88, no. 3-4, pp. 154–164, 2010.

[59] L. Mainini and K. E. Willcox, "Data to decisions: Real-time structural assessment from sparse measurements affected by uncertainty," *Computers & Structures*, vol. 182, pp. 296–312, 2017.

[60] A. B. Kebbie-Anthony, N. A. Gumerov, S. Preidikman, B. Balachandran, and S. Azarm, "Fast multipole method for nonlinear, unsteady aerodynamic simulations," in *2018 AIAA Modeling and Simulation Technologies Conference*, p. 1929, 2018.

[61] A. B. Kebbie-Anthony, N. A. Gumerov, S. Preidikman, B. Balachandran, and S. Azarm, "Fast multipole accelerated unsteady vortex lattice method based computations," *Journal of Aerospace Information System*, vol. 11, no. 6, pp. 237–248, 2019.

[62] T. Cebeci, M. Platzer, H. Chen, K.-C. Chang, and J. P. Shao, *Analysis of Low-Speed Unsteady Airfoil Flows.* Springer Berlin Heidelberg, 2005.

[63] L. R. Ceballos, *Aeroelasticidad No-Lineal de Vehculos Areos No-Tripulados con una Configuracin No-Convencional de Alas Unidas.* PhD thesis, Universidad Nacional de Cordoba, Cordoba, Argentina, 2017.

[64] R. D. Cook, D. S. Malkus, M. E. Plesha, and R. J. Witt, *Concepts and Applications of Finite Element Analysis*. John Wiley & Sons, 2007.

[65] B. Carnahan, H. A. Luther, and J. O. Wilkes, *Applied Numerical Methods*. John Wiley and Sons, Inc., 1969.

[66] O. A. Kandil, D. T. Mook, and A. H. Nayfeh, "New convergence criteria for the vortex-lattice models of leading-edge separation," *Vortex-Lattice Utilization*, vol. 76, p. 285, 1976.

[67] Y. C. Fung, *An Introduction to the Theory of Aeroelasticity*. Courier Dover Publications, 2008.

[68] T. W. Strganac, *A Numerical Model of Unsteady, Subsonic Aeroelastic Behavior*. PhD thesis, Virginia Polytechnic Institute and State University, Blacksburg, Virginia, USA, 1987.

[69] A. H. Nayfeh and B. Balachandran, *Applied Nonlinear Dynamics: Analytical, Computational, and Experimental Methods*. John Wiley & Sons, 2008.

[70] J. J. Thomsen, *Vibrations and stability*, vol. 2. Springer, 2003.